Characterising the deep structure and seismic signature of an exhumed ductile shear zone.

Katie Farrell

Submitted in accordance with the requirements for the degree of
Doctor of Philosophy.

The University of Leeds

School of Earth and Environment

January 2017

Acknowledgements

First of all, I would like to thank my supervisors; Geoffrey Lloyd, Richard Phillips and Sebastian Rost. Thank you to Geoff for the invaluable discussions that ranged from science to drizzle cake and for your diligence in reading all the work I sent (even if I didn't change all the comma's to semi-colons). Thank you to Richard for your initial guidance on the project and not judging me too harshly for forgetting to bring a hammer on sample collecting fieldwork. Finally, thank you to Sebastian for stepping in to be my second supervisor and helping me through the confusing world of seismic modelling.

To the Geobabes and the WI, thank you for being the best bunch of pals I could ask for. Katie, Liz and Tamsin thank you for the laughter, the good food, the adventures and the WI housekeeping tips. When I look back over the last year I really do cherish those weekends, no words could ever do it justice, you really are just the best. Being the last Geobabe over the hurdle has its advantages, thanks for all your messages of support and encouragement over the last few months. A special thanks needs to go to Hannah, without whom, I don't think I would have written chapter six! Your help with gmt, modelling and interpreting those damn wiggles really did help me out of a hole. Also thanks to Laura, whose unending enthusiasm and big smiles really do brighten the day, even when I think my figures are crap.

Office 8.152 (the best office) thank you for providing advice, answering my silly science questions, helping me with gmt code and Matlab and for the welcome distractions. Delia, Fiona, Amicia and Becky thanks for all the dinners (when is it Amicia's turn) and for providing most of the aforementioned distraction, even when I really just wanted you to shut up. Special mention has to go to Bobbi – puppy therapy really does work!

Two people who I have immeasurable gratitude to are Ad and Suz who welcomed me into their home without question last year. I did say I was only staying for 3 months so as I sit here 6 months later I really can't thank them enough. Coming home each day to two genuinely happy souls has been an absolute lifeline. Also, thanks for introducing me to pomegranates, I never looked back.

Thanks must go to the staff of Earth and Environment and Engineering as without them, I would have a pile of awful thin sections, wouldn't be able to analyse them and wouldn't be able to do anything with the data afterward. Harri Wyn Williams, thank you for your patience in guiding me through the process of making thin sections and SEM samples. Richard Walshaw and Duncan Hedges, thank you for your help with all things SEM and for always keeping me in mind when someone cancelled a session. Richard Rigby, thank you

for all your help with broken codes and for never making me feel stupid for asking silly questions. A large part of this project would not have been possible without your help, so thank you.

Lastly, thank you to my family. Mum and Dad for being the best parents, always being in when I wanted to come home, fish and chips, visiting me in Leeds, the endless house moves where you have helped pack, transport and clean and for reading my thesis and removing spurious semi-colons. Also to my sister who I once laughed at for wanting to change her cards to 'Dr Michelle Farrell', I now know exactly what you mean. I guess I should probably mention Dave who, for some unknown reason, decided to stick around. He has seen me at my worst and it is now that I sit down and write this, that I have realised just how much he has helped me get to the end. Now can we go on holiday and climb some rocks?

Abstract

Understanding the behaviour of active continental scale fault zones at depth and how surface displacement is accommodated through the crust is important to improve understanding of large scale tectonics. Various studies on exhumed ductile shear zones have been carried out to investigate the processes that were active during deformation in the mid to lower-crust. This study adds to the growing knowledge by investigating processes recorded in the Uludağ Massif, NW Turkey. The Uludağ Massif and constituent faults provide an analogue for the mid-crust beneath the North Anatolian Fault (NAF) and forms part of a wider study incorporating geodesy and seismology. This study contributes to the wider project by providing a geological context to geodetic and seismological observations made using the DANA array over the NAF.

In the first instance initial field observations are used to analyse the structural architecture of the shear zone to define the large scale structure and kinematics. Microstructures are observed and analysed to provide information on deformation kinematics, temperature, stress and strain rate for the exhumed shear zone. Techniques such as Electron Back Scatter Diffraction (EBSD) provide a data set from which crystal preferred orientation (CPO), CPO intensity and visco plastic self-consistency (VPSC) calibrations are used to consider how strain is distributed across shear zones. Concomitantly, Schmid factor analysis is used to ascertain active crystal slip systems in calcite across the shear zone related to strain localisation and effects such as strain hardening. Seismic properties are then calculated from the CPO to examine how different lithologies and structures within the Uludağ Massif affect the seismic properties using modelling techniques. Synthetic receiver functions are then created from these models and compared against the real seismic data and receiver functions from the DANA array on the NAF itself.

Information on stress, shear strain, temperature and strain-rate build up a picture of localised deformation on strands including the Eskişehir and Bursa Faults over the shear zone on the scale of 100m – 10km. Thin section analysis and Schmid factor analysis show several weakening mechanisms are active along the Eskişehir Fault zone, whilst fault strengthening can be inferred within calcite deformation respectively. These observations have important implications for the contemporary seismogenic response if similar lithologies and structures comprise the current mid-crust beneath the NAF. However, the seismic properties of different lithologies and fabric orientations show little difference on the seismic response but the presence of a fault is obvious and could account for results of natural receiver function study via the DANA array.

Table of Contents

List of Figures

CHAPTER ONE

CHAPTER TWO

CHAPTER THREE

CHAPTER FOUR

CHAPTER FIVE

CHAPTER SIX

CHAPTER SEVEN

1. CHAPTER ONE

Characterising the deep crustal structure of an exhumed ductile shear zone – rationale, objectives and thesis outline.

1.1. Rationale: Aims and objectives

Understanding the behaviour of active continental-scale fault zones at depth, and in particular how displacements observed at the Earth's surface are accommodated through the crust, is crucial to improving understanding of large scale tectonics. Numerous geological studies have been performed on exhumed mid to deep crustal shear zones, specifically to investigate how strain is distributed over the zone of deformation (Norris and Toy, 2014). Advances in techniques over recent years have allowed this approach to be considered in increasing detail and complexity on a variety of scales.

Continental scale faults often have relatively discrete zones of deformation expressed in surface exposures of the brittle upper crust, although these may comprise of damage zones (Rempe et al., 2013). Of major concern is whether this discrete zone of high strain continues down into the ductile regime of the mid-lower crust, splits into numerous higher strain strands or diffuses into relatively wide zones of pervasive ductile deformation (Figure 1.1).

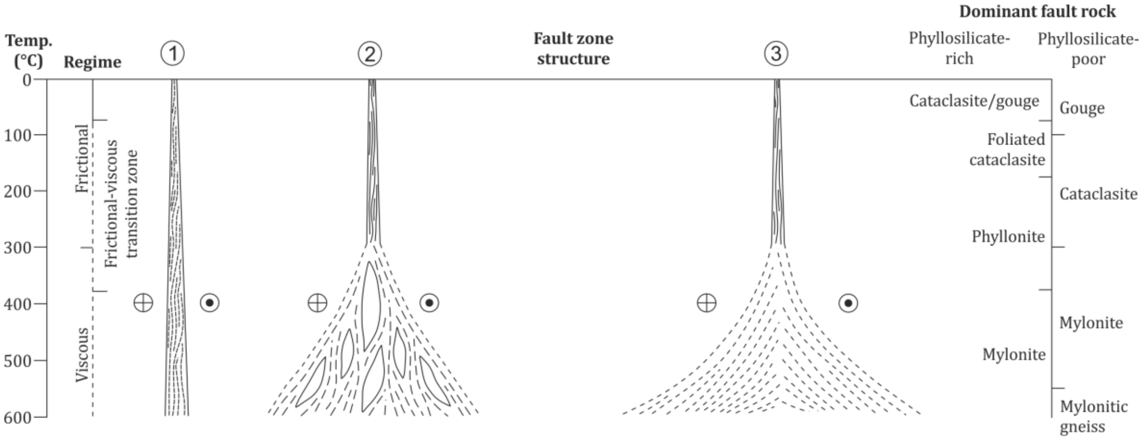

Figure 1.1. Modified from Wallis et al (in press), compiled from (Sibson, 1983, Imber et al., 2008, Norris and Toy, 2014). Fault 1 represents a narrow fault at the surface that extends into the lower crust as a narrow localised feature. Fault 2 shows a narrow fault that divides into localised strands in the lower crust and fault 3 represents a narrow fault at the surface that extends as a diffuse decollement-style zone of deformation in the lower crust.

How strain partitions at depth has important consequences for active fault behaviour over time, including the period of the earthquake cycle. If strain is distributed over wide, creeping, volumes how is this deformation represented in the brittle region of potentially seismogenic behaviour at the 'near surface'.

The North Anatolian Fault (NAF) that runs the length of northern Turkey from east to west is one such continental scale strike slip shear zone. Studying any large scale shear zone is important for the reasons outlined above but it is particularly poignant in this case due to the recent history of the NAF. The NAF has been rupturing progressively westward over its seismic history (Figure 1.2), which proves a real threat to one of Turkey's most populated cities, Istanbul, as the next segment runs close to the city and based on current recurrence times, could be within the next ~30 years.

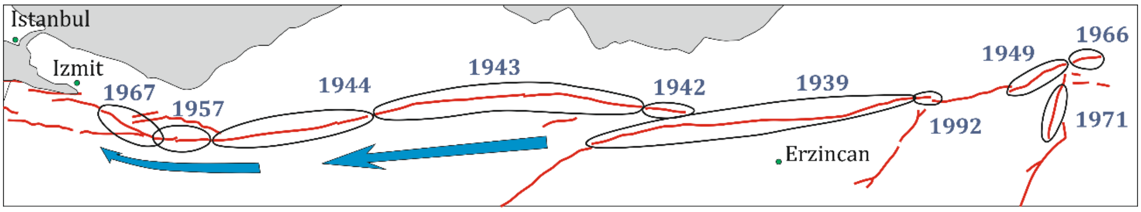

Figure 1.2. Showing the earthquake progression from east to west of the seismic history of the North Anatolian Fault (Stein et al., 1997).

Studying large scale tectonic features such as the NAF requires a multi-faceted approach in order to acquire a detailed picture of the structure beneath the surface. These approaches include geodesy to monitor how the ground is moving at the surface, seismology to understand what the crust looks like beneath the surface and geology to be able to provide context. The geological context comes from studying exhumed mid-crustal shear zones as analogues for the mid-crust beneath active shear zones.

This project is part of a wider study, FaultLab that incorporates the above techniques of geodesy, seismology and geology to study the NAF. A dense array of ~71 stations was installed over the NAF in the area of the 1999 Izmit rupture (Figure 1.3) which was used to image the subsurface and a picture of the ground movement was built up in the same area using geodesy (Kahraman et al., 2015, Hussain et al., 2016, Yamasaki et al., 2014). This study aims to contribute to this wider project by providing a geological context to geodetic and seismological observations using an exhumed ductile shear zone as an analogue for the mid crust beneath the NAF.

Understanding the geology plays a big role in understanding the rheology of the mid crust. Forward modelling using real rock data from an exhumed ductile shear zone used in conjunction with geophysical techniques, such as seismology, can be a really powerful tool when looking at the mid-crust in active shear zones. It allows the features in real seismological data to be attributed to specific modelled structures or lithologies based on their seismic response and seismic properties. Once the structures or rock types are identified the processes that are active within a shear zone, such as strain partitioning or strain hardening, can be investigated together with their effect on the seismological response of the crust and the earthquake cycle.

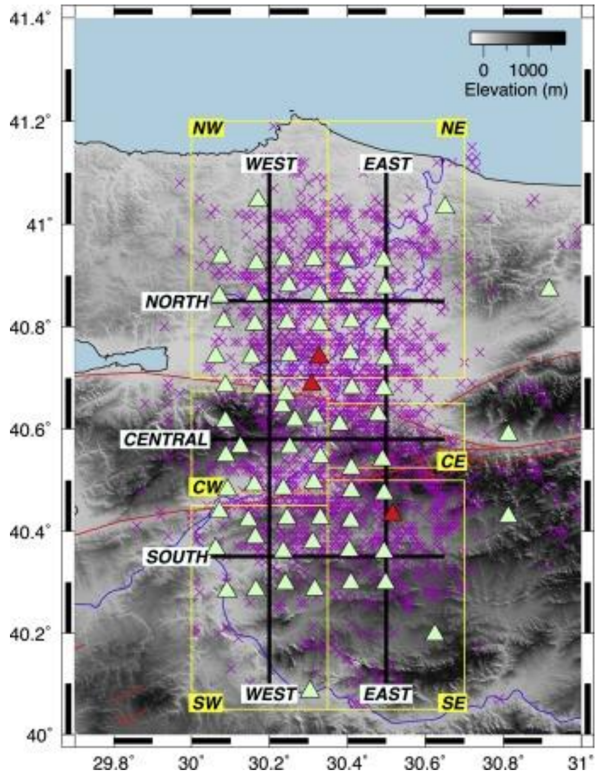

Figure 1.3. Map of the DANA array showing cross sections for receiver functions, relevant in Chapter 6. Green triangles are seismic stations installed as part of the FaultLab study and red triangles are the permanent stations (Kahraman et al., 2015). The general location of this array is shown in Figure 1.4.

At the macro and micro scale, determining the architecture of faults in the mid-lower crust, particularly how the strain is partitioned has important implications on how faults behave on the seismic related time scale. Examining microstructures reveals information on the conditions of deformation (especially temperature), from which estimates of depths at which deformation occurred can be constrained (Burkhard, 1993, Covey-Crump and Rutter, 1989, Stipp et al., 2002, Wallis et al., 2013, Parsons et al., 2016). Microstructures also permit estimations of stress magnitudes via palaeopiezometry (Stipp and Tullis, 2003, Rutter, 1995). From the stress and temperature estimates, strain-rates can be estimated (Rutter, 1995, Stipp et al., 2002), which provide major constraints on how strain is accumulated in ductile regimes and consequently how the ductile deformation feeds back into the seismogenic upper crust. Thus, understanding the detail of the small scale processes that occur during deformation including how strain is partitioned, and fault weakening and strain hardening processes, are important in understanding the deformation and activity of any large scale fault zone.

Using data from in-situ samples to investigate the effects of lithology and structure on seismic properties provides important insights into what governs the seismic response of fault zones. Such ‘real rock’ seismic properties can be used to populate seismic models to investigate how different lithologies and structures (eg rock textures and fabrics such as foliations) influence the seismic response used to interpret shear zones. This directly links into the geophysical study on the North Anatolian fault. By populating models created from field data, the cause of certain responses in seismic studies can be looked at in detail, revealing the structure of shear zones beneath the surface.

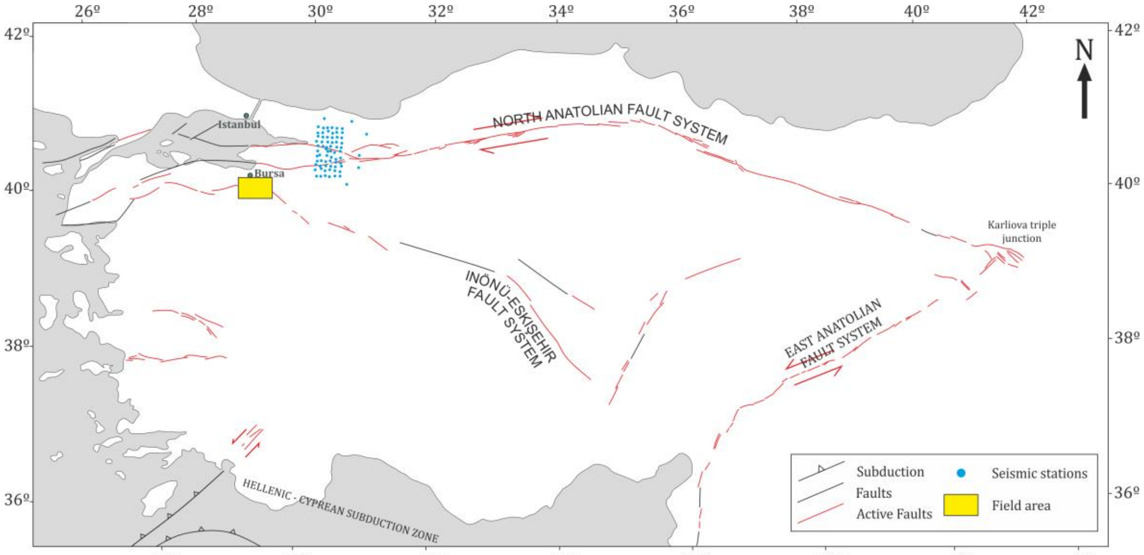

Figure 1.4. Location of the Uludağ Massif study area (yellow box) and the DANA array over the NAF. Active faults from General Directorate of Mineral Reserach and Exploration Publications (Emre et al., 2013).

1.2. Thesis outline

To address the aims and objectives stated in the previous section a number of techniques will be used. These are based around using data obtained from rock samples collected across an exhumed ductile shear zone, the Uludağ Massif, in north western Turkey. The chosen field area to carry out this study is located in NW Turkey, just south of Bursa (Figure 1.4). It is a mid-crustal shear zone comprising predominantly of deformed marble and gneiss, with syn-kinematic (south Uludağ granite) and post-kinematic (central Uludağ granite) intrusions. This area was chosen because it provides an excellent analogue for mid-crust beneath the NAF. It is located within the same terrane, the Sakarya, so it is likely the rocks exhumed here are the same rocks that comprise the mid-crust fault zone of the NAF. It also developed in a comparable tectonic regime, right lateral shear sense with an estimated ~100km of offset. It preceded the NAF in development, initiating in the Oligocene, whilst the NAF developed in the Miocene.

The relevant background literature to the field area and the wider geological context of Anatolia, including the NAF is presented in Chapter 2.

In the first instance initial field observations are used to analyse the structural architecture of the shear zone on the macro-scale in Chapter 3 to obtain information on the large scale structure and kinematics.

Microstructure is observed and analysed in Chapter 4 to provide deformation kinematics, temperature, stress and strain rate information for the exhumed shear zone. From this information how deformation is distributed across the Uludağ Shear Zone can be studied.

Techniques such as Electron Back Scatter Diffraction (EBSD) provides a data set from which crystal preferred orientation (CPO), CPO intensity and visco plastic self-consistency (VPSC) calibration are used to look at how strain is distributed across shear zones in Chapter 5. Alongside this Schmid factor analysis is used to ascertain active slip systems in calcite across the shear zone related to strain localisation and effects such as strain hardening (Chapter 5).

The seismic properties are calculated from the CPO in Chapter 6 to examine how different lithologies and structures within the Uludağ Massif affect the seismic properties. From this, the effects on the seismic response is investigated using cross sections constructed from maps and field observations, populated with the seismic properties of the samples collected. Synthetic receiver functions are then created from these models and compared against the real seismic data and receiver functions from the DANA array on the NAF itself (Figure 1.4).

2. CHAPTER TWO

Geology and tectonics of Anatolia and the Uludağ Massif field area.

2.1. Introduction

This chapter presents background information on the tectonic and geological framework of the large scale tectonics of Anatolia, the North Anatolian Fault (NAF) and the field area (Figure 2.1 and Figure 2.2). Anatolia is widely considered to be located on a small tectonic plate, the Anatolian plate, which is situated between the northward converging Arabian plate and African plates, and the Eurasian plate (McKenzie, 1972). Due to its location, the Anatolian plate exhibits complicated tectonics, with escape-like strike-slip tectonics to the north and extension in the south west (Reilinger et al., 2006). Anatolian tectonics are further complicated by its long accretion history with numerous seaways opening and closing during its formation (Stampfli, 2000). The following information is compiled from existing literature and provides a tectonic and geological context to the whole study.

2.2. Large scale geology and tectonics

Turkey is located at the point where the Arabian, African and Eurasian plates interact which results in the complicated tectonics expressed on the surface (Figure 2.3) (McKenzie, 1972). Broadly, the tectonics can be split into four main regimes based on present day tectonic activity, these are the North and Central, Eastern and Western Anatolian provinces (Figure 2.1) (Selçuk and Göktan, 2012). The complicated tectono-stratigraphy due to the evolution of Anatolia can also be considered according to provenance and dominant units as the Pontides, the Anatolide-Taurides and the Arabian Platform (Figure 2.2) (Okay, 2008, Okay and Tuysuz, 1999).

2.2.1. Tectono-stratigraphic terranes

Anatolia consists of three main tectonic units; the Pontides, the Anatolide-Taurides and the Arabian Platform (Okay, 2008). Figure 2.1 shows these tectonic units and their relationship with each other. The Pontides show characteristics of the Laurasian continent (north of the Tethys oceans) and consist of three main terranes, the Strandja, İstanbul and Sakarya (Okay, 2008, Okay et al., 2001). This tectonic unit has been heavily deformed and shows evidence for Variscan (250Ma), Cimmeride (200-150Ma) and Alpide (65-2.5Ma) orogenic events (Okay, 2008). The Sakarya Zone is of particular interest in this study as the field area, the Uludağ Massif, is located within the crystalline basement of this terrane.

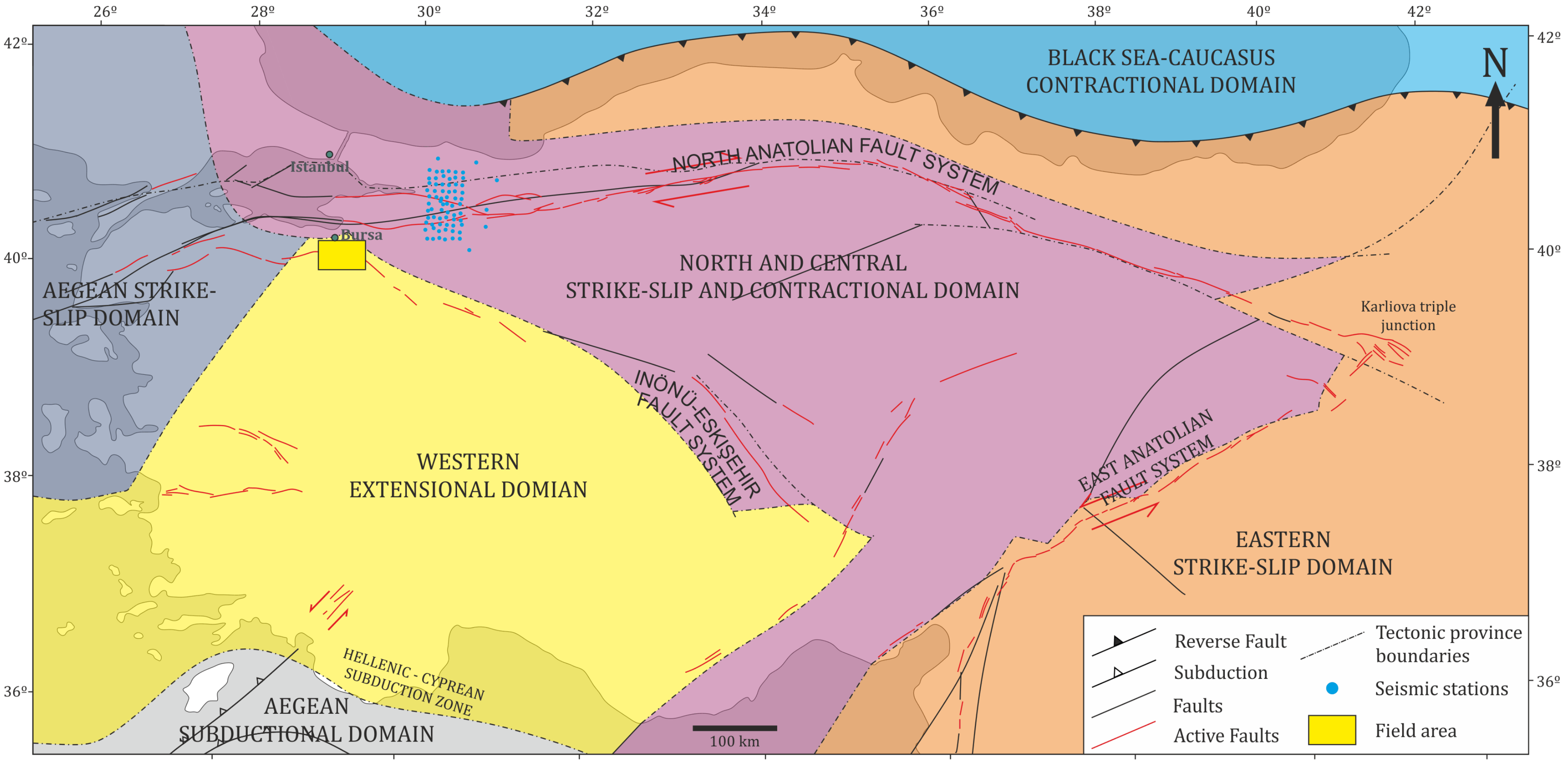

Figure 2.1. Tectonic provinces of Anatolia based on present day activity. Adapted from (Selçuk and Göktan, 2012). Arrows indicated shear sense on strike slip faults. The field area is located at the boundary between extensional tectonics to the south west and strike slip and contractional regimes associated with ‘escape’ tectonics to the north, which includes the North Anatolian Fault. The eastern strike-slip domain contains the East Anatolian Fault and is dominated by strike-slip tectonics, as is the Aegean strike-slip domain. The Aegean subductional domain contains the Hellenic-Cyprean subduction zone.

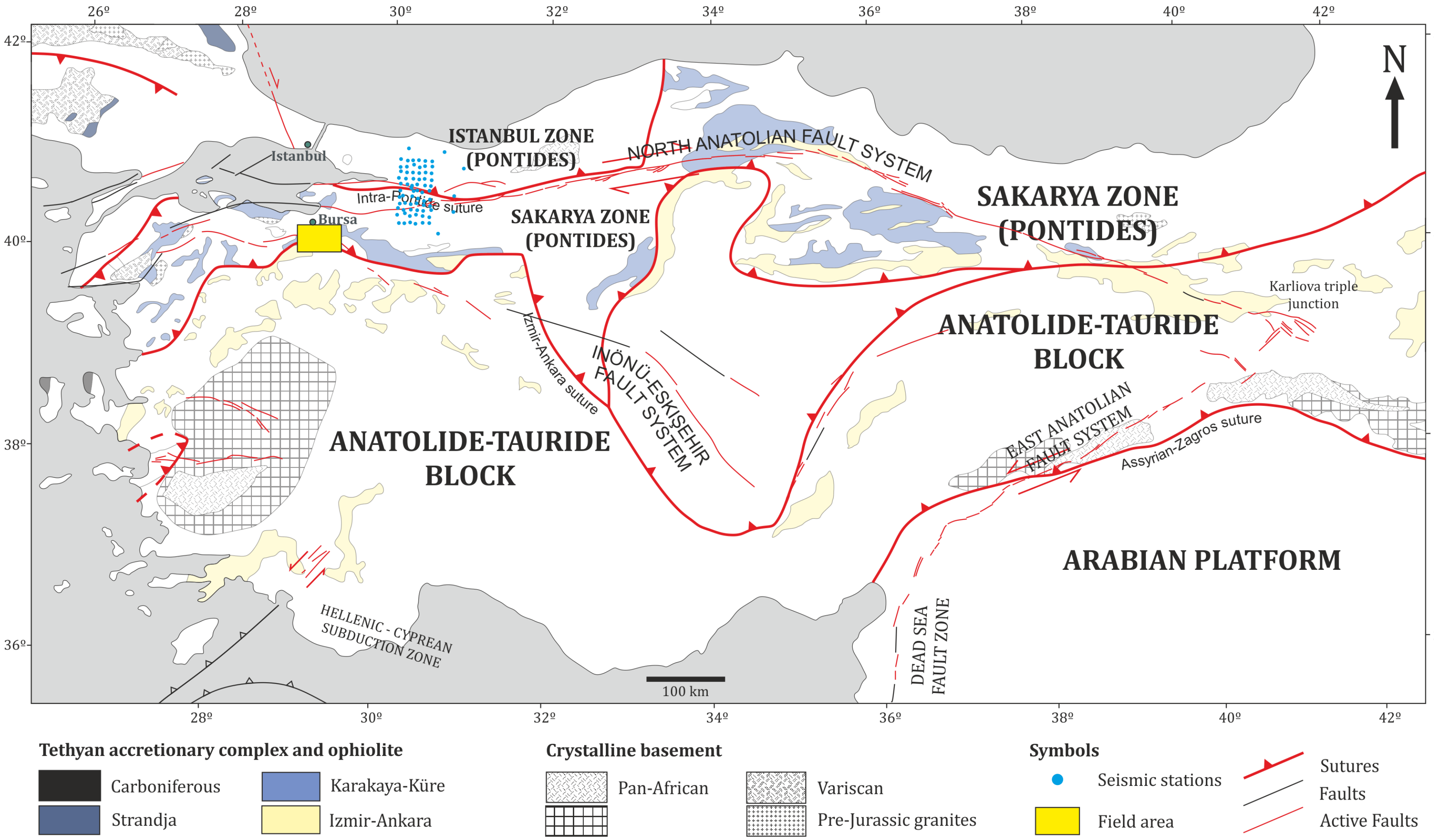

Figure 2.2. Showing the terranes and sutures within Turkey. The field area and location of the DANA seismometer stations are also shown, yellow box and blue dots respectively (Okay, 2008, Okay and Tuysuz, 1999).

The North Anatolian Fault Zone (NAFZ) border the Sakarya Zone and will be discussed in more detail later.

The Anatolide Taurides comprise a Palaeozoic stratigraphy similar to the Arabian Platform to the southeast (Figure 2.7). This terrane was situated in the footwall of collision during the Alpide orogeny and underwent strong deformation and metamorphism (Okay, 2008, Okay and Tuysuz, 1999). The varying degrees of Alpide deformation within the thrust pile have led to the division of the Anatolide-Taurides into 3 zones; the northern Tavşanlı Zone consisting of Cretaceous blueschists; the central Afyon Zone comprising Palaeocene Barrovian-type metmorphism; and the southern Menderes Massif characterised by Eocene Barrovian-type Eocene metamorphics (Okay and Tuysuz, 1999). The Anatolide-Taurides that lie to the south of the Uludağ Massif belong to the Tavşanli Zone. The Arabian Platform displays Gondwana affinity and consists of a Pan-African basement overlain by a Palaeozoic to Tertiary sedimentary sequence (Okay, 2008). Continental collision occurred during the Miocene resulting in Anatolide-Tauride terrane material also being emplaced over the Arabian Platform (Moix et al., 2008).

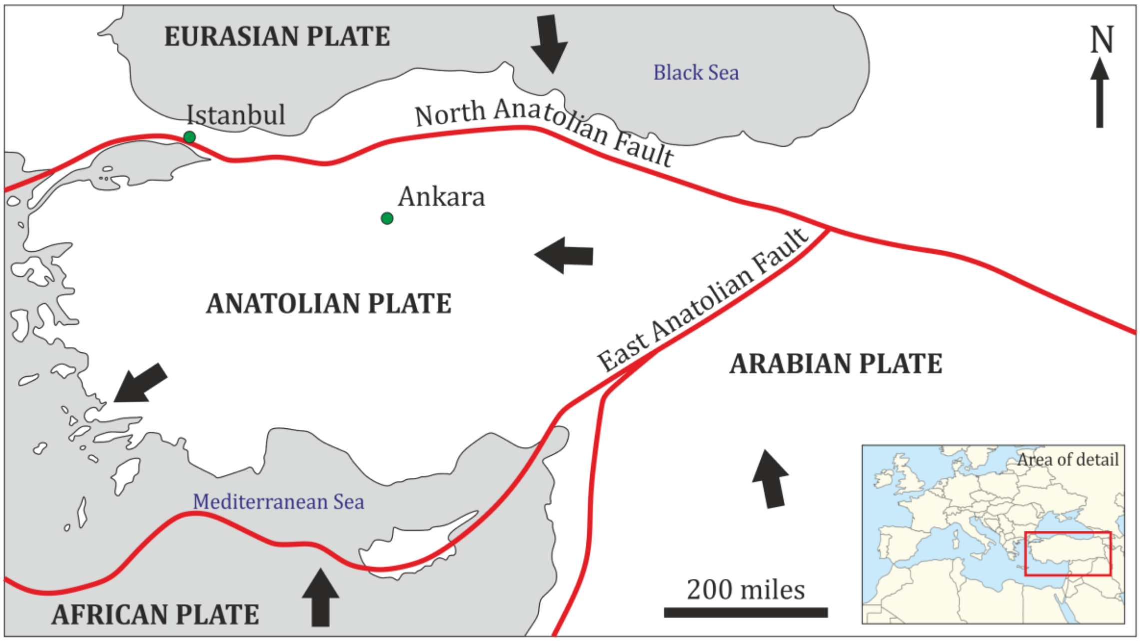

Figure 2.3. Large scale tectonics of Turkey and surrounding area showing the interaction of the Eurasian, African and Arabian plates. Black arrows indicate relative motion and the inset map shows the area covered.

2.2.2. Tectonics

Anatolia can be divided into neotectonic provinces (Figure 2.1 and Figure 2.2) (Selçuk and Göktan, 2012); the North and Central, Eastern and Western Anatolian Provinces. The Eastern Anatolian Province is subdivided into the regions east and west of the Karlıova triple junction. The former is characterised by N-S compression and the latter consists of sinistral and dextral strike slip faults, including the NAFZ (Bozkurt, 2001, Reilinger et al., 1997). The North Anatolian Province is the area north of the NAFZ and comprises strike slip faults with a strong E-W thrust component (Bozkurt, 2001). The Central Anatolian Province is under approximate NW-SE extension and NE-SW shortening related to collision between the Anatolian and African plates (Şengör, 1985). Western Anatolia is one of the most seismically active and rapidly extending regions of the world, extension rates are ~30 – 40 mm yr^{-1} in a N-S orientation (Bozkurt, 2001). The cause and origin of this extensional regime is attributed to the mechanisms associated with the westward extrusion of the Anatolian plate (Şengör, 1985, Dewey and Şengör, 1979, Sengör, 1979).

It is apparent from GPS measurements (Figure 2.4) that Anatolia is moving westwards toward the Hellenic Trench in the southern Aegean, due to the motion of the African and Arabian plates northwards into the Eurasian plate (Reilinger et al., 2006). Tectonic escape, or extrusion tectonics, was first proposed by Tapponnier et al. (1982) to explain continental-continental collision of India into Asia (Molnar and Tapponnier, 1975, Molnar and Tapponnier, 1978). According to the GPS, the rate of motion increases from east to west along an arc through Anatolia and the Aegean from 17.8 ± 1.1 mm/yr to 31.1 ± 0.9 mm/yr (Reilinger et al., 2006). From the results presented by Reilinger et al. (2006) the westward motion of Anatolia is also largely associated with slab roll back along the Hellenic Trench, and the counter clockwise rotation of the Arabian plate, which is enhanced by slab pull from the NE beneath the Makran and possibly the southern Zagros.

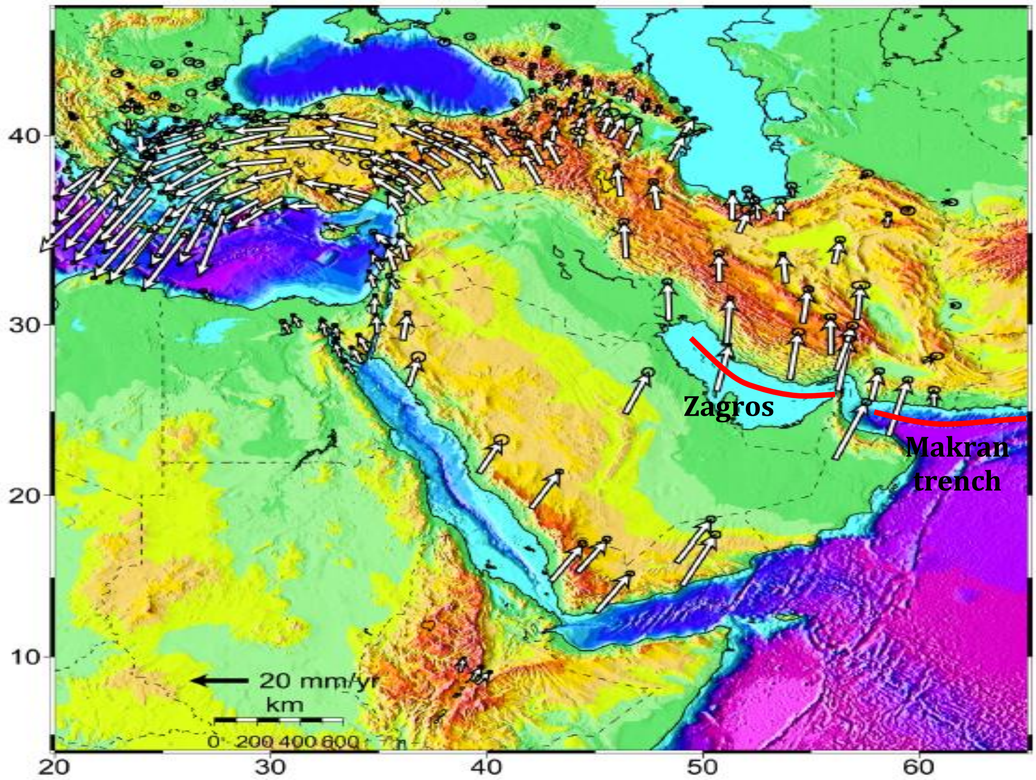

Figure 2.4 GPS velocities relative to Eurasia showing the anti-clockwise rotation of Anatolia (Reilinger et al., 2006).

2.2.3. Sutures and Evolution

Between the terranes outlined above are sutures recording the palaeo-seas and oceans that have closed during the evolution of Anatolia (Figure 2.2) (Stampfli, 2000, Okay, 2008). A number of seas have been opened and closed from the Early Paleozoic to the Eocene, leaving behind evidence of sutures running across Anatolia (Stampfli, 2000). The Ankara-Erzincan Suture is situated between the Pontides and the Anatolide-Taurides. To the south of the Anatolide-Taurides is the Assyrian suture (Okay, 2008, Sengör and Yilmaz, 1981), whilst within the Pontides is the Intra-Pontide suture (Okay and Tuysuz, 1999) (Figure 2.2). These sutures exert important controls on the neotectonics of the region as many large structures such as the NAFZ and Eskişehir Fault Zone follow their trace.

During most of the Phanerozoic the margins of Laurasia and Gondwana were continuously rifted forming continental fragments separated by various seaways (Stampfli, 2000). The earliest ocean is the very controversial Prototethys. Little is known about the evolution of the Prototethys and the exact age of this ocean is unknown. Stampfli (2000) suggested the Prototethys Ocean opened in the early Paleaozoic and its closure is thought to have promoted the formation of an active Gondwanan margin. The closure caused back-arc rifts to develop, some of which became larger oceanic realms such as the Rheic and Palaeotethys oceans (Stampfli and Kozur, 2006).

The Intra-Pontide suture zone extends for ~400km, separating the Istanbul Zone from the Sakarya Zone (Figure 2.2). It comprises Upper Cretaceous to Palaeocene ophiolitic melange (Wong et al., 1995, Görür et al., 1984, Sengör and Yilmaz, 1981). Along much of its length, the suture is defined by the NAFZ (Okay and Tuysuz, 1999). The Intra-Pontide ocean probably existed in the Carboniferous as the eastern extension of the Rheic Ocean, closing in the Mid-Carboniferous (Okay et al., 2006).

The Palaeotethys ocean that separated Laurasia and Gondwana has had a complicated evolution as continental fragments were rifted off either side, giving rise to a number of seaways (Okay and Tuysuz, 1999). The main Palaeotethys ocean opened as a result of slab roll back from the southward subduction of the mid ocean ridge of the Rheic ocean (Stampfli, 2000). The closure of the Palaeotethys occurred diachronously along an oblique convergence zone from the Moscovian to early Triassic (Stampfli, 2000). The subduction of the Palaeotethys promoted the opening of another ocean, the Neotethys, as a series of back-arc basins.

The area of the eastern Mediterranean corresponding to the location of the Neotethys records the development and closure of a number of narrow seaways and microcontinental fragments rifted off Gondwana (Floyd et al., 2000). Şengör (1987) suggested the Neotethys is possibly related to the Alpine Tethys-Atlantic opening, beginning in the Late Triassic or Early Jurassic. However, newer interpretations suggest that the Neotethys has existed since the Late Palaeozoic (Stampfli et al., 2001, Malpas et al., 1993, Niko et al., 1996, Kozur, 1995, Stampfli, 2000). The northward subduction of the Neotethys began between the Late Triassic and Liassic (Berberian and Berberian, 1981). Closure occurred within the Late Cretaceous (Stampfli and Kozur, 2006) due to convergence between the African and Eurasian plates (Bozkurt, 2001).

The Izmir-Ankara-Erzincan suture is the main suture in Turkey stretching from the border with Georgia in the east (where it continues eastwards as the Sevan-Akera suture) to the Aegean Sea in the west where it joins the Vardar suture (Okay and Tuysuz, 1999) (Figure 2.2). Along much of its length, the Eskişehir Fault corresponds to the Izmir-Ankara-Erzincan suture (Okay et al., 2008). Okay and Tuysuz (1999) suggested that the Izmir-Ankara-Erzincan suture represents the northern branch of the Neotethys between the Sakayra microcontinent and the leading edge of the Anatolide-Tauride platform (Floyd et al., 2000). According to Stampfli (2000), however, the Izmir-Ankara-Erzincan suture does not represent the Neotethys. In his reconstructions, the Izmir-Ankara-Erzincan suture represents a Jurassic back arc basin formed as a result of the northward subduction of the Neotethys.

2.3. The North Anatolian Fault

Many large scale structures have developed due to the Anatolian plate being located at such a complicated zone of interaction between the Eurasian and Arabian plates (Figure 2.2). Some of these structures facilitate the westward extrusion of Anatolia (eg. the NAFZ), others accommodate deformation associated with the movement (eg. extensional province in the southwest). Arguably the most prominent crustal weakness in this region is the North Anatolian Fault Zone, but others such as the East Anatolian and Dead Sea Fault Zones and the Aegean Arc also play major roles in the regional tectonics.

2.3.1. Structure

The NAFZ is an approximately 1200km long, dextral strike slip fault zone and initiated between 13 to 11 Ma (Sengör, 1979). It is currently one of the largest active strike slip systems in the world and is part of a wide associated deformation belt in Northern Turkey, forming part of the boundary between the Anatolian and Eurasian plates (Figure 2.5) (Sengör, 1979, Şengör et al., 2005). The damage zone associated with the NAFZ comprises multiple subsidiary faults surrounding the main trace of the NAF)

The NAFZ generally becomes wider from east to west (Figure 2.5), in accordance with the late Paleozoic and early Tertiary accretionary complexes that form a crustal weakness (Şengör et al., 2005). The fault zone is mainly a single feature varying in width from a few hundred metres to 40km, with short subparallel faults along its length (Okay, 2008).

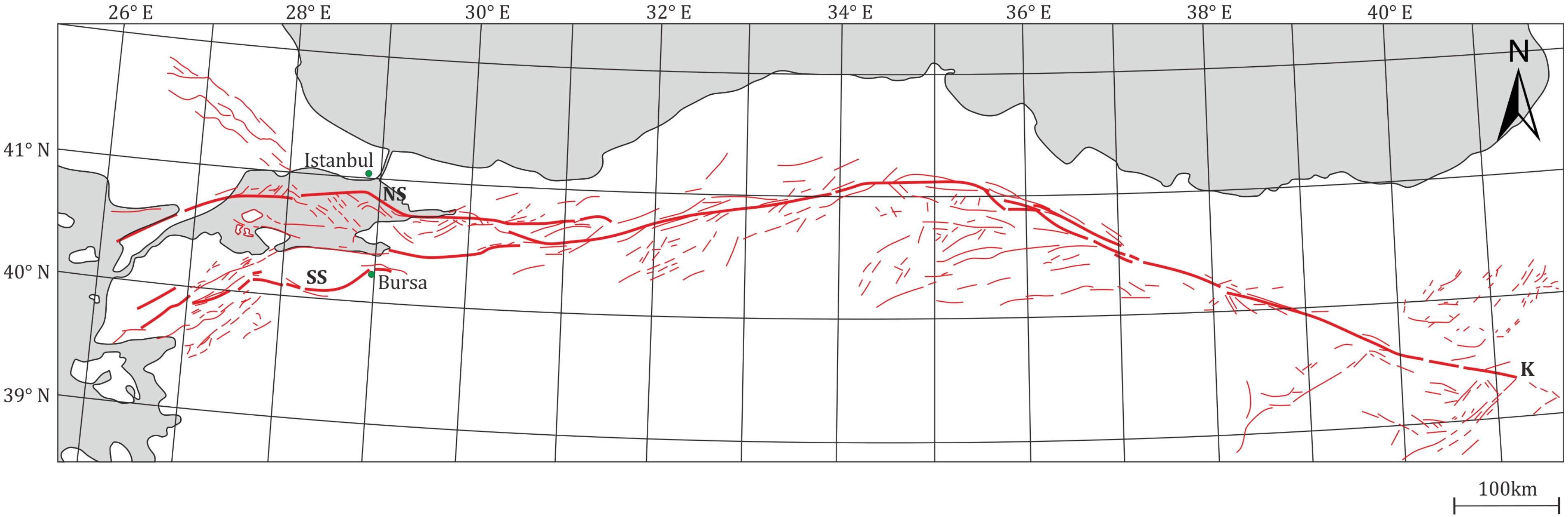

Figure 2.5. North Anatolian Fault Zone. Main strands shown by thicker red lines, the damage zone faults and subsidiary faults are marked in the thinner red lines. K = Karlıova triple junction, NS - Northern Strand of NAFZ, SS - Southern Strand of NAFZ (Modified from Şengör et al. (2005)).

It consists of two main strands, the junction of which is just east of Istanbul and the Sea of Marmara (Figure 2.5). The northern strand enters the Sea of Marmara and the southern strand passes just north of Bursa (Dewey and Şengör, 1979). Surface deformation and fault plane solutions indicate right lateral movement on both strands, the incompatibility accommodated by extension in the Sea of Marmara (McKenzie, 1972). There is debate on the continuation of the two strands into the Sea of Marmara, specifically as to whether both strands are active and continue into the Aegean or if only one strand accommodates deformation and the other terminates (Alptekin, 1973, Brinkmann, 1976, Bingöl, 1976, Sengör, 1979). The northern strand is considered to be the most active, however, and includes the segment that slipped in the 1999 Düzce earthquake which is where the DANA array has been installed (Figure 2.2) (Bozkurt, 2001).

2.3.2. Evolution and Timing

There is some controversy over the timing and reasons for initiation of the NAF. McKenzie (1970) suggests that right lateral motion started in the middle Miocene as a result of the collision between Arabia and Eurasia and the westward translation of Anatolia.Others propose that the NAFZ did not initiate until the latest Miocene or Early Pliocene (Barka and Kadinsky-Cade, 1988, Koçyigit, 1991, Saroglu, 1988, Koçyiğit, 1988). However, Bozkurt (2001) thought this unlikely as too much slip has accrued in the west based on the current slip rate for this shorter time frame. There is also some speculation that the fault developed first in the east (~16Ma) and propagated west to the Sea of Marmara (Sengör, 1979, Gautier et al., 1999). This suggestion is based on simple observations that the fault damage zone is wider in the east than in the west and also that there is a larger mapped offset in the east (Okay, 2008, Sengör, 1979).

More recently the general agreement is that the NAFZ initiated in the Neogene, most likely the mid Miocene, as a response to the tectonic escape of Turkey (Okay, 2008). Whether it began in the east and propagated west remains open for discussion. Mapping and geological observations of lithological units indicate an average estimate on the offset along the NAFZ of between 85 ± 5km to 20-25 km (Şengör et al., 2005). In more recent times the neotectonics of Turkey has been governed by the convergent plate boundary in the south Aegean, where the African plate is being subducted beneath the Anatolian plate to the north, the right lateral North Anatolian fault and the sinistral East Anatolian Fault Zone (Bozkurt, 2001).

2.3.3. Activity

The NAFZ is one of the most seismically active faults on the Earth, and has a long history of large earthquakes in which many thousands of people have died (Sengör, 1979, Şengör et al., 2005).

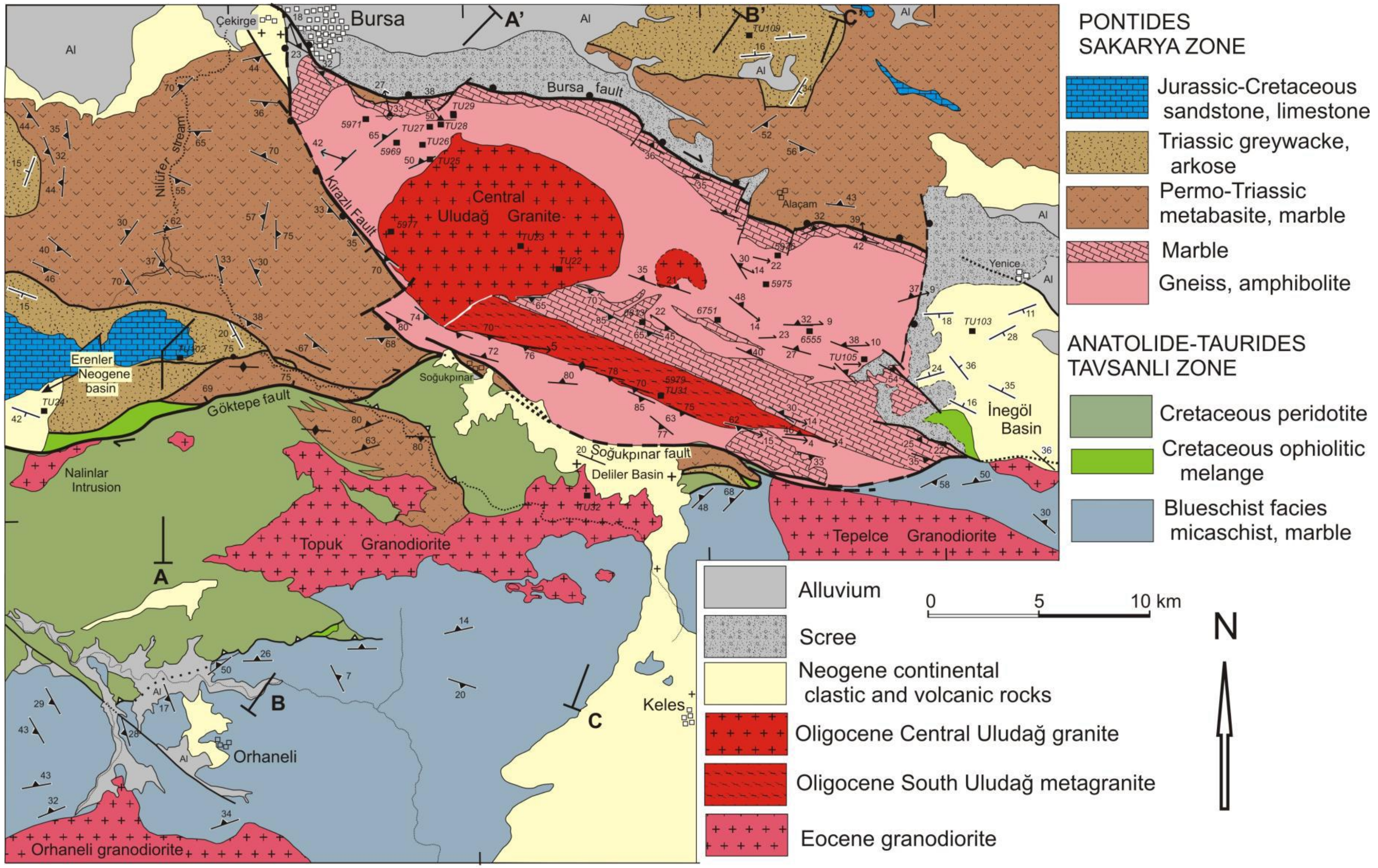

Figure 2.6. Map of the Uludağ Massif and surrounding area. The Eskişehir Fault discussed corresponds to the Soğukpınar Fault on this map. To the north of this fault the rocks belong to the Sakayra Zone of the Pontides and to the south lies the Anatolide-Taurides (Okay et al., 2008).

During the past 60 years the NAF has caused earthquakes along different sections in a sequentially westward progression: these earthquakes, including 26 December 1939 Erzincan (M = 7.9-8.0), 20 December 1942 Erbaar-Niksar (M = 7.1), 26 November 1943 Tosya (M = 7.6), 1 February 1944 Bolu-Gerede (M = 7.3), 26 May 1957 Abant (M = 7.0), 22 July 1967 Mudurnu valley (M = 7.1), 13 March 1992 Erzincan (M = 6.8), 17 August 1999 Kocaeli (M = 7.4), and 12 November 1999 Düzce earthquakes (McKenzie, 1970, Koçyiğit, 1988, Bozkurt, 2001) (Chapter 1, Figure 1.2).

2.4. The Uludağ Massif

This section focuses on the background to the Uludağ Massif which is the field area for this study. The Uludağ Massif is located in north western Turkey, just to the south of Bursa (Figure 2.2). It is at the northern most tip of the Eskişehir Fault (part of the Inönü-Eskişehir Fault System), which is currently displaying oblique dip-slip movement but was formerly active as the strike-slip Uludağ Shear Zone (Okay et al., 2008). The first map of the study area was published by Ketin (1947), the later updated version produced by Okay et al. (2008) is shown in Figure 2.6.

The Uludağ Group

The Uludağ Group within the Uludağ Massif are the lowest member of the Sakarya terrane (Figure 2.7). This group consists of a high-grade metamorphic basement and a Permo-Triassic sedimentary cover sequence (Ketin, 1947). The metamorphic basement comprises of marbles, gneisses and amphibolites which were metamorphosed and deformed during the Hercynian (Variscan) orogeny in the Carboniferous (Okay and Tuysuz, 1999, Okay and Satir, 2006, Okay, 2000). An estimate for the age of peak metamorphism in the Uludağ Group yields latest Cretaceous (~64 Ma) based on peak temperature conditions of 670°c and closure temperatures for muscovite and biotite yielding a cooling rate of ~12°c/m.y. (Okay et al., 2008). As for a protolith age for the Uludağ Group; it is very poorly constrained. Badly preserved corals in the marbles suggest the age is post-Ordovician, but a tighter constraint has not been found (Okay et al., 2008).

The granites intruding the Uludağ Group are Oligocene age. The South Uludağ granite is presented as a synkinematic intrusion, evident from the pervasive fault parallel foliation, presence of solid-state microstructure and prolonged crystallisation age of 30 to 39 Ma (Okay et al., 2008).

Karakaya Complex

The Karakaya Complex overlies the Uludağ Group (Figure 2.7). It is a complex unit and its chaotic nature makes establishing a coherent interpretation difficult (Okay et al., 2008).

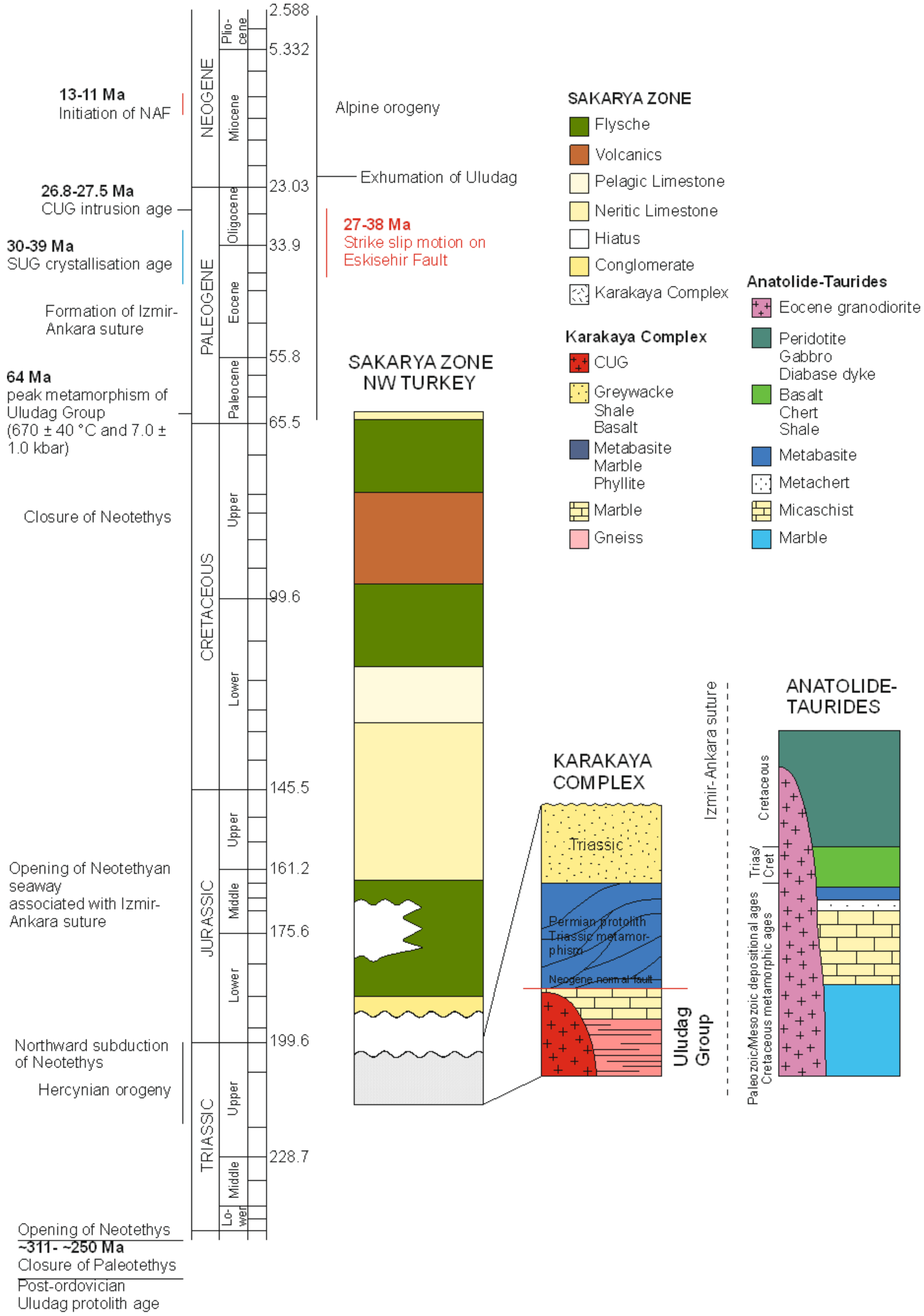

Figure 2.7. Stratigraphic column of the different terranes either side of the Izmir-Ankara suture and Eskişehir Fault (Okay and Satir, 2006).

There are two main interpretations for the geodynamic evolution of the complex; the first, continental-rift initiated by Early Triassic extensional tectonics (Bingöl et al., 1973) and the second, that it represents a subduction/accretion prism based on the melange character of the unit and the existence of high-pressure lithologies (Sayıt and Göncüoglu, 2013). Based on observations in NW Anatolia the Karakaya Complex was similarly subdivided into the Lower Karakaya Complex, which comprises of the Nilüfer unit, and the Upper Karakaya Complex which includes the Çal, Hodul and Orhanler units (Okay and Göncüoğlu, 2004, Okay et al., 1991). Overall in NW Anatolia it represents mass transport deposits, a mélange of mafic extrusives and associated oceanic sediments with slightly deformed stratigraphic successions (Sayit et al., 2011).

Lower Karakaya Complex/Nilüfer unit

In NW Anatolia this unit is characterised by deformed metabasite interbedded with recrystallised limestone and phyllite (Okay et al., 1991). The majority of the rocks in this unit were metamorphosed under greenschist facies conditions. However in some areas blueschist and eclogites are found (Okay et al., 2002). It spans a time period from Early to Late Triassic based on palaeontological evidence (Kozur et al., 2000, Sayıt and Göncüoglu, 2009). There are a number of reasons why this unit does not represent a continental rift setting. Firstly, no continental detritus is found within the succession. Secondly, the metabasaltic rocks are typical of a seamount chain. Thirdly, the HP/LT varieties of rock suggest the unit has undergone subduction/accretion processes (Sayit et al., 2011, Okay et al., 1991).

Upper Karakaya Complex/Eymir unit

This unit mainly consists of arkosic sandstones and greywackes alternating with shales. The unit has undergone variable degrees of metamorphism, in areas of low grade metamorphic slates, phyllites and coarser grained metaclastics all show a well-developed foliation (Sayit et al., 2011, Sayıt and Göncüoglu, 2013). The less metamorphosed portions yield ages of Carnian-Norian (Late Triassic) (Sayit et al., 2011, Okay et al., 1991). Sayıt and Göncüoglu (2013) concluded that the evolution of the Karakaya Complex was neither a continental-rift setting nor a subduction/accretion prism, but that it represented oceanic island and/or seamounts on the Palaeotethyan oceanic crust during the Middle-Late Triassic.

Overlying sequences

The complex basement is overlain by a sedimentary and volcanic succession dated as Early Jurassic culminating in the deposition of deep sea sandstones and shales in the mid-Cretaceous, marking the onset of the Alpide orogeny (Okay et al., 2008) (Figure 2.7).

The Uludağ Group is of most interest, as these are the rocks exposed within the Massif. They represent the deep crustal shear zone that was active during the Oligocene, along with the Permian-Triassic rocks of the Karakaya Complex that bound the northern and western margins of the Massif. The overlying sedimentary and volcanic deposits do not outcrop near the study area.

2.4.1. Structure

The Uludağ Massif represents the ductile portion of an exhumed mid-crustal strike slip shear zone. The general strike of the structures and foliation within the Massif is broadly ESE-WNW (~110°) (Figure 2.6). It is bounded by the Bursa Fault to the north, which is a normal fault with a slight right lateral oblique component (Okay et al., 2008) and the Eskişehir Fault to the south. The Eskişehir Fault was initiated in the Oligocene as a right lateral strike slip fault according to Okay et al. (2008) and is currently active as a normal fault close to the town of Eskişehir (SE of the field area) (Figure 2.8).

Exhumed ductile shear zone

Evidence for ductile shear is the presence of a prevalent fabric dominating the Uludağ group. This fabric is parallel to the trend of the mountain range and to the Eskişehir fault to the south. The fabric displays various shear sense indicators which indicate right lateral movement (Okay et al., 2008). As well as the prevalent foliation, there is also a sub horizontal mineral stretching lineation that is pervasive throughout the massif, becoming weaker towards the margins (Okay et al., 2008). Other evidence includes the varying mineral compositions within the same gneiss and amphibolite rock samples suggestive of a prolonged re-equilibration during deformation within a shear zone (Okay et al., 2008). The South Uludağ Granite has a dominant WNW-ESE fabric which is parallel to the dominant fabric of the massif, meaning it was likely intruded during the strike slip movement stretching out along the fault zone (Figure 2.6) in a similar manner to other contemporaneous shear and magmatic activity described elsewhere (eg. Donegal, NW Ireland (Hutton, 1982) and Red River, SW China (Anczkiewicz et al., 2007) shear zones).

Eskişehir Fault

The Eskişehir Fault is part of a larger fault system, the Inönü-Eskeşehir Fault System (IEFS) which stretches from Uludağ in the west to Tuz Gölü (Lake Tuz) in the east (Koçyiğit, 2003) (Figure 2.8). Some infer the system to carry on further south east past Lake Tuz (Koçyiğit, 2009) to Sultanhanı in the east making it ~470km long (Özsayın and Dirik, 2007). This fault system contains many fault zones, between which there is some degree of connectivity, and is a major structure within Aegean tectonics (Özsayın and Dirik, 2007).

The mapped Eskişehir Fault Zone (EFZ) is approximately 225km long with an estimated 100 ± 20km of right lateral offset (Okay et al., 2008).

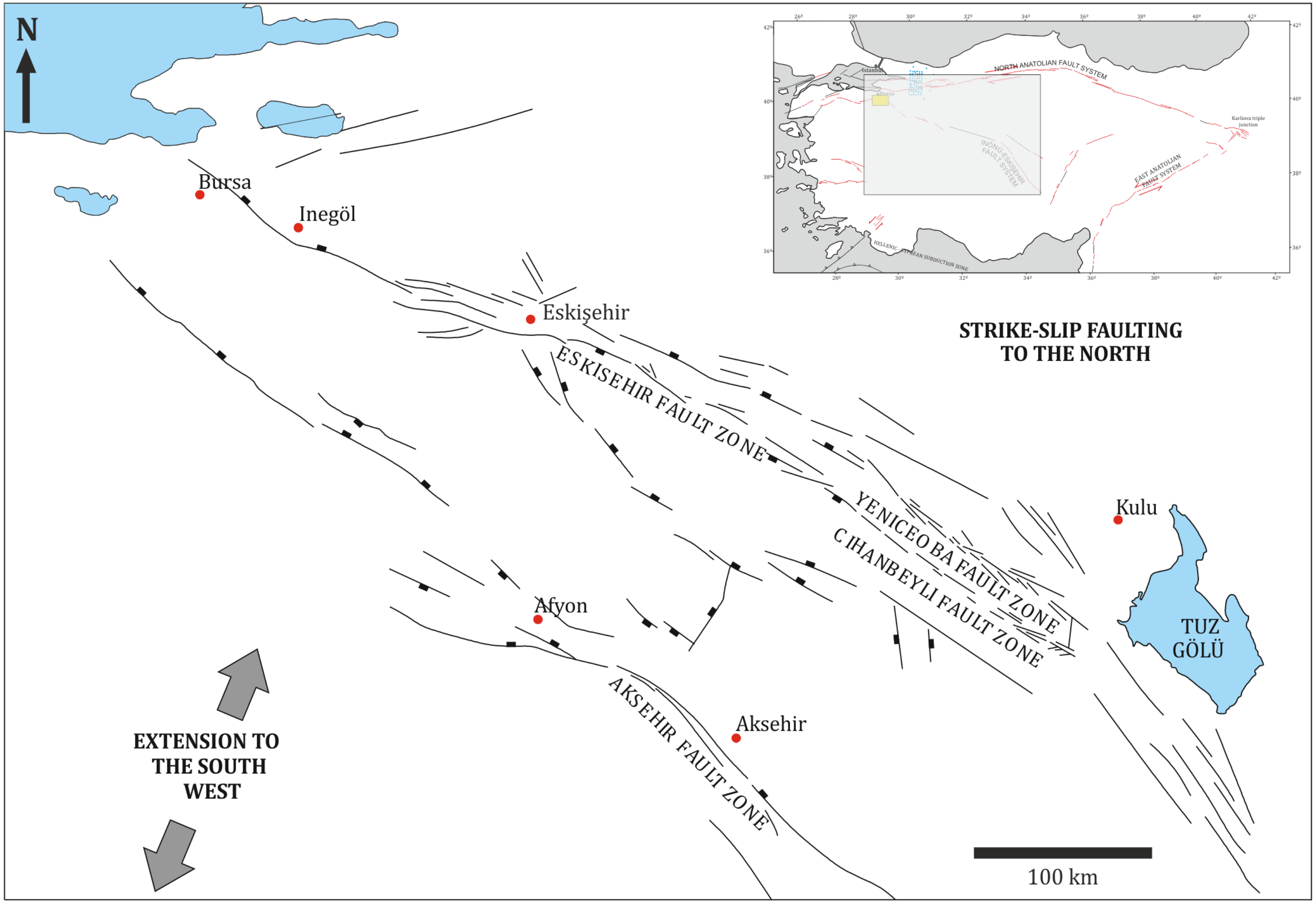

Figure 2.8. Map of the Inönü-Eskişehir Fault System modified from Özsayın and Dirik (2007).

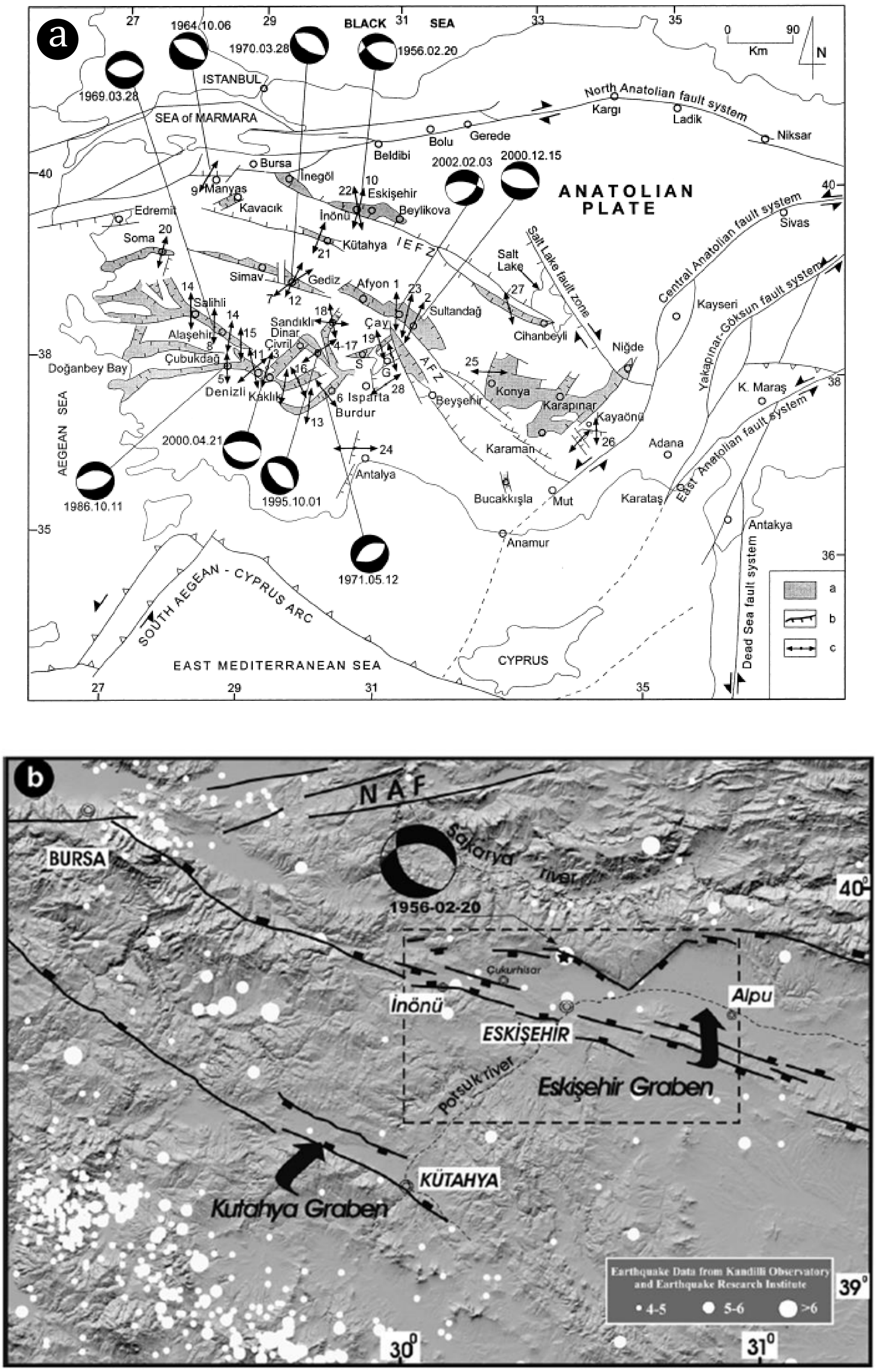

Figure 2.9. (a) displays the focal mechanisms for selected earthquakes on the Inönü-Eskişehir and neighbouring fault systems (Koçyiğit, 2005). The dates are shown by the relevant focal mechanisms, all recorded after the 1950s. IEFZ refers to the IEFS or the EFZ. a. denotes graben fill, b. normal fault and c. extension direction. (b) shows the epicentres for present day activity in the IEFS (Ocakoğlu, 2007).

It initiated in the Oligocene as a strike slip fault in response to the onset of subduction in the Aegean, facilitating the westward translation of Anatolia, before the Arabia-Anatolia collision (Meulenkamp et al., 1988, Ocakoğlu, 2007). Pure strike slip motion on the fault has since ceased and most of the present day activity along sections of the fault shows oblique normal motion indicated by the focal mechanisms in Figure 2.9. (Özsayın and Dirik, 2007).

The Eskişehir Fault is also the boundary between varying tectonic regimes. To the south of the Eskişehir Fault Zone (EFZ) extension commenced following orogenic collapse in the middle Miocene to middle Pliocene, starting as NNW-SSE directed but later major NNE-SSW directed (Koçyiğit, 2005). To the north of the EFZ strike slip tectonics dominate (Okay and Tuysuz, 1999, Barka et al., 1995). Along most of its length the fault also corresponds to the Izmir-Ankara suture (Okay and Tuysuz, 1999, Barka et al., 1995, Koçyiğit, 2005). Barka et al. (1995) determined different rates of movement for Central Anatolia north of the EFZ (15-20 mm/yr) and Western Anatolia to the south of the EFZ (30-40 mm/yr) from GPS measurements. Slickenside and fault plane measurements taken from scarps along the EFZ indicate both sub horizontal and sub vertical motion; fault scarp: 150/90, Slickensides: 81/323 and 03/038 (Ocakoğlu, 2007).

Bursa Fault

The Bursa Fault which bounds the northern side of the Uludağ Massif forms a steep topographical feature that drops away to the Bursa Plain (Figure 2.6). The fault is a brittle structure and the fault plane can be observed at several locations measured by Okay et al. (2008) to be shallowly dipping structure to the north east (eg. 140/25 NE). The fault is split into four segments by Selim and Tüysüz (2013); Kayapa-Çalı, Misiköy, Çekirge-Hamamlıkızık and Saitabat (Figure 2.10).

The first two segments form the northern boundary to the field area and strike quite differently to the segments bordering the north eastern side of the massif. Selim and Tüysüz (2013) measured fault planes within the Çekirge-Hamamlıkızık segment to be dipping at 50° to the north, and within the more easterly striking Saitabat segment at 35° to the north. The Bursa Fault, along with the Eskişehir Fault is part of the Eskişehir Fault system Figure 2.8.

2.4.2. Metamorphism and Shear Zone activity

Prior to strike slip activity, the Uludağ Group had undergone amphibolite facies metamorphism indicated by the predominant mineral assemblage within the gneisses (Yıldırım et al., 2005, Okay et al., 2008). The majority is biotite gneiss with an assemblage of quartz, plagioclase, biotite, muscovite and garnet, that grades locally into amphibolite gneisses containing quartz, plagioclase, amphibole, biotite, muscovite and garnet (Okay et al., 2008). The gneisses in the Uludağ Group yielded peak metamorphism conditions of 670 ± 40 °C and 7.0 ± 1.0 kbar.

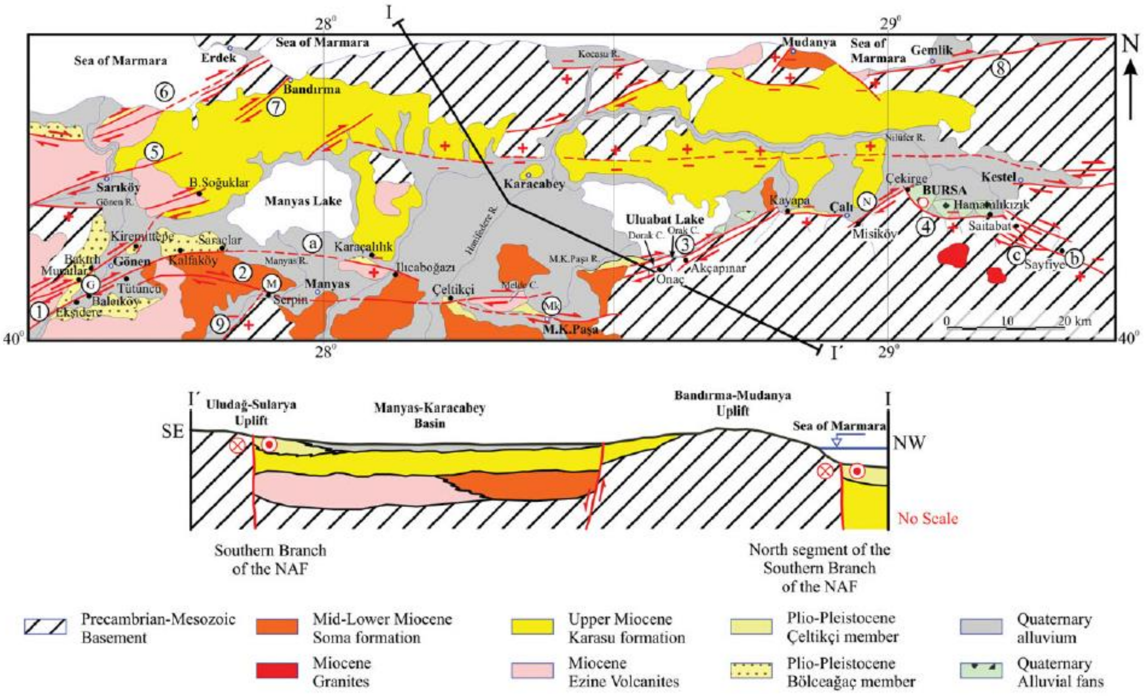

Figure 2.10. showing locations of Bursa Fault strands (Selim and Tüysüz, 2013).

However, the age of the peak metamorphism is poorly constrained, with estimates suggesting latest Cretaceous to early Paleocene, contemporaneous with Anatolide-Tauride, Pontide collision (Okay et al., 2008).

The Uludağ Group is intruded by Oligocene age granites, Bingöl et al. (1982) and Delaloye and Bingöl (2000) obtained K-Ar biotite ages ranging from 26.8 and 24.7 Ma. Okay et al. (2008) attained slightly older ages for Rb/Sr muscovite and biotite (27.5 ± 0.5 Ma and 27.2 ± 0.3 Ma respectively) (Figure 2.11). Rb/Sr geochronology also yielded ages for the gneisses of latest Eocene to Oligocene (36 to 24 Ma), the youngest ages are hard to interpret as they are younger than the intrusion ages of the granite so it is likely they were affected by the heat of intrusion (Okay et al., 2008).

The South Uludağ granite has also been dated. It is a synkinematic intrusion highlighted by the dominant fault parallel foliation that has developed within the unit (Okay et al., 2008). Due to the high temperature deformation this unit has undergone, U/Pb zircon dating was used to obtain a crystallisation age of 30 to 39 Ma (Figure 2.11). This age is compatible with being sheared and deformed during movement along the Eskişehir Fault, and therefore provides a constraint on shear zone actvity (Okay et al., 2008) (Figure 2.11). Quartz and feldspar fabrics suggest a deformation temperature of ~400°c (Okay et al., 2008).

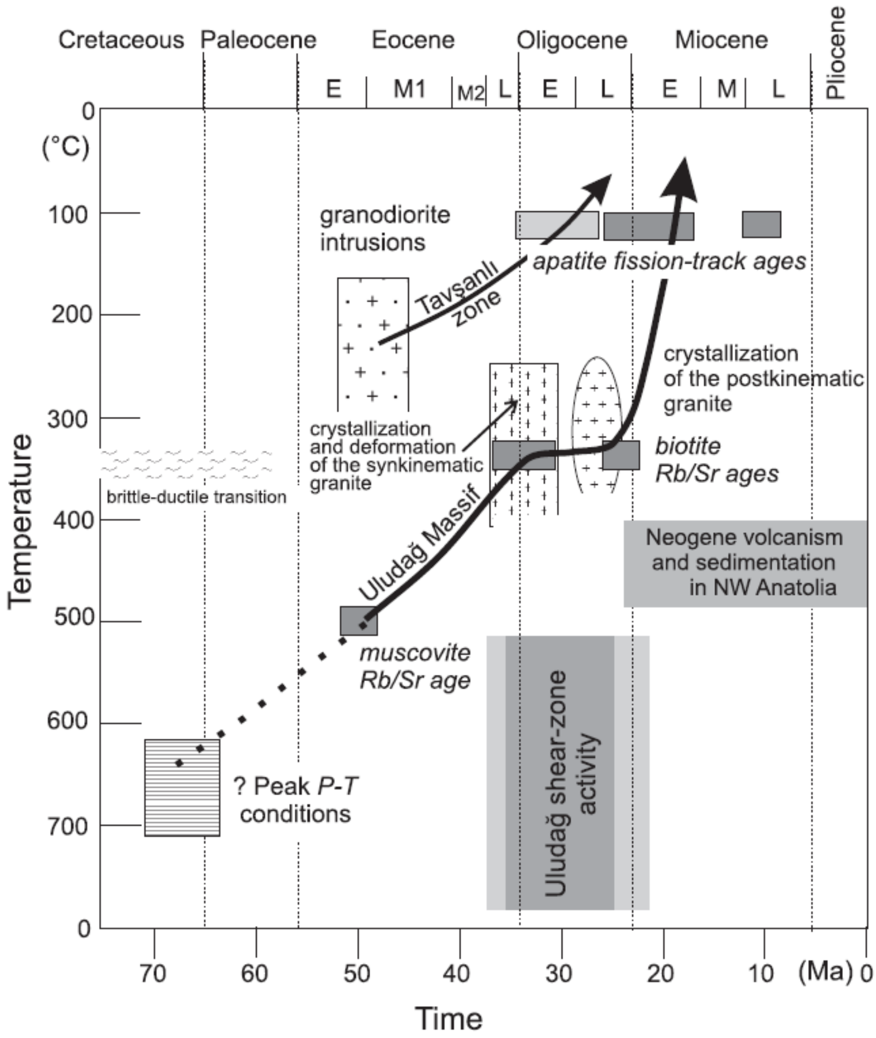

Figure 2.11. Data from Okay et al. (2008) showing the evolution of the Uludağ Massif from peak P-T conditions to exhumation in the Oligocene and Miocene.

2.4.3. Exhumation

The Exhumation of the Uludağ Massif to the surface occurred during the Oligocene-Miocene with the major exhumation event during the Early Miocene (Figure 2.11) (Okay et al., 2008). According to Okay et al. (2008), the hanging wall of the massif (to the south) has been stable with respect to the Earth's surface since the Eocene. From emplacement depths of the Topuk granodiorite the total exhumation is about 3-4km at a rate of 0.2-0.3 km/m.y. between 48Ma – 30Ma) for the Tavşanlı Zone (Harris et al., 1994, Okay and Satir, 2006, Okay et al., 2008). Similarly the northeastern side of the massif was likely buried at 4-5km and the mid Eocene apatite fission track (AFT) ages (39.4 ±4.8Ma) suggest exhumation is unrelated to strike-slip activity which occurred during the Oligocene (Figure 2.11 and Figure 2.12) (Ketin, 1947, Imbach, 1992, Okay et al., 2008). Several Neogene basins with terrigenous sediments occur along the Uludağ shear zone(Okay et al., 2008). The Deliler and Erenler basins to the south of the Massif are Oligocene in age (26.3 ± 2.3 Ma), from AFT data obtained by Okay et al. (2008), signifying significant uplift on normal faults during this period (Figure 2.12). The İnegöl Basin to the north east of the Massif extends WNW-ESE along the trend of the shear zone (Saroglu et al., 1992). AFT ages from gneiss detritus derived from the Uludağ Massif which was found within the sediments of the basin and dated fossils indicate a middle Miocene age of 14.3 ± 2.2 Ma, indicating the Uludağ Massif was being eroded at this time of deposition (Okay et al., 2008, Genc, 1987).

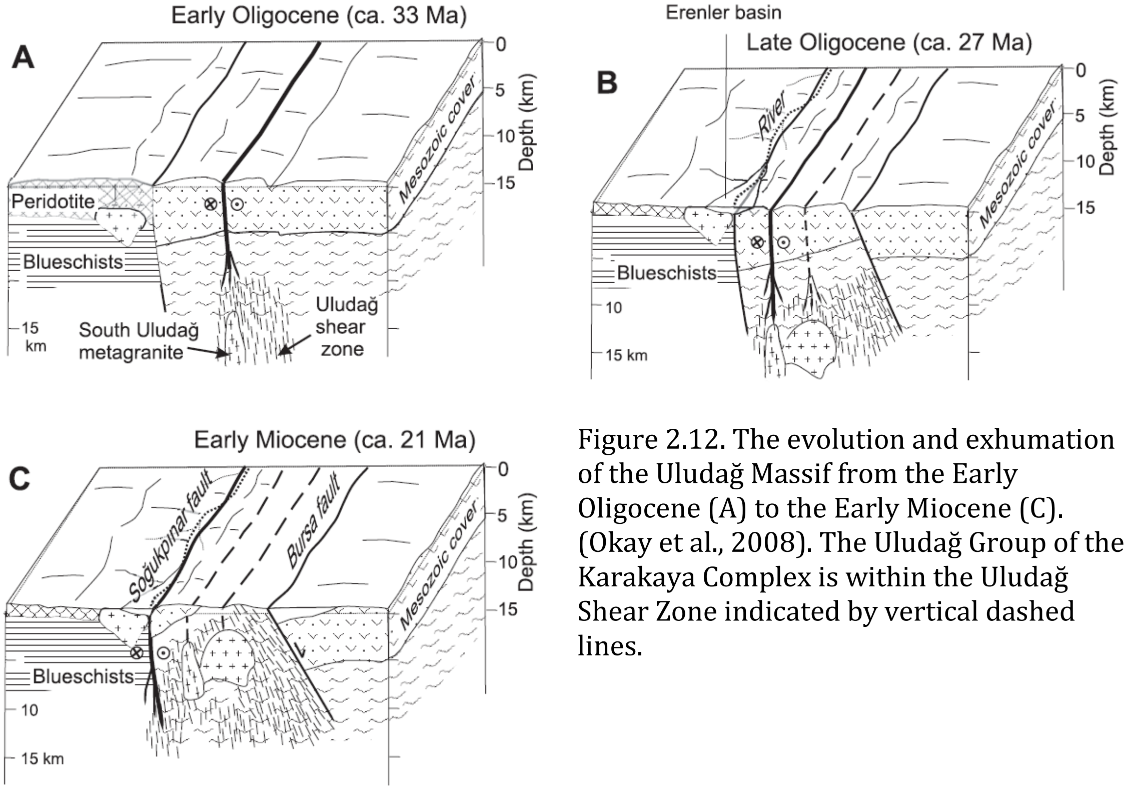

Figure 2.12. The evolution and exhumation of the Uludağ Massif from the Early Oligocene (A) to the Early Miocene (C). (Okay et al., 2008). The Uludağ Group of the Karakaya Complex is within the Uludağ Shear Zone indicated by vertical dashed lines.

The Uludağ Massif was not exhuming during shear zone activity (38 – 27 Ma) as there is no vertical motion indicated in mineral stretching lineations and no transpression or transtension structures in the basins to the south (Okay et al., 2008). Okay et al. (2008) obtained AFT ages around 22-20 Ma for the lithologies within the massif indicating that major exhumation occurred during the early Miocene (Okay and Satır, 2000, Işik and Tekeli, 2001). Exhumation was possibly aided by the density and viscosity inversion between the warm quartzo-feldspathic Uludağ Massif and cold overlying mafic Lower Karakaya Complex (Okay et al., 2008).

2.4.4. Present day activity

The city of Bursa is located within the Bursa-Gönen basin between the exhumed Uludağ Massif and the Bandirma-Mudanya exhumed basement. It has been struck by devastating earthquakes in the past (Selim and Tüysüz, 2013). Documented by Sandison (1855), an earthquake occurred on the 28th February 1855 (widely believed to have been on the

Bursa fault) and a further shock on the 11th April that was of 'about 30 seconds duration, almost every stone-building left standing was overturned…the loss of life in the town is variously estimated of up to 400'. More recently, during recorded history, other notable earthquakes have occurred near Bursa: 5th September 1992 M_w 4.6, 21st October 1983 M_w 4.9 and 21st February 1994 M_w 3.5 (Sellami et al., 1997).

Locations for the above mentioned earthquakes and others in the Bursa basin are shown in Chapter 3, Figure 3.6 and the mechanisms for some earthquakes shown in Figure 2.9a. The rates of movement on the Bursa Fault are calculated at 8.0 ± 4.3 mm yr^{-1} for normal offset and 3.6 ± 2.0 mm yr^{-1} for strike-slip movement (Meade et al., 2002). As well as recorded seismicity in the region of Bursa other field observations such as hot springs, alluvial fan deposits, slope wastes and debris flows indicate the Bursa Fault remains active (Selim and Tüysüz, 2013).

The Eskişehir Fault Zone is still active, being the source of a destructive earthquake on 20th February 1956 near Eskişehir (MW 6.5) (Ocakoğlu, 2007, Ocakoğlu and Açikalin, 2010). This earthquake was due to normal fault movement, with a slight right-lateral component (McKenzie, 1972). The EFZ is characterised by dextral strike slip motion with a considerable normal component (Selçuk and Göktan, 2012). The present deformation rate along the IEFS is estimated from GPS measurements and geological observations to be 0.15 mm yr-1 (Kahle et al., 1998). However, more recent evidence from the dating of terrace deposits yields rates of 1 mm yr-1 (Ocakoğlu, 2007). Figure 2.9b shows the epicentres of earthquakes over the last ~100 years, with a cluster of earthquakes near Bursa where the IEFS truncates against faults associated with the NAF (Ocakoğlu, 2007).

3. CHAPTER THREE

Geology of the Uludağ Massif from macro-scale field observations

3.1. Introduction

This chapter will present the geological observations of the Uludağ Massif on the macro-scale from field observations. A map of the geology of the Uludağ Massif and surrounding area is shown in Figure 3.1. Field observations on the lithologies that comprise the massif as well as the structure, along with any corroborating evidence from previous literature will be presented. The part referred to as the Uludağ Massif is the gneiss, marbles and granites that are bounded by the two faults; the Bursa fault in the north and the Eskişehir Fault in the south. The field area will be split according to geographic position relative to these two faults. The tectono-stratigraphic units will be split into; the basin north of the Bursa Fault, the Uludağ Massif and the basin to the south of the Eskişehir Fault and will be presented in Section 3.2.1. The structures of the Bursa Fault and Eskişehir Fault, along with any structural information found in the tectono-stratigraphic units will be presented in Section 3.2.2.

Field data and samples were collected by myself (accompanied by field assistants) over two field seasons totalling 6 weeks. A total of 171 samples were collected over this six weeks and approximately 30 samples were collected by a previous student that were added to make a sample suite of ~200. Whilst sample collecting I also mapped structure and recorded observations at each sample site, including lithology, lineations, foliations and fault rocks. Sample data is included in Appendix 7A.

3.2. Tectono-stratigraphic units

From field observations, four main lithological units were identified belonging to the tectono-stratigraphic unit of the Uludağ Massif between the two major fault structures shown on the map (Figure 3.1). This massif is surrounded by units belonging to different tectono-stratigraphic terranes, the Sakarya Zone to the north and the Anatolide-Taurides to the south (Chapter 2, Figure 2.2) (Okay et al., 2008). The lithological units will be described according to their geographical position which has been outlined above.

3.2.1. North of the Bursa Fault

North of the Bursa Fault is part of the Sakarya Zone (Chapter 2, Figure 2.2) (Okay et al., 2008). Outcrops on the north side of the massif were mainly found to be schists and units of basic mineralogy with little internal structure.

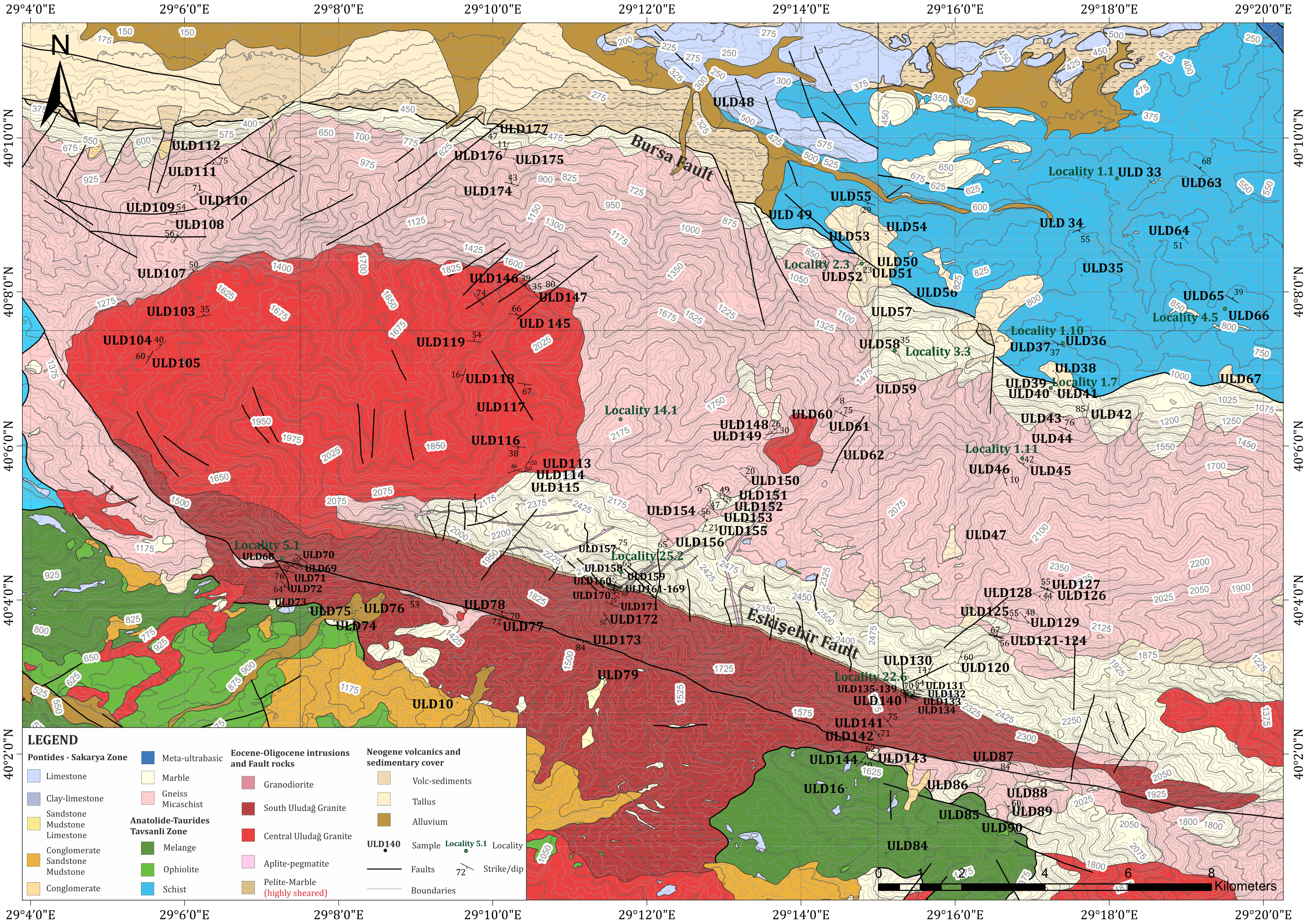
29°4'0"E
29°6'0"E
29°8'0"E
29°10'0"E
29°12'0"E
29°14'0"E
29°16'0"E
29°18'0"E
29°20'0"E
40°10'0"N
40°8'0"N
40°6'0"N
40°4'0"N
40°2'0"N
N
Bursa Fault
Eskişehir Fault
Locality 1.1
Locality 1.7
Locality 1.10
Locality 1.11
Locality 2.3
Locality 3.3
Locality 4.5
Locality 5.1
Locality 14.1
Locality 22.6
Locality 25.2
ULD112
ULD111
ULD110
ULD109
ULD108
ULD107
ULD103
ULD104
ULD105
ULD177
ULD176
ULD175
ULD174
ULD146
ULD147
ULD 145
ULD119
ULD118
ULD117
ULD116
ULD113
ULD114
ULD115
ULD48
ULD55
ULD 49
ULD54
ULD53
ULD50
ULD51
ULD52
ULD56
ULD57
ULD58
ULD59
ULD60
ULD61
ULD62
ULD148
ULD149
ULD150
ULD151
ULD152
ULD153
ULD154
ULD155
ULD156
ULD157
ULD158
ULD159
ULD160
ULD161-169
ULD170
ULD171
ULD172
ULD173
ULD 33
ULD63
ULD 34
ULD64
ULD35
ULD65
ULD66
ULD36
ULD37
ULD38
ULD39
ULD40
ULD41
ULD42
ULD43
ULD44
ULD45
ULD46
ULD47
ULD67
ULD68
ULD69
ULD70
ULD71
ULD72
ULD73
ULD74
ULD75
ULD76
ULD77
ULD78
ULD79
ULD10
ULD120
ULD121-124
ULD125
ULD126
ULD127
ULD128
ULD129
ULD130
ULD131
ULD132
ULD133
ULD134
ULD135-139
ULD140
ULD141
ULD142
ULD143
ULD144
ULD16
ULD84
ULD85
ULD86
ULD87
ULD88
ULD89
ULD90
0
2
4
6
8
Kilometers
LEGEND
Pontides - Sakarya Zone
Limestone
Clay-limestone
Sandstone Mudstone Limestone
Conglomerate Sandstone Mudstone
Conglomerate
Meta-ultrabasic
Marble
Gneiss Micaschist
Anatolide-Taurides Tavsanli Zone
Melange
Ophiolite
Schist
Eocene-Oligocene intrusions and Fault rocks
Granodiorite
South Uludağ Granite
Central Uludağ Granite
Aplite-pegmatite
Pelite-Marble (highly sheared)
Neogene volcanics and sedimentary cover
Volc-sediments
Tallus
Alluvium
ULD140 Sample
Locality 5.1 Locality
Faults
72 Strike/dip
Boundaries

Figure 3.1. Map of the Uludağ Massif and field area data from General Directorate of Mineral Research and Exploration (MTA) and field observations (namely the location of the Eskişehir Fault) (Akbaş et al.). Localities and sample numbers referred to throughout the thesis are shown in green and black respectively.

Both of these rock units were found to be highly weathered and friable, making interpretation of mineralogy and structure challenging in both hand specimen and thin section. The schists, found at locality 1.10, contain a high proportion of sheet micas that form a dominant foliation/schistosity. This micaschist contains more that 70% quartz and plagioclase feldspar, with muscovite and biotite highlighting the foliation.

The basite, found at locality 1.1, is a very fine grained (<0.5mm), dark rock in hand specimen, predominantly made up of mafic minerals, weathered orange, with feldspar. Some quartz/feldspar rich layers contain a green coloured mineral, possibly epidote. Outcrops of limestone was also encountered on the northern side, the outcrops being grey in colour, fine grained with no internal structure. The weathering pattern was typical of a limestone (Figure 3.2a, Locality 4.5) with dissolution karsts on the top surfaces. Close to the Bursa Fault, but still on the north side, the lithology is predominantly marble. The outcrops often show an orange-colour weathering and in some areas evidence of bedding can be observed (Locality 1.7). The bedding was measured at 113/24N, and identified with silty horizons and sections of honeycomb style weathering picking out horizons.

3.2.2. Uludağ Massif

The Uludağ Massif lies between the Bursa Fault in the north and the Eskişehir Fault in the south. Adjacent to the Bursa Fault is a unit of pure white calcite marble. It often forms large outcrops, and on the northern side they do not show any internal features. Continuing south towards the Eskişehir Fault the lithology changes to show a polymineralic unit with a pervasive foliation and visible alignment of minerals into a preferred orientation, a type locality shown on Figure 3.2b, Locality 1.11. The gneiss samples collected in the north of the area are mainly biotite-quartz-plagioclase gneisses with smaller amounts of amphibole, muscovite and a minority of samples containing garnet. Within this unit are numerous outcrops of a more mafic gneiss containing ~50% amphibole and ~50% plagioclase. This is termed an amphibolite and also shows a pervasive foliation. Further south, the marble outcrops again and bounds the southern side of the massif, adjacent to the Eskişehir Fault. Again, the marble is almost pure calcite with minor amounts of quartz identified by its contrast in hardness. This marble caps the highest peaks of the mountain range, running at approximately 110°, seen on Figure 3.1 and the photo in Figure 3.3.

The outcrop here is extensive and shows a pervasive foliation and obvious mineral alignment in hand specimen. In the north west of the massif, Figure 3.1, there is a large igneous intrusion. The outcrops within the centre of this intrusion are rounded in shape and show no internal structure. The mineralogy is quartz, plagioclase, k-feldspar, biotite and minor amounts of muscovite, giving a typical granitic composition. Towards the edges of the granite a foliation is present, the strike of which varies between 010° - 120°.

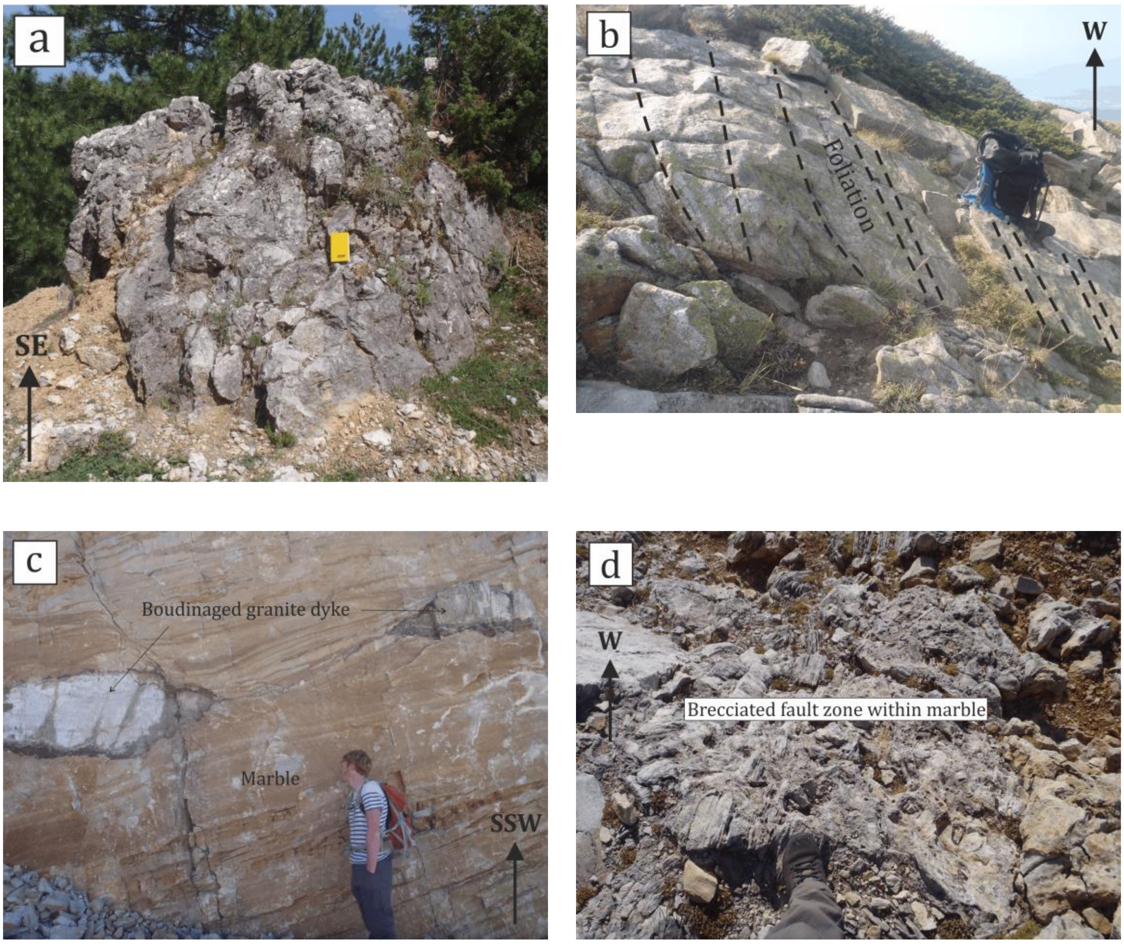

Figure 3.2. Field photographs. a) Limestone found north of the fault at Locality 4.5. b) Gneiss showing foliation parallel to dominant foliation of the massif (Locality 1.11). c) Boudinaged granitic dyke with chilled margins at Locality 14.1. d) Marble breccia at Locality 25.2.

3.2.3. South of Eskişehir Fault

The area south of the Eskişehir Fault belongs to the Anatolide-Taurides (Chapter 2, Figure 2.2) (Okay et al., 2008). Ouctrops found on the south side of the massif, south of the Eskişehir Fault, include mylonitised and metamorphosed granite, gneiss and marble (Figure 3.1). The basin to the south consists of ophiolitic melange and schists (Okay et al., 2008). The granite is a typical composition with quartz, feldspar, biotite and muscovite, with a little chlorite. Marble and gneiss are found within the granite and the composition of each is the same as has been previously described for the Uludağ Massif.

The ophiolitic melange consists of sheared serpentinite along with ultramafic units such as peridotite characterised by an orange and blocky weathering. The outcrops of ophiolite were heavily jointed and faulted.

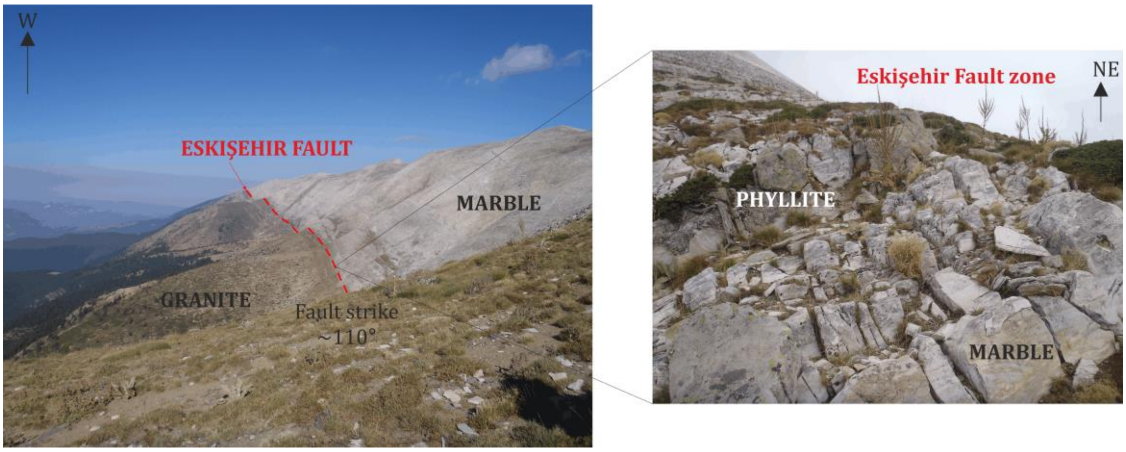

Figure 3.3. The location of the Eskişehir Fault in the field. The fault is located at the boundary between the deformed granite and the marble forming the ridge line to the north of the fault. The fault itself consists of relatively thinly bedded phyllites and marbles that appeared to be highly deformed and show the shear sense indicators discussed in section 3.3.3, Figure 3.5.

3.3. Structure

This section will present the structural information gathered from the field area, split into the tectono-stratigraphic units and major structures outlined previously.

They are in order according to their geographical position relative to the major structures. All lithologies referred to in this section have been named and described under the relevant titles in Section 3.2.

3.3.1. North of the Bursa Fault

The schist outcropping on the northern side displayed a pervasive foliation that varied between 060-130° in strike; this foliation was defined by the high mica content in the rock. The basite outcrops did not show any foliation, but often had quartz veining although there was not enough outcrop containing quartz veins to assess any preferred orientation of the veins. The limestone showed no signs of deformation, the outcrop was largely massive with no internal structure. Bedding was not visible in the outcrops seen.

3.3.2. Bursa Fault

The Bursa Fault bounds the northern margin of the exhumed Uludağ Massif and can be seen on Figure 3.1. Outcrops along the trace of the Bursa Fault are predominantly marble. At locality 2.3, along the trace of the Bursa Fault, recent brittle segments of the fault are visible in cliff sections. On the metre scale, brittle movement on the fault is evidenced by eroded portions of fault breccia (Figure 3.4b) and brittle structures either side of the fault zones, including compression style faulting with evidence of drag folding and kink folding. The inset in Figure 3.4bc is a stereonet of jointing close to these brecciated zones and, based on Andersonian faulting, displays a cross cutting geometry consistent with strike-slip faulting geometry in approximately an NW-SE orientation with a component of normal dip slip movement to the north (Anderson, 1951).

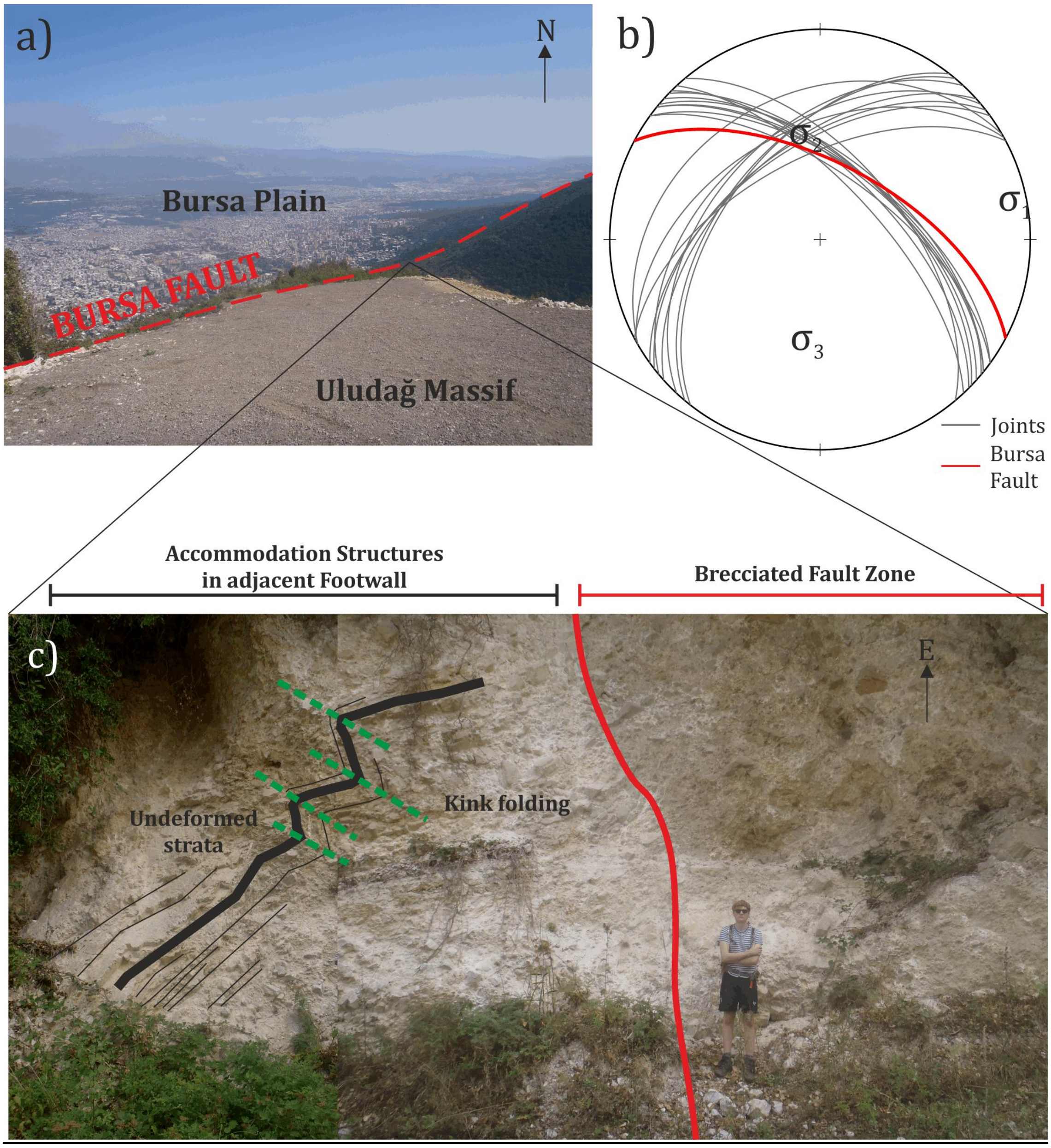

Figure 3.4. Field observation on the Bursa Fault. a) The dramatic change from the Uludağ Massif and the Bursa Plain which is attributed to the activity on the Bursa Fault. b) Stereonet showing the joints in the adjacent hangingwall of fault shown in c) along with approximate principle stress directions, displaying a strike-slip fault geometry parallel to the Eskişehir Fault striking ~110° with a component of normal dip slip movement to the north. c) Picture of a brittle fault along the trace of the Bursa Fault showing fault breccia within the brecciated fault zone.

The Bursa fault anastomoses, changing slightly in strike along its length, following the marble that is present on the north side of the Uludağ Massif. The fault is a brittle fault with a relatively wide zone of deformation when compared to the Eskişehir Fault, mainly consisting of jointing, fracturing, fault brecciation and cataclasis.

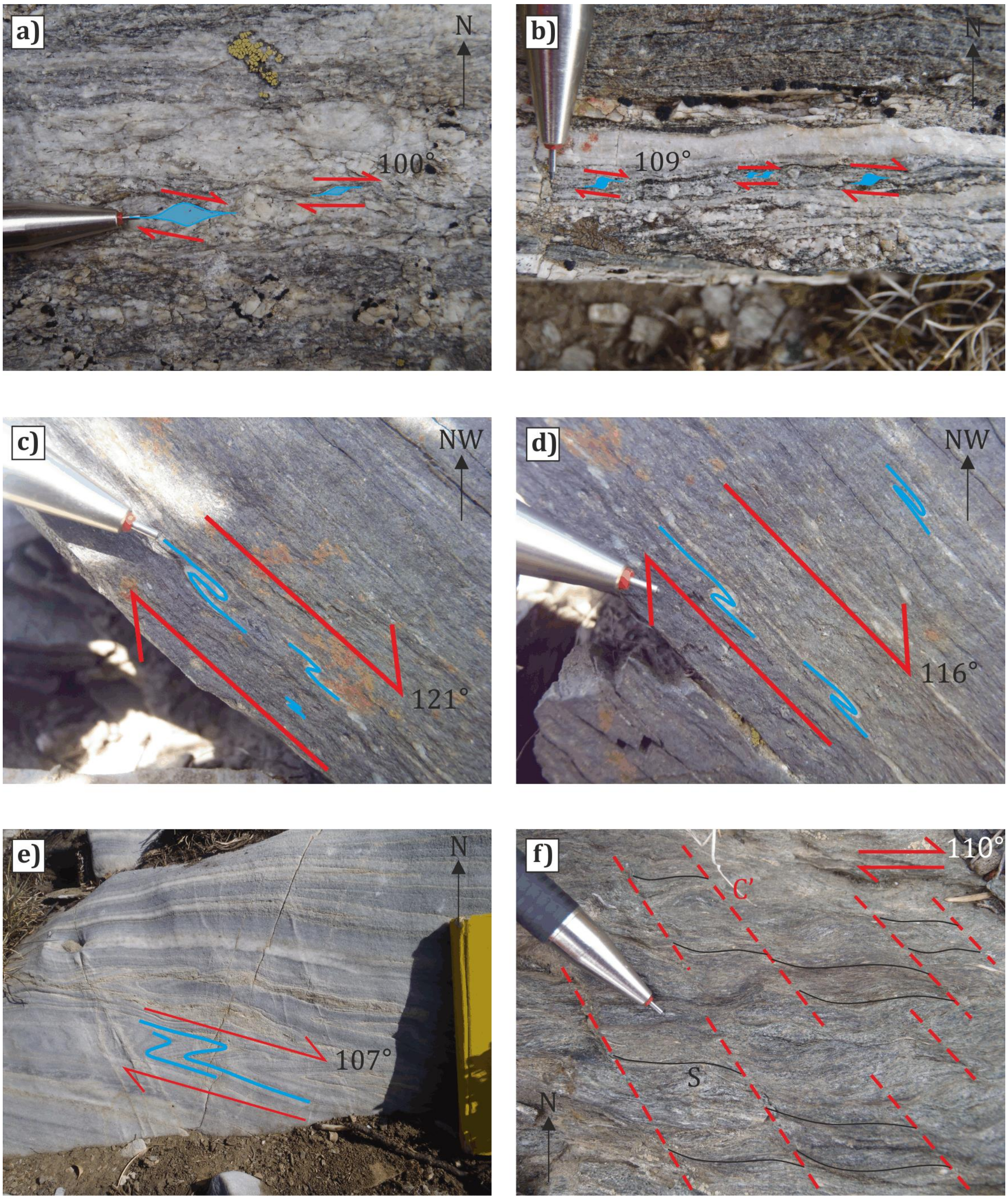

Figure 3.5. Shear sense indicators within the ductile Eshişehir Fault Zone. a), b) both show σ-type winged mantled clasts within a quartzo-feldspathic layer. c), d) show mylontic quartz/feldspar veinlets that have been sheared into folds. e) shows shear folding within the marble unit close to the fault. f) displays C'-type shear bands. All examples show right lateral movement on the fault, as indicated (~110°).

3.3.3. Uludağ Massif

The gneiss and the marble on the southern side of the massif show a pervasive foliation with a mean orientation of 116° that is broadly parallel to the Eskişehir Fault. The foliation within the marble falls into two categories; one running parallel to the fault and one at approximately 80° to this striking at ~30°. The second foliation orientation was predominantly found in the marble unit bounding the southern side of the Uludağ Massif along with the dominant fault parallel foliation. It is possible that this second foliation represents a reidel shear to the shear zone running at ~110°.

The marble unit also contains dykes of which some are boudinaged at Locality 14.1 (Figure 3.2c). The dykes were of granitic composition and showed chilled margins. The boudinaged dyke was found at locality 14.1 (Figure 3.1) and the coherent dyke was found on top of the ridge at locality 3.3 (Figure 3.1). There is a breccia zone within this marble, at Locality 25.2 (Figure 3.1), striking approximately 123°, shown on Figure 3.2d.

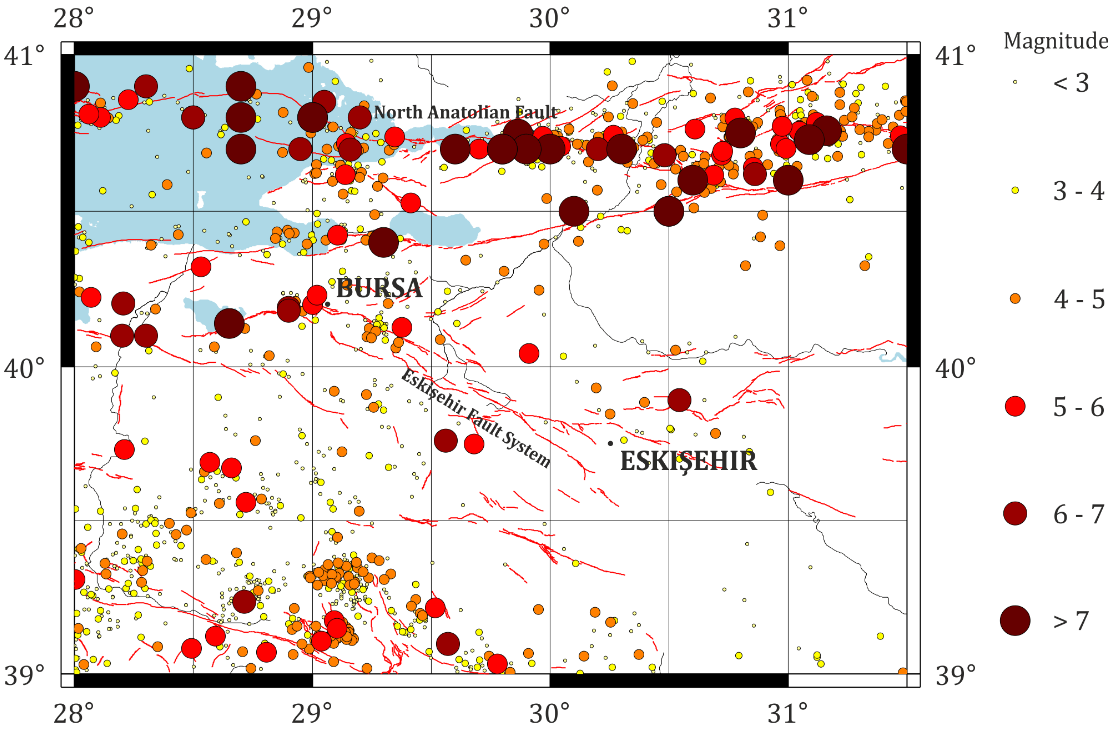

Figure 3.6. A historical seismicity map, showing all magnitude earthquakes for the time period 1950 – present, and earthquakes larger than 6 M_w from the 1st century to 1950. Faults are shown in red for reference. Data from ANSS Comprehensive Earthquake Catalogue (ComCat) (Storchak et al., 2013, Young et al., 1996). Other historial data from Ambraseys and Jackson (2000), Gok and Polat (2011).

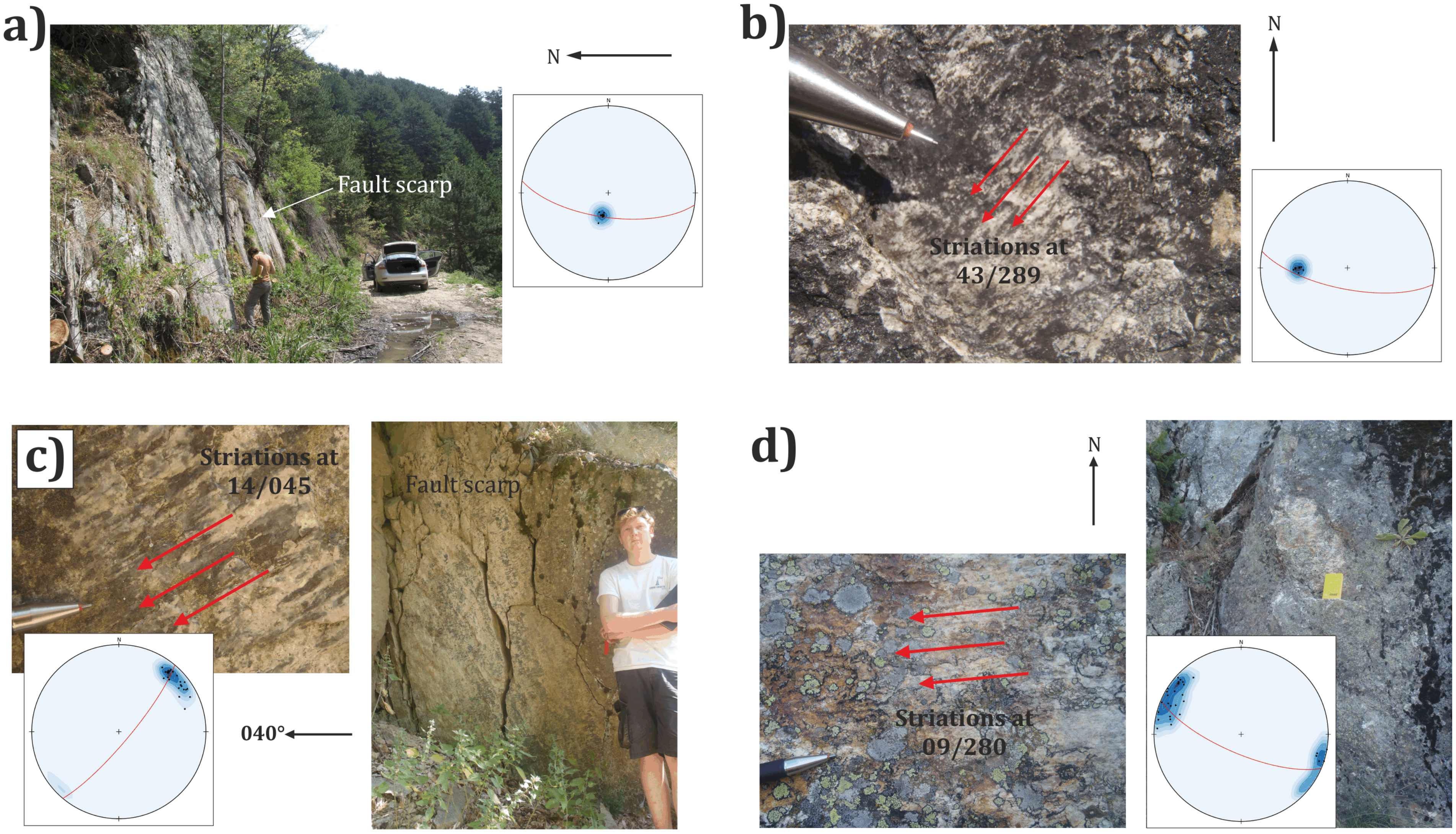
a)
N
Fault scarp
N
b)
N
Striations at
43/289
N
c)
Striations at
14/045
N
040°
Fault scarp
d)
N
Striations at
09/280
N

Figure 3.7. Fault scarps found within the deformed granite unit (Locality 5.1, Figure 3.1), south of the Eskişehir Fault. a) Fault 1 scarp and stereonet. b) Fault 2 striations on fault scarp and stereonet. c) Fault 3 scarp, striations and stereonet. d) Fault 4 scarp, striations and steronets. On all stereonets, the strike and dip of the fault scarp is the red great circle and the striations are plotted as black poles to planes, which are also contoured in blue. Red arrows show the direction of movement indicated by striations.

3.3.4. Eskişehir Fault

The south-bounding Eskişehir Fault has shown some activity in the field area, shown on the historical seismicity map in Figure 3.6, but compared to the Bursa Fault it is quite inactive (Ocakoğlu, 2007, Ocakoğlu and Açikalin, 2010, McKenzie, 1972). The most significant earthquake was on the same fault system but further to the southeast near to Eskişehir where a $M_w = 6.4$ earthquake was recorded in February 1956 (McKenzie, 1972). Unlike the Bursa Fault, it does not show a significant geomorphic expression, instead it lies close to the top of the ridge which can be seen in Figure 3.3. The fault lies adjacent to the marble of the massif, described above, which becomes increasingly deformed as you get closer to the fault displaying shear sense indicators in the form of folding (Figure 3.5e, Locality 22.6). The fault zone is comprised of intensely sheared phyllites and marbles that are interbedded on a ~10m scale.

Adjacent to the fault on the southern side is a deformed granite which also displays evidence for shear. The granite contains quartz, feldspar, biotite, muscovite and some chlorite. The outcrop is very well exposed and almost continuous, the phyllites show much more weathering than the sheared marbles. Both rock types within the fault are well foliated, Figure 3.3. The phyllite contains quartz, feldspar and a high proportion of sheet silicates, namely biotite, muscovite and chlorite.The marble is mainly calcite with a small amount of quartz and is banded on a centimetre to millimetre scale, Figure 3.5. All lithologies show shear sense indicators visible in hand specimen. In the phyllite and adjacent granite these shear sense indicators (Figure 3.5) are manifested in the harder quartz and feldspar minerals. In the marble shear sense indicators take the form of folds.

The fault strikes at ~110° and bounds the southern side of the Uludağ Group marbles. Mineral stretching lineations in the rocks comprising the fault zone fall into two groups, sub-horizontal and sub-vertical. Shear sense indicators show right lateral movement (eg. Figure 3.5). The sense of shear is consistently in a right lateral sense, top to ~110°. The fault is a linear, single strand striking similarly along its length, with quite a narrow zone of intense ductile deformation (~30m). Adjacent to the fault, in the South Uludağ Granite and the marble to the north the rocks exhibit a mylonitic fabric.

3.3.5. South of Eskişehir Fault

The granite found near the Eskişehir Fault appears as an elongate intrusion along the length of the fault. There are some fault scarps found in this unit, with slickensides that show a sense of motion (Figure 3.7). The following 4 fault scarps were found in the same vicinity, Location 5.1, Figure 3.1. Fault 1 (Figure 3.7a) shows a fault plane that is parallel to the main Eskişehir Fault. The striations on this fault plane are steeply plunging to the south (68/195). Fault 2 (Figure 3.7b) is again parallel to the main fault and striations on the surface plunge much more shallowly to the west (43/289). Fault 3 (Figure 3.7c) is at 040° strike, ~70° from the main fault trace and shows sub horizontal striations plunging very shallowly to the north east (14/045). The striation measurements on fault 4 (Figure 3.7d) are sub horizontal (09/280) and are on a fault plane that is parallel to the Eskişehir Fault.

3.4. Discussion

Due to the incompetent nature of the micaschist unit the large variation in foliation strike is likely to be caused by localised variations in the stress field producing a foliation that is not parallel to the regional tectonic foliation of the rest of the massif. It could also be due to minor folding within this unit. The foliation measurements do not show any pattern, making it hard to determine what is causing the variation. The quartz veins in the basite are likely a product of metamorphism, but due to the lack of reliable outcrop (i.e. not intensely weathered or too small and fractured) this could not be determined. The green epidote in the quartz rich layers is an alteration of feldspar, indicating greenschist metamorphism. These two units form part of the Triassic accretionary Karakaya Complex (Okay et al., 1991, Okay et al., 2002, Okay et al., 2008). Above these units are the overlying undeformed sequences deposited in the Early Jurassic, of which the limestone forms a part (Okay et al., 2008). The stratigraphic sequence of the area has been discussed in more detail in Chapter 2, Section 2.4.

The Bursa Fault strikes roughly the same as the entire Uludağ Massif, ~110° and dips to the north, approximately 60-70°. Slickensides on fault planes indicate a normal sense of movement with a component of right lateral strike-slip motion which is consistent with observations made by Yıldırım et al. (2005). It is part of the Eskişehir Fault System, which has been discussed in Chapter 2, Section 2.4.1. The Eskişehir Fault System has had a number of large earthquakes throughout recorded history which are documented on Figure 3.6. The Bursa Fault is currently active as a normal fault (Sellami et al., 1997, Selim and Tüysüz, 2013, Sandison, 1855, Meade et al., 2002), and the last known activity was reported by Sandison (1855) as the M ~6.6 1855 Bursa earthquake. The expression of the Bursa Fault in the landscape is very obvious; it lies at the northern margin of the exhumed

Massif where it drops off onto the Bursa Plain, with an elevation change of ~1000m (Figure 3.4a).

There is little variation in the gneiss over the massif indicating an igneous origin. There is a lack of any metasedimentary layers, or local variations in mineralogy to suggest a sedimentary, paragneiss origin. The same observations have been made previously by Okay et al. (2008). The amphibolite outcrops suggest smaller dykes or intrusions of a more mafic lithology within the igneous body protolith of the unit. The gneiss, along with the marble, forms part of the exhumed terrane of the Uludağ Group. Of the dykes found within the marble unit most originate from the granite intrusion in the northwest of the massif. This large granitic intrusion is the Central Uludağ Granite (Okay et al., 2008). The brecciated zone found with the marble at Locality 25.2 (Figure 3.2) is evidence for later stage brittle faulting, possibly during exhumation as it is running close to parallel to the massif-bounding faults (Bursa and Eskişehir Faults). The two foliation groups within the marble show evidence for reidel shear formation at approximately 90° to the fault. The lack of foliation in the centre of the Central Uludağ Granite along with the dykes that show clear chilled margins is evidence to support the fact that this intrusion was post kinematic, intruded after strike slip activity had ceased. The foliation that is seen on the margins of the granite is typical from large igneous intrusions and is formed due to the stress increase as it is being forced into the host rock.

The Eskişehir Fault was the focus of a large amount of dextral strike slip deformation before reactivating as an oblique normal fault during uplift in the Miocene (Okay et al., 2008, Özsayın and Dirik, 2007). In the field this is evidenced by the two groups of mineral stretching lineations, the sub-horizontal belonging to the ductile strike slip shear, and the sub-vertical formed within the ductile regime during exhumation. Shear sense indicators, such as asymmetric quartz and feldspar clasts and folds in the units within the fault zone also support right lateral strike slip shear, top to 107° (Figure 3.5).

The geological map of Okay (2008) is based largely on the map produced by Ketin (1947) and shows the main strand of the Eskişehir Fault to be south of the deformed granite and a band of gneiss. The Mineral Research and Exploration General Directorate (MTA) maps, which have been used to construct the map in Figure 3.1, show the Eskişehir Fault running through the deformed granite (Akbaş et al.). From field observations presented above both of these representations appear to be partly incorrect for the main Eskişehir Fault strand. It is more likely that the main fault is actually located within the phyllite-marble band encountered on both transects (Figure 3.3 and map in Figure 3.1). This is a similar situation to that described by Phillips and Searle (2007) and Wallis et al. (2013) on the dextral strike-slip Karakoram Fault Zone, Ladakh, India, where fault strands are located at strength contrast interfaces between metasediments (eg. phyllites and marbles). The phyllite and granite both contain a small amount of chlorite which is evidence for greenschist metamorphism.

The deformed granite that bounds the southern side of the Eskişehir Fault is the South Uludağ Granite. The four faults within the South Uludağ Granite can be used to infer the tectonic history of the area. Slickenfibres are a type of striations that can give the sense of shear from the stepped topography of the mineral growth, ie on the exposed footwall of a normal fault slickenfibres will step up, up dip. Fault 4 (Figure 3.7d) shows the strike slip faulting in the area, with a dextral sense of shear from the stepped topography of the quartz slickenfibre growth, stepping up to the ESE, top to ~100°. Fault 3 (Figure 3.7c) is at 040° strike, which is ~70° to the main Eskişehir Fault suggesting a reidel shear associated with the fault. The quartz slickenfibres on the fault plane show a shallow pitch to the NE and the quartz mineral fibres display a stepped topography, stepping up towards ~220° suggesting a left lateral sense of motion.

The initiation of exhumation is recorded on fault 2 (Figure 3.7b) with the recording of a right lateral oblique slip motion, again coming from the stepped topography of quartz slickenfibre growth, stepping up, up dip. Quartz slickenfibres on fault 1 (Figure 3.7a), again step up, up dip, suggesting a normal sense of movement, which would represent the later reactivation of this fault. Okay et al. (2008) presents evidence that the South Uludağ Granite is syn-kinematic; there is no contact metamorphism between it and the surrounding rocks meaning it was emplaced at depth with high ambient temperatures, sheet like geometry, parallel to the dominant foliation of the massif, elongated tail, solid-state and crystal-plastic strain fabrics. The ophiolitic melange in the basin south of the granite was emplaced onto the Anatolide-Taurides during the closure of the Tethys in the mid-Cretaceous, and represents a highly sheared accretionary complex (Okay, 2008).

The observations presented above result from tectonic stresses that are mainly exhibited as strain throughout the massif. The presence of a pervasive fault-parallel foliation and mylonitic fabric suggest that the rocks contained within the massif (gneiss, marble and the South Uludağ Granite) have been subjected to the same tectonic stress field within a ductile shear zone. Outside of the massif, and shear zone, exist variations in the strain orientations which are mainly exhibit through variations in foliation orientation. The rocks showing these variations belong to different tectonic terranes from the Uludağ massif and shear zone, possibly related with accretionary tectonics as the Eskişehir Fault Zone does represent the Izmir-Ankara-Erzincan suture (Okay, 2008). The brittle structures seen on the northern side of the massif, along the Bursa Fault, represent a switch in the regional tectonics as the massif was exhumed through the brittle-ductile transition zone to the surface.

4. CHAPTER FOUR

Compiling a structural and thermal history for the Uludağ from microstructure.

4.1. Introduction

The chapter outlines the geology of the Uludağ Massif, NW Turkey (location in Chapter 2, Figure 2.1 and Figure 2.2) from micro-scale observations and data from thin sections analysis. The micro-scale observations from thin sections, will include grain size, twinning and microstructural analyses. Microstructural analysis will provide information on temperature and deformation conditions. Grain size analysis can also reveal information about temperature but also can provide stress estimates from defined flow laws. From these stress and temperature estimates strain-rate can be obtained. How deformation is distributed across the shear zone can then be looked at in relation to temperature, stress and strain rate variations. Thin sections analysis and stress distributions can also reveal information on fault weakening mechanisms, the overall outcome being a construction of the structural and thermal history of the area.

4.2. Microstructure Analysis - Background

The microstructure of samples can be used to determine information about the conditions of deformation (Wallis et al., 2015, Parsons et al., 2016). For example, calcite twins are prevalent in most marble samples collected from the massif and their morphology, distribution and shape can be attributed to the temperature of deformation (Burkhard, 1993). Calcite grain size can be used as a paleopiezometer and in conjunction with experimentally derived flow laws and temperatures from microstructure can reveal information on strain rate (Rutter, 1995). In other lithologies such as the gneiss, pelite and granite, quartz recrystallisation mechanisms (Stipp et al., 2002) and quartz c-axis opening angles (Kruhl, 1998) can be used to ascertain the temperature of deformation for quartz. Microstructures can also provide information relating to deformation mechanisms, kinematics and principal stress orientations (e.g. calcite twins, shear sense indicators).

The microstructure of the samples was investigated through optical microscopy of uncovered polished thin sections. The thin sections were cut perpendicular to foliation and parallel to the lineation, or transport direction, and are kinematic XZ sections.

4.2.1. Calcite

A large proportion of the Uludağ Massif consists of marble (Chapter 3, Figure 3.1). These marbles, for the most part, mainly comprise calcite with minor dolomite and quartz.

Calcite twins very easily due to its low critical resolved shear stress and almost no temperature dependence (Burkhard, 1993). Almost all of the samples within the Uludağ sample suite show some degree of twinning. Analysis of calcite twins can be used to obtain information on a number of deformation parameters. Early work by Turner (1953) found that twinning can be used to identify the orientations of principal stress axes.

Further experimental work on calcite twinning identified its use as a palaeopiezometer, as Friedman and Heard (1974) observed that twin lamellae increase in adundance with increasing differential stress. This has subsequently been built on to provide a robust palaeopiezometer using calcite twinning (e.g. Jamison and Spang (1976), Spiers and Rutter (1984), Ferrill et al. (2004)). Burkhard (1993) also discovered that the appearance of calcite twins can be a useful tool to estimate the temperature of deformation.

(a) Twinning Crystallography and Conditions

The twinning looked at in this study is a mechanical twinning formed during deformation as the result of stress on a crystal after it has been formed. Twinning in calcite occurs on the e-planes $\{\bar{1}018\}<40\bar{4}1>$ and is a process by which atoms rearrange themselves in a way that the twin becomes a mirror image of the host crystal along the twin plane (Figure 4.1b) (Motohashi et al., 1976). The process of twinning is often referred to as a slip system as twinning, like crystal slip, occurs on specific planes in certain directions (Rowe and Rutter, 1990). Calcite has trigonal symmetry and therefore has three planes of symmetry orientated at 60° to each other around the c-axis. The crystallography of calcite and a schematic of the twinning mechanism is shown in Figure 4.1. Twinning of the e-planes can be described as a zone of perfect simple shear during which the crystal axes are rotated (Spang, 1972). The difference between the orientation of the c-axis in the host grain and the c-axis in the twin is approximately 52° (Burkhard, 1993) (Figure 4.1). At temperatures below 400°C, e-twinning is an important deformation mechanism, initiated at low critical resolved shear stresses (CRSS) of 5-15 MPa (Passchier and Trouw, 2005, De Bresser and Spiers, 1997) (Figure 5.4). However twinning alone cannot accommodate large strains as twin sets will hinder each other in development and eventually leads to strain hardening (Burkhard, 1993). Calcite also deforms easily at low to moderate strains and high temperatures. Deformation through twinning leads to strain heterogeneities between grains, and grains favourably orientated for twinning accommodate twice as much strain as would be expected from the resolution of the bulk strain on the twinning planes (Spiers, 1979). Whilst temperature affects the size and shape of twins (Burkhard, 1993), it does not have a strong effect on twinning and neither does strain-rate or total strain (Rowe and Rutter, 1990).

(b) Principal stress orientation

Calcite twins have also been used to measure the principal stress orientations, which can be useful in determining the tectonic history of an area. Turner (1953) and Weiss (1954) recognised that the most favourably orientated compression and tension directions can be measured from the geometry of twinning in calcite. The c-axis, pole to e-twin and glide direction all lie in the same plane (Spang, 1972). The compression and extension axes lie in this same plane at 45° and 135° from the twin plane respectively, with the compression axis in the opposite quadrant to the c-axis of the host grain. The host c-axes and pole to the twin plane are measured and plotted on a stereonet. The compression axis is found at 45° to (e)-pole in the direction away from (c), in the (e) – (c) plane and the extension axis is found 90° to this in the same plane (Turner, 1953, Carter and Raleigh, 1969) (Figure 4.1c).

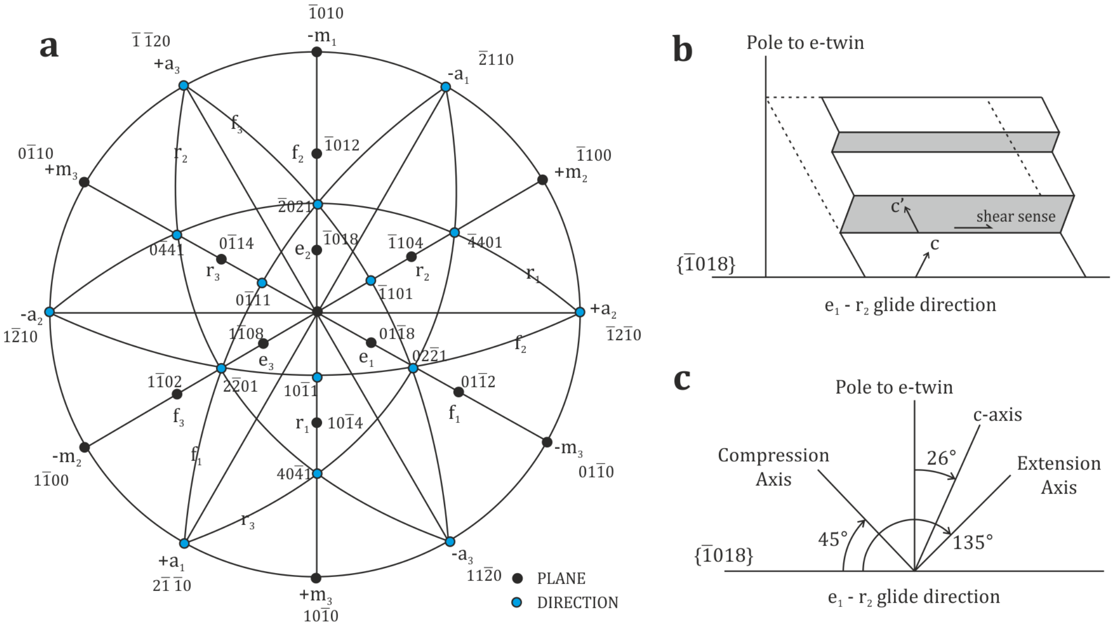

Figure 4.1. Calcite twin crystallography. a) Crystallographic planes and slip directions in calcite. b) Schematic representation of twinning in calcite, the stippled areas are the twinned portions and the dashed line indicates the original grain before twinning (Spang, 1972). c) The geometry of calcite related to the principal compression and extension axes (Spang, 1972).

(c) Grain size palaeopiezometer

Deformation in fault zones, both brittle and ductile, can be characterised by grain size reduction through dynamic recrystallisation, cataclasis or metamorphic reaction. Early work by Twiss (1977) used experimental information on olivine and identified that dynamically recrystallised grain size could be used to infer stress. Subsequently a lot of experimental work on calcite samples from Yule and Carrara marble has been done, providing a large database to investigate the relationship between grain size and stress in calcite. Heard and Raleigh (1972) worked on determining the stress-strain behaviour of

Yule marble through experiments ranging in temperature from 500 - 800°c, and Schmid et al. (1980) carried out further experimental work to determine flow laws and also looked into the effects of dynamic recrystallisation. Subsequently, Rutter (1995) advanced the previous work to larger strains and also again looked into recrystallisation mechanisms and their effect. The following equation derived by Rutter (1995) will be used in this study to determine stress:

$$\log \sigma = 2.22 + 0.37 \log d - 0.30\ (\log d)^2 \qquad (4.1)$$

Where σ is differential stress in MPa and *d* is grain size in µm. Equation 4.1 is based on the experimental migration-recrystallised data from the same study by Rutter (1995), along with grain size and temperature data from Naxos, Greece (Covey-Crump and Rutter, 1989).

(d) Temperature of Deformation

Optical microscopy of calcite microstructure such as twinning, brittle structures, pressure solution structures and recrystallisation can reveal information about the deformation temperature. At very low-grade conditions (below 200°C and 300MPa), calcite deforms by brittle fracturing and cataclasis, although twinning also contributes (Kennedy and Logan, 1998). At low-grade conditions with the presence of water, stylolite development occurs due to pressure solution; again, twinning is also important below 300°C (Burkhard, 1993, Kennedy and Logan, 1998, De Bresser and Spiers, 1997). At ~250°C dynamic recrystallisation, bulging at low temperatures, sub grain rotation at high temperatures of calcite becomes important and it is the dominant deformation mechanism between 300-400°C (Evans and Dunne, 1991, Weber et al., 2001).

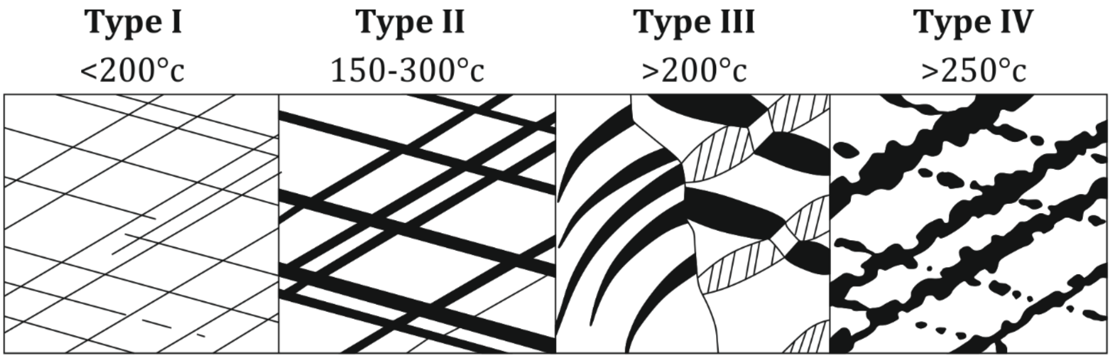

Figure 4.2. Twin geometries and associated temperatures. Thin, rational and straight type I twins indicate temperatures of less than 200°C. Type II twins are thick, rational and straight and are formed in a range of temperatures from 150-300°C. Type III twins occur at temperatures above 200°C and are irrational, showing curved twins, twins within twins and grains are almost completely twinned. At the highest temperatures, above 250°C, grain boundary migration occurs resulting in patchy, thick, irrational twins. Modified from (Burkhard, 1993).

At low to medium-grade conditions (>300-400°C), besides deformation twinning, dislocation glide on {r}- and {f}-planes is important (Figure 4.1a), and (c)<a> slip occurs at higher temperatures (550-800°C) (De Bresser and Spiers, 1997, Pieri et al., 2001, Bestmann and Prior, 2003).

It has been suggested from numerous experimental and field observations that twin thickness and type is mainly a function of deformation temperature, with differential stress and strain rate playing a minor role (Burkhard, 1993, Groshong et al., 1984, Rowe and Rutter, 1990, Ferrill, 1991). Figure 4.2 shows this relationship between twin shape and thickness with temperature. At low temperatures thin type I twins develop and as temperature increases these thin twins become thicker type II twins. Thickness also depends on shear strain; at low temperatures and increasing shear strain more thin twins will develop, whilst at higher temperatures and increasing shear strain thicker twins preferentially develop (Ferrill et al., 2004, Rowe and Rutter, 1990). One reason for the development of thicker twins at higher temperatures is the stress dependence of twinning; it becomes easier for existing twins to enlarge rather than to create new ones (Burkhard, 1993). The transition between thin and thick twins is between 150 and 200°C in naturally deformed limestones, which is much lower than the temperature found in experiments due to the lower natural strain rates (Ferrill, 1991).

Lab experiments by Rowe and Rutter (1990) reveal that at temperatures above 400°c twins become lens shaped (type III twins). The formation of curved type III twins is attributed to slip on either the {r}- or {f}-planes ($\{10\bar{1}4\}\langle\bar{2}021\rangle$ and $\{\bar{1}012\}\langle10\bar{1}1\rangle$ respectively) within the crystals (Burkhard, 1993) (Figure 4.1a). Slip on these two slip systems requires the critical resolved shear stress (CRSS) to have been overcome, which is strongly temperature dependent. Slip on r- and f-planes becomes important above ∼400°C because their CRSS values are lower than other slip systems at this temperature (Figure 5.4) (De Bresser and Spiers, 1997). Irregularly shaped twin boundaries (type IV twins) suggests the occurrence of twin boundary migration recrystallisation, which is a thermally activated process and therefore strongly temperature dependent (Burkhard, 1993). Figure 4.2 was devised using samples from the Helvitic Nappes of western Switzerland, with independent constraints on temperature, such as thermobarometry, and stable isotope thermometry, from which an accurate temperature profile could be constructed and correlated with twin appearance (Burkhard, 1993). This relationship between twin geometry and temperature is only qualitative, other methods exist that relate mean twin width to temperature which provide a more quantitative analysis (Ferrill et al., 2004).

Previously, experimental studies have been carried out to ascertain if there is a relationship between grain size and temperature of deformation (eg. Schmid et al. (1980), Covey-Crump and Rutter (1989), and Rutter (1995)). Estimating temperature from strain-rate presents problems because there have been numerous flow laws established for calcite under different conditions (eg. Rutter (1974), Schmid et al. (1980), and Walker et al. (1990)). It has been identified by numerous authors that extrapolating flow laws to geological conditions should be done with caution as every application will involve different parameters (e.g. kinematics, temperature, strain-rate) (Schmid et al., 1980). The graph in Figure 4.3 is based on various flow laws derived from experimental work on calcite deformation and can be used as a cautious estimate for temperature (Rutter, 1974, Schmid et al., 1980, Walker et al., 1990).

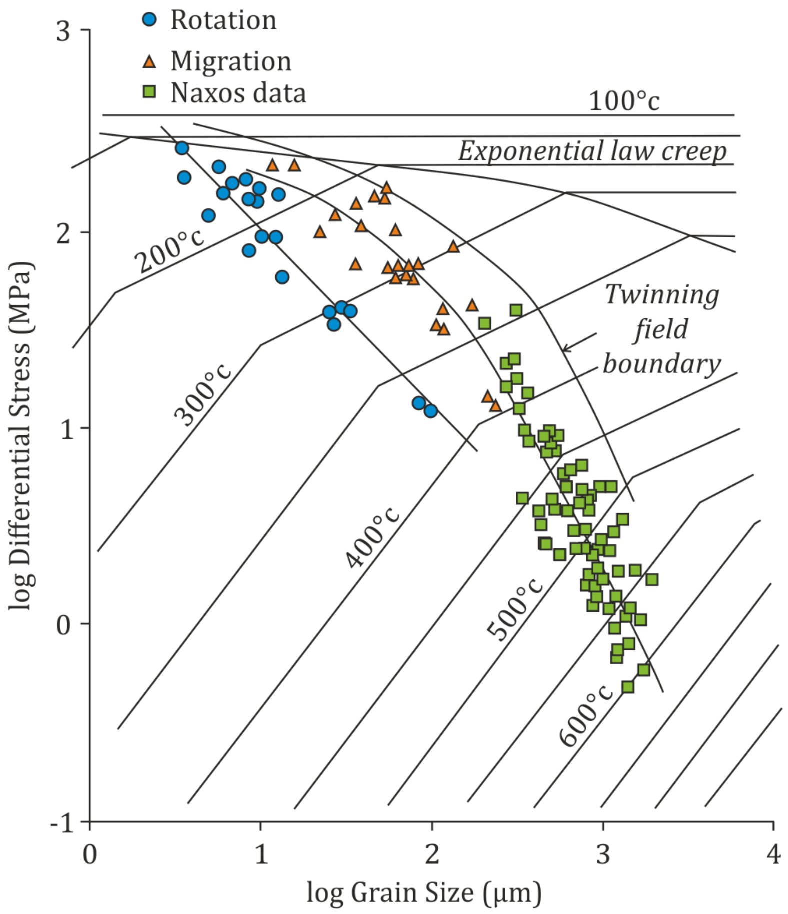

Figure 4.3. Graph showing the relationship between differential stress, grain size and temperature using the exponential flow law of Rutter (1974), the dislocation creep laws of Schmid et al. (1980) and laws for finer grain sizes from Walker et al. (1990). Experimental data for rotation (linear best fit) and migration (quadratic best fit) recrystallisation, along with Naxos temperature/grain size data are shown (Rutter, 1995). Graph modified from (Rutter, 1995).

Grain size of samples was determined via HKL Channel5, version 5.12.60.0 (©1998-2015 Oxford Instruments NanoAnalysi) using the linear intercept method from electron backscatter diffraction (EBSD) derived grain maps. The methodology for acquisition of EBSD will be described in detail in Chapter 5. This method measures grain boundary intersections on two orthogonal axes, of which the geometric mean can be taken (Sun et al., 2010):

$$d_{lin} = \sqrt{L_x L_y} \qquad (4.2)$$

Where d is the grain size in microns, L_x is the grain size from linear intercept in the x-axis and L_y is the grain size from linear intercept in the y-axis. In Channel5 boundaries between twins can be discounted when detecting grain boundaries by setting a particular axis and misorientation angle to ignore. This is important as twins are not separate grains so would skew the results. Grain size can also be determined in Channel5 using grain detection and reconstruction. The post processing noise reduction that can be performed in Channel5 can have an effect on grain sizes measured using the reconstruction method and lead to an underestimation of the mean (Sun et al., 2010, Mingard et al., 2007). For this study, the linear intercept method is favoured and results using this method only are presented.

4.2.2. Quartz

Quartz is a common mineral in all but one of the samples within the granite and gneiss lithologies. Similar to calcite, quartz microstructures can reveal information relating to deformation temperature and will be the primary focus of the study of the quartzo-feldspathic samples. Quartz grain size can also be used as a palaeopiezometer and subsequently also to estimate strain rate.

(a) Temperature

At temperatures below 300°C, quartz typically displays brittle fracturing, undulose extinction, and pressure solution and redeposition of SiO_2 in veins (Stipp et al., 2002, Passchier and Trouw, 2005). At low metamorphic grades (300 - 400°C), basal<a> ({c}<a>) dislocation glide and creep become important, with undulose extinction and dynamic recrystallisation via bulging crystallisation (BLG) also characteristic of this temperature range (Figure 4.4) (Stipp et al., 2002, Tullis, 1970). At 400 - 500°C, prism<a> slip ({m}<a>) and rhomb<a> ({r/z}<a>) become dominant and abundant recovery and recrystallisation by sub grain rotation recrystallisation (SGR) is observed (Figure 4.4) (Lloyd and Freeman, 1994, Passchier and Trouw, 2005, Stipp et al., 2002). Microstructures typical of SGR and BLG are core and mantle structure, which show relict large grains with recrystallised rims, but also grains can be completely replaced. At high-grade temperatures (500 - 700°C) the most common microstructure is grain boundary migration (GBM) recrystallisation (Figure 4.4) and most grains show no internal deformation due to rapid recovery (Stipp et al., 2002). The most common slip system at these temperatures is prism<c> ({m}<c>) slip (Mainprice et al., 1986)

Temperature can also be determined using grain size. The method to determine grain size for quartz is the same linear intercept method outlined in section 3.2.1. Stipp et al. (2002) developed a method for determining temperature from recrystallised grain size.

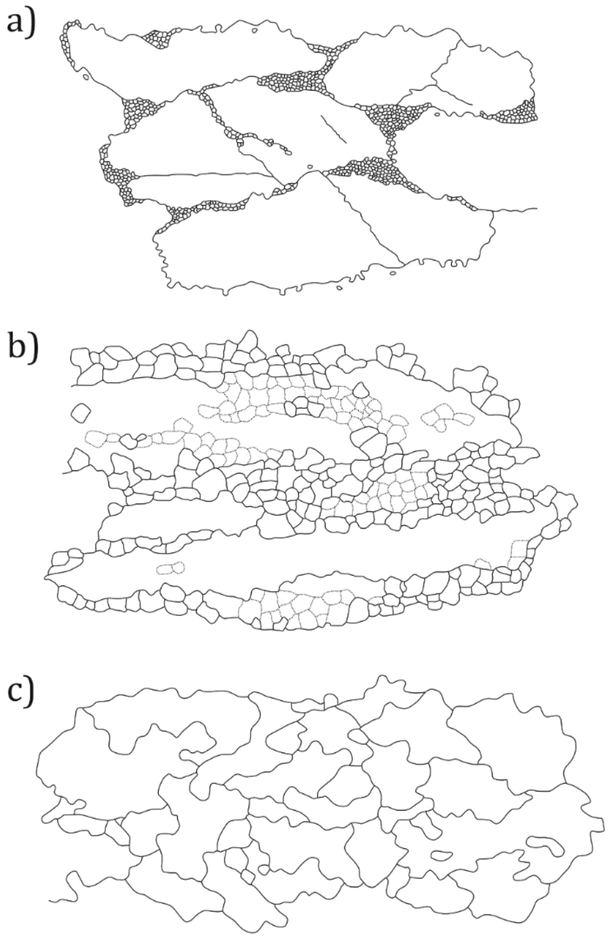

Figure 4.4. Microstructures of the three recrystallisation mechanisms. a) BLG along grain boundaries and microcracks. b) SGR core mantle structures, ribbon grains consumed by recrystallized grains. c) GBM irregular grain shapes and grain sizes, interfingering sutures (Stipp et al., 2002).

They use data from the Tonale fault zone, Italian Alps, and acquired independent temperature estimates from syn-kinematic mineral assemblages in the surrounding host rock (Stipp et al., 2002). They found that the transition between frictional and viscous regimes occurs at ~280°C, BLG recrystallisation is dominant between ~280 and 400°C, SGR recrystallisation between 400 and 500°C and the transition to GBM recrystallisation above 500°C (Stipp et al., 2002). The results from their study are shown in Figure 4.5. The grain size obtained from the samples can then be compared to this graph to derive a temperature estimate.

(b) Grain size palaeopiezometer

Grain size can also be used to determine differential stress using a recrystallised grain size piezometer. The piezometer used in this study is that developed by Stipp and Tullis (2003) based on deformation experiments performed on Black Hills Quartzite. The experiments were carried out at 1.5 GPa, 800-1100° and strain rates between 2 x10^{-7} and 2 x10^{-4} s^{-1}. The data obtained from these experiments give the piezometer for recrystallised grain size in quartz as;

$$D = 10^{3.56 \pm 0.27} \, x \, \sigma^{-1.26 \pm 0.13} \qquad (4.3)$$

Where D is the grain size in microns and σ is the differential stress. Equation 4.3 applies only in dislocation creep regimes 2 and 3, defined by Hirth and Tullis (1992), which corresponds to grain size above ~2μm and a flow stress below ~130MPa, which these data fall into. It is noted by Stipp and Tullis (2003) that the flow stress estimates up to a grain size of 46μm are reliable, reasonable between 46-120μm and anything above 120μm is significantly underestimated.

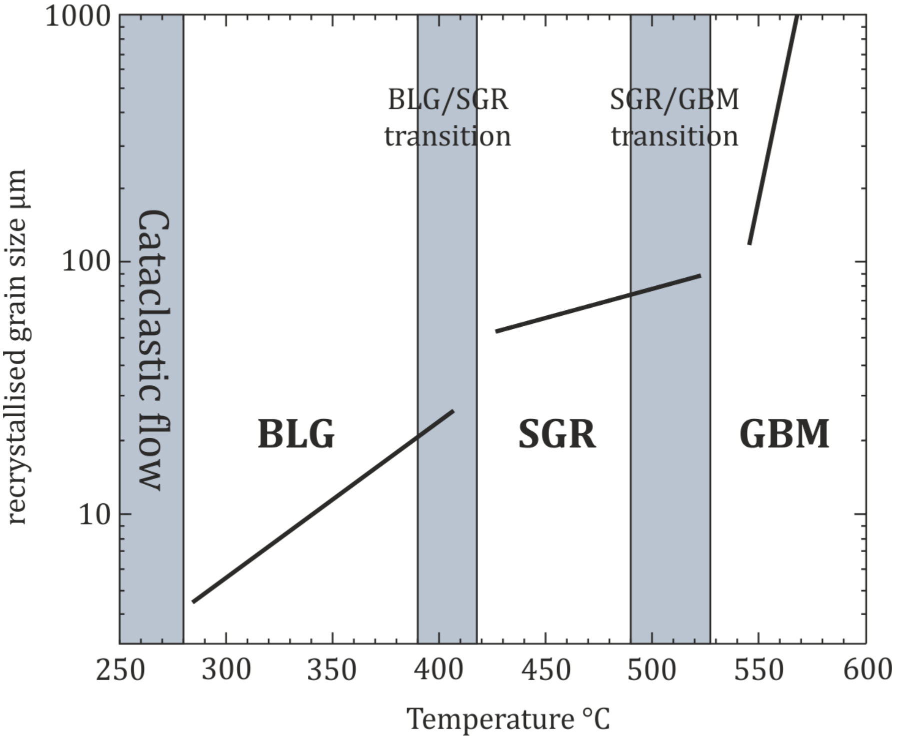

Figure 4.5. Temperature as a function of grain size for quartz from Stipp et al. (2002). Best fit lines only for each recrystallisation type are shown for the data.

4.2.3. Feldspar

Feldspars are more stable than quartz, deforming by brittle fracturing and cataclasis up to 400°C (Tullis and Yund, 1987). Grains within the cataclasite often exhibit intracrystalline deformation, including bent cleavage and twins planes and patchy undulose extinction and sub grains with vague boundaries (Passchier and Trouw, 2005). In plagioclase, deformation twinning on pericline and albite law planes is important at these temperatures (Borg and Heard, 1969, Passchier and Trouw, 2005). Between 400 and 500°C, dislocation glide starts to become important, resulting in bent twins, undulose extinction and deformation bands (Pryer, 1993). BLG recrystallisation may occur at high stress sites (eg. at grain boundaries), whilst perthite structures may develop in K-feldspar (Pryer and Robin, 1995, Pryer, 1993). At medium grade conditions, from 450 - 600°C, recrystallisation becomes important as dislocation climb is activated, with BLG recrystallisation forming core and mantle grain structures (Borges and White, 1980, Tullis and Yund, 1991). Towards higher temperatures, deformation twins become less abundant whilst myrmekite growth along boundaries and flame perthite becomes more prevalent in K-feldspar (Simpson and Wintsch, 1989). At high grade conditions (>600°C) both SGR and BLG recrystallisation occur, in both plagioclase and K-feldspar, with less pronounced boundaries between core and mantle structures (Olsen and Kohlstedt, 1985, Pryer, 1993). Above 850°C GBM recrystallisation has been observed in plagioclase with a melt phase also present, it looks similar to GBM in quartz (Figure 4.4) (Lafrance et al., 1996, Rosenberg and Stünitz, 2003).

Feldspars do not have many active slip systems, so as a deformation mechanism to accommodate strain, recrystallisation is very important. Due to the low number of available slip systems, two mantled porphyroclast structures can form depending on whether the crystal is unfavourably, or favourably orientated for slip. Relatively undeformed 'globular' porphyroclasts attest to unfavourable orientations, whilst ribbon plagioclase grains indicate favourably oriented grains (Ji and Mainprice, 1990).

4.2.4. Shear sense indicators

Ductile fault rocks often exhibit shear sense indicators at the grain scale which can be used to infer the kinematics of how a fault has moved. These can take the form of mineral clasts with asymmetric strain shadows or 'mantles', rotated clasts or cleavage interactions with shear zone boundary and foliation orientations.

Shear band cleavage can be used to infer the sense of shear on outcrop scale but also in thin sections, and are divided into three variants: C-type, C'-type and C''-type, dependent on their orientation relative to the shear zone boundary. All shear band cleavage types are shown in Figure 4.6a. C-type shear bands are parallel to shear zone boundaries and usually appear straight and continuous. This microstructure is common in medium grade, weakly foliated mylonites containing a little mica (Passchier, 1991). C'-type shear band cleavage is oblique to the shear zone boundary and is often discontinuous and anastomosing. C'-type shear usually develops during later stages of shearing after a strong crystallographic preferred orientation (CPO) has developed (Platt, 1984). C''-type shear band cleavage form conjugate to C'-type, making a large angle to the shear zone boundary and are antithetic to the shear sense of the whole shear zone.

Mantled porphyroclasts can also be used as shear sense indicators. Two types can form: the first where the mantle strain shadow surrounding the clast is the same composition as the porphyroclast, and the second where the strain shadow is a different composition (Figure 4.6b). These can often display a sense of asymmetry in the recrystallised mantle surrounding the clast which is formed from a rigid clast rotating in a simple shear flow field. 4 types of mantled porphyroclasts have been identified based on the shape of the ‘wings’; ϕ-type, σ-type, δ-type and complex, which are all shown in Figure 4.6c (Passchier and Trouw, 2005).

Mineral ‘fish’ are common in mylonites and consist of elongate or lozenge shaped single crystals. Mica fish are the most abundant and can also be used to infer the sense of shear (Figure 4.6c). They most likely form because the mica crystal has a weak bonding with its matrix and this is a stable position in non-coaxial flow (ten Grotenhuis et al., 2002). Sigmoids are another σ-type clast differing in that they are composed of completely recrystallised grains, ie. there is no central porphyroclast.

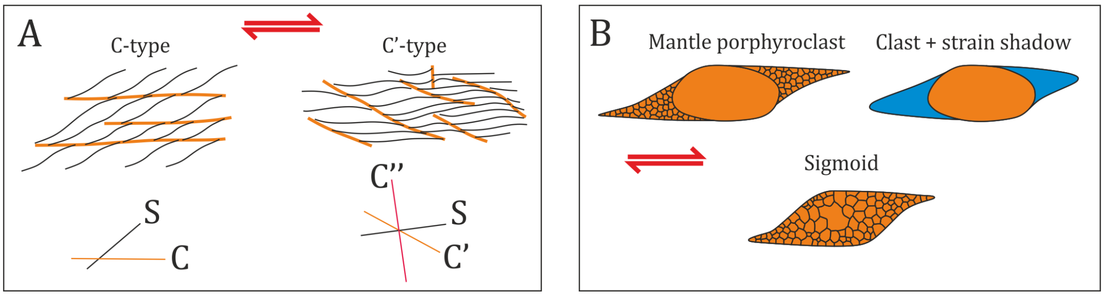

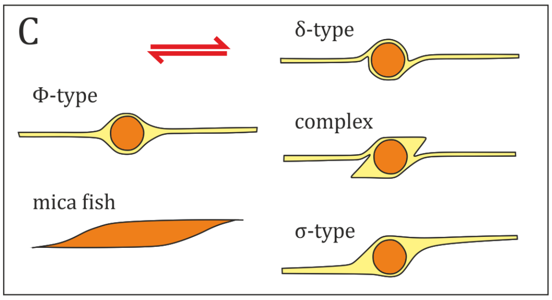

Figure 4.6. A) C, C’ and C’’-type shear, shear sense indicated. B) shear sense indicated by strain shadows and mantle prophyroclast structures. C) shear sense indicated by rigid rotation of clasts and strain shadows. Adapted from (Passchier and Trouw, 2005)

4.3. Results

The results from all the analysis discussed above will be presented in this section. First dealing with the microstructural analysis for calcite, quartz and feldspar, grain size derived temperatures and finally the palaeopiezometer results for both calcite and quartz.

4.3.1. Microstructural Analysis

The results for microstructural analysis will be split into the following tectono-stratigraphic units and structures; north of the Bursa Fault, Bursa Fault, Uludağ Massif, Eskişehir Fault zone and south of the Eskişehir Fault. All sample numbers referred to in this section can be found on Figure 3.1, Chapter 3. Within each section microstructural observations will be presented from marble samples first, followed by quartz-feldspathic samples (eg. gneiss and granite).

(a) North of the Bursa Fault

There are three marble samples from the north of the Bursa Fault, ULD16, ULD53 and ULD55. The basite and micaschist samples from this side of the Bursa Fault were too small or too weathered to thin section, meaning quartz-feldspathic samples from this tectono-stratigraphic unit are lacking.

Sample ULD16 has been recrystallised to a very fine grain size (<10μm) which is pervasive across the entire sample. There are also some veins cross cutting the recrystallised rock. These veins exhibit a much coarser (100-500μm) grain size and display type I and type II twins (Figure 4.8). ULD55 shows obvious deformation with a clear shape preferred orientation, which defines a foliation. The grain size is ~50μm. The majority of the grains are twinned, with pervasive type I and type II twins and some grains displayed type III twins within twins (Figure 4.8). This sample also contains some brittle fracturing. ULD53 has a coarser grain size of approximately 1mm. Thin type I and thick type II twins are pervasive in the sample with some thin twins offset by thicker twins. Again there are some twins within twins which are type III twins (Figure 4.8).

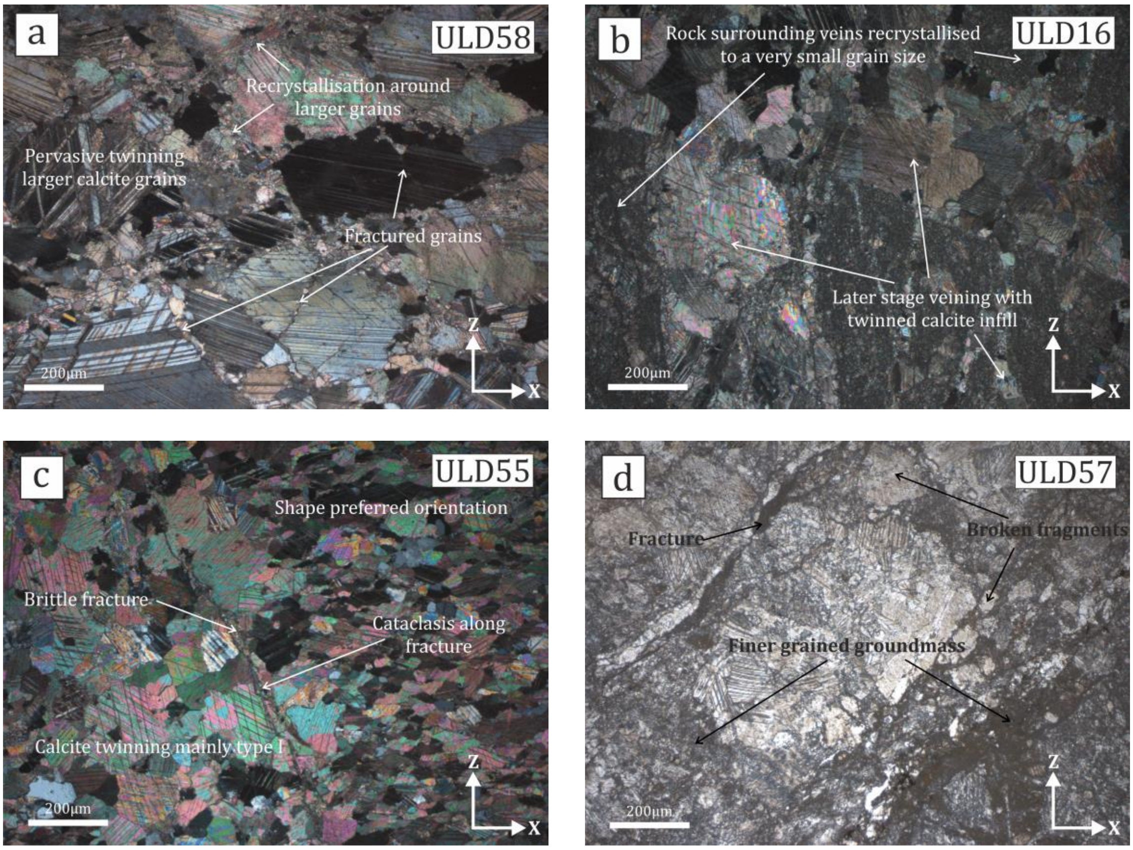

Figure 4.7. Brittle microstructure from close to the Bursa Fault. a) XPL fractured grains and recrystallisation around larger grains (ULD58). b) XPL later stage veining (ULD16). c) XPL brittle fracture and cataclasis along fracture (ULD55). d) PPL cataclasis (ULD57). All sections in XZ, X and Z directions indicated on photomicrographs.

(b) Bursa Fault

There is only one marble sample from close to the Bursa Fault; ULD49. The sample has a wide range of grain sizes from 100μm – 1mm. Some of the larger grains are fractured and these fractures have very small grains along their length.

(c) Uludağ Massif

Two samples within the Uludağ Massif are within the marble that bounds the southern side of the Bursa Fault, these are ULD57 and ULD58. ULD 57 shows very angular clasts that display a lot of fractures. Surrounding the larger grains is a matrix of smaller grains. There are some veins within the sample that show larger grains with no recrystallisation or twinning evident. ULD58 has a bimodal grain size, the larger grains ~500µm and the smaller grains are approximately 50µm. The smaller grains surround the larger ones forming a core and mantle recrystallisation structure. Most of the large grains display type I and type II twins, with some grains showing curved type III twins (Figure 4.8).

In the middle portion of the Uludağ Massif there are a number of marble samples. The grain size in these samples is usually between 50-150µm. All of these samples show type I and type II twinning, and type II twinning is pervasive in most with some samples (eg. ULD122) showing offsetting twins. Some of the samples such as; ULD122, ULD127 and ULD152 show irrational type III curved twins and twins within twins. There are type IV twins in some samples too displaying patchy, incomplete twins (Figure 4.8). Samples with type IV twins include ULD122, ULD124, ULD152, ULD155 and ULD157. Sample ULD124 also shows pervasive recrystallisation, with only the large twins showing the twinning. In addition ULD155, ULD157 and ULD158 show recrystallisation. ULD153 has some patchy type IV twins but the majority of this sample displays no twinning at all.

Samples were also taken close to the Eskişehir Fault within the marble bounding the northern side of the structure. The samples in this portion of the Uludağ Massif show a wide range of grain sizes between 50 and 250µm. All samples show pervasive type II twinning in visible grains with only some samples displaying thin, type I twins (Figure 4.8). Sample ULD163 shows offsetting of thick twins by thinner twins. Type III twins within twins can be seen in samples ULD132, ULD133 and curved type III twins in ULD134, ULD135 and ULD163. All samples in this vicinity contain irrational, patchy type IV twins (Figure 4.8). ULD131 is almost completely recrystallised. ULD133, ULD134 and ULD163 also show some recrystallisation and core and mantle structures. In these samples only the larger grains show any twinning (Figure 4.8).

Quartz-feldspathic samples of the Uludağ Massif are gneisses and primarily contain quartz, feldspar, biotite and amphibole with some minor chlorite, epidote and muscovite. One sample, ULD125 is an amphibolite, containing feldspar and amphibole, whilst ULD156 is the only sample to contain garnet. There is a range in grain size, from medium grained (500µm) samples to quite fine grained samples (~50-100µm). There is a clear fabric evident in all samples, but not all have developed into a mylonitic fabric.

Not all gneiss samples show evidence for pervasive recrystallisation (eg. ULD125 and ULD154; see Figure 4.10a). Of the samples that do show recrystallisation it is predominantly SGR in quartz, with some GBM. ULD121 shows alternating bands of GBM and SGR recrystallisation (Figure 4.9f).

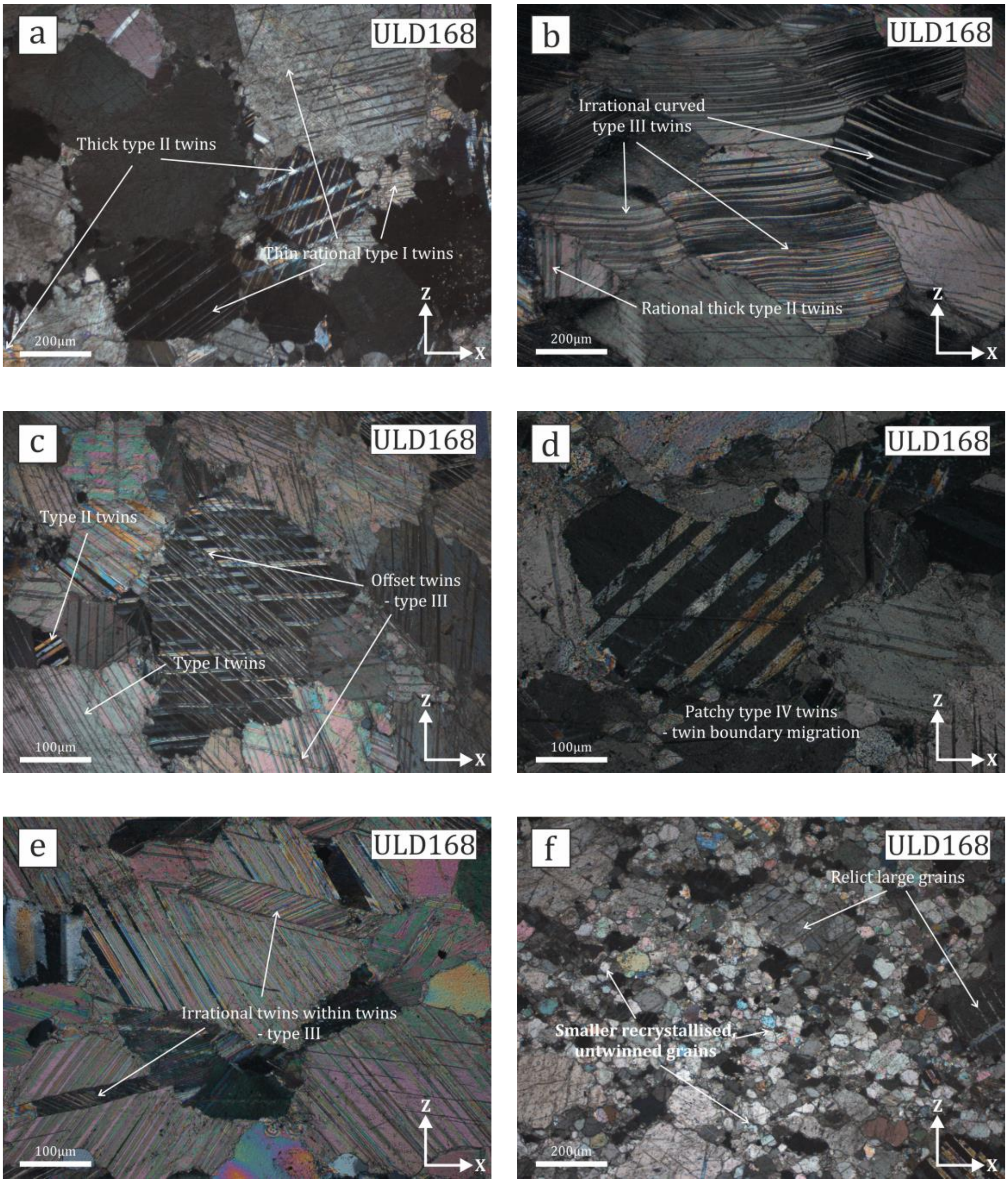

Figure 4.8. Calcite microstructure. a) Thin type I and and thicker type II twins (ULD120). b) Curved type III twins and some twin boundary migration, type IV twins (ULD127). c) Offset twins (ULD53). d) Patchy type IV twins showing high temperature twin boundary migration (ULD166). e) Type III twins within twins (ULD135). f) Recrystallisation with relict larger grains (ULD158). All sections are XZ, X and Z directions shown on each section and all are in XPL.

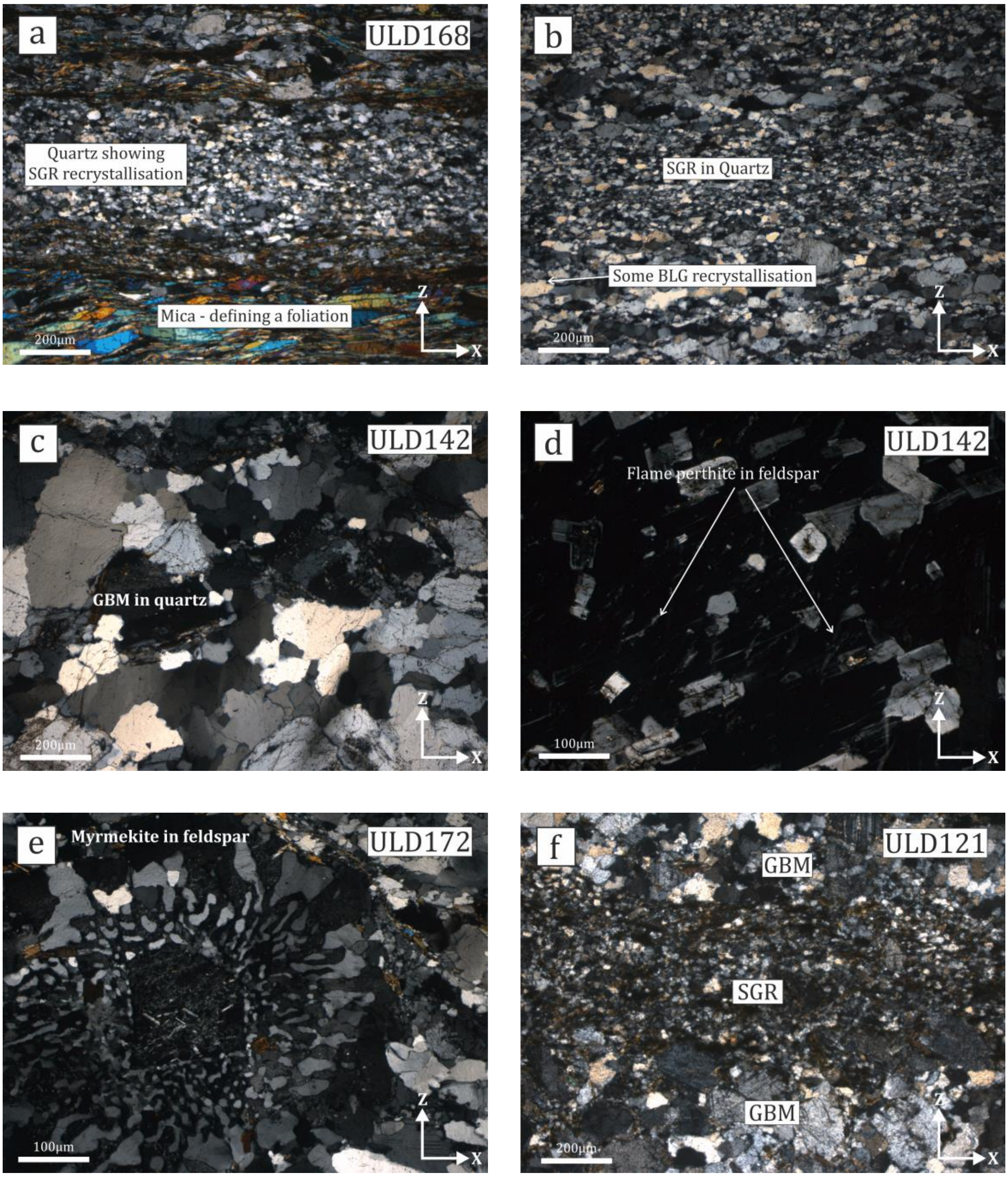

Figure 4.9. Quartz microstructure. a) SGR recrystallisation in quartz (ULD168). b) SGR recrystallisation in quartz with some BLG recrystallisation (ULD168). c) GBM recrystallisation in quartz (ULD142). d) Flame perthite in feldspar from South Uludağ Granite (ULD142). e) Myrmekite in feldspar from South Uludağ Granite (ULD172). f) Alternating GBM and SGR recrystallisation in quartz (ULD121). All sections are XZ, X and Z directions shown on each section and all are in XPL.

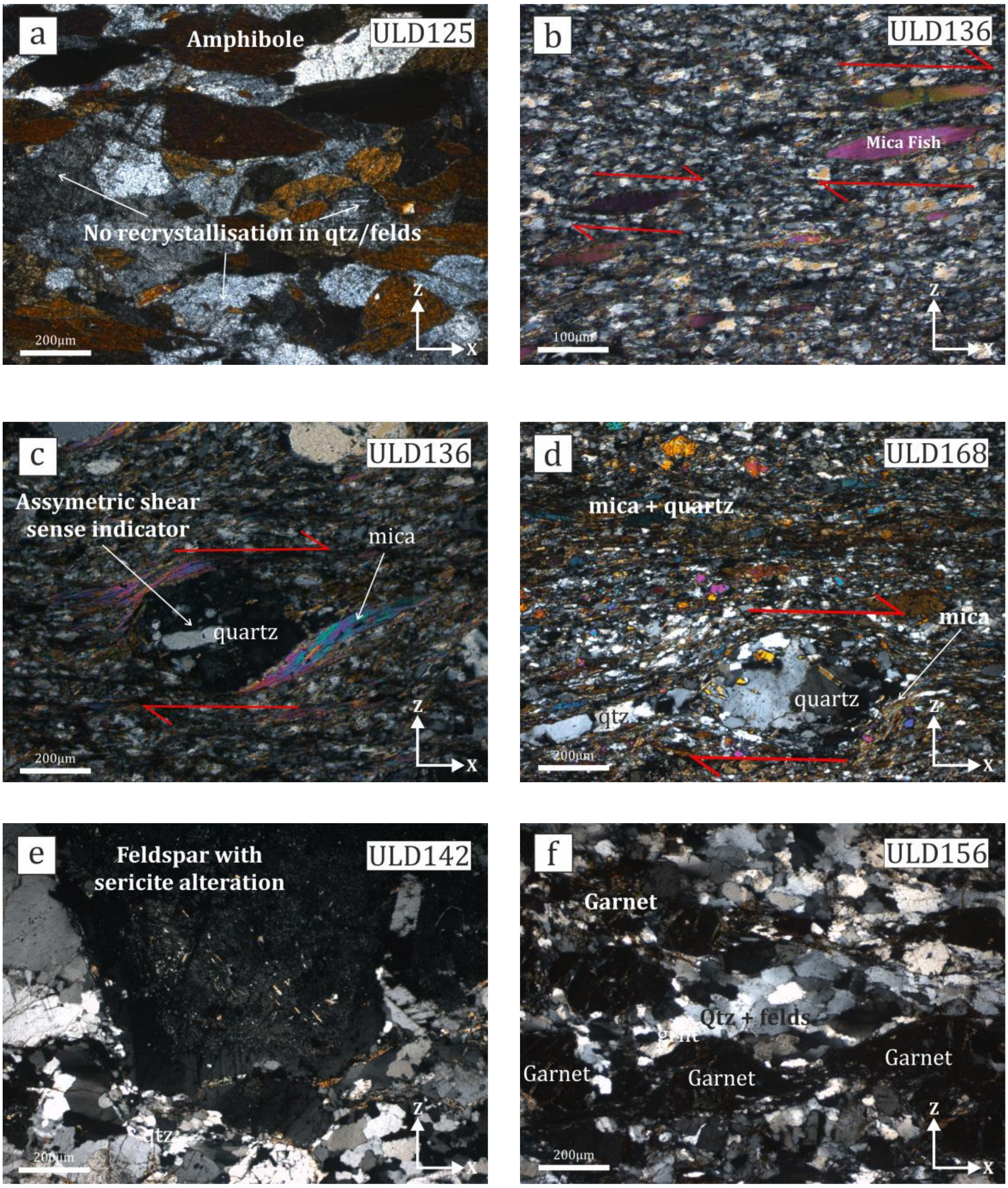

Figure 4.10. Quartz microstructure. a) No recrystallisation in amphibolite (ULD125). b) Mica fish shear sense indicators (ULD136). c) Asymmetric shear sense indicator, quartz clast with recrystallised mica strain shadow (ULD136). d) Asymmetric shear sense indicator, quartz clast and recrystallised quartz and mica strain shadow (ULD168). e) Feldspar with sericite alteration (ULD142). f) Boudinaged garnet (ULD156). All sections are XZ, X and Z directions shown on each section and all are in XPL.

The presence of microcline and albite twinning indicates the presence of both plagioclase and K-feldspar; however there are no other deformation related microstructures in the feldspars. Only a few samples show shear sense indicators (eg. ULD126 and ULD128) and in general they show a right lateral shear sense (Figure 4.10d). ULD156 is the only sample to contain garnet, these garnets are deformed as shown in Figure 4.10f. There are fractures running through the garnet crystals where the garnet has altered to chlorite indicating brittle behaviour during deformation.

(d) Eskişehir Fault zone

As described previously in Section 3.2.2, the Eskişehir Fault zone contains foliated, alternating bands of marble and phyllite (Chapter 2, Figure 3.3). For the marble, two samples that were thin sectioned were taken from the Eskişehir Fault zone, ULD137 and ULD166. Sample ULD137 has a grain size between 100-500μm and predominantly shows type II twins. Some grains show type III curved and twins within twins as well as patchy type IV twins showing twin boundary migration. Some grains within this sample are almost completely twinned with little of the host grain left. Sample ULD166 shows some recrystallisation and the smaller grains do not show any twinning. There is pervasive type II twinning and in some grains these thick type II twins are offset by thinner type I twins. Many of the larger grains show patchy type IV twinning.

Quartz-feldspathic samples within the fault are well foliated phyllites (Chapter 2, Figure 3.3). The phyllite in the fault zone represents a meta-sediment. All samples contain quartz, feldspar, biotite and chlorite, with minor amounts of clinozoisite and epidote in some. Both plagioclase and K-feldspar can be identified in the majority of samples identified from simple and cross-hatched, microcline twinning. Some samples are very fine grained, and show signs of weathering with grains bounded by orange/opaque iron deposits.

All samples of phyllite within the fault zone have developed mylonitic fabrics and display pervasive SGR recrystallisation in quartz (eg. Figure 4.9b). Some samples show GBM in quartz but this is not at all pervasive (Figure 4.9c) and is often confined to coarser grained veins. The feldspar in the samples shows simple and microcline twinning, and also in some there is evidence for BLG recrystallisation, flame perthite (Figure 4.9d) and myrmekite (Figure 4.9e) structures.

A few samples (eg. ULD136, ULD164 and ULD168) exhibit asymmetric structures as shear sense indicators showing a right lateral shear sense with top to 110° (eg. Figure 4.10c). The porphyroclasts are invariably feldspar, showing some degree of intracrystalline deformation, with strain shadows consisting of quartz, feldspar and mica. There are both σ-type and δ-type shear sense indicators in the samples, with both indicating a right lateral shear sense (top to the ESE Figure 4.10c). Other shear sense indicators included mica fish (Figure 4.10b), again indicating a right lateral shear sense, again with top to the ESE.

(e) South of Eskişehir Fault

There are some marble outcrops that lie to the south of the Eskişehir Fault, ULD10, ULD79 and ULD144. ULD10 is a sample showing larger grains (500μm-1.3mm) within a smaller grained matrix (50μm). The larger grains predominantly show type II twinning and some type IV patchy twins. The large grains that are not twinned display some undulose extinction. The smaller grains do not show any twinning. There are some un-twinning calcite veins in the sample also. ULD79 displays extensive recrystallisation and core and mantle structures. The large relic grains are twinned with a high volume of thin type I twins and some type II thicker twins. There are also some irrational type II twins as well as some thicker, patchy type IV twins. ULD144 is also pervasively recrystallised and has a very small grain size. There are some veins that have a larger grain size and these grains show some thin type I twins.

Quartz-feldspathic samples found to the south of the Eskişehir Fault are granites and belong to the South Uludağ Granite which bounds the Eskişehir Fault zone (Chapter 3, Figure 3.1). These sample show clear signs of deformation at outcrop and grain scale. All samples are medium to coarse grained and contain quartz, feldspar, biotite, chlorite and some muscovite. There is evidence of weathering in the granite samples with iron staining coating some grain boundaries.

All samples show some degree of mylonitic fabric that, in general, becomes more developed closer to the Eskişehir Fault. Also, in all samples, quartz displays pervasive GBM and some SGR recrystallisation (Figure 4.9a,b). Feldspar shows both microcline and albite twinning and also flame perthite and myrmekite structures (Figure 4.14d,e). There is some evidence for mantled clast and strain shadow structures but they do not show conclusive asymmetric shear.

4.3.2. Palaeopiezometers

For all calcite samples, the grain size was determined using the linear intercept method outlined in Section 3.2.1 (Equation 4.2). The results are shown in Figure 4.11 and were calculated using Equation 4.1. It is clear that there is quite a range in differential stresses across the massif, ranging from ~20MPa to ~140MPa. The highest values (138MPa and 137MPa) occur at the Eskişehir Fault, however there are also some lower values on the fault; 38MPa (ULD137). Within 1km north of the fault there is wide variation with some high values of 131MPa (ULD131) and 111MPa but also some of the lowest values of 18MPa and 25MPa (ULD157 and ULD158 respectively). Within the massif, from 1-4km, most calcite differential stresses are between ~40-60MPa.

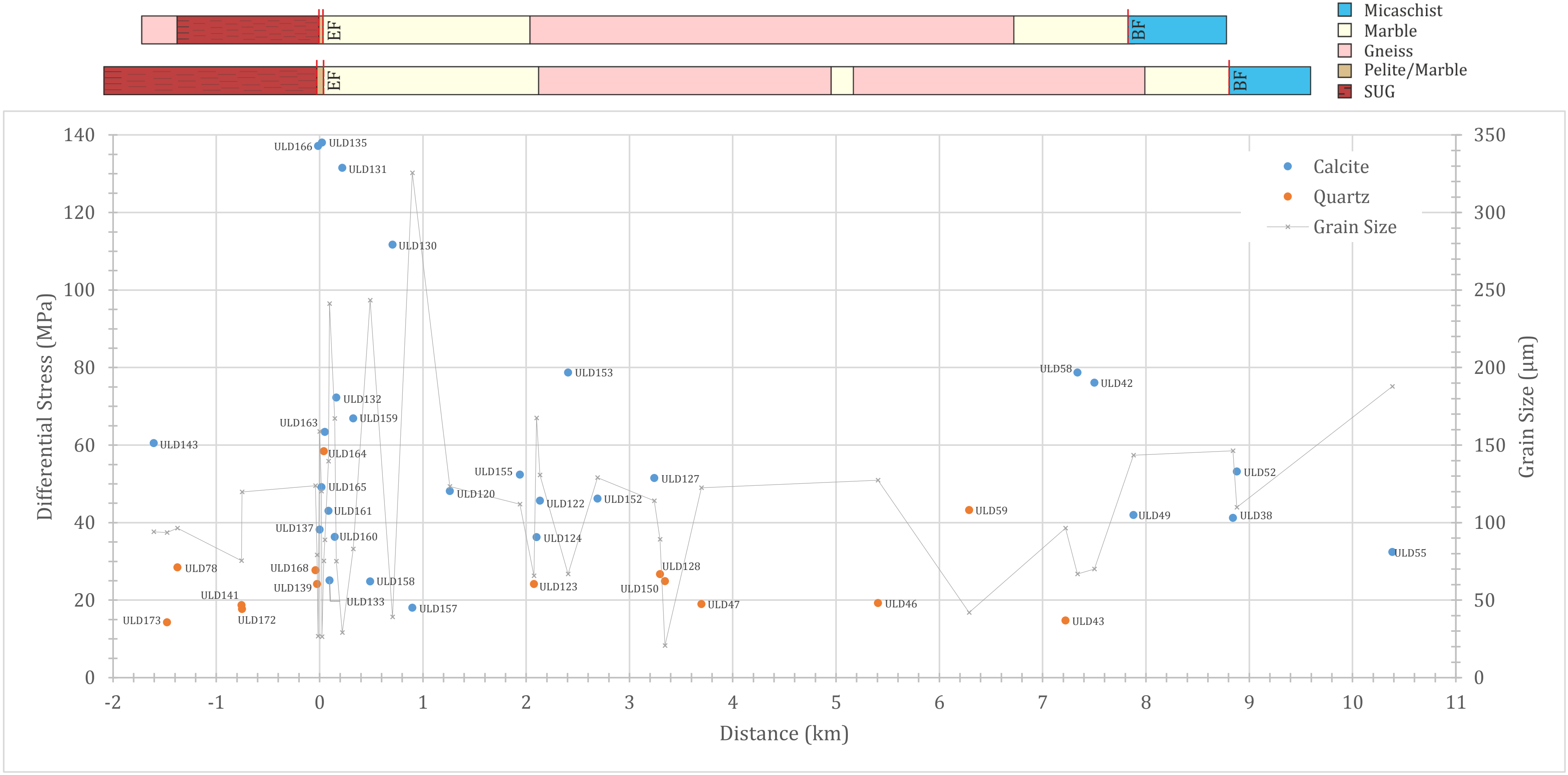

Figure 4.11. The differential stress (MPa) from grain size. The differential stress for calcite using the palaeopiezometer outlined in Rutter (1995) is plotted in blue (Equation 4.1). The differential stress for quartz from the palaeopiezometer from Stipp and Tullis (2003) is in orange (Equation 4.3). Grey points/line are the grain sizes for all the samples. Distance in kilometres is relative to the Eskişehir Fault which is at 0km. EF – Eskişehir, BF - Bursa Fault.

Towards the Bursa Fault the values range from 75-80MPa (ULD42 and ULD58) and between 32-53MPa north of the fault. The results for the area around the Eskişehir Fault are shown in detail Figure 4.12. This highlights the fact that there is quite a lot of variation close to, and on, the Eskişehir Fault. ULD135, ULD137, ULD165-166 are all within the fault core (Chapter 3, Figure 3.1, Figure 3.3) and range from 38MPa to 138MPa. The variation 1km north of the fault can also be seen clearly on Figure 4.12, with the two peaks with samples ULD131 and ULD130.

For all samples containing quartz the grain size was, again, obtained using the linear intercept method described in Section 3.2.1 (Equation 4.2). The flow stress was then calculated using Equation 4.3 and the results are shown in Figure 4.11. It is clear there is an inverse relationship between grain size and stress, as grain size increase, stress decreases. ULD164 shows the highest differential stress of 58MPa. The other two samples on the Eskişehir Fault have lower values of 24 and 27MPa (ULD139 and ULD169 respectively. South of the Eskişehir Fault the differential stress varies between 14-28MPa. North of fault, in the Uludağ Massif, the majority of the samples are between 14MPa (ULD43) and 27MPa (ULD128). ULD59 has the highest value within the massif of 43MPa.

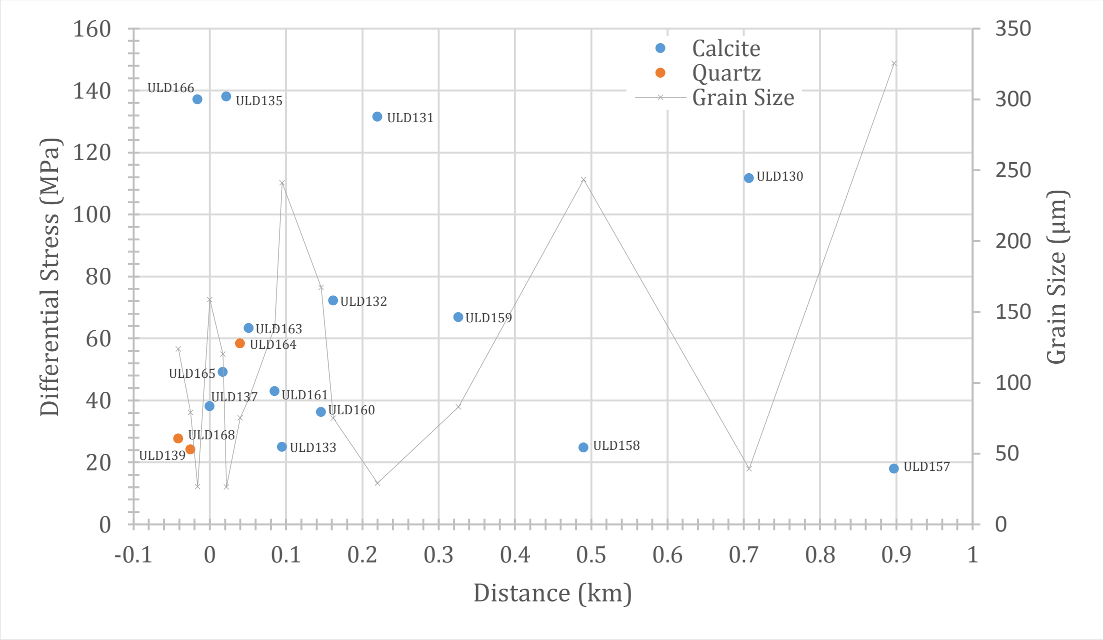

Figure 4.12. Section of graph in Figure 4.11 showing the samples closest to the Eskişehir Fault. Differential stress in orange and grain size in grey. Distance is relative to the Eskişehir Fault which is at 0km.

4.4. Discussion

What follows is a discussion of the presented evidence for the deformation conditions of the Uludağ Massif. Firstly from the regional geology and large scale structural architecture and secondly from microstructural evidence, ascertaining temperature of deformation, differential stress and how it is distributed and then determining a strain rate for the shear zone.

4.4.1. Temperature of deformation

All marble samples displayed at least rational type I and/or thicker type II twins (Figure 4.8a). This indicates that the marbles have undergone deformation constrained between 150 – 300°C (Figure 4.2) (Burkhard, 1993). The samples within the massif and especially close to the Eskişehir Fault also show irrational twinning, whilst some curved, thick type III twins occur (Figure 4.8b). A few samples show rational twins within twins and offsetting of larger twins by smaller ones Figure 4.8c. Almost all samples display type IV twinning, with patchy twins as a result of twin boundary migration Figure 4.8d. The type III and IV twinning suggests that these samples were subject to deformation temperatures of above 250°C (Figure 4.2) (Burkhard, 1993). Figure 4.8e shows irrational twins within twins, type III twinning.

Some samples, such as that shown in Figure 4.8f, show pervasive recrystallisation with some later stage veining. The larger grains, in the veins, are often twinned with thin type I twins. This suggests that the later stage vein infill occurred as deformation was still progressing but at temperatures below 200°C due to the brittle nature of the veins (Kennedy and Logan, 1998). Samples to the south of the shear zone, near the Bursa Fault, such as ULD10, ULD53 and ULD55 do not show type IV twinning, but do show some type I and type II twinning in the larger visible grains. Samples ULD16 and ULD55 show evidence from brittle deformation in the form of veins and fractures (Figure 4.7), again, suggesting temperatures of below 200°C (Kennedy and Logan, 1998). ULD57 also shows some cataclasis and vein infill. This brecciation, cataclasis and vein opening and infill was caused by the later stages of exhumation during the early Miocene (Okay et al., 2008) (Figure 4.7).

The majority of gneiss samples within the Uludağ Massif displayed SGR recrystallisation in quartz suggesting temperatures of 400-500°C (Lloyd and Freeman, 1994, Stipp et al., 2002). This coupled with the mineralogy, and the presence of amphibolite gneisses (ULD125) suggest the gneiss in the massif is of amphibolite grade. Further evidence from the presence of garnet in a few samples suggests the rocks were within the garnet zone of amphibolite grade with temperatures of between 500-600°C. The garnet has also undergone brittle deformation (Figure 4.9), suggesting temperatures below 600°C as above this temperature garnet is ductile (Voegelé et al., 1998). The presence of chlorite in garnet fractures and replacing biotite is evidence for retrogression through greenschist facies (350°C - 500°C).

On the Eskişehir Fault the biotite in the phyllite samples behaved in ductile manner to form mica fish (Figure 4.10b). This behaviour occurs at temperatures above 250°C (Stesky et al., 1974). From the pervasive SGR recrystallisation in quartz and BLG recrystallisation in feldspar, it can be deduced that temperatures reached at least between 400-500°C (Lloyd and Freeman, 1994, Stipp et al., 2002). The myrmekite growth in feldspar suggest temperatures may have reached a little higher, towards 600°C (Simpson and Wintsch, 1989). A large proportion of mica has undergone retrogression to chlorite, suggesting that as the massif was exhumed the shear zone spent some time at greenschist facies temperatures/pressures, between 350°C - 500°C. Some samples have fractures running through, indicating brittle deformation and much lower temperatures still, below 300°C (Stipp et al., 2002, Tullis and Yund, 1987). Some of the feldspar has also been sericitised, where the feldspar crystals have retrograded to a weaker clay-like mineral, sericite (Figure 4.10e). This again suggests temperatures between 100-300°C (Verati and Jourdan, 2014). The right lateral shear sense indicators (top to the ESE) fit with the regional kinematics of the shear zone (Chapter 3, Figure 3.5).

Samples in the South Uludağ Granite, to the south of the Eskişehir Fault displayed GBM recrystallisation in quartz suggesting temperatures between 500-700°C (Stipp et al., 2002). In the feldspars, flame perthite indicates deformation temperatures of 400-500°C and myrmekite structures temperatures towards 600°C (Simpson and Wintsch, 1989). Again, some of the biotite has retrograded to chlorite, suggesting the granite body has spent time at greenschist facies temperatures (350°C - 500°C). As before, some of the feldspar is now sericite indicating lower temperatures between 100-300°C (Figure 4.10e) (Verati and Jourdan, 2014).

Further to the microstructural analysis to ascertain the temperature of deformation, temperature can also be calculated from the grain size of calcite and quartz. This was included in the discussion due to the assumptions connected with strain rate and deformation temperature that have to be made using this approach. These assumptions are that strain rate is constant and changes in grain size relate to changes in temperature.

For calcite, temperatures obtained using the relationship derived by Covey-Crump and Rutter (1989) and used to plot the temperature contours on the graph shown in Figure 4.3 (Stipp et al., 2002) are displayed in Figure 4.13. The equation used to calculate temperature from grain size is shown in Equation 4.4 where D is grain size in microns and T is temperature in °C.

$$D^{0.5} = 0.1068T - 19.1508 \qquad (4.4)$$

The Eskişehir Fault records high values of 338°C (ULD137) and low values of 214°C (ULD135). This variation continues in the 1km portion north of the fault, with the lowest at 0.2km of 220°C (ULD131) and the highest value over the whole area of 386°C at 0.9km (ULD157). The rest of the massif between 1km and the Bursa Fault show temperatures between ~280°C and 340°C, and the sample north of the Bursa Fault (ULD55) showing a temperature of 349°C.

For quartz the temperature from grain size was obtained using the graph in Figure 4.5 was constructed using independently obtained temperatures (mineral assemblages in the host rock) from the Tonale shear zone (Rutter, 1995). More detail can be found in Section 4.2. The results for temperature are shown in Figure 4.13. The samples to the south of the Eskişehir Fault, within the South Uludağ Granite show the highest temperatures, between 523°C (ULD141) and 558°C (ULD173). On the Eskişehir Fault the temperatures are lower and ULD164 has the lowest temperature across the whole massif of 390°C. To the north, the temperature is lower still, before increasing again at ~3.75km. Sample ULD43, closest to the Bursa Fault has a high temperature derived from its atypically large grain size due to pegmatitic, graphic textures.

The low temperatures seen in both the calcite and quartz datasets on the Eskişehir Fault are not typically what would be expected. During the process of shear, heat is produced through shear heating making it likely that any localised shear zones would have been subject to higher temperatures than the surroundings (Leloup et al., 1999). These low temperatures come from smaller grain sizes, which are a result of localisation of shear and an increase in strain rate which is discussed in the next section. Whilst using grain size to ascertain temperature in a shear zone is based on assumptions that cannot be upheld, the temperature ranges from this method are in agreement with those from microstructural evidence. Discounting samples found within the Eskişehir Fault zone, the ranges are between 400-600°C for quartz. This fits with most of the samples displaying some degree of SGR recrystallisation, which is bracketed between 400-500°C, in the massif and the samples south of the fault showing GBM recrystallisation which is between 500-700°C. For calcite, the temperatures range between ~300°C-400°C (again ignoring the ones on the Eskişehir Fault). This fits with the majority of samples showing type II and type IV twinning (<250°C).

Calcite records lower temperature deformation. Twinning occurs at lower temperatures so will record deformation at lower temperatures. Also the temperature from grain size records lower temperature deformation in calcite because recrystallisation is an important deformation mechanism at lower temperatures in calcite than it is in quartz (Kennedy and Logan, 1998).

Temperatures vary significantly over the Uludağ Massif and also there is a large variation on the Eskişehir Fault within a more localised zone (Figure 4.13). Both quartz and calcite record high temperatures within the pelite/marble fault zone (Figure 3.3), which is a combination of grain size reduction through ductile deformation deeper in the crust and focussing of shear during exhumation and further grain size reduction. There is no evidence in thin sections for brittle processes such as cataclasis or brecciation. The central part of the massif records the grain size reduction due to ductile deformation. Cataclasis is evidenced from thin sections, particularly on the northern side of the massif (Figure 4.7).

Temperatures from microstructure are similar to those obtained by Okay et al. (2008) for the Uludağ Shear Zone where they noted quartz and feldspar fabrics suggest deformation temperature of ~400°C. Deformation of the Nubra Formation within the Karakoram Fault Zone is recorded at 400°C and within the leucogranite the temperature of deformation was 500°C (Wallis et al., 2015, Wallis et al., 2013). Phillips and Searle (2007) found that temperatures did not exceed greenschist to lower amphibolite facies within the Karakoram Fault.

Estimating temperature from grain size has similar errors and limitations that are associated with estimating stress from grain size. These errors originate from the grain estimation in Channel5 (Oxford Instruments plc). For both calcite and quartz the grain sizes have quite a large range (17-1412μm and 13-954μm respectively) meaning the standard deviation is often equal to or larger than the mean resulting in a coefficient of variance of 1 or above. This is largely due to the points within the EBSD map not being indexed, therefore creating artificial grain boundaries between indexed and non-indexed points. Also an added problem with the calcite grain size is Channel5 not ignoring twinning, even though it is set to ignore rotations of a certain amount around a certain axis it still picks up some twins, which are often small, leading to a large amount of small grain sizes that are not representative of the sample.

Errors also arise when using the derived relationships to calculate temperature from the obtained grain size. As stated previously, the relationship between grain size and temperature in calcite from Covey-Crump and Rutter (1989) is calibrated for grain growth during static annealing. The temperatures using this relationship therefore provide only a lower bound on the deformation temperature as the protolith grain size (before deformation) would generally have been larger. For the relationship between temperature and grain size derived for the Tonale Shear Zone Stipp et al. (2002) reported an error of ±30°C for all of the inferred temperatures.

4.4.2. Palaeopiezometers and Strain-rate

(a) Palaeopiezometer

From the calcite palaeopiezometer it is evident that there is quite a large amount of variation in grain size, and therefore stress estimates, close to the fault which could represent the distribution of stress onto smaller distributed strands during shearing. This is not evident from field observations but because of the homogeneous nature of the marble it might be there, but just not visible at outcrop scale. The highest stresses are found within the alternating phyllites and marbles at the Eskişehir Fault core, which is what would be expected. It is obvious from field observations that there has been a large amount of localisation on this fault zone.

The variation across the field area and at the Eskişehir Fault can be explained through shear localisation onto numerous strands across the massif. Where there was no localisation during shear samples will have been subject to static recrystallisation (Covey-Crump and Rutter, 1989). The relationship between stress and grain size for these samples is displayed in Figure 4.11 and Figure 4.12.

Unlike the calcite there is much less variation in quartz, apart from the two obviously higher values. This is potentially due to the quartz-bearing lithologies taking up shear stress more homogeneously than the marble, where high stress appears to be much more distributed. Again, the highest differential stress was found on the Eskişehir Fault, showing the strain localisation during shear activity.

There is a large range in differential stress across the massif, evidenced by the calcite values and to a lesser extent, the quartz values. If stress was partitioned into specific strands during ductile shear activity, the areas of lower differential stress would maintain a higher grain size, as opposed to the high stress areas promoting dynamic recrystallisation and a decrease in grain size. The calcite values are, on average, much higher than the differential stress estimates from quartz. This is because, as stated previously, dynamic recrystallisation is an important deformation mechanism to lower temperature in calcite than it is in quartz (Kennedy and Logan, 1998). This means the reduction in grain size in calcite continues to shallower depths and lower temperatures during exhumation therefore resulting in a lower grain size. The samples close to the Bursa Fault on the northern side of the massif also display evidence for brittle grain size reduction through processes such as cataclasis, so the higher stresses seen in these samples is not a product of ductile shear alone (eg. ULD58, Figure 4.7).

Rheological differences between calcite marbles and quartz-bearing lithologies could also explain the differences between stresses seen in the two minerals (Figure 4.11). Under some circumstances calcite is weaker than quartz due to grain size sensitive flow within calcite (Brodie and Rutter, 2000). However, under hydrous amphibolite conditions quartz rich rocks in the mid-lower crust can be weaker than coarse calcite and flow at lower stresses than under dry conditions (Mancktelow and Pennacchioni, 2010).

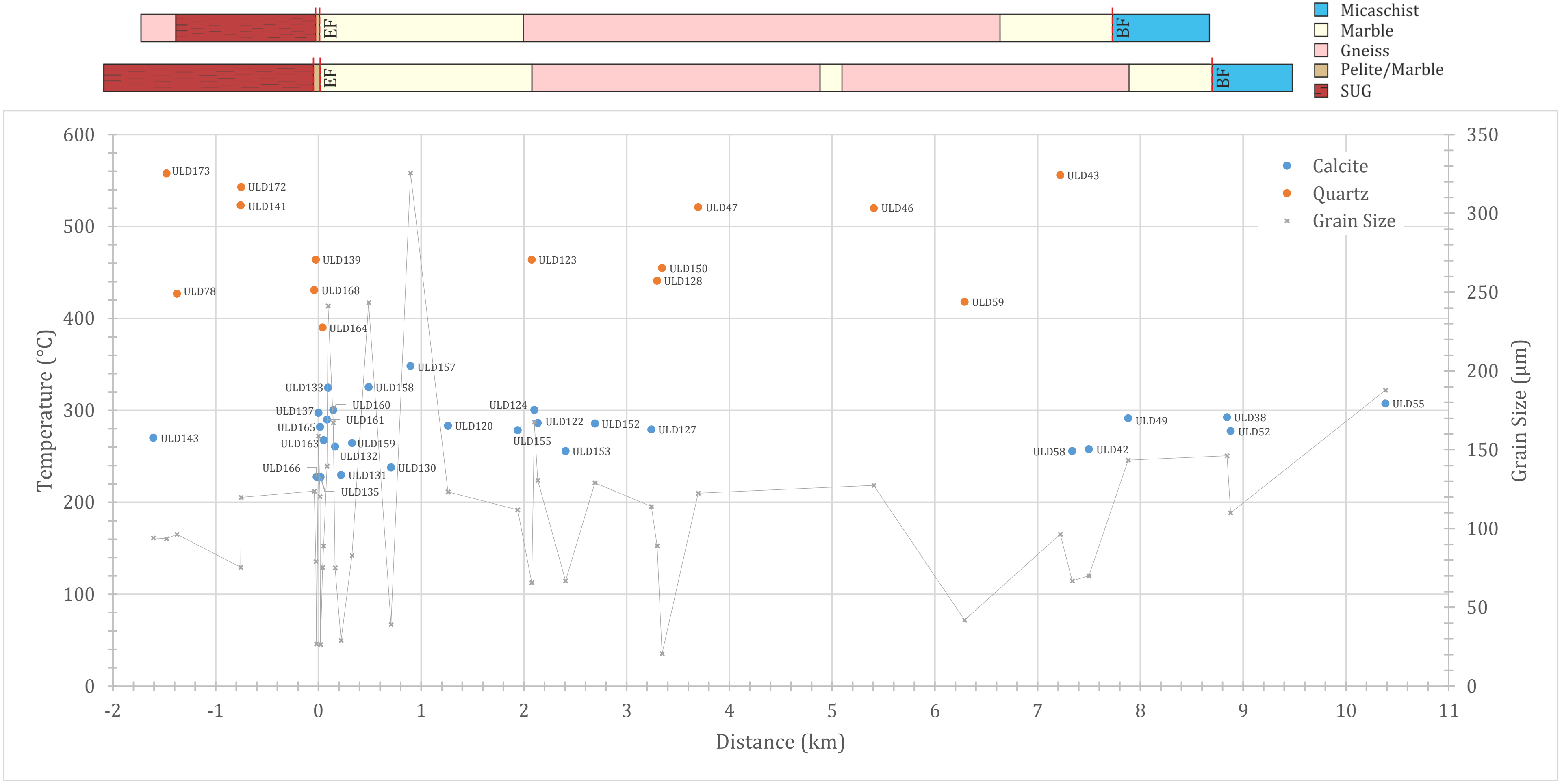

Figure 4.13. Temperature vs distance for calcite and quartz samples. The results for calcite are in orange and are from the graph shown in Figure 4.3, and in blue are the results for quartz from the graph in Figure 4.5. Grain size is shown in grey, for both calcite and quartz. Distance is in kilometres and relative to the Eskişehir Fault which is at 0km. EF – Eskişehir, BF - Bursa Fault.

The gneisses within the Uludağ Massif do contain hydrous minerals such as biotite and muscovite, but they are not hydrous rocks as the modal percentages of these minerals is relatively low compared to quartz and feldspar. There are some small lenses of amphibolite which can be considered hydrous, but they do not make up a significant portion of the massif (eg. ULD125, Figure 4.10). There is also no evidence for fluid migration such as cracks and veins. Therefore it is likely, in this situation, that the higher overall stress recorded in the calcite is due to marble being rheologically weaker than the quartz-bearing lithologies and also because grain size reduction due to dynamic recrystallisation is important to lower temperatures, as mentioned previously.

In both the calcite and quartz datasets, the highest differential stress was found in the Eskişehir Fault zone, showing the strain localisation on this fault core during shearing. The massif has also been exhumed along the Eskişehir Fault, leading to further re-working and dynamic recrystallisation. The exhumation could explain why there is also lower differential stress present at the fault. As the massif exhumed and decreased in temperature, some sections accommodated more stress than others, leading to static recrystallisation and a grain size increase in some sections of the fault zone.

(b) Strain rate

A number of experiments have been carried out on calcite and quartz at a range of temperatures and strain rates in order to determine flow laws. These flow laws can then be used to calculate strain rate using the temperature obtained from microstructural analysis and differential stress derived from grain size. As can be seen in Section 3.5.2 most calcite samples contain type II and type IV twins which give a temperature of 300°C, giving us a lower temperature bound (Burkhard, 1993). The samples that contain quartz all show SGR recrystallisation with some showing GBM, which gives us an upper bound temperature of 500°C. Strain rates will be calculated based on these two bounding temperatures.

For calcite, there are numerous published flow laws. The first is from Rutter (1974), based on experiments on Carrara limestone between 20-500°C at 1.5kbar.

$$\log \dot{\varepsilon} = 5.8 - \left(\frac{250000}{2.303RT}\right) + 0.038\,\sigma \qquad (4.5)$$

A calcite flow law for dislocation creep is from Schmid et al. (1980):

$$\log \dot{\varepsilon} = 3.1 - \left(\frac{420000}{2.303RT}\right) + 7.6 \log \sigma \qquad (4.6)$$

$$\log \dot{\varepsilon} = 8.1 - \left(\frac{428000}{2.303RT}\right) + 4.2 \log \sigma \qquad (4.7)$$

Equation 4.6 applied to their experiments above 1000bars pressure and below 500°C and Equation 4.7 applied between 200-1000 bars pressure and results mainly around 800°C and 900°C (Schmid et al., 1980). Also flow laws from Walker et al. (1990) who investigated the influence of grain size using synthetic calcite rocks with controlled grain sizes:

$$\log \dot{\varepsilon} = 4.93 - \left(\frac{190000}{2.303RT}\right) + 1.67 \log \sigma - 1.87 \log d \qquad (4.8)$$

$$\log \dot{\varepsilon} = 2.00 - \left(\frac{190000}{2.303RT}\right) + 3.33 \log \sigma - 1.34 \log d \qquad (4.9)$$

Equation 4.8 is for low stresses (<25MPa) and Equation 4.9 is for higher stresses (25-250MPa). In all of the above equations $\dot{\varepsilon}$ is strain rate (sec^{-1}), σ is differential stress (MPa) and *d* is grain size (µm), *R* is the gas constant (8.314 J K^{-1} mol^{-1}) and *T* is temperature (K).

As a test of which flow law is most appropriate, the results for three samples from these equations, for both the upper and lower bounding temperatures, is shown in Table 4.1. High stress and low stress in the Schmid et al. (1980) flow laws refers to Equation 4.6 and Equation 4.7 respectively. High stress and low stress in the Walker et al. (1990) flow laws refers to Equation 4.8 and Equation 4.9 respectively.

As can be seen from Table 4.1, there is a variation in strain rate using the 5 different equations. All the flow laws, aside from the low stress Walker et al. (1990) give reasonable geological estimates for the upper temperature bound. For the lower temperature bound, however, the two Schmid et al. (1980) flow laws give very slow strain rates for samples ULD143 and ULD135 which have the highest stresses of the three, therefore not realistic for a shear zone. As well as this the low stress Schmid et al. (1980) flow law gives the fastest strain rate for the sample with the lowest stress (ULD157), which, again, is unrealistic. Therefore these two flow laws from Schmid et al. (1980) will be discounted.

	ULD143		**ULD135**		**ULD157**	
Grain size (µm)	94		26		325	
Stress (MPa)	60		138		18	
Temperature (K)	573.15	773.15	573.15	773.15	573.15	773.15
Rutter (1974)	2.07 x10^{-15}	1.62 x10^{-09}	1.84 x10^{-12}	1.48 x10-^{06}	5.05 x10^{-17}	3.95 x10^{-11}
Schmid et al. (1980) **(low stress)**	3.81 x10^{-24}	4.68 x10^{-14}	1.22 x10-^{22}	1.5 x10^{-12}	2.36 x10^{-16}	2.9 x10^{-16}
Schmid et al. (1980) **(high stress)**	2.33 x10-^{22}	1.85 x10^{-12}	1.23 x10^{-19}	9.82 x10^{-10}	2.35 x10^{-26}	1.87 x10^{-16}
Walker et al. (1990) **(low stress)**	7.95 x10-^{14}	2.39 x10^{-09}	3.41 x10^{-12}	1.02 x10^{-07}	1.03 x10^{-15}	3.12 x10^{-18}
Walker et al. (1990) **(high stress)**	9.34 x10^{-17}	2.54 x10^{-09}	4.01 x10^{-15}	4.31 x10^{-07}	1.21 x10^{-18}	4.45 x10^{-12}

Table 4.1. The strain rates (s^{-1}) from the 5 different flow laws detailed above, for three samples.

The low stress Walker et al. (1990) flow law gives faster strain rates at lower temperatures, so this law will also be discounted. The grain size used in the Walker et al. (1990) experiments was very small (2-40μm) which is much smaller than the recrystallised grain sizes of the marble samples within this dataset which have a mean grain size between 20-320μm. Alternatively the experiments in (Rutter, 1974) were done on coarse grained Carrara marble so this is the flow law that will be used in this study.

Strain rate estimates have also been calculated for quartz using the upper and lower bound temperatures outlined previously and the stress data from Section 3.4.2. Experiments on quartz have been carried out to ascertain flow laws including Hirth et al. (2001) that used natural and experimental (100Mpa pressure, 300°C and a 5×10^{-14} s^{-1} strain rate) data to determine the law,

$$\dot{\varepsilon} = Af_{H2O}^{m}\,\sigma^{n}\exp(-\frac{Q}{RT}) \qquad (4.10)$$

Where $\dot{\varepsilon}$ is strain rate, A is a material parameter (log(A)=11.2±0.6 MPa), m is the water fugacity exponent (m=1), σ is stress, n is the stress exponent (n=4), Q is the activation energy (135±15 kJ mol^{-1}), R is the gas constant (8.314 J K^{-1} mol^{-1}) and T (K) is the temperature (Hirth et al., 2001).

Rutter and Brodie (2004) carried out experiments on synthetic, fine-grained quartzite at 300MPa and temperatures of 1273 and 1473 K and found that ductile flow was defined by the law,

$$\dot{\varepsilon} = 10^{-4.93}\,\sigma^{2.97}\,f(H_2O)\exp(-\frac{242000}{RT}) \qquad (4.11)$$

Again, $\dot{\varepsilon}$ is strain rate, R is the gas constant (8.314 J K^{-1} mol^{-1}), σ is stress and T is the temperature. Both equations contain a water fugacity term. This parameter varies with temperature and pressure and is difficult to constrain reliably. Hirth et al. (2001) estimate a maximum water fugacity of ~37MPa based on the lithostatic pressure and temperature at ~15km; 400MPa and 300°C (using a geothermal gradient of ~20°C/km) (Tödheide, 1972, Hirth et al., 2001). Water fugacity was also estimated using a geothermal gradient of ~40°C at 76MPa, and an upper boundary value of 314MPa (Francsis, 2012). It has been noted that a 2-fold change in water fugacity causes a change in strain rate that is less than the error on the grain size estimate (Francsis, 2012). All three of the water fugacity values will be used to estimate the strain rate using the law given by Hirth et al. (2001). The Rutter and Brodie (2004) equation gave strain rate estimates in the order of 10^{-15} s^{-1} to 10^{-21} s^{-1}, which seem too slow. This is possibly because the experiments started with a very fine grain size of 0.4μm, which is unrealistic as the dynamically recrystallised grain sizes in the Uludağ samples are all larger than this value.

The strain rates for the lower temperature bound for both calcite and quartz (at the range of water fugacities) are shown in Figure 4.14, and those at the upper temperature bound are shown in Figure 4.15. At both temperatures the calcite, on average, shows faster strain rates than quartz, reflecting the results of the stress calculations in Section 3.4.2, where calcite differential stresses were much higher on average. This, again, suggests that the marble accommodates more stress than quartz-bearing lithologies and therefore deforms at a faster rate.

At 300°C the difference between calcite and quartz strain rates is less than at 500°C. The overall pattern at 300°C shows high strain rates on the Eskişehir Fault that decrease both south into the South Uludağ Granite, and northwards across the massif. There is an increase in strain rate again at the Bursa Fault. At 500°C the difference between the strain rates of calcite and quartz is more pronounced. At these temperatures quartz bearing lithologies are rheologically stronger than marble. The pattern for both calcite and quartz is the same as that at 300°C. Faster strain rates at the Eskişehir and Bursa faults with slower strain rates either side of them. Again, the localisation of deformation is clear especially on the Eskişehir Fault, but also with sharp increases in strain rate at ~0.65 and ~2.4km in calcite.

4.1.1. Structural and thermal evolution

The peak metamorphic age of the gneisses and marble of the Uludağ Group was ~64 Ma, with P-T conditions of 670 ± 40°C and 7.0 ± 1.0 kbar (Okay et al., 2008). Muscovite and biotite ages show when the gneisses cooled from 350 to 250°C (the closure temperatures of the minerals), between ~50 to 33 Ma (Okay et al., 2008). If a geothermal gradient of ~30°C/km is assumed a constant exhumation rate can be deduced from these data (Figure 4.16).

Okay et al. (2008) proposed the range in crystallisation ages of the South Uludağ Granite (30-39Ma) was due to prolonged crystallisation in an active shear zone. This study found the presence of numerous solid state deformation microstructures such as anastomosing foliation defined by weaker minerals, dynamic recrystallisation and grain size reduction, microcline twinning, myrmekite and flame perthite (Figure 4.9d, e). There were no microstructures present that suggest magmatic flow in an active shear zone (Vernon, 2000). The granite also displays a well-developed mylonitic fabric close to the Eskişehir Fault and further south into the granite. As well as this the boundary between the granite and the fault zone is extremely sharp, suggesting that the granite formed a rheological weakness at the boundary for the fault to exploit (Chapter 3, Figure 3.1).

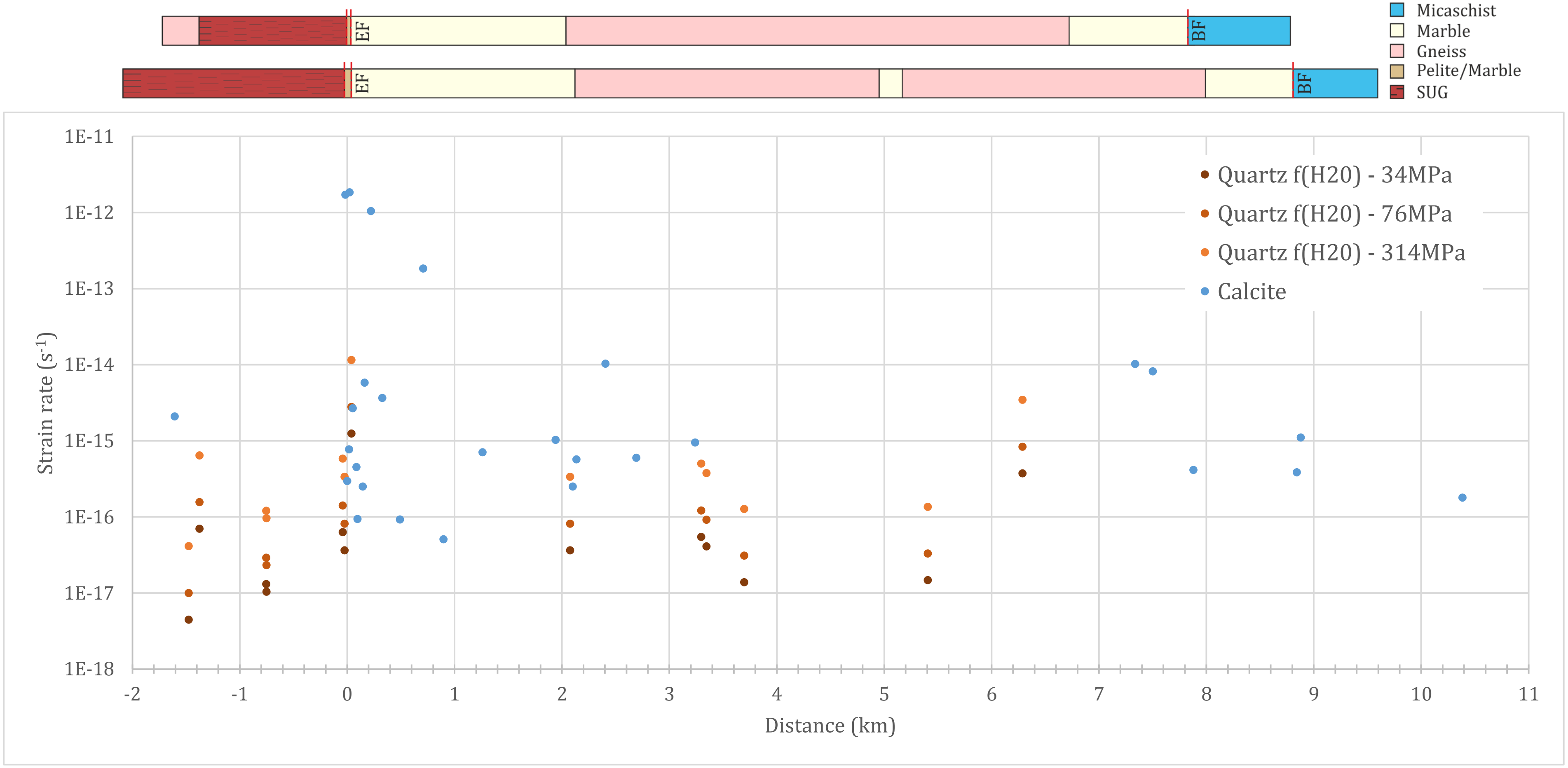

Figure 4.14. Strain rate results for calcite and quartz at the lower bound temperature of 300°C. For quartz, strain rates were calculated using the flow law of Hirth et al. (2001) at the three values of water fugacity and are plotted in varying shades of orange. For calcite strain rates were calculated using the flow law of Rutter (1974) and are plotted in blue. Distance is in kilometres and are relative to the Eskişehir Fault which is at 0km. EF – Eskişehir, BF - Bursa Fault.

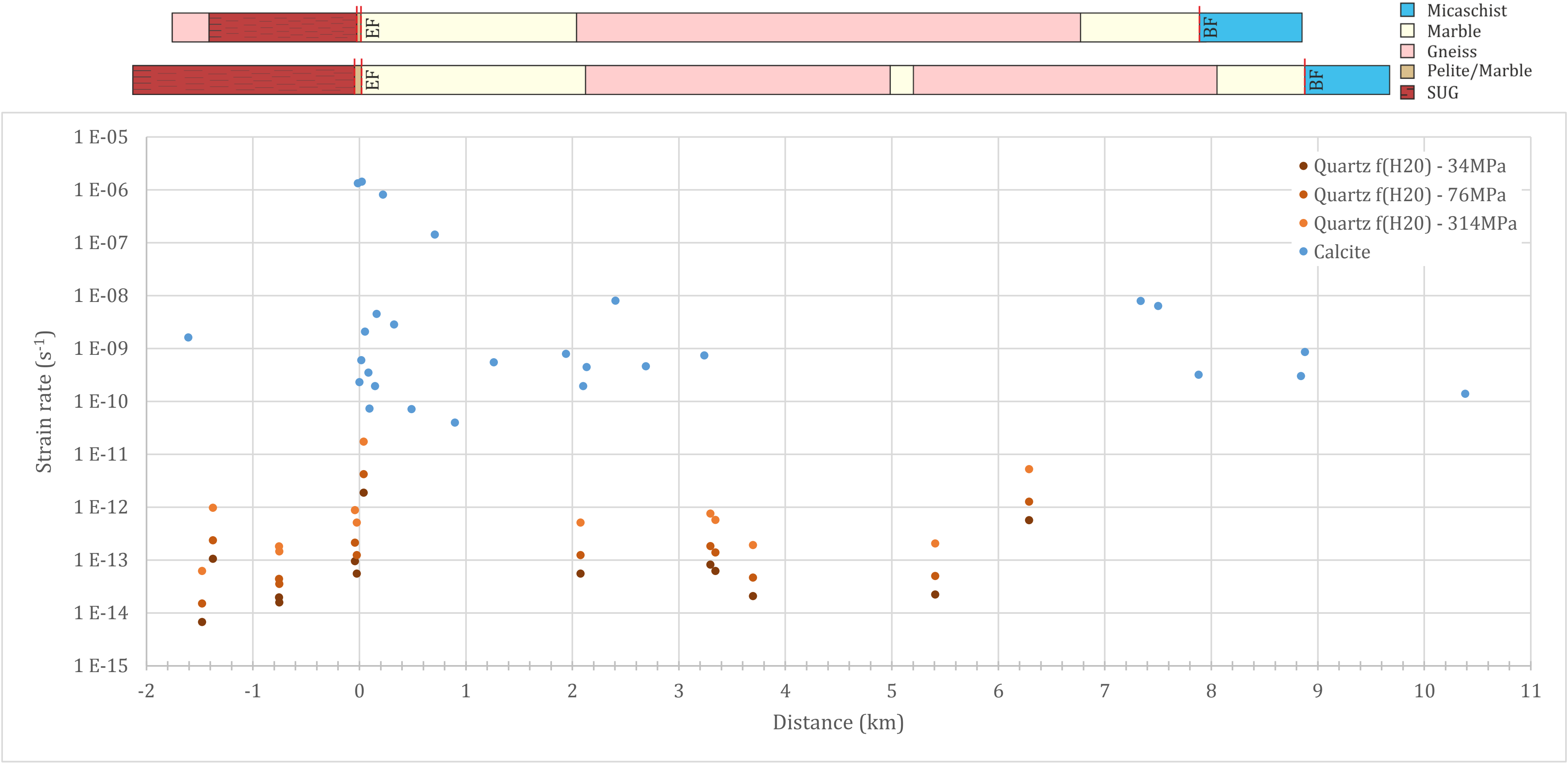

Figure 4.15. Strain rate results for calcite and quartz at the upper bound temperature of 500°C. For quartz, strain rates were calculated using the flow law of Hirth et al. (2001) at the three values of water fugacity and are plotted in varying shades of orange. For calcite strain rates were calculated using the flow law of Rutter (1974) and are plotted in blue. Samples are plotted relative to the Eskişehir Fault which is at 0m. EF – Eskişehir, BF - Bursa Fault.

However the South Uludağ Granite does display a higher temperature dynamic recrystallisation fabric (GBM) that is not seen in any other lithology in the shear zone. Along with the feldspar myrmekite and flame perthite structures this clearly shows the temperature difference between the granite and the rest of the massif. This suggests the granite was probably still at an elevated temperature compared to its surroundings during deformation. It is therefore proposed by this study that the granite was intruded before shear activity but had not completely cooled to ambient temperature before shear initiated. Further development and localisation of the Eskişehir Fault occurred during the exhumation, when the rheological difference between the granite and the massif would have been large.

The kinematics of the shear zone were right lateral strike slip shear evidenced from the pervasive fault parallel foliation containing right lateral shear indicators (Section 3.4.1). The conditions of this deformation were ductile with temperatures between 300-500°C obtained from calcite and quartz-feldspathic microstructure. Calcite gives us this lower bound as it is more sensitive to deformation at lower temperatures, when quartz is deforming by brittle processes.

Differential stress values for both the calcite and quartz palaeopiezometers varied considerably, between ~50-300MPa for calcite and ~15-60MPa for quartz. The highest stresses were found on the Eskişehir Fault, where there has been a large amount of localisation. The higher stresses in the middle of the massif reflect the localisation of strain in different strands over time as well as the clear strain localisation that is seen in the phyllites and marbles on the Eskişehir Fault. The differential stress and temperature estimates (500°C) gave average geological strain rates of 1.34 $x10^{-14}$ for calcite and between 1.98 $x10^{-12}$ and 4.79 $x10^{-13}$ for quartz. Again, there were faster strain rates on the Eskişehir Fault showing localisation over the deformation history.

The lack of evidence of magmatic flow within the South Uludağ Granite has important implications for the timing of the Uludağ shear zone. The undeformed Central Uludağ Granite gives an intrusion age of 27Ma (Okay et al., 2008), which defines an absolute age to the end of deformation in a strike slip shear zone. Therefore it is proposed by this study that the age for shear activity was between ~30Ma to 27Ma, putting it in the early Oligocene.

Apatite fission track ages from Okay et al. (2008) show the end of exhumation with age clusters at 20-22Ma, and at 10-9Ma indicating two periods of accelerated uplift. Exhumation resulted in the overprinting of previously ductile fabrics with more brittle structures, which can be seen mainly in the north of the Uludağ Massif, close to the Bursa

Fault. These include fault breccia at a macro-scale, and veins, cataclasite and brittle fracturing of grains within marble at a micro-scale.

4.1.2. Fault weakening mechanisms

There are several key weakening mechanisms active in fault zones; low friction phyllosilicate-rich fault gauges, elevated pore pressure, friction-viscous flow within phyllonitic rocks, grain size reduction, reaction weakening, thermal perturbations, addition of melt (Summarised in Wallis et al. (2013)). On the Eskişehir Fault, one major weakening mechanism is grain size reduction through dynamic recrystallisation. All samples containing quartz, and some marble samples, are either completely or partially recrystallised. It is widely accepted that dynamic recrystallisation leads to rheological weakening (De Bresser et al., 2001), because a decrease in grain size promotes grain size dependent deformation mechanisms, such as diffusion creep and grain boundary sliding (Passchier and Trouw, 2005). It has been suggested that this may not be the most efficient mechanism for weakening (De Bresser et al., 1998)

The samples on the Eskişehir Fault are phyllites, containing a large proportion (~30-50%) of phyllosilicates: eg. biotite-muscovite-chlorite. Biotite and muscovite are relatively weak during ductile deformation, with coefficients of friction (μ) between 0.25 and 0.45 (Scruggs and Tullis, 1998). Biotite is significantly weaker than muscovite, with μ of 0.35-0.43 for muscovite and 0.25-0.40 for biotite (Scruggs and Tullis, 1998, Ikari et al., 2011, Wallis et al., 2013). The high proportion of weak minerals in these rocks result in a low shear strength of the bulk rock, allowing for easier strain localisation and deformation (Wallis et al., 2013).

From analysis of microstructure in Section 3.3 the deformation temperature in the Eskişehir Fault zone was at least between 400-500°c, putting it at upper greenschist/lower amphibolite grade. The presence of chlorite, which defines a foliation along with biotite and muscovite, suggests retrogression at pressure and temperature conditions indicative of greenschist facies. Chlorite has a similar frictional strength as biotite and muscovite of μ = 0.42 (Shimamoto and Logan, 1981). Again, adding to the low bulk shear strength of the rock allowing easier strain localisation and deformation. Some feldspar, as described previously, has been partially sericitised, and sericite has a much lower frictional strength than feldspar, which further reduces the frictional strength of the bulk rock. It was proposed in Section 3.5.4 that the South Uludağ Granite was intruded before ductile shear began but had not cooled to ambient temperature. This increase in heat could lead to lower frictional strength of the granite, but also surrounding lithologies and help to localise shear.

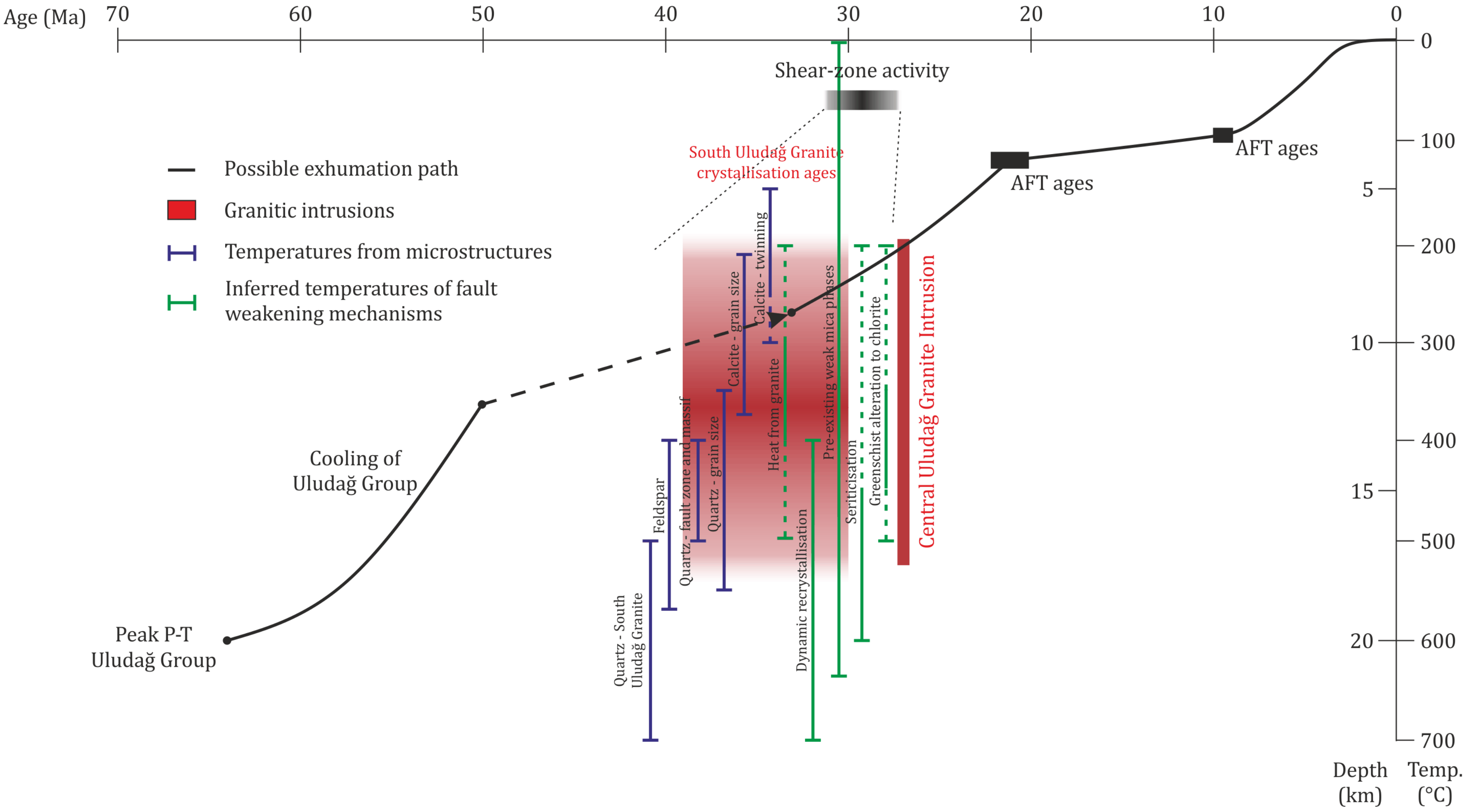

Figure 4.16. Exhumation, shear activity and volcanic activity in the Uludağ Massif. Exhumation profile taken from information in Okay et al. (2008). Shear zone timing expanded (indicated by dotted black lines) to incorporate all microstructure and weakening mechanisms.

All of the above mechanisms aided in the localisation of the strike slip shear onto the Eskişehir Fault, the most important being the abundance of phyllosilicates in the fault rocks as they are so weak when compared to the stronger surrounding lithologies. All the weakening mechanisms and their inferred temperatures of operation are shown in Figure 4.16.

5. CHAPTER FIVE

Strain analysis and strain calibration.

5.1. Introduction

This chapter presents data on temperature, strain and active slip systems from electron backscatter diffraction (EBSD) data of samples from the ductile Uludağ Shear Zone. Firstly the EBSD derived crystallographic preferred orientation (CPO) data will be shown which can be used to infer temperature, shear sense and active slip system estimates. Gathering slip system information from CPO pole figures is only qualitative however, Schmid factor analysis provides a much more robust constraint on active slip systems within minerals. For example, in calcite, whether or not a slip system becomes active is based on whether the critical resolved shear stress is overcome by the applied stress field and this is strongly temperature dependent. Therefore when looking at the activity of slip systems, the temperature and stress field must be taken into account. The second part of the chapter will look at the CPO strength quantitatively using different fabric strength parameters such as the intensity parameter (*I*), J-index and M-index and profiles of mineral fabric strength constructed to look at variation across the massif. This fabric strength will then be calibrated with shear strain across the massif using visco-plastic self-consistent modelling (VPSC). The overall aim of this chapter is to add to the data from the previous Chapter (Chapter 4) on strain localisation and distribution and also the evolution of the shear zone through space and time.

CPO can be measured efficiently and accurately via EBSD in the scanning electron microscope (SEM). The SEM used in this study is an FEI Quanta 650 FEG-ESEM with AZtec software and an Oxford/HKL Nordlys S EBSD system. The samples used in the EBSD analysis are small (~13-16mm), but representative, blocks set in resin that are ground and polished down to 1µm and then polished further with a colloidal silica solution (Lloyd, 1987, Nowell et al., 2005). CPO data are collected as orientations of three crystal axes (Euler angles) within a defined sample reference frame (eg. Kinematic, geographic), which is then converted into an orientation distribution function (ODF) which is used to create the pole figure (stereographic projection). The reference frame used in this chapter is the XYZ (X≥Y≥Z) kinematic reference frame and pole figures represent the XZ plane, where X is parallel to the inferred transport direction/stretching lineation and Z is normal to the foliation. The raw data are processed and the figures produced in MTEX (version 4.0.23) a MatLab (MathWorks, Inc.) toolbox (Bachmann et al., 2010a).

It has been noted recently that the reference frame used when collecting the EBSD data differs from the convention when plotting the data (Britton et al., 2016). Aztec plots the positive Y direction (perpendicular to the XZ plane) downwards in the EBSD maps to match the scanning direction, whereas in the pole figure plots within this thesis the positive Y direction is plotted out of plane, X is to the right and Z is plotted to the top.

5.2. Background theory and methods

CPO develop primarily as a result of crystal plastic deformation, such as dislocation creep, in the plastic deformation regime (Tullis, 1977, Sylvester and Christie, 1968, Schmid and Casey, 1986, Rosenberg and Stünitz, 2003, Barnhoorn et al., 2004, Heilbronner and Tullis, 2006), and as a result of dissolution-precipitation creep at lower temperatures (Bons and den Brok, 2000, Hippertt, 1994, Bestmann and Prior, 2003).

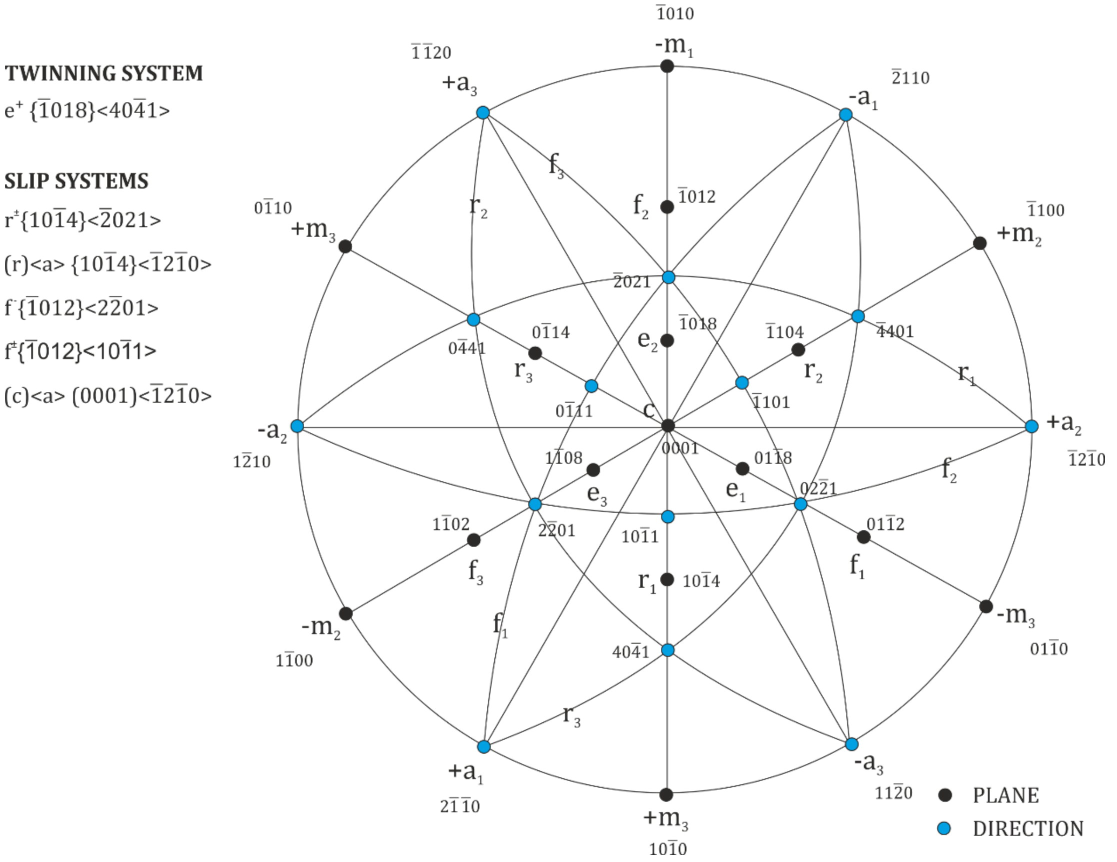

Figure 5.1. Upper hemisphere plot of planes and slip directions in calcite. Important twinning planes and slip systems are also displayed (Bestmann and Prior, 2003).

Other mechanisms such as rigid body rotation can also develop CPO (Stallard and Shelley, 1995, Díaz Azpiroz et al., 2007, Wallis et al., 2011). For calcite and quartz, dislocation creep is the most important mechanism responsible for CPO development, and occurs on specific crystal slip systems (Tullis, 1977, Schmid and Casey, 1986, De Bresser and Spiers, 1997). Slip systems are different for each mineral and the type of CPO that develops is dependent on which and how many slip systems in a mineral are activated. The activation of a slip system depends on the deformation conditions. In particular, the critical resolved shear stress (CRSS) that needs to be overcome before the mineral can slip along a specific crystal plane which is highly temperature dependent (Nicolas and Poirier, 1976, Lister and Williams, 1979, Mainprice et al., 1986, De Bresser and Spiers, 1997, Heilbronner and Tullis, 2006). These behaviours and relationships are now explained in detail for calcite and quartz.

5.2.1. Calcite

Calcite has trigonal symmetry (space group: $R\bar{3}c$) which means there are three f, r, e and m poles to planes and three a axes distributed around the c-axis (Figure 5.1) (Maslen et al., 1993). Wenk et al. (1987) investigated the development of calcite CPO by simple shear deformation via experimental, numerically simulated and natural samples. The results show that CPO patterns differ not only for coaxial and non-coaxial deformations but also for high and low temperatures (Figure 5.2).

In low temperature examples, the c-axis maxima are parallel to the compression direction in pure shear while in simple shear they rotate away from the shear plane normal against the sense of shear (Figure 5.2). At higher temperatures, a cross-like structure develops, symmetrical in pure shear and, again, rotated against the sense of shear in simple shear (Figure 5.2). According to Wenk et al. (1987) the two c-axis maxima labelled β and γ indicate that all major slip ({r} and {f}) and e-twinning systems were active, whilst the component labelled δ develops when e-twinning becomes less important at higher temperature (~500°C). Other experiments (Schmid et al., 1987, Trullenque et al., 2006) are in agreement with these behaviours (Figure 5.3). In particular, in simple shear, the c-axis maxima are again rotated away from the normal to the shear plane in the opposite direction to the sense of shear (Schmid et al., 1981).

Figure 5.2 and Figure 5.3 suggest that the asymmetry of c-axis maxima can be used to infer the sense of shear. However, there are situations where this does not apply. Trullenque et al. (2006) found that in some samples the asymmetry was rotated towards the sense of shear. Whether the c-axis maxima rotate with or against the sense of shear depends on the degree to which e-twinning has contributed to the deformation. If twinning is dominant during texture evolution, the c-axes rotate against the sense of shear (Figure 4.1b) (Schmid et al., 1987, Behrmann, 1983). If twinning is suppressed, through recrystallisation (as recrystallised grains are generally not twinned) and elevated temperatures, the c-axes rotate with the sense of shear (Trullenque et al., 2006). Recrystallisation is easy to recognise in thin section so it will be easy to identify if twinning has been supressed through recrystallisation. Calcite undergoes bulging recrystallisation at low to medium metamorphic grade, and sub grain rotation recrystallisation is active under a range of temperatures (200-500°C) (Bestmann and Prior, 2003).

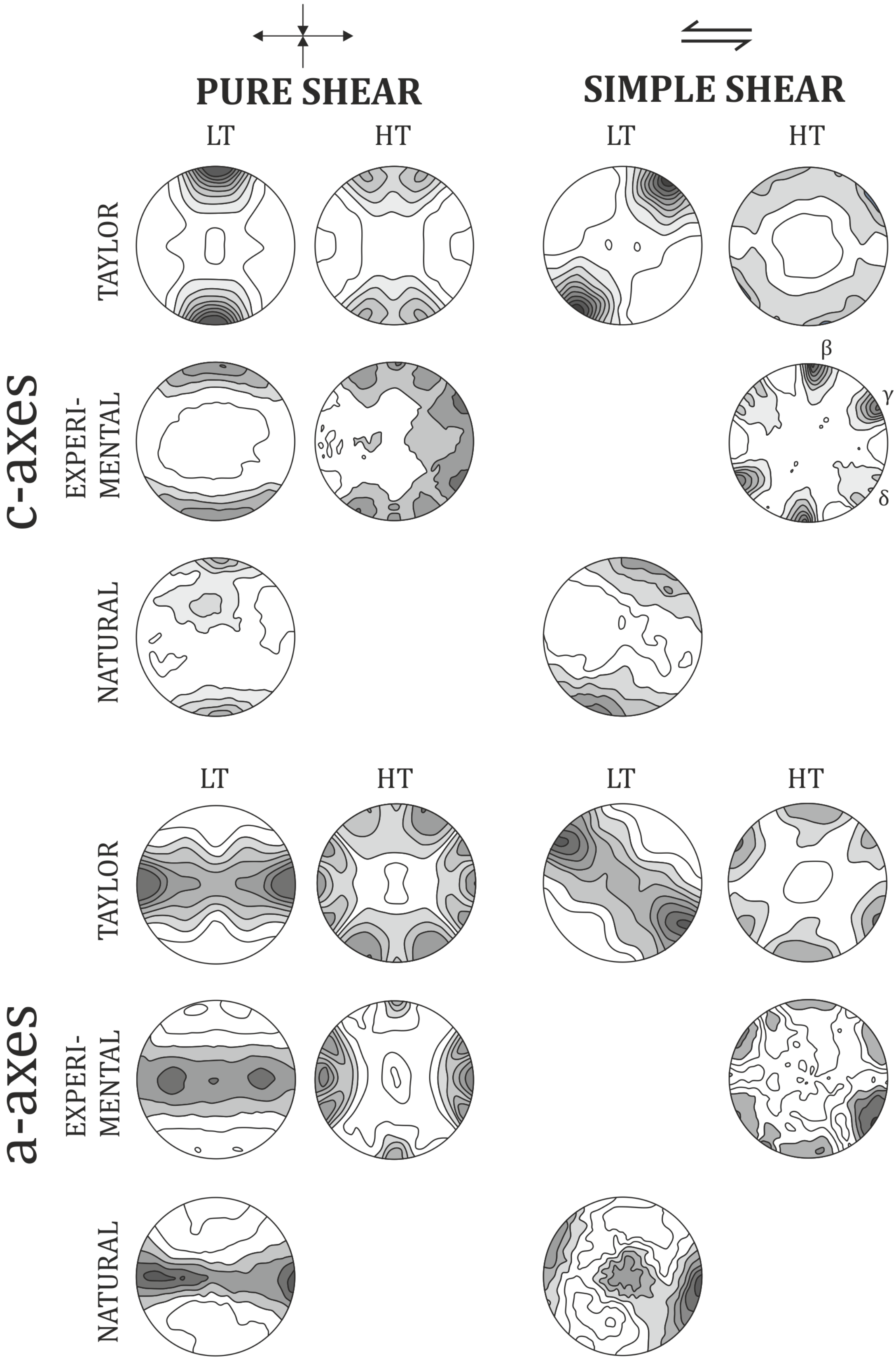

Figure 5.2. Simulated (Taylor), experimental and natural CPO textures for calcite, showing the c-axis and a-axis distributions for both low temperature (LT) and high temperature (HT) in pure shear and simple shear kinematics. Shaded to highlight CPO maxima (Wenk et al., 1987). Contours are in multiples of uniform distribution (m.u.d) with an interval of 0.2. β, γ and δ are indicated on the experimental c-axis distribution.

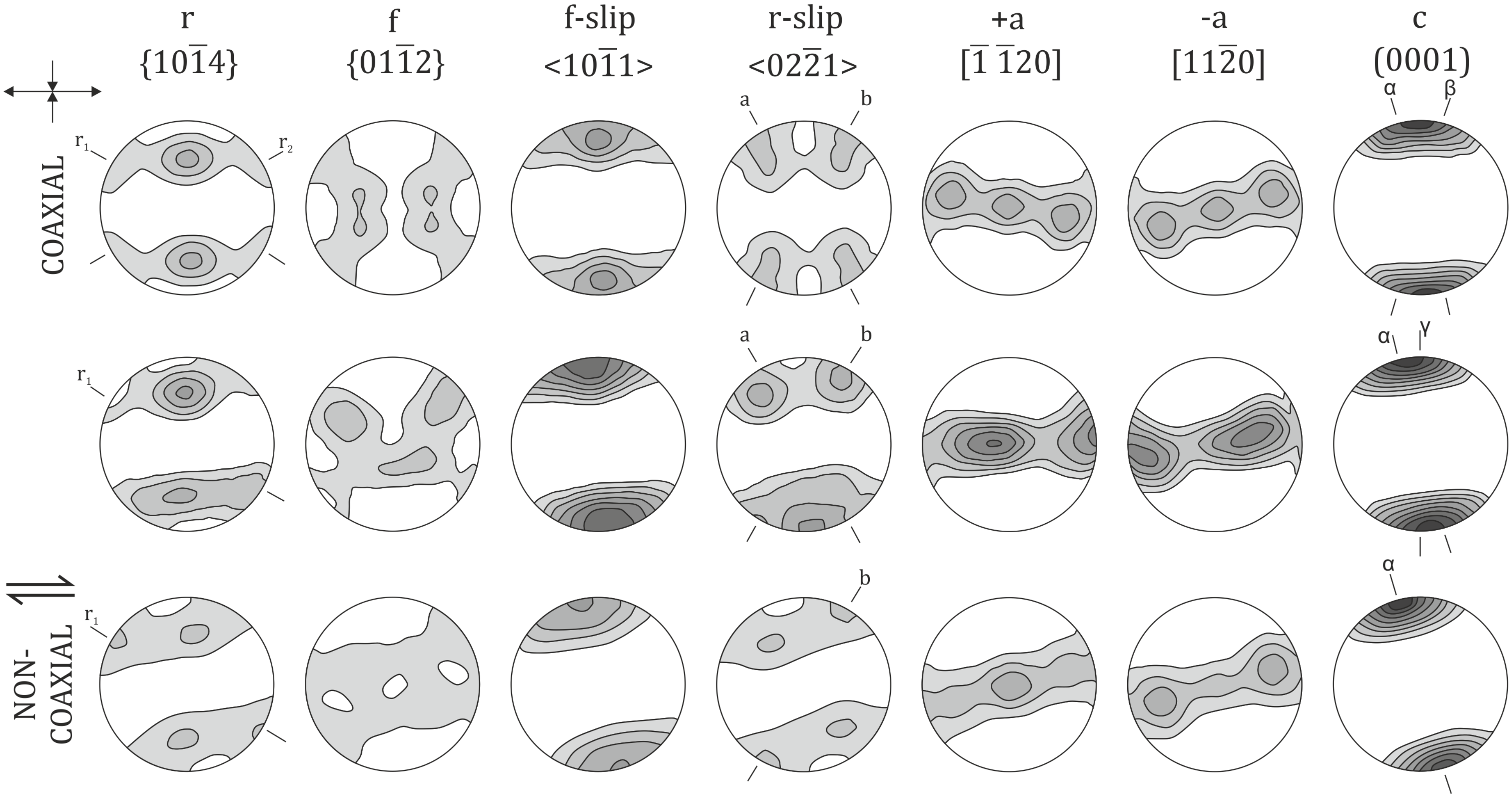

Figure 5.3. Pole figures for three models, from coaxial (pure shear) to non-coaxial (simple shear) deformation. Plots are transport direction (X) to the east and the foliation plane (XZ) is east-west (Trullenque et al., 2006). Contours are in multiples of uniform distribution (m.u.d) with an interval of 0.2, starting at 1 m.u.d.

There are three main slip systems and one twinning regime that facilitate deformation in calcite. The slip systems are r-slip {10$\bar{1}$4}<$\bar{2}$021>, f-slip {01$\bar{1}$2}<10$\bar{1}$1> (high temperature), f-slip {01$\bar{1}$2}<2$\bar{2}$01> (low temperature) and basal<a> (0001)<a>, and the e-twinning system is {$\bar{1}$018}<40$\bar{4}$1>, see Figure 5.1 (Turner, 1954, De Bresser and Spiers, 1997, Weiss and Turner, 1972, Spiers and Wenk, 1980).

The activity and relative contribution of these slip systems to the overall texture evolution depends on their relative critical resolved shear stress (CRSS). Experimental observations have shown that slip occurs when the resolved shear stress (τ^s) acting in the slip direction on the slip plane reaches some critical value (τ_c), known as the CRSS (Schmid, 1928, Schmid and Boas, 1950). The value of τ_c depends on material and environmental parameters, such as dislocation density, impurities in the crystal lattice, temperature, strain rate and deformation state (De Bresser and Spiers, 1997, Morales et al., 2014). Pieri et al. (2001b) used self-consistent plasticity theory to model simple shear deformation and dynamic recrystallisation of calcite. A model favouring nucleation and the activation of a different slip system r<a>, 10$\bar{1}$4<$\bar{1}$2$\bar{1}$0> matched the experimental data most closely (Pieri et al., 2001b). However, whilst common in dolomite, this slip system has only been modelled, and not actually observed in natural calcite samples (Barber et al., 1981, Barber and Wenk, 2001).

The graph in Figure 5.4 is taken from De Bresser and Spiers (1997), and shows the different slip systems and their relative CRSS It clearly indicates that e-twinning is the easiest deformation mechanism to be activated and is the most dominant system at low to medium temperatures (eg. 0°C - 500°C), activating at relatively low CRSS between 2 and 12 MPa (Turner et al., 1954, Burkhard, 1993). However, twinning can only accommodate a limited amount of strain (Rowe and Rutter, 1990), leading to accommodation structures at grain boundaries, such as grain boundary migration, pressure solution and grain boundary sliding (Behrmann, 1983). These are evident from dissolved twin boundaries or twins that end before the grain boundary is reached (Passchier and Trouw, 2005). Also at low to medium (200-600°C) temperatures slip on r and f planes is important alongside e-twinning whilst at higher temperatures (600-800°C) c<a> slip becomes active (De Bresser and Spiers, 1997, Schmid et al., 1987).

The crystal system(s) most responsible for accommodating deformation can often be deduced from CPO patterns. With increasing shear strain, the angle between the shear zone boundary and the foliation decreases, such that the maximum shear stress is resolved on to the foliation plane. One assumption made when interpreting textures from pole figures is that during simple shear and accompanying recrystallisation, one or more slip planes align with the bulk shear plane and slip directions align with the bulk shear direction (Nicolas, 1976, Schmid, 1994). The slip system that is most likely to be active in a given sample is the one on which the highest shear stress is resolved. In simple shear therefore it is the slip plane closest to the foliation plane (Trullenque et al., 2006). Slip is easiest on the slip plane orientated parallel to the shear plane and the main slip direction is towards the shear direction (Pieri et al., 2001b).

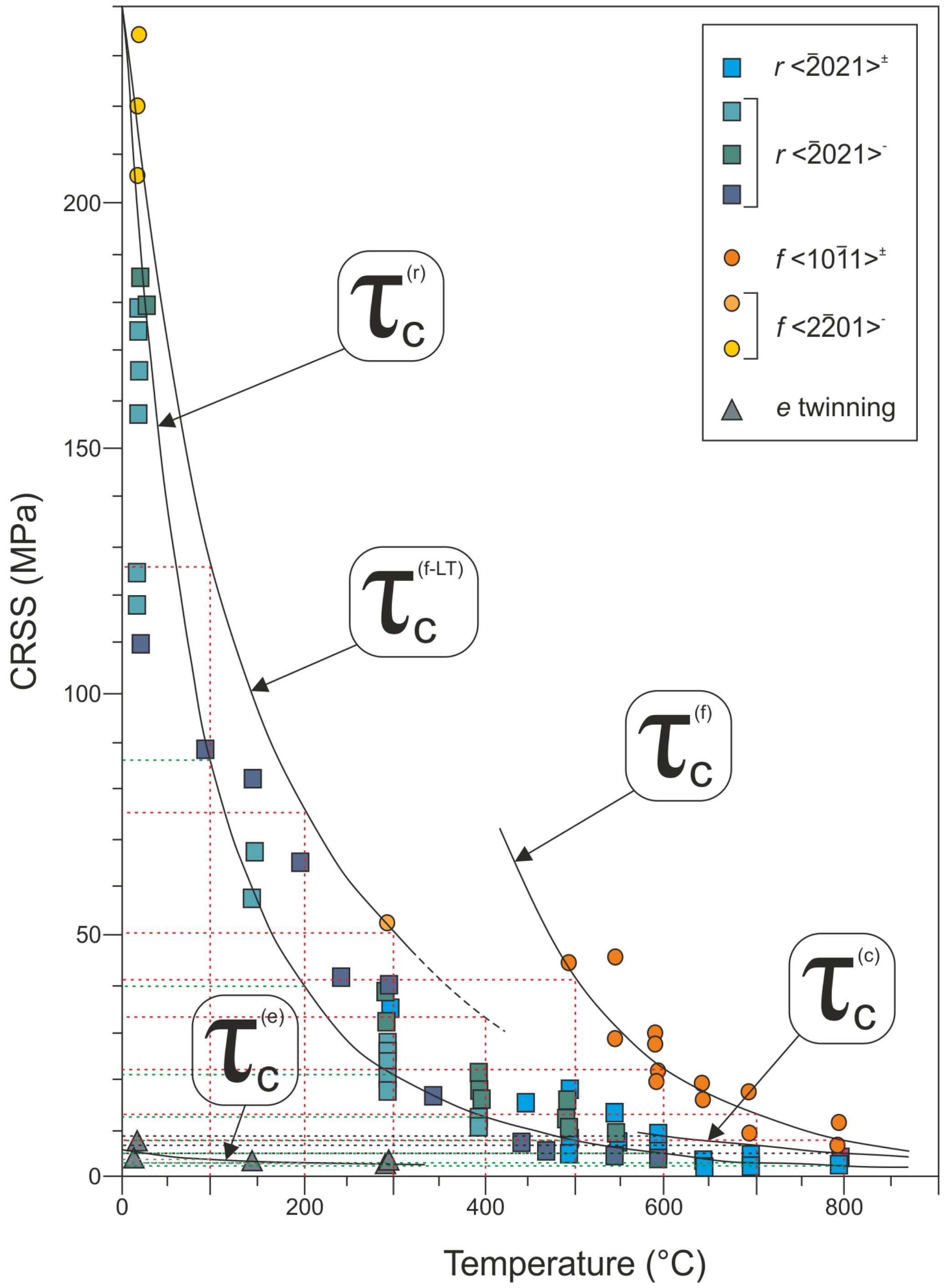

Figure 5.4 Compilation of CRSS data showing temperature dependence of slip systems in calcite (Turner et al., 1954, Griggs et al., 1960, Braillon and Serughetti, 1976).

Texture evolution is influenced by dynamic recrystallisation (Trullenque et al., 2006). Grains with c-axes rotated against the sense of shear are unsuitably orientated for slip on the basal plane, and therefore cause localised stress perturbations that promote recrystallisation, nucleating grains that are more suitably orientated for slip (Schmid, 1994, Trullenque et al., 2006). Thus interpretation of slip systems in calcite, and also shear sense, from CPO should be done in conjunction with microstructural analysis to identify the potential contribution(s) from twinning and/or dynamic recrystallisation (Trullenque et al., 2006).

5.2.2. Quartz

Quartz also shows trigonal symmetry (space group: $P3_121$, $P3_221$) and similar to calcite has three a axes and three z, r and m poles to planes distributed around a c-axis (Figure 5.5a). In quartz, different c-axes patterns develop depending on temperature and the amount and type of strain the sample has experienced. During coaxial deformation symmetric cross girdles or point maxima parallel to Z in c-axis CPO are common. In non-coaxial deformation asymmetric cross girdles are present at low temperatures which develop into point maxima at higher temperatures (Figure 5.5b) (Lister and Hobbs, 1980, Behrmann and Platt, 1982, Schmid and Casey, 1986). The slip systems active can be inferred from the distributions of c- and a-axes (Figure 5.5c) (Lister and Williams, 1979, Schmid and Casey, 1986, Lloyd et al., 1992, Lloyd and Freeman, 1994).

In simple shear, at lower greenschist facies conditions (300-400°C), slip on the basal<a> ($(0001)\langle\bar{1}\bar{1}20\rangle$) systems is most prevalent giving c-axis maxima sub-parallel to the Z direction (Baëta and Ashbee, 1969). At mid greenschist facies conditions (400-500°C), basal <a> slip is still important, with prism<a> and rhomb<a> becoming increasingly active with increasing temperature (Schmid and Casey, 1986, Lloyd et al., 1992, Lloyd and Freeman, 1994). In these conditions c-axes form an asymmetric cross girdle with clusters at the periphery (Figure 5.5b) (Wilson, 1975, Law et al., 1990, Bouchez, 1977).

As deformation temperature increases (500-700°C) prism <a> ($\{10\bar{1}0\}\langle\bar{1}\bar{1}20\rangle$) and rhomb <a> ($\{10\bar{1}1\}\langle\bar{1}\bar{1}20\rangle$) are the most active slip systems (Figure 5.5b) (Wilson, 1975, Bouchez, 1977, Law, 1990). At these temperatures c-axes become more clustered parallel to the Y axis (Figure 5.5b) (Law et al., 1990). At temperatures >650°c, c-axis point maxima cluster close to the transport direction of the sample, the X direction (Figure 5.5b) (Mainprice et al., 1986). This indicates prism<c> slip ($\{10\bar{1}0\}[0001]$) is active under high temperatures, low strain rates and low stress intensity and the increased importance of water weakening processes (Lister and Dornsiepen, 1982, Mainprice et al., 1986, Law et al., 1990).

The distribution of quartz c-axes can also be used to infer the sense of shear at lower temperatures (400-500°C) where there are asymmetric fabrics present. These asymmetric cross girdles and single girdles rotate with the sense of shear (Figure 5.5b) (Schmid and Casey, 1986, Behrmann and Platt, 1982, Law et al., 1990).

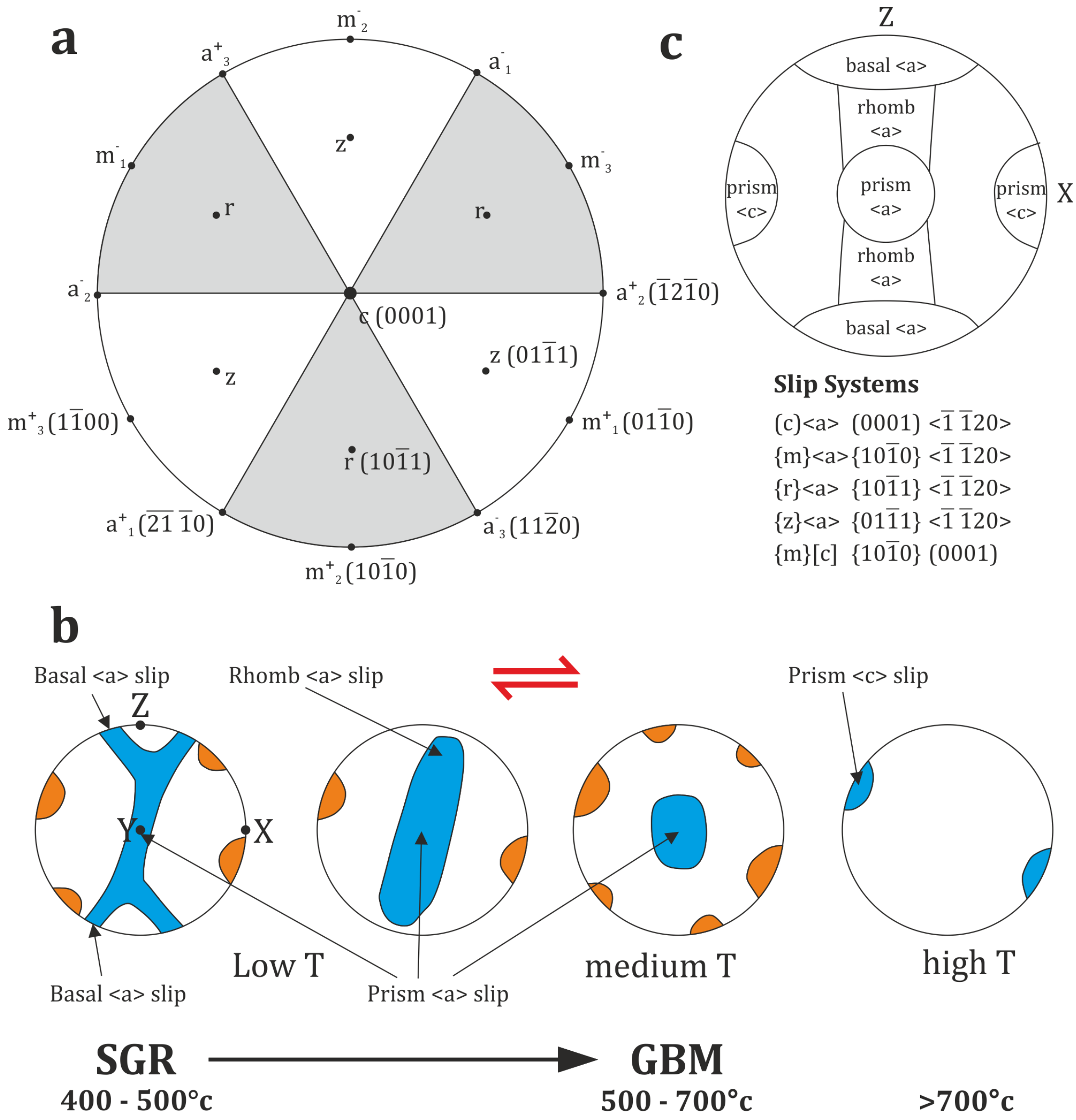

Figure 5.5. a) Quartz symmetry and axis distributions. b) Quartz slip systems. c) Quartz CPO textures evolving with increasing temperature. C-axis distributions shown in blue, a-axes shown in orange. Compiled from (Passchier and Trouw, 2005, Stipp et al., 2002, Schmid and Casey, 1986).

5.2.3. Schmid Factors

Using CPO is the common approach when trying to ascertain active slip systems, as outlined in the previous section (Wenk et al., 1987, Toy et al., 2008). More recently, the advent of EBSD has reinvigorated a well-known technique based on the Schmid factor (Schmid, 1928, Schmid and Boas, 1950, Farla et al., 2011). Wallis et al. (*Unpublished Manuscript*) have further developed Schmid factor analysis and applied it to calcite marbles within the Karakoram Fault Zone.

Schmid factor analysis not only allows an alternative and quantifiable approach to determine active slip systems in a deformation zone, but also allows investigation into the transition from plastic to seismogenic behaviour (Wallis et al., *Unpublished Manuscript*). Samples within the sample suite that display different temperature microstructure can be used in conjunction with Schmid Factor analysis to assess the change in slip system dominance as the shear zone exhumes and cools. This can have important implications on the depth dependence for earthquake nucleation (Scholz, 1988, Wallis et al., *Unpublished Manuscript*).

The Schmid factor (m^s) gives the relationship between resolved shear stress (τ^s) and the applied stress state (σ_A) for a particular slip or twin system (Schmid, 1928, Schmid and Boas, 1950, Wallis et al., *Unpublished Manuscript*). The Schmid factor relates the applied differential stress ($\sigma_d = \sigma_{max} - \sigma_{min}$) to the shear stress that is resolved on to a particular slip or twin system. As the max fraction of applied stress that can be resolved is 0.5, the Schmid factor is constrained to the range 0-0.5.

$$\tau^s = m^s \sigma_d \qquad (5.1)$$

The Schmid factor of a slip system is described as:

$$m^s = \cos\phi \cos\lambda \qquad (5.2)$$

where s is the slip system, ϕ is the angle between the maximum principle stress (σ_{max}) direction and the slip or twin plane normal and λ is the angle between the maximum principle stress directions and the slip or twin direction (Schmid, 1928, Schmid and Boas, 1950).

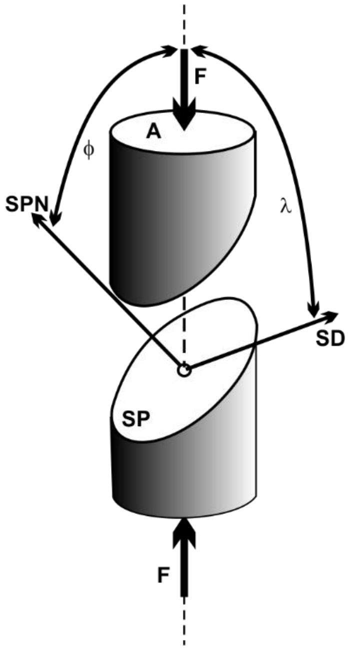

Figure 5.6. Relationship between the applied stress (F) and the slip direction (SD) and slip plane normal (SPN) of a specific slip plane (SP), described in Equation 5.2.

The above describes the Schmid factor as scalar, but an alternative 2nd rank tensor description exists that can be used to handle more complex stress states (Pokharel et al., 2014, Wallis et al., *Unpublished Manuscript*),

$$\tau^s = \frac{1}{2}\,(b^s \otimes n^s + n^s \otimes b^s) : \sigma = m^s : \sigma \qquad (5.3)$$

where m^s is the Schmid tensor, σ is the deviatoric stress tensor, b^s and n^s are the slip or twin direction and slip or twin plane normal, respectively, of a particular slip system (s). The Schmid tensor describes the fraction of each component in the deviatoric stress tensor that is resolved on a slip or twin plane in a slip or twin direction of a particular slip system (Pokharel et al., 2014, Wallis et al., *Unpublished Manuscript*).

During plastic deformation crystals only deform by dislocation glide or twinning on a particular slip system if the resolved shear stress (τ^s) exceeds the CRSS (τ_c^s) of that slip system (Schmid, 1928, Schmid and Boas, 1950). The value of τ_c^s varies with mineral, slip system and the temperature of deformation (De Bresser and Spiers, 1997, Morales et al., 2014). For calcite, experimental work has been carried out to constrain the CRSS variability with temperature of the slip and twinning systems which is critical in the application of Schmid factor to calcite (Figure 5.4) (De Bresser and Spiers, 1997).

Constraints on palaeostress magnitude for this study come from calcite palaeopiezometry in Chapter 3, Section 3.4.2. Also the temperature of deformation in the Uludağ Massif has been ascertained from microstructural analysis in Chapter 3, Section 3.5.2. The shape of the stress tensor in this study reflects the simple shear kinematics (σ_1 horizontal and orientated at 45° to the shear plane) of the Uludağ Massif (Chapter 3, Section 3.5.4). The stress tensor is defined by the product of the normalised tensor ($\hat{\sigma}$) and differential stress (σ_d), where the normalised tensor is given by

$$\hat{\sigma} = \begin{bmatrix} 0 & 1/2 & 0 \\ 1/2 & 0 & 0 \\ 0 & 0 & 0 \end{bmatrix} \qquad (5.4)$$

To determine which slip systems are activated by the palaeostress conditions $\hat{\sigma}$ is transformed into the crystal coordinate systems for each measured orientation and the Schmid tensor (m^s) is computed for each slip system (Wallis et al., *Unpublished Manuscript*). Equation 5.3 is then used to calculate the resolved shear stress (τ^s), whilst m^s and σ_d are used to calculate the τ^s resolved on each slip system. Once the Schmid factor and resolved shear stress for each slip system have been ascertained, it can be compared with the applied stress to see if it was sufficient to activate glide (i.e. is $\tau^s > \tau_c^s$) (Wallis et al., *Unpublished Manuscript*).

From this, maps of m^s can be plotted, but to determine the fraction of slippable grains the minimum value of m^s needed to activate glide or twinning on each system must be calculated,

$$m_{min} = \tau_c/\sigma_d \qquad (5.5)$$

where τ_c is the CRSS from Figure 5.4 at temperatures determined in Chapter 3, and σ_d is the differential stress from palaeopiezometry (Chapter 3) (Wallis et al., *Unpublished Manuscript*). Wallis et al. (*Unpublished Manuscript*) developed a script for use with MTEX in MatLab to do these calculations detailed above and plot maps of slippable grains for each slip system.

5.2.4. Fabric Strength

There are a number of controls behind the development of CPO, of which strain is the most important at constant temperature and stress (Sylvester and Christie, 1968, Lister and Hobbs, 1980, Schmid and Casey, 1986, Barnhoorn et al., 2004, Heilbronner and Tullis, 2006, Morales et al., 2011, Morales et al., 2014). However, other factors that could influence the strength of the fabric must be considered when using CPO intensity as a proxy for strain and these are outlined below.

CPO development in polymineralic rocks is controlled by the proportions of strongest to weakest minerals (Handy, 1990, Czaplińska et al., 2015, Herwegh et al., 2011). Two end members can be considered; the first where the rock consists of an interconnected strong phase containing small, disconnected pockets of a weaker phase and the second, a weaker deformed matrix containing undeformed clasts of a stronger phase (Handy, 1990). Between these two end members exists a sliding scale of weak to strong mineral proportions and proportion of strain accommodated by each phase (Herwegh et al., 2011). In the case of the first end member the strongest phase controls the strength of the rock and impedes the development of CPO, in the second end member the strength is controlled by the weaker phase which accommodates a large amount of strain and develops a strong CPO (Herwegh et al., 2011).

Small (micro-) scale variations in CPO can be due to strain heterogeneities including partitioning of coaxial and non-coaxial deformation, or grain size variations (prophyroclast and matrix) (Lister and Williams, 1983, Larson et al., 2014). Pre-existing fabrics (either sedimentary layering or a pre-existing CPO) can mean mineral slip systems can already be either in a favourable or unfavourable orientation for slip when a stress field is applied, resulting in a stronger or weaker than expected CPO respectively (Lister and Williams, 1983, Knipe and Law, 1987, Wilson, 1984). Strain paths and changing stress fields also affect the resultant CPO. Once a steady state has been achieved, increasing strain does not increase the CPO strength (Lister and Hobbs, 1980, Wenk and Christie, 1991).

Deciphering the variation or intensity of deformation over a large scale structure is often very difficult due to lack of continuous strain markers (eg. deformed burrows, pebbles or boudinaged features). However, CPO can generally be measured in samples for most locations with such structures. It is argued here that CPO strength can be used as a proxy for strain providing it can be quantified. Several methods exist to quantify CPO strength and are described below.

1. *J-index*

The J-index (Bunge, 1982) is mathematically defined as the second moment of an orientation distribution function (ODF) (Skemer et al., 2005),

$$\mathrm{J} = \int \mathrm{f}(\mathrm{g})^2 \mathrm{dg} \qquad (5.6)$$

where J is the dimensionless J-index, f(g) is density of the ODF at orientation g, and dg = $d\varphi_1 d\phi d\varphi_2 \sin\phi / 8\pi^2$, where φ_1, ϕ, φ_2 are the Euler angles (Mainprice and Silver, 1993, Ismaıl and Mainprice, 1998). The J-index has a value of 1 for a random fabric and infinity for a single crystal, although the maximum is typically capped at 250 for most studies (Ismaıl and Mainprice, 1998). The J-index method is highly sensitive to the number of grains measured and arbritary smoothing methods applied during calculation, which means the results can be difficult to interpret (Wenk, 2002, Matthies and Wagner, 1996, Skemer et al., 2005). This means this it must be applied with care using analysis involving an ODF calculated from one point per grain in the sample.

2. *M-index*

Another quantification for CPO strength is the M-index (Skemer et al., 2005), which is based on the distribution of misorientation angles (Wheeler et al., 2001). Misorientation is defined as the rotation around a common axis required to bring two crystal lattices into the same orientation (Randle and Ralph, 1986, Mainprice et al., 1993). Energy is a function of misorientation; the higher the misorientation on a boundary, the more energy that boundary contains (Randle and Ralph, 1986). Metallurgical experiments have shown that grains rotate to minimise that energy (Randle and Ralph, 1986, Mainprice et al., 1993, Skemer et al., 2005). When the fabric is strong, the misorientation angles are small as many grains have similar orientations, providing the basis for the M-index (Skemer et al., 2005). The M-index is defined as the difference between the normalised distribution of measured misorientations with a misorientation angle θ, and the theoretical distribution of misorientations in a random fabric with misorientation angle θ.

$$\mathrm{M} \equiv \frac{1}{2} \int \left| \mathrm{R}_i^T(\theta) - R_i^0(\theta) \right| \mathrm{d}\theta \, . \qquad (5.7)$$

where R_i^T is the theoretical distribution of misorientation angles for a random fabric, R_i^0 is the observed distribution of misorientation angles (Skemer et al., 2005). The M-index increases with fabric strength from 0 – 1 (random to single crystal) (Skemer et al., 2005).

3. Eigenvalue methods

The intensity of crystal pole distributions and their fabrics was first quantified by Woodcock (1977), who developed a plot similar to a Flinn plot (Flinn, 1965) using eigenvalues rather than the x/y/z axes of deformed objects (Figure 5.7). Where Flinn plots compare the ratios of the kinematic axes (X/Y vs Y/Z, where X≥Y≥Z), Woodcock (1977) proposed using the 3 eigenvalues of the CPO distribution. On the plot (Figure 5.7) $k > 1$ represents constrictional strain (i.e. X>>Y≈X) and c-axis point maxima, $k = 1$ is plane strain (i.e. X≈Y) and $k < 1$ represents flattening strains (i.e. X≥Y>>Z) and c-axis girdle distribution similar to the Flinn plot (Flinn, 1965). The parameter k is defined as:

$$k = \frac{(S_1/S_2)}{(S_2/S_3)} \qquad (5.9)$$

Where $S_1 \geq S_2 \geq S_3$ are the normalised eigenvalues. The plot in Figure 5.7 can be used in conjunction with the concentration parameter (C), which is defined as:

$$C = \ln(S_1/S_3) \qquad (5.10)$$

The parameter C ranges from 0 (random fabric) to infinity (single crystal).

Whilst the C parameter is relatively simple, it was noted by Lisle (1985) that it behaves differently for girdle and point fabrics; whilst it can also depend on sample size (Woodcock and Naylor, 1983). Lisle (1985) therefore developed the intensity (I) parameter (I),

$$I = \frac{15}{2} \sum_{i=1}^{3} \left(S_i - \frac{1}{3}\right)^2 \qquad (5.11)$$

where S_i are the normalised eigenvalues of the orientation tensor. The intensity parameter ranges from 0 to 5 for linear fabrics and from 0 to 3.75 for planar fabrics (Lisle, 1985). Using this parameter overcomes the problem of sample size affecting the outcome encountered with the method proposed by Woodcock (1977), and it is the least sensitive to distribution shape.

1. P-G-R index

This is another eigenvalue based method to describe CPO fabrics (Vollmer, 1990). Here,

$$P = (\lambda_1 - \lambda_2/N) \qquad (5.12)$$

$$G = 2(\lambda_2 - \lambda_3)/N \qquad (5.13)$$

$$R = 3(\lambda_3)/N \qquad (5.14)$$

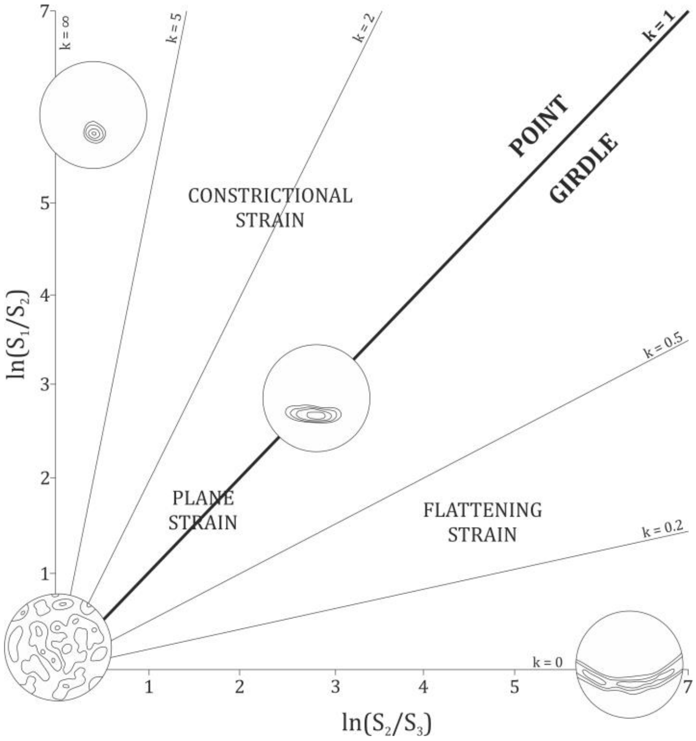

Figure 5.7. Graph similar to Flinn plot displaying the difference between flattening and constrictional strain in pole figure patterns (Woodcock, 1977).

and,

$$N = \lambda_1 + \lambda_2 + \lambda_3 \qquad (5.15)$$

Again, $\lambda_1 \geq \lambda_2 \geq \lambda_3$ are the normalised eigenvalues for the CPO fabric. P+G+R should equal 1 and can be plotted on a triangular diagram or simplified by using (1 – R), where 0 is a random fabric and 1, a perfect girdle or maxima.

2. Comparison of strength parameters

To ascertain which of the CPO strength parameters described above is the most appropriate to use in this study, all five have been calculated for a small sample size of 8 c-axis CPO with varying maximum multiples of uniform distributions (m.u.d) and fabrics (girdle or point). The results of this comparison are shown in Figure 5.8. No smoothing has been applied to any of the pole figures and the data used to plot consisted of all indexed points within the sample. It is evident that each parameter gives quite different results.

The two texture parameters, J and M, are shown in Figure 5.8b-c respectively. The J-index shows a similar bias towards girdle-type fabrics as the C parameter. Again, ULD165 has a higher J-index than ULD49, but displays a weaker girdle on the pole figure. The same situation exists between ULD131 and ULD134, ULD134 shows a weaker girdle but a higher J-index. ULD38 has a lower J-index than ULD124, again displaying a preference for girdle-fabrics. The M-index shows the same behaviour as the intensity parameter (I); in fact when they are normalised to one (Figure 5.8g) the two parameters overlie each other.

The M-index seems less sensitive to fabric variations than the C-parameter or the 1-R calculation (noted between the samples of ULD49 and ULD165).

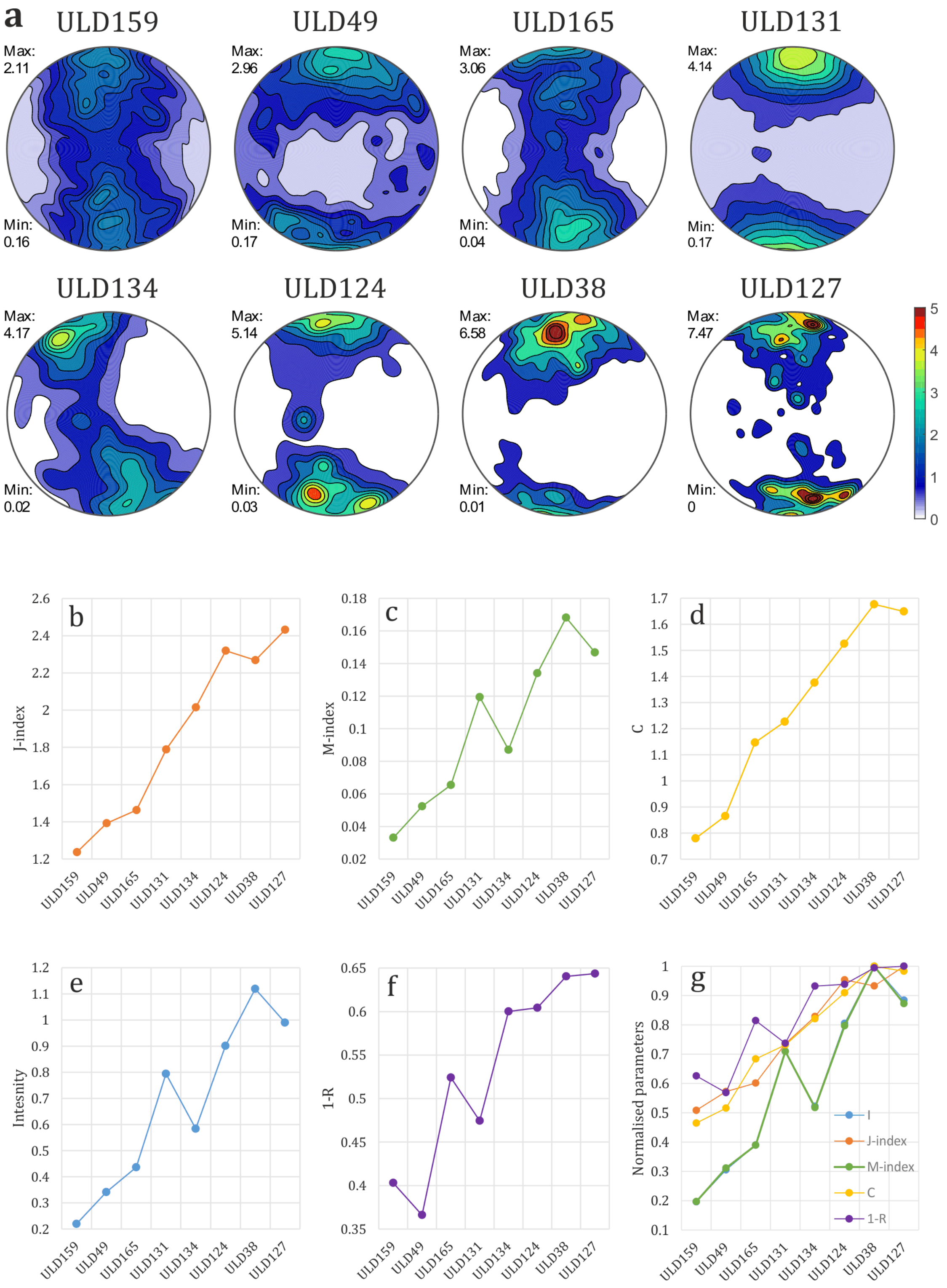

Figure 5.8. Eight calcite c-axis CPO’s were taken that roughly increase in maximum values of multiples of uniform distribution (m.u.d) from ULD159 to ULD127, with variation between girdle and point fabrics (a). Parameters on plots (b), (c) and (e) were calculated using scripts developed in MTEX (Mainprice et al., 2014, Lisle, 1985, Bunge, 1982, Skemer et al., 2005). Parameters on plots (d) and (f) were both calculated using equations in Woodcock (1977) and Vollmer (1990) respectively. Plot (f) shows all of the parameters, normalised to 1, for comparison.

The C-parameter (Figure 5.8d) shows a steady increase in values, aside from a dip at the final sample with ULD127. There is a large increase in C between ULD49 and ULD165 but qualitatively ULD165 has a less well developed girdle fabric than the point fabric of ULD49, so there should be a decrease. This behaviour suggests a bias towards girdle fabrics.

Figure 5.8e shows the I parameter variation for the 8 samples. ULD131 and ULD134 have similar CPO strength based on the m.u.d but ULD131 has a higher intensity value. ULD134 has a less well-developed girdle fabric and ULD131 is a well-ordered point fabric so a decrease in fabric strength is likely. Also between ULD38 and ULD127, ULD127 has a higher m.u.d but a lower I value because the fabric is not as well ordered which can be seen visually.

The final eigenvalue based parameter, 1-R, is displayed in Figure 5.8f. This graph shows a distinct bias towards girdle fabrics, notably with ULD159 having a higher 1-R value but a lower m.u.d than ULD49. Samples ULD131 and ULD134 also show this preference for girdle-type fabrics, both samples have similar m.u.d but ULD134, the sample showing a weak girdle, has a much higher 1-R value. The next sample (ULD124) shows a similar 1-R value to ULD134 but visually the CPO seems more organised and better ordered in the pole figure.

From this test it appears that the intensity parameter (I) and M-index show the least sensitivity to one or other fabric type (ie girdle, cluster etc). The J-index is also included for comparison but due to the problems mentioned earlier (ie sample size and smoothing effects) affecting the outcome, the results can be difficult to interpret (Wenk, 2002, Matthies and Wagner, 1996, Skemer et al., 2005).

5.2.5. Visco plastic self-consistency

Visco plastic self-consistency (VPSC) simulates the plastic deformation of polycrystalline aggregates subjected to external stresses. It is based on the deformation mechanisms of slip and twinning producing the response due to strain-rate or an imposed stress and accounts for strain hardening processes whereby with increasing strain deformation becomes more difficult, crystal reorientation and shape change of individual grains with regards to CPO development (Lebensohn and Tomé, 1993, Lebensohn et al., 1998). The input into the VPSC modelling is the Euler angles of a random distribution of 500 or 1000 data points (grains), representing an undeformed ‘protolith’ sample. The random selection of grains is then subjected to deformation in increments of strain to a predefined total. This deformation occurs on slip or twinning systems, their relative contributions come from the CRSS, which is temperature dependent.

Temperature (°C)	**CRSS (MPa)**				**Normalised to r-slip**			
	r-slip	**f-slip**	**Basal-slip**	**e-twinning**	**r-slip**	**f-slip**	**Basal-slip**	**e-twinning**
100	86	126		4	1.0	1.5		0.05
200	40	75		3	1.0	1.9		0.08
300	21	50		3	1.0	2.4		0.14
400	13	33		2	1.0	2.5		0.15
500	8	42			1.0	5.1		
600	5	22	9		1.0	4.4	1.8	
700	3	13	7		1.0	4.5	2.3	
800	3	8	5		1.0	2.9	1.8	

Table 5.1. The table displays the CRSS values for the activation of each slip system in calcite, along with those values normalised to r-slip. These normalised values are inputted into the VPSC model (De Bresser and Spiers, 1997). The values in red for r-slip represent when low temperature f-slip is taken over by high temperature f-slip.

The CRSS values specific to calcite are provided in Table 5.1, taken from the graph in Figure 5.4 (De Bresser and Spiers, 1997). They are normalised one slip system, r-slip in this case, to ascertain the ease at which a slip system becomes active during deformation at specific temperatures (i.e. in terms of easy:hard)

The Euler angles in the input file are progressively deformed at each increment of strain during the VPSC modelling and written to an output file. Therefore for each strain step, the intensity (I), J and M-index can be calculated from the new deformed Euler angles again to produce shear strain vs. I, J and M fabric strength curves. This means that the previously calculated fabric strength values from the other samples can be plotted onto this curve and calibrated with shear strain. The objective of this is to produce a shear strain profile across the massif using all of the samples to ascertain variations in deformation.

The VPSC simulation uses the 1-site approach where each grain is treated as an ellipsoidal visco-plastic inclusion deforming in a viscoplastic homogeneous effective medium (HEM) to determine the microscopic state of strain and stress of each grain. The HEM is an average of the behaviour of the aggregate (all the grains in the input). Therefore interaction between grains is not considered in VPSC, but rather the interaction between each grain and the surrounding HEM. The Eshelby approach solves the problem of an ellipsoidal inclusion within an infinite homogeneous domain (Equation 5.16) (Eshelby, 1957):

$$\dot{\varepsilon} - \dot{E}_{ij} = -\alpha\,\tilde{M}_{ijkl}(s_{kl} - \Sigma_{kl}) \qquad (5.16)$$

Where $\tilde{M}$ in the interaction tensor (dependent on grain shape and the plastic properties of the HEM), α is a constant ranging from 0 to ∞ which is used to parameterise the interaction between the HEM and then grains, S_{kl} is the matrix representation of the visco-plastic Eshelby tensor, $\dot{\varepsilon}$ is the strain-rate in the grain and $\dot{E}$ is the macroscopic imposed strain-rate a time interval (Eshelby, 1957, Lebensohn and Tomé, 1993). Zero represents the upper bound average of homogeneous strain and infinity represents the lower bound average of all grains experiencing the same state of stress (Taylor, 1938, Sachs, 1928).

In VPSC each grain is deformed when one or more slip system is activated based on the values taken from Table 5.1. The shear rate induced in a slip system(s) by a local deviatoric stress (s_{ij}) can be described by the viscoplastic law:

$$\dot{\gamma}^s = \dot{\gamma}_0 \left(\frac{\tau_r^s}{\tau_0^s}\right) = \dot{\gamma}_0 \left(\frac{r_{ij}^s\, s_{ij}}{\tau_0^s}\right)^{n^s} \qquad (5.17)$$

Where r^s is the Schmid factor and τ_r^s and τ_0^s are, respectively, the CRSS and activation stress of the specific slip or twin system (s), $\dot{\gamma}_0$ is a reference strain-rate and n is stress exponent (Lebensohn et al., 1998). Deviatoric stress is found by subtracting the mean stress from the three diagonal components of the stress tensor, whereas the differential stress is the difference between the maximum and minimum principle stresses. However, they both describe a change in shape of a volume.

The crystal rotation and reorientation in relation to the external reference frame is given by;

$$\omega_{ij} = \Omega_{ij} - \textstyle\sum_s \frac{1}{2} \left(b_i n_j - b_i n_j\right)^s \dot{\gamma} + \widetilde{\omega}_{\sim ij} \qquad (5.18)$$

where ω_{ij} is the rotation, Ω_{ij} is the anti-symmetric component of the velocity gradient defining the deformation regime (Equation 5.19). The spin of the crystal is given by the summation term where b is the Burgers vector, n is the normal to the slip or twin plane (s) and $\widetilde{\omega}$ is the reorientation rate of the inclusion (Lebensohn and Tomé, 1993). The velocity gradient for simple shear is:

$$\begin{matrix} 0 & 1 & 0 \\ 0 & 0 & 0 \\ 0 & 0 & 0 \end{matrix} \qquad (5.19)$$

The modelling takes into account the effect of twinning reorientation on texture development via the predominant twin reorientation scheme (Tomé et al., 1991) and recrystallisation from stored strain energy in grains via nucleation and growth (Wenk et al., 1997, Lebensohn et al., 1998). If recrystallisation is growth controlled, the models predict that 'hard' (i.e. less deformed) grains would grow at the expense of others and dominate the recrystallisation texture (Lebensohn et al., 1998). If nucleation is active during recrystallisation the most highly deformed grains nucleate, become strain free and consume the less deformed non-nucleated grains (Lebensohn et al., 1998).

5.3. Results

The results for the analyses discussed above are presented in this section. Firstly the calcite and quartz CPO, followed by Schmid factor analysis for calcite, CPO fabric strength for quartz and calcite and finally VPSC simulations and shear strain calibration.

5.3.1. Calcite CPO

This section presents the data from the pure calcite marble (~95% calcite <5% quartz) samples of the data set. The CPO for these samples are shown in Figure 5.9a-f. All samples are plotted in the kinematic (XZ) reference frame, with the inferred transport direction (X) plotted to the east and the normal to foliation plane (Z) is to the north. The (c)-, and {a}-axes and the {e}, {r}, and {f} poles to planes have been plotted along with the e-twinning direction <40$\bar{4}$1>, the r-slip direction <$\bar{2}$021> and the f-slip direction <10$\bar{1}\bar{1}$> (see Figure 5.1). Textural analysis of calcite pole figures can indicate the sense of shear in non-coaxial deformation, active slip systems and also the temperature of the deformation responsible for the texture. Again, samples are described according to tectono-stratigraphic units and structures from north to south, representing locations north of the Bursa Fault, Bursa Fault, Uludağ Massif, Eskişehir Fault and south of the Eskişehir Fault. Sample locations are all shown in Chapter 3, Figure 3.1.

(a) North of Bursa Fault

The calcite CPO in samples located north of the Bursa Fault show a range from visually weak and disperse (ULD16) to well-ordered and strong (ULD53) (Figure 5.9a). In both ULD55 and ULD53 there are point maxima in both the (c) and the {e} CPO, and more dispersed fabrics in the {r}, {f} poles to planes and {a}-axes. All three slip direction CPO show similar patterns, and ULD55 and ULD53 show girdle fabrics sub-parallel to foliation (XY) (Figure 5.9a).

(b) Bursa Fault

There are three samples located close to, or on, the Bursa Fault; ULD52, ULD38 and ULD49 (Figure 5.9a). All three samples show well-developed point maxima fabrics in the (c) and {e} CPO. The a-axes show a girdle fabric sub-parallel to the XY foliation plane, especially in ULD38. The {r} and {f} CPO appear very distributed. In ULD52 and ULD38 all three slip directions show girdle fabrics sub-parallel to the XY foliation, whereas in ULD49 the CPO are more dispersed.

(c) Uludağ Massif

Close to the Bursa Fault, in the Uludağ Massif the CPO display quite well-ordered fabrics with (c) and {e} CPO point maxima (ULD39, ULD42 and ULD58) (Figure 5.9b). The {a}-

axes fabrics display girdles sub parallel to the XY foliation plane, as do the three slip directions. The {r} and {f} CPO are again, much more dispersed.

Between 1km and 3.5km north of the Eskişehir Fault, within the Uludağ Massif, there is more variation in the CPO. Some samples show well-ordered (c)-axes point maxima (eg ULD127 and ULD124), whilst others are more dispersed (eg UL122, ULD155 and ULD120) (Figure 5.9b,c). The {e} CPO reflect the patterns seen in the (c)-axes. All samples in this part of the massif show quite dispersed {r} and {f} CPO fabrics, and most show dispersion of the {a}-axes also (eg ULD155 and ULD120). Samples ULD127 and ULD124 show girdle fabrics in the a-axes that are sub-parallel to the XY foliation plane (Figure 5.9b,c). Some samples (eg ULD127, ULD152 and ULD124) show girdle fabrics in all three slip directions, others (eg ULD155 and ULD120) show more dispersed CPO (Figure 5.9c,d).

Within 1km of the Eskişehir Fault there is significant variation in the calcite CPO. Samples such as ULD130 and ULD131 show well organised CPO, with (c) and {e} point maxima, and girdle fabrics in the a-axes and the three slip directions (Figure 5.9c,d). Sample ULD157 shows a less well-ordered CPO. Other samples show girdle fabrics in (c) and {e} CPO (eg ULD158, ULD159 and ULD132). In samples ULD158 and ULD157, however, this fabric is quite weak and {r}, {f}, {a} and all three slip directions show distributed fabrics (Figure 5.9d).

(a) Eskişehir Fault

Samples within 100m of, and on, the Eskişehir Fault predominantly show girdle distributions in (c) and {e} CPO (eg ULD133 and ULD137) (Figure 5.9e). All samples have quite dispersed fabrics in {r} and {f} CPO and a girdle sub-parallel to the XZ foliation in the a-axes. In all samples, all three slip directions have girdle fabrics that are, again, sub-parallel to the XZ foliation plane.

(b) South of Eskişehir Fault

There are two samples that are within the South Uludağ Granite, south of the Eskişehir Fault, ULD143 and ULD144 (Figure 5.9f). Both of these samples show strong CPO and in the case of ULD144 an almost single crystal distribution (Figure 5.9f). Both (c) and {e} show strong point maxima sub-parallel to Z, {r} and {f} are more dispersed, and the {a}-axes show a girdle sub-parallel to the XZ foliation plane. All three slip directions show girdle fabrics sub-parallel to the XZ foliation plane.

Figure 5.9a

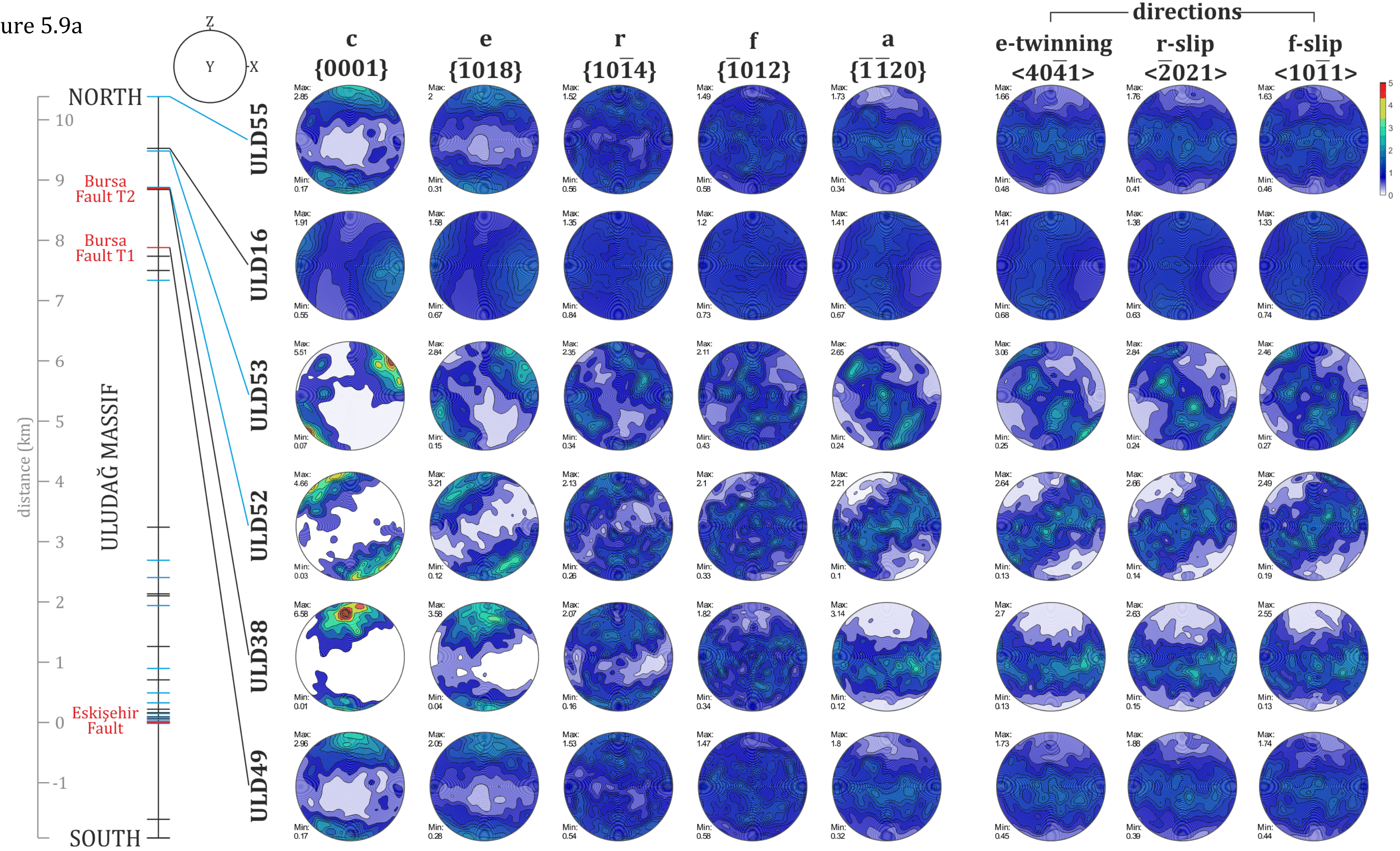
directions
c {0001}
e {$\bar{1}018$}
r {$10\bar{1}4$}
f {$\bar{1}012$}
a {$\bar{1}\bar{1}20$}
e-twinning <$40\bar{4}1$>
r-slip <$\bar{2}021$>
f-slip <$10\bar{1}1$>
Z
Y
X
NORTH
SOUTH
10
9
8
7
6
5
4
3
2
1
0
-1
distance (km)
ULUDAĞ MASSIF
Bursa Fault T2
Bursa Fault T1
Eskişehir Fault
ULD55
ULD16
ULD53
ULD52
ULD38
ULD49
Max: 2.85 Min: 0.17
Max: 2 Min: 0.31
Max: 1.52 Min: 0.56
Max: 1.49 Min: 0.58
Max: 1.73 Min: 0.34
Max: 1.66 Min: 0.48
Max: 1.76 Min: 0.41
Max: 1.63 Min: 0.46
Max: 1.91 Min: 0.55
Max: 1.58 Min: 0.67
Max: 1.35 Min: 0.84
Max: 1.2 Min: 0.73
Max: 1.41 Min: 0.67
Max: 1.41 Min: 0.68
Max: 1.38 Min: 0.63
Max: 1.33 Min: 0.74
Max: 5.51 Min: 0.07
Max: 2.84 Min: 0.15
Max: 2.35 Min: 0.34
Max: 2.11 Min: 0.43
Max: 2.65 Min: 0.24
Max: 3.06 Min: 0.25
Max: 2.84 Min: 0.24
Max: 2.46 Min: 0.27
Max: 4.66 Min: 0.03
Max: 3.21 Min: 0.12
Max: 2.13 Min: 0.26
Max: 2.1 Min: 0.33
Max: 2.21 Min: 0.1
Max: 2.64 Min: 0.13
Max: 2.66 Min: 0.14
Max: 2.49 Min: 0.19
Max: 6.58 Min: 0.01
Max: 3.58 Min: 0.04
Max: 2.07 Min: 0.16
Max: 1.82 Min: 0.34
Max: 3.14 Min: 0.12
Max: 2.7 Min: 0.13
Max: 2.63 Min: 0.15
Max: 2.55 Min: 0.13
Max: 2.96 Min: 0.17
Max: 2.05 Min: 0.28
Max: 1.53 Min: 0.54
Max: 1.47 Min: 0.58
Max: 1.8 Min: 0.32
Max: 1.73 Min: 0.45
Max: 1.88 Min: 0.39
Max: 1.74 Min: 0.44
5
4
3
2
1
0

Figure 5.9b

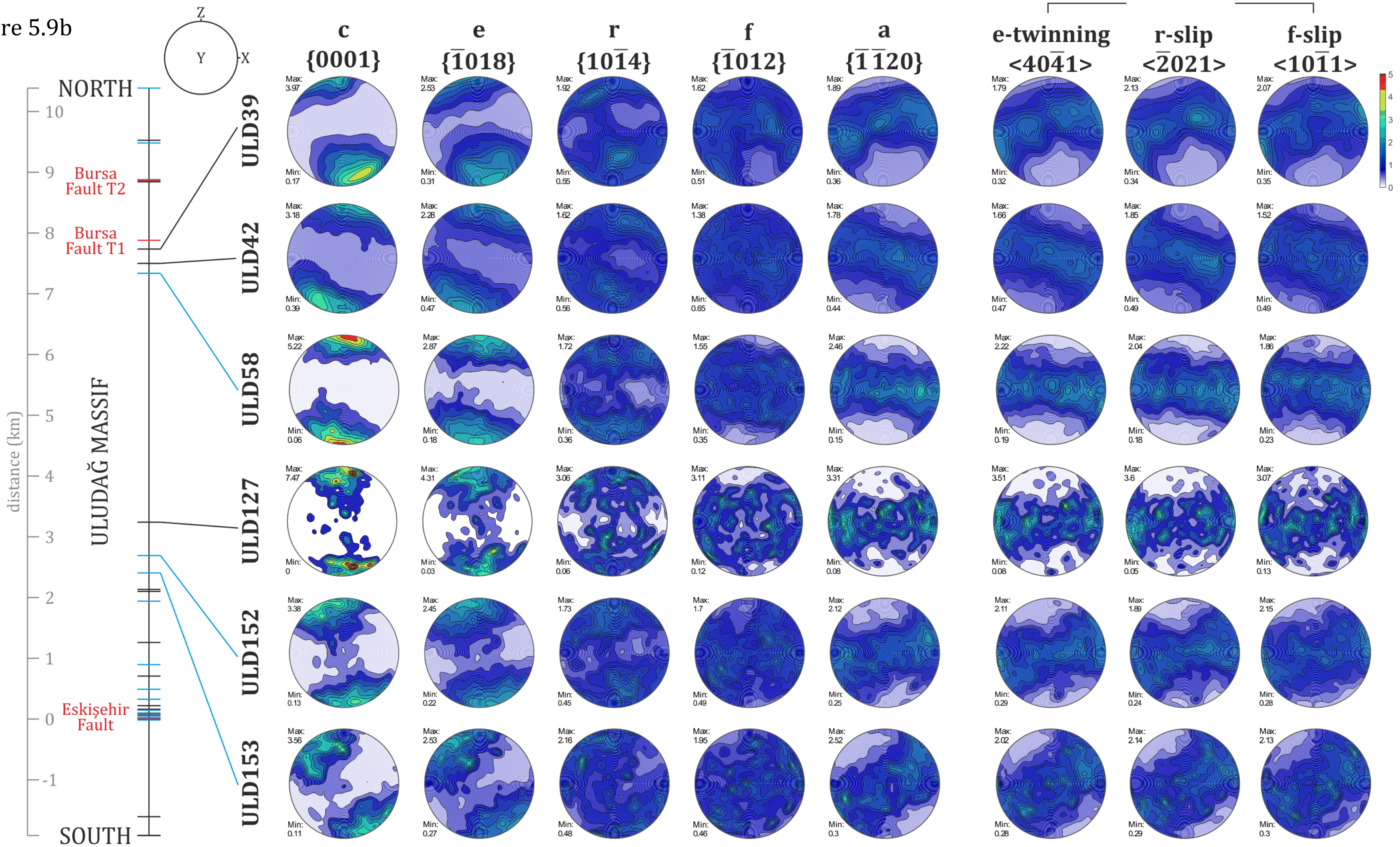
Z
Y
X
NORTH
SOUTH
distance (km)
10
9
8
7
6
5
4
3
2
1
0
-1
Bursa Fault T2
Bursa Fault T1
Eskişehir Fault
ULUDAĞ MASSIF
ULD39
ULD42
ULD58
ULD127
ULD152
ULD153
c {0001}
e {$\bar{1}$018}
r {10$\bar{1}$4}
f {$\bar{1}$012}
a {$\bar{1}\bar{1}$20}
e-twinning <40$\bar{4}$1>
r-slip <$\bar{2}$021>
f-slip <10$\bar{1}$1>
Max: 3.97 Min: 0.17
Max: 2.53 Min: 0.31
Max: 1.92 Min: 0.55
Max: 1.62 Min: 0.51
Max: 1.89 Min: 0.36
Max: 1.79 Min: 0.32
Max: 2.13 Min: 0.34
Max: 2.07 Min: 0.35
Max: 3.18 Min: 0.39
Max: 2.28 Min: 0.47
Max: 1.62 Min: 0.56
Max: 1.38 Min: 0.65
Max: 1.78 Min: 0.44
Max: 1.66 Min: 0.47
Max: 1.85 Min: 0.49
Max: 1.52 Min: 0.49
Max: 5.22 Min: 0.06
Max: 2.87 Min: 0.18
Max: 1.72 Min: 0.36
Max: 1.55 Min: 0.35
Max: 2.46 Min: 0.15
Max: 2.22 Min: 0.19
Max: 2.04 Min: 0.18
Max: 1.86 Min: 0.23
Max: 7.47 Min: 0
Max: 4.31 Min: 0.03
Max: 3.06 Min: 0.06
Max: 3.11 Min: 0.12
Max: 3.31 Min: 0.08
Max: 3.51 Min: 0.08
Max: 3.6 Min: 0.05
Max: 3.07 Min: 0.13
Max: 3.38 Min: 0.13
Max: 2.45 Min: 0.22
Max: 1.73 Min: 0.45
Max: 1.7 Min: 0.49
Max: 2.12 Min: 0.25
Max: 2.11 Min: 0.29
Max: 1.89 Min: 0.24
Max: 2.15 Min: 0.28
Max: 3.56 Min: 0.11
Max: 2.53 Min: 0.27
Max: 2.16 Min: 0.48
Max: 1.95 Min: 0.46
Max: 2.52 Min: 0.3
Max: 2.02 Min: 0.28
Max: 2.14 Min: 0.29
Max: 2.13 Min: 0.3
5
4
3
2
1
0

Figure 5.9c

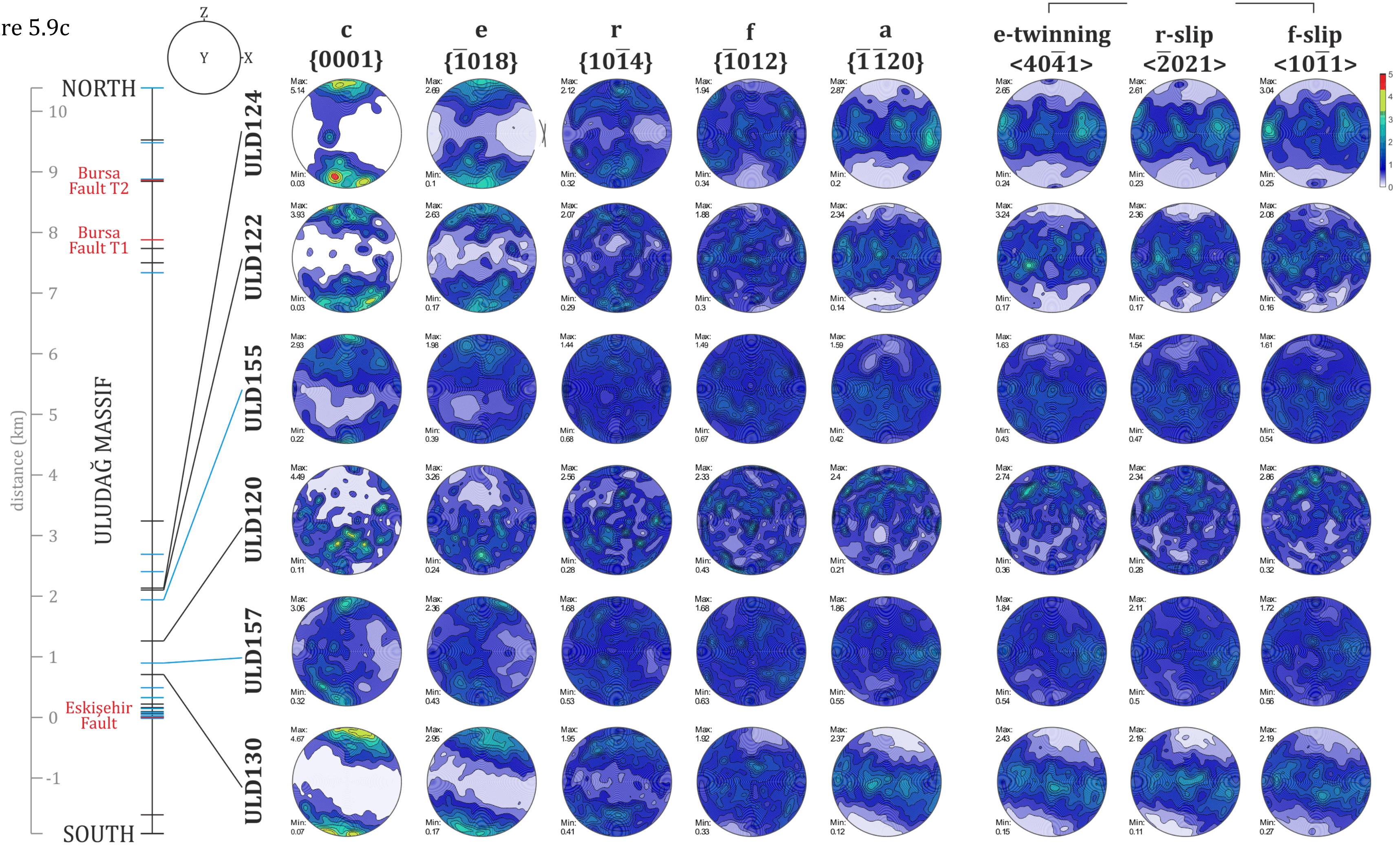
Z
Y
X
NORTH
SOUTH
distance (km)
10
9
8
7
6
5
4
3
2
1
0
-1
Bursa Fault T2
Bursa Fault T1
Eskişehir Fault
ULUDAĞ MASSIF
ULD124
ULD122
ULD155
ULD120
ULD157
ULD130
c $\{0001\}$
e $\{\bar{1}018\}$
r $\{10\bar{1}4\}$
f $\{\bar{1}012\}$
a $\{\bar{1}\bar{1}20\}$
e-twinning $<40\bar{4}1>$
r-slip $<\bar{2}021>$
f-slip $<10\bar{1}1>$
Max: 5.14 Min: 0.03
Max: 2.69 Min: 0.1
Max: 2.12 Min: 0.32
Max: 1.94 Min: 0.34
Max: 2.87 Min: 0.2
Max: 2.65 Min: 0.24
Max: 2.61 Min: 0.23
Max: 3.04 Min: 0.25
Max: 3.93 Min: 0.03
Max: 2.63 Min: 0.17
Max: 2.07 Min: 0.29
Max: 1.88 Min: 0.3
Max: 2.34 Min: 0.14
Max: 3.24 Min: 0.17
Max: 2.36 Min: 0.17
Max: 2.08 Min: 0.16
Max: 2.93 Min: 0.22
Max: 1.98 Min: 0.39
Max: 1.44 Min: 0.68
Max: 1.49 Min: 0.67
Max: 1.59 Min: 0.42
Max: 1.63 Min: 0.43
Max: 1.54 Min: 0.47
Max: 1.61 Min: 0.54
Max: 4.49 Min: 0.11
Max: 3.26 Min: 0.24
Max: 2.56 Min: 0.28
Max: 2.33 Min: 0.43
Max: 2.4 Min: 0.21
Max: 2.74 Min: 0.36
Max: 2.34 Min: 0.28
Max: 2.86 Min: 0.32
Max: 3.06 Min: 0.32
Max: 2.36 Min: 0.43
Max: 1.68 Min: 0.53
Max: 1.68 Min: 0.63
Max: 1.86 Min: 0.55
Max: 1.84 Min: 0.54
Max: 2.11 Min: 0.5
Max: 1.72 Min: 0.56
Max: 4.67 Min: 0.07
Max: 2.95 Min: 0.17
Max: 1.95 Min: 0.41
Max: 1.92 Min: 0.33
Max: 2.37 Min: 0.12
Max: 2.43 Min: 0.15
Max: 2.19 Min: 0.11
Max: 2.19 Min: 0.27
5
4
3
2
1
0

Figure 5.9d

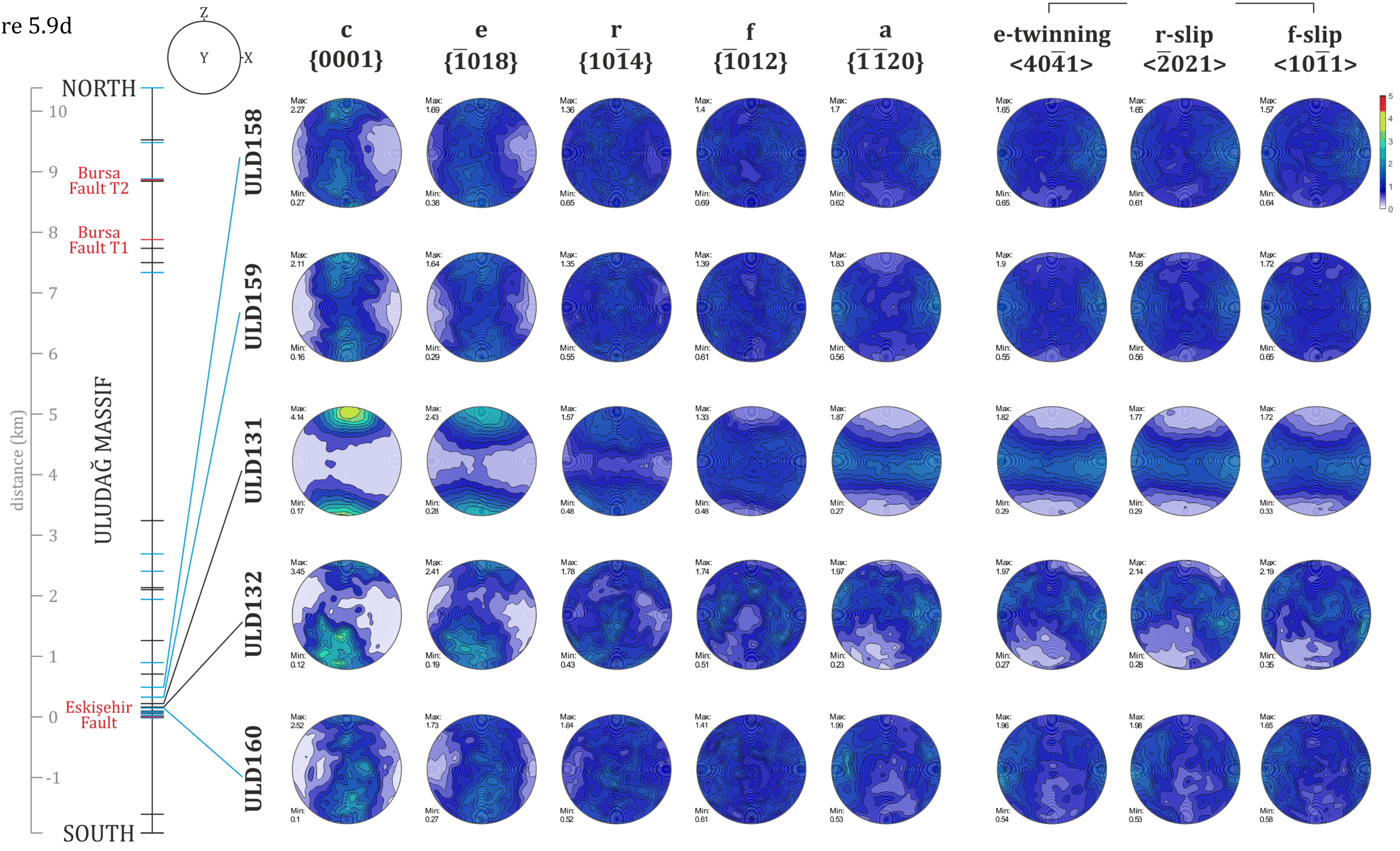
Z
Y
X
NORTH
SOUTH
10
9
8
7
6
5
4
3
2
1
0
-1
distance (km)
ULUDAĞ MASSIF
Bursa Fault T2
Bursa Fault T1
Eskişehir Fault
c {0001}
e {1̄018}
r {101̄4}
f {1̄012}
a {1̄1̄20}
e-twinning <404̄1>
r-slip <2̄021>
f-slip <101̄1>
ULD158
ULD159
ULD131
ULD132
ULD160
Max: 2.27 Min: 0.27
Max: 1.69 Min: 0.38
Max: 1.36 Min: 0.65
Max: 1.4 Min: 0.69
Max: 1.7 Min: 0.62
Max: 1.65 Min: 0.65
Max: 1.65 Min: 0.61
Max: 1.57 Min: 0.64
Max: 2.11 Min: 0.16
Max: 1.64 Min: 0.29
Max: 1.35 Min: 0.55
Max: 1.39 Min: 0.61
Max: 1.83 Min: 0.56
Max: 1.9 Min: 0.55
Max: 1.58 Min: 0.56
Max: 1.72 Min: 0.65
Max: 4.14 Min: 0.17
Max: 2.43 Min: 0.28
Max: 1.57 Min: 0.48
Max: 1.33 Min: 0.48
Max: 1.87 Min: 0.27
Max: 1.82 Min: 0.29
Max: 1.77 Min: 0.29
Max: 1.72 Min: 0.33
Max: 3.45 Min: 0.12
Max: 2.41 Min: 0.19
Max: 1.78 Min: 0.43
Max: 1.74 Min: 0.51
Max: 1.97 Min: 0.23
Max: 1.97 Min: 0.27
Max: 2.14 Min: 0.28
Max: 2.19 Min: 0.35
Max: 2.52 Min: 0.1
Max: 1.73 Min: 0.27
Max: 1.64 Min: 0.52
Max: 1.41 Min: 0.61
Max: 1.99 Min: 0.53
Max: 1.96 Min: 0.54
Max: 1.98 Min: 0.53
Max: 1.65 Min: 0.58
5
4
3
2
1
0

Figure 5.9e

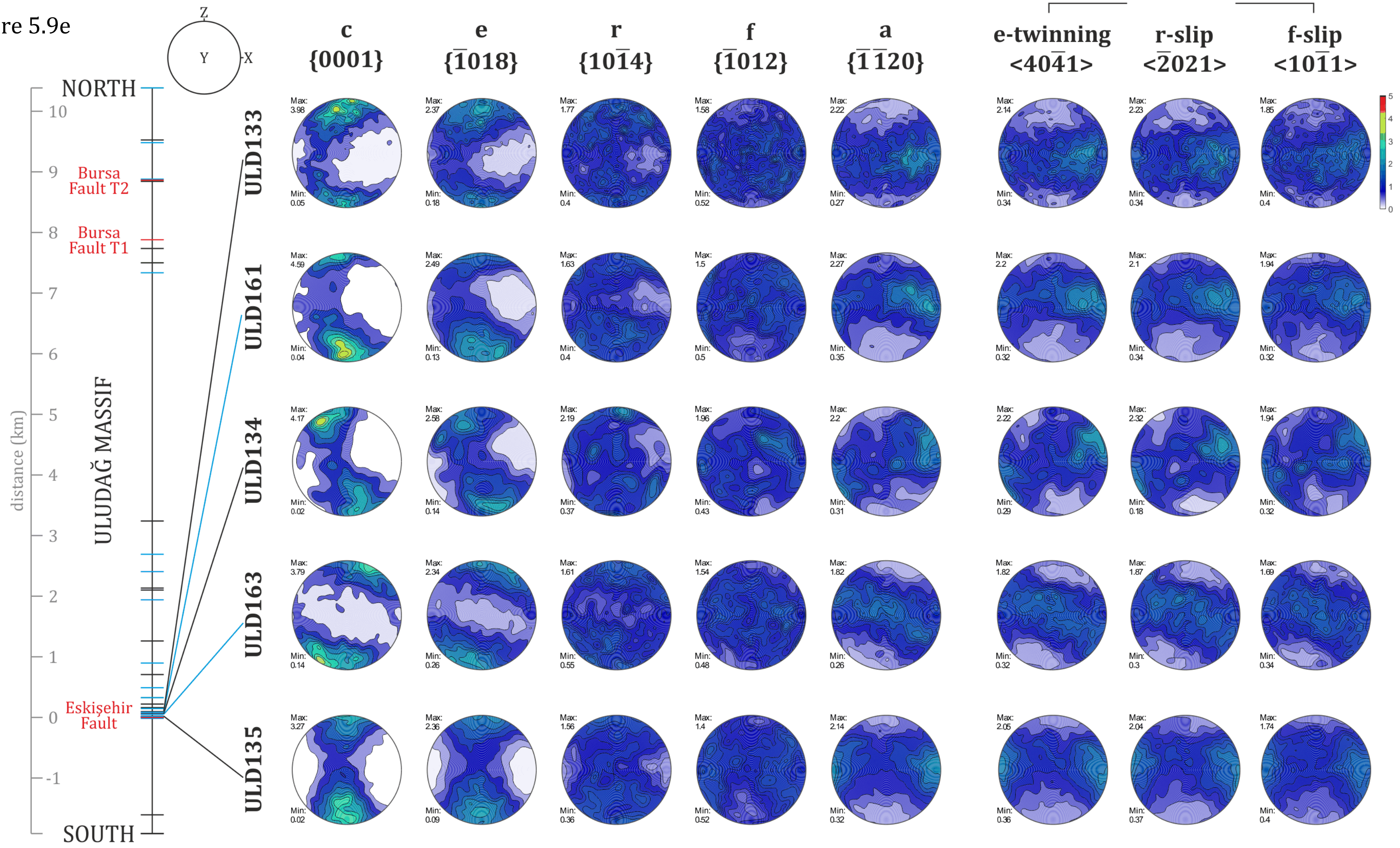
Z
Y
X
NORTH
SOUTH
10
9
8
7
6
5
4
3
2
1
0
-1
distance (km)
ULUDAĞ MASSIF
Bursa Fault T2
Bursa Fault T1
Eskişehir Fault
ULD133
ULD161
ULD134
ULD163
ULD135
c {0001}
e {$\bar{1}$018}
r {10$\bar{1}$4}
f {$\bar{1}$012}
a {$\bar{1}\bar{1}$20}
e-twinning <40$\bar{4}$1>
r-slip <$\bar{2}$021>
f-slip <10$\bar{1}$1>
Max: 3.98 Min: 0.05
Max: 2.37 Min: 0.18
Max: 1.77 Min: 0.4
Max: 1.58 Min: 0.52
Max: 2.22 Min: 0.27
Max: 2.14 Min: 0.34
Max: 2.23 Min: 0.34
Max: 1.85 Min: 0.4
Max: 4.59 Min: 0.04
Max: 2.49 Min: 0.13
Max: 1.63 Min: 0.4
Max: 1.5 Min: 0.5
Max: 2.27 Min: 0.35
Max: 2.2 Min: 0.32
Max: 2.1 Min: 0.34
Max: 1.94 Min: 0.32
Max: 4.17 Min: 0.02
Max: 2.58 Min: 0.14
Max: 2.19 Min: 0.37
Max: 1.96 Min: 0.43
Max: 2.2 Min: 0.31
Max: 2.22 Min: 0.29
Max: 2.32 Min: 0.18
Max: 1.94 Min: 0.32
Max: 3.79 Min: 0.14
Max: 2.34 Min: 0.26
Max: 1.61 Min: 0.55
Max: 1.54 Min: 0.48
Max: 1.82 Min: 0.26
Max: 1.82 Min: 0.32
Max: 1.87 Min: 0.3
Max: 1.69 Min: 0.34
Max: 3.27 Min: 0.02
Max: 2.36 Min: 0.09
Max: 1.56 Min: 0.36
Max: 1.4 Min: 0.52
Max: 2.14 Min: 0.32
Max: 2.05 Min: 0.36
Max: 2.04 Min: 0.37
Max: 1.74 Min: 0.4
5
4
3
2
1
0

Figure 5.9f

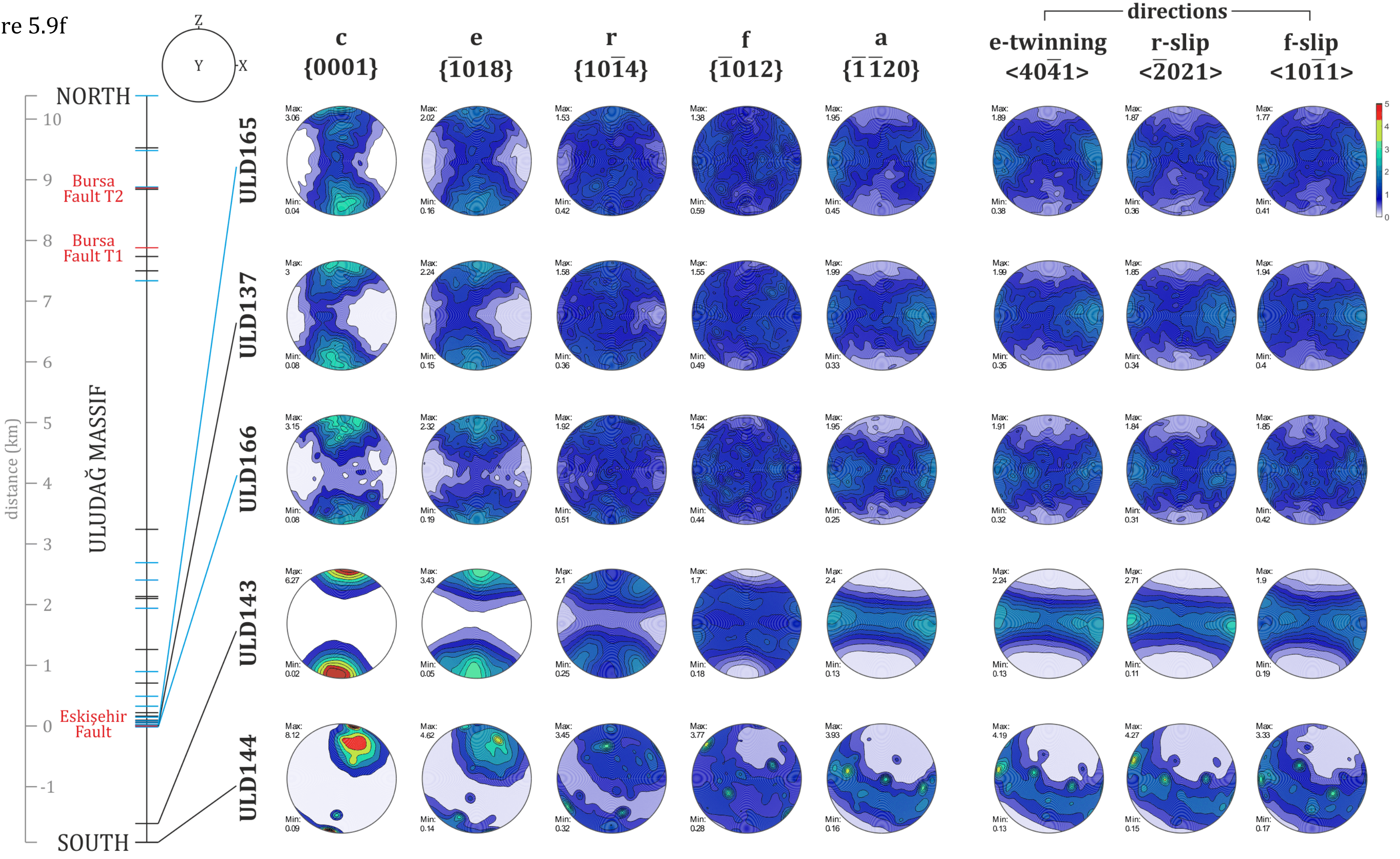
Z
Y
X
NORTH
SOUTH
10
9
8
7
6
5
4
3
2
1
0
-1
distance (km)
ULUDAĞ MASSIF
Bursa Fault T2
Bursa Fault T1
Eskişehir Fault
ULD165
ULD137
ULD166
ULD143
ULD144
c {0001}
e {$\bar{1}018$}
r {$10\bar{1}4$}
f {$\bar{1}012$}
a {$\bar{1}\bar{1}20$}
directions
e-twinning <$40\bar{4}1$>
r-slip <$\bar{2}021$>
f-slip <$10\bar{1}1$>
Max: 3.06 Min: 0.04
Max: 2.02 Min: 0.16
Max: 1.53 Min: 0.42
Max: 1.38 Min: 0.59
Max: 1.95 Min: 0.45
Max: 1.89 Min: 0.38
Max: 1.87 Min: 0.36
Max: 1.77 Min: 0.41
Max: 3 Min: 0.08
Max: 2.24 Min: 0.15
Max: 1.58 Min: 0.36
Max: 1.55 Min: 0.49
Max: 1.99 Min: 0.33
Max: 1.99 Min: 0.35
Max: 1.85 Min: 0.34
Max: 1.94 Min: 0.4
Max: 3.15 Min: 0.08
Max: 2.32 Min: 0.19
Max: 1.92 Min: 0.51
Max: 1.54 Min: 0.44
Max: 1.95 Min: 0.25
Max: 1.91 Min: 0.32
Max: 1.84 Min: 0.31
Max: 1.85 Min: 0.42
Max: 6.27 Min: 0.02
Max: 3.43 Min: 0.05
Max: 2.1 Min: 0.25
Max: 1.7 Min: 0.18
Max: 2.4 Min: 0.13
Max: 2.24 Min: 0.13
Max: 2.71 Min: 0.11
Max: 1.9 Min: 0.19
Max: 8.12 Min: 0.09
Max: 4.62 Min: 0.14
Max: 3.45 Min: 0.32
Max: 3.77 Min: 0.28
Max: 3.93 Min: 0.16
Max: 4.19 Min: 0.13
Max: 4.27 Min: 0.15
Max: 3.33 Min: 0.17
5
4
3
2
1
0

Figure 5.9a-f. Calcite CPO pole figures for samples from transect 1 and 2 (black and blue lines respectively). Distance on the transect is relative to the Eskişehir Fault which is at 0m. The pole figures are plotted in the kinematic XZ plane with X to the east, Z to the north and Y out of plane. Plotted in antipodal equal area projection and contours are of multiples of uniform distribution (m.u.d).

5.3.2. Quartz CPOs

This section presents quartz CPO from quartzo-feldspathic lithologies in the field area (gneiss, granite and phyllite). CPO are shown in Figure 5.10a-d. All samples are plotted in the kinematic (XZ) reference frame, with the inferred transport direction (X) plotted to the east and the normal to foliation (Z) to the north. The (c)- and {a}- axes plus the {m}-, {r}- and {z}- poles to planes have been plotted and are shown in Figure 5.10a-d. Textural analysis of quartz pole figures can indicate the sense of shear in non-coaxial deformation, active slip systems and also the temperature of the deformation that produced the texture (Stipp et al., 2002, Schmid and Casey, 1986). Again, samples are described according to tectono-stratigraphic units and structures from north to south; Uludağ Massif, Eskişehir Fault and south of the Eskişehir Fault. Sample locations are all shown in Chapter 3, Figure 3.1.

(a) Uludağ Massif

In the north of the Uludağ Massif, towards the Bursa Fault the samples show point maxima (c)-axes CPO parallel to Y. Samples ULD43, ULD60 and ULD61 show single crystal CPO distributions (Figure 5.10a).

In the central portion of the Uludağ Massif, between 1km-4km, most of the samples also show (c)-axes maxima parallel to Y (eg ULD150, ULD151 and ULD123). The {a}- axes distributions in these samples are around the periphery of the pole figure, sub-parallel to XZ plane, whilst {r} and {z} in samples ULD128, ULD154 and ULD123 show a cross girdle like distribution (Figure 5.10b). ULD47 exhibits quite a diffuse CPO compared to the other samples (Figure 5.10a).

Towards the Eskişehir Fault, within 1km north, there is only one sample, ULD164, which shows a dispersed CPO (Figure 5.10b). None of the crystallographic directions show any discernable fabric and they all have weak CPO.

(a) Eskişehir Fault

There are two samples from the phyllites from the Eskişehir Fault (other samples did not index well), ULD136 and ULD138 (Figure 5.10b,c). Both samples have weak CPO, although (c)-axes maxima can be discerned sub-parallel to Y and the {a}-axes clusters around the periphery, parallel to the XZ plane. In ULD138, {r} shows a weak cross girdle-like distribution (Figure 5.10c).

Figure 5.10a

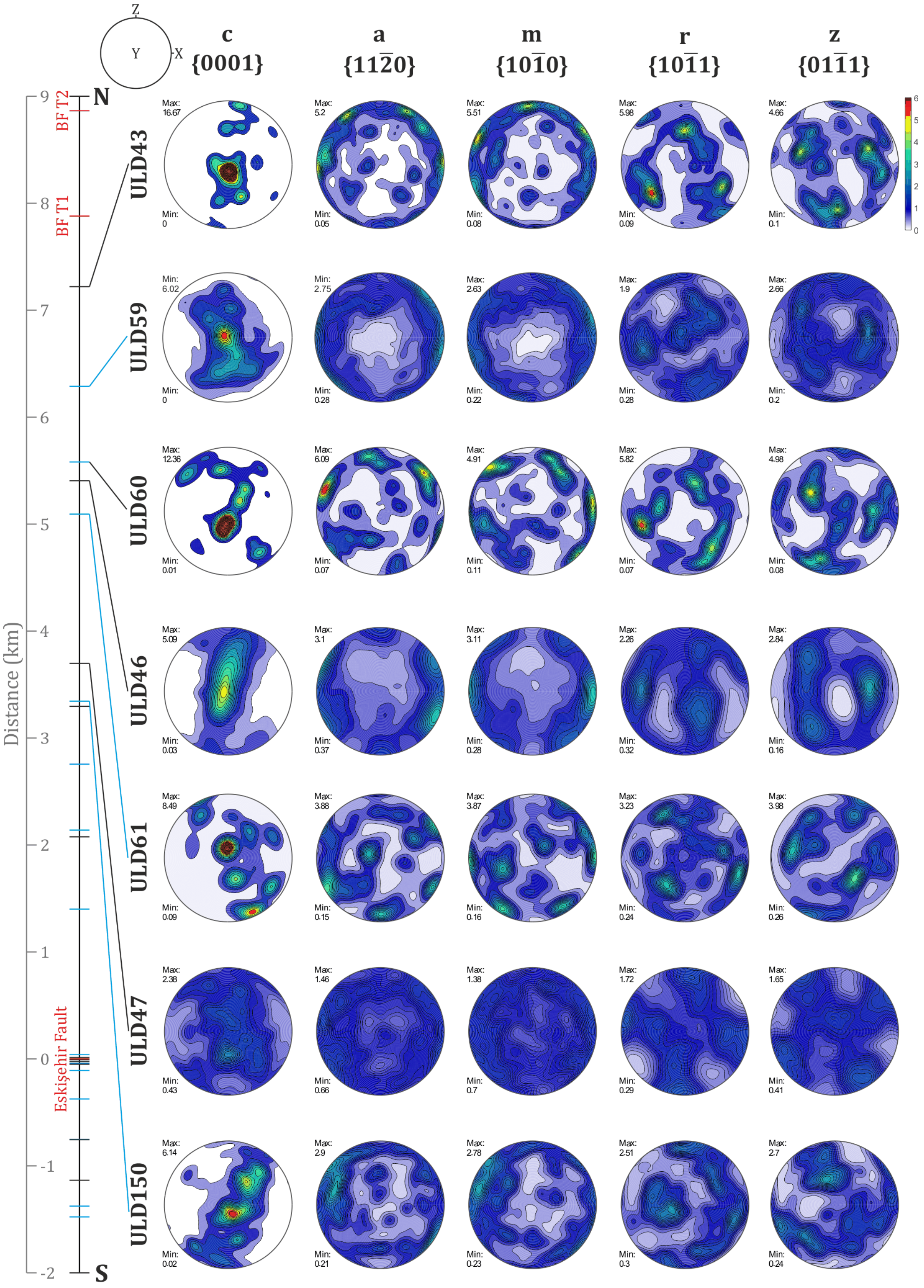
Z
Y
X
c {0001}
a {11$\bar{2}$0}
m {10$\bar{1}$0}
r {10$\bar{1}$1}
z {01$\bar{1}$1}
N
S
9
8
7
6
5
4
3
2
1
0
-1
-2
Distance (km)
BF T2
BF T1
Eskişehir Fault
ULD43
ULD59
ULD60
ULD46
ULD61
ULD47
ULD150
Max: 16.67
Min: 0
Max: 5.2
Min: 0.05
Max: 5.51
Min: 0.08
Max: 5.98
Min: 0.09
Max: 4.66
Min: 0.1
6
5
4
3
2
1
0
Min: 6.02
Min: 0
Min: 2.75
Min: 0.28
Max: 2.63
Min: 0.22
Max: 1.9
Min: 0.28
Max: 2.66
Min: 0.2
Max: 12.36
Min: 0.01
Max: 6.09
Min: 0.07
Max: 4.91
Min: 0.11
Max: 5.82
Min: 0.07
Max: 4.98
Min: 0.08
Max: 5.09
Min: 0.03
Max: 3.1
Min: 0.37
Max: 3.11
Min: 0.28
Max: 2.26
Min: 0.32
Max: 2.84
Min: 0.16
Max: 8.49
Min: 0.09
Max: 3.88
Min: 0.15
Max: 3.87
Min: 0.16
Max: 3.23
Min: 0.24
Max: 3.98
Min: 0.26
Max: 2.38
Min: 0.43
Max: 1.46
Min: 0.66
Max: 1.38
Min: 0.7
Max: 1.72
Min: 0.29
Max: 1.65
Min: 0.41
Max: 6.14
Min: 0.02
Max: 2.9
Min: 0.21
Max: 2.78
Min: 0.23
Max: 2.51
Min: 0.3
Max: 2.7
Min: 0.24

Figure 5.10b

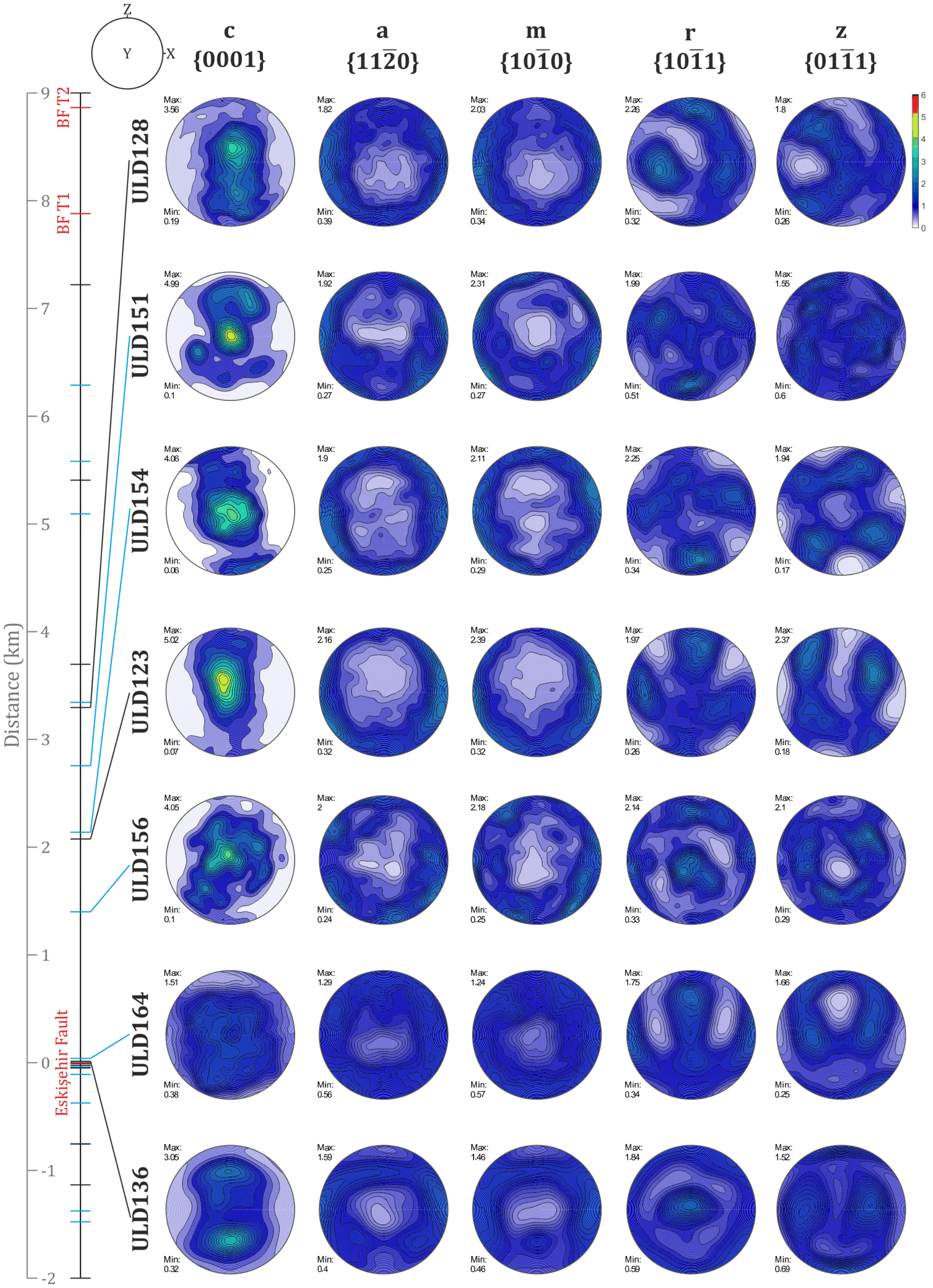
Z
Y
X
c
{0001}
a
$\{11\bar{2}0\}$
m
$\{10\bar{1}0\}$
r
$\{10\bar{1}1\}$
z
$\{01\bar{1}1\}$
6
5
4
3
2
1
0
Distance (km)
9
8
7
6
5
4
3
2
1
0
-1
-2
BF T2
BF T1
Eskişehir Fault
ULD128
Max: 3.56 Min: 0.19
Max: 1.82 Min: 0.39
Max: 2.03 Min: 0.34
Max: 2.26 Min: 0.32
Max: 1.8 Min: 0.26
ULD151
Max: 4.99 Min: 0.1
Max: 1.92 Min: 0.27
Max: 2.31 Min: 0.27
Max: 1.99 Min: 0.51
Max: 1.55 Min: 0.6
ULD154
Max: 4.06 Min: 0.06
Max: 1.9 Min: 0.25
Max: 2.11 Min: 0.29
Max: 2.25 Min: 0.34
Max: 1.94 Min: 0.17
ULD123
Max: 5.02 Min: 0.07
Max: 2.16 Min: 0.32
Max: 2.39 Min: 0.32
Max: 1.97 Min: 0.26
Max: 2.37 Min: 0.18
ULD156
Max: 4.05 Min: 0.1
Max: 2 Min: 0.24
Max: 2.18 Min: 0.25
Max: 2.14 Min: 0.33
Max: 2.1 Min: 0.29
ULD164
Max: 1.51 Min: 0.38
Max: 1.29 Min: 0.56
Max: 1.24 Min: 0.57
Max: 1.75 Min: 0.34
Max: 1.66 Min: 0.25
ULD136
Max: 3.05 Min: 0.32
Max: 1.59 Min: 0.4
Max: 1.46 Min: 0.46
Max: 1.84 Min: 0.59
Max: 1.52 Min: 0.69

Figure 5.10c

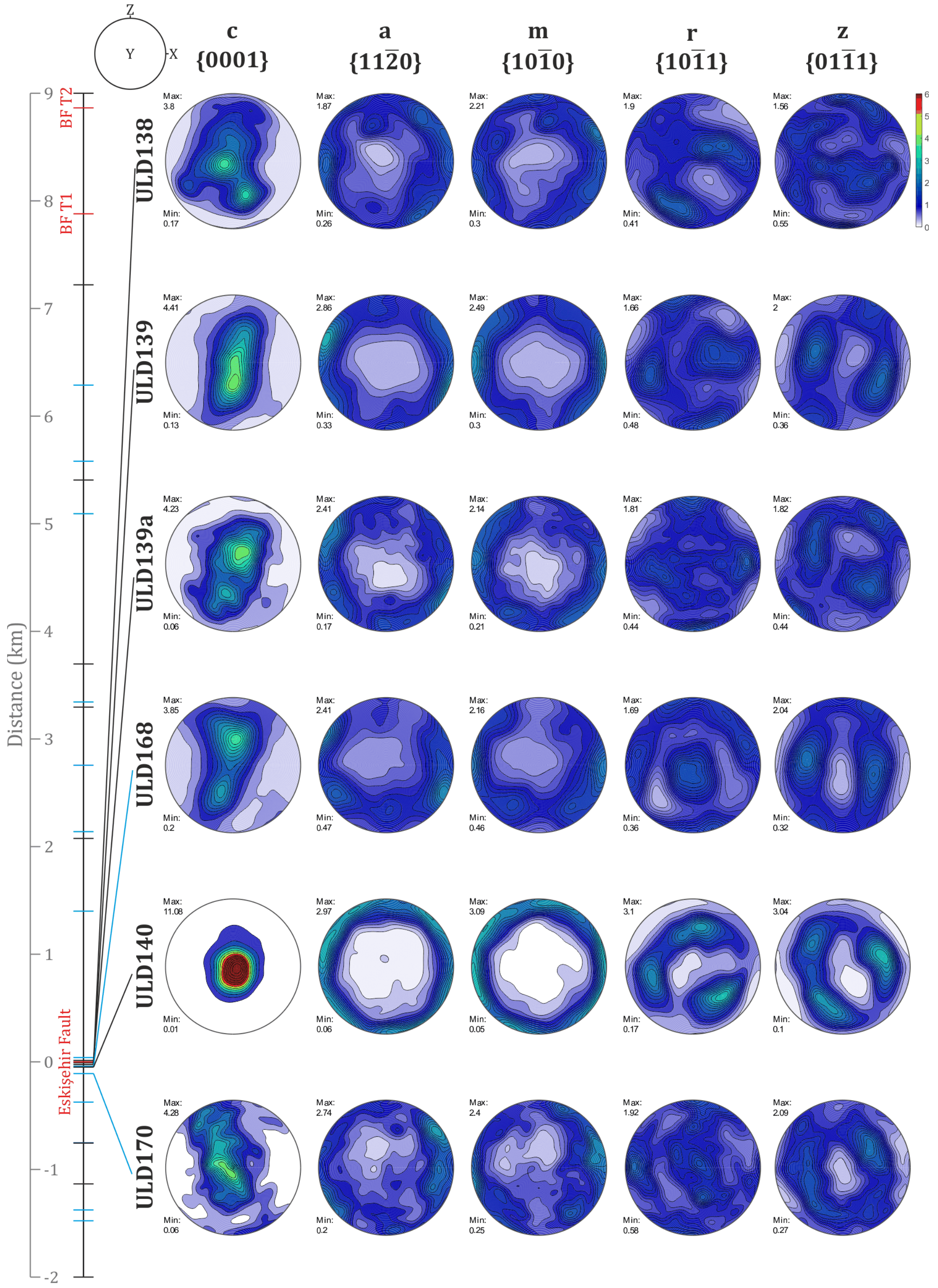
Z
Y
X
c
{0001}
a
$\{11\bar{2}0\}$
m
$\{10\bar{1}0\}$
r
$\{10\bar{1}1\}$
z
$\{01\bar{1}1\}$
ULD138
Max: 3.8
Min: 0.17
Max: 1.87
Min: 0.26
Max: 2.21
Min: 0.3
Max: 1.9
Min: 0.41
Max: 1.56
Min: 0.55
6
5
4
3
2
1
0
ULD139
Max: 4.41
Min: 0.13
Max: 2.86
Min: 0.33
Max: 2.49
Min: 0.3
Max: 1.66
Min: 0.48
Max: 2
Min: 0.36
ULD139a
Max: 4.23
Min: 0.06
Max: 2.41
Min: 0.17
Max: 2.14
Min: 0.21
Max: 1.81
Min: 0.44
Max: 1.82
Min: 0.44
ULD168
Max: 3.85
Min: 0.2
Max: 2.41
Min: 0.47
Max: 2.16
Min: 0.46
Max: 1.69
Min: 0.36
Max: 2.04
Min: 0.32
ULD140
Max: 11.08
Min: 0.01
Max: 2.97
Min: 0.06
Max: 3.09
Min: 0.05
Max: 3.1
Min: 0.17
Max: 3.04
Min: 0.1
ULD170
Max: 4.28
Min: 0.06
Max: 2.74
Min: 0.2
Max: 2.4
Min: 0.25
Max: 1.92
Min: 0.58
Max: 2.09
Min: 0.27
Distance (km)
9
8
7
6
5
4
3
2
1
0
-1
-2
BF T2
BF T1
Eskişehir Fault

Figure 5.10d

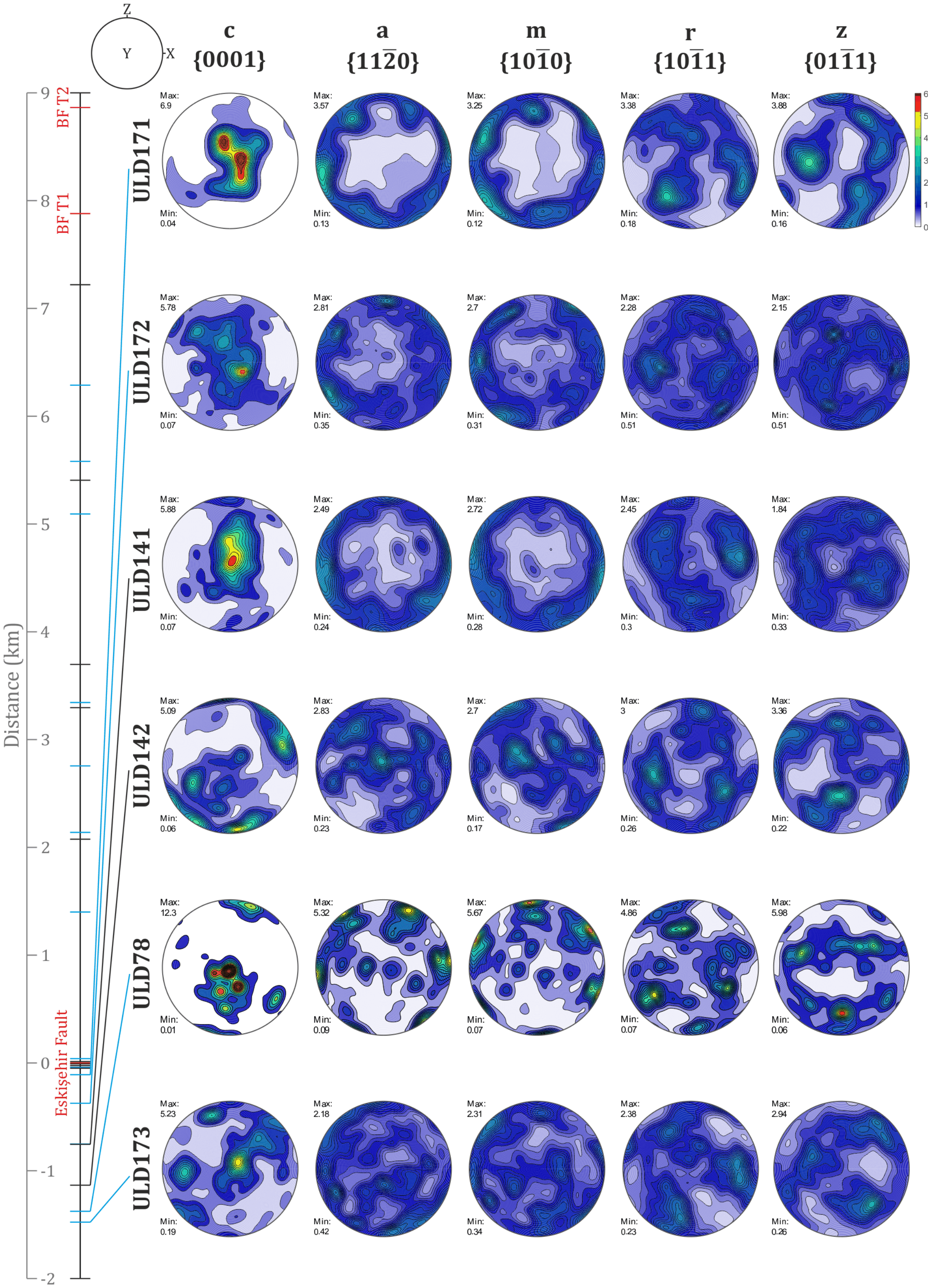
Z
Y
X
c
{0001}
a
{11$\bar{2}$0}
m
{10$\bar{1}$0}
r
{10$\bar{1}$1}
z
{01$\bar{1}$1}
Distance (km)
9
8
7
6
5
4
3
2
1
0
-1
-2
BF T2
BF T1
Eskişehir Fault
ULD171
Max: 6.9
Min: 0.04
Max: 3.57
Min: 0.13
Max: 3.25
Min: 0.12
Max: 3.38
Min: 0.18
Max: 3.88
Min: 0.16
ULD172
Max: 5.78
Min: 0.07
Max: 2.81
Min: 0.35
Max: 2.7
Min: 0.31
Max: 2.28
Min: 0.51
Max: 2.15
Min: 0.51
ULD141
Max: 5.88
Min: 0.07
Max: 2.49
Min: 0.24
Max: 2.72
Min: 0.28
Max: 2.45
Min: 0.3
Max: 1.84
Min: 0.33
ULD142
Max: 5.09
Min: 0.06
Max: 2.83
Min: 0.23
Max: 2.7
Min: 0.17
Max: 3
Min: 0.26
Max: 3.36
Min: 0.22
ULD78
Max: 12.3
Min: 0.01
Max: 5.32
Min: 0.09
Max: 5.67
Min: 0.07
Max: 4.86
Min: 0.07
Max: 5.98
Min: 0.06
ULD173
Max: 5.23
Min: 0.19
Max: 2.18
Min: 0.42
Max: 2.31
Min: 0.34
Max: 2.38
Min: 0.23
Max: 2.94
Min: 0.26
6
5
4
3
2
1
0

Figure 5.10a-d. Quartz CPO pole figures for samples from transect 1 and 2 (black and blue lines respectively). Distance on the transect is relative to the Eskişehir Fault which is at 0m. The pole figures are plotted in the kinematic XZ plane with X to the east, Z to the north and Y out of plane. Plotted in antipodal equal area projection and contours are of multiples of uniform distribution (m.u.d).

(b) South of Eskişehir Fault

All other samples on the transect are south of the Eskişehir Fault, within the South Uludağ Granite. Most of these samples (eg ULD140, ULD171 and ULD141) show strong (c)-axes CPO sub-parallel to Y (Figure 5.10c,d). In these samples, {a}-axes shows maxima around the periphery parallel to the XZ plane, whilst the {r} and {z} have weak cross girdles. Other samples (eg ULD142 and ULD78) have CPO that show single crystal distributions with maxima parallel to the specific axis and pole to plane orientations on Figure 5.5. Samples ULD139(a), ULD168 and ULD170 show weak CPO and more dispersed fabrics (Figure 5.10c).

5.3.3. Schmid Factor

Schmid factor maps have been produced for all calcite samples across the massif (Figure 5.11a-c). For each sample the absolute Schmid factor has been calculated for the e-twin and both r- and f-slip (high or low temperature slip depends on individual temperature of sample) systems along with the Schmid factor maps with an imposed flow stress for the same three slip/twin systems. The flow stresses were obtained from grain size using the flow law of Rutter (1995) (Chapter 4, Section 4.4.2). The CRSS for the slip/twin systems is individual to each sample taken at the temperature from grain size (Covey-Crump and Rutter, 1989). These sample specific stresses and temperatures are shown in Appendix 7A.

The absolute Schmid factor maps, for all samples, show some degree of activity in all slip and twin systems. There are three groups of Schmid factor distribution within the sample, the first where f-slip seems most favourable, the second where both e-twinning and f-slip seem similarly favourable and the thirdly where all three twin/slip systems are almost equally favourable. For the first case (eg ULD52, ULD135 and ULD158) the probability density of Schmid factor graphs clearly show peaks in the f-slip at the highest Schmid factors displaying this slip system as the most favourable (Figure 5.12a-c). In the second case (eg ULD131 and ULD143) the probability density graphs show similar peaks in similar places for both the e-twinning and r-slip systems (Figure 5.12d,e). Finally for the third case, of which only two samples exhibit this pattern; (ULD120 and ULD122), the probability density graphs show similar peaks for all three slip and twin system (eg. ULD120 Figure 5.12f).

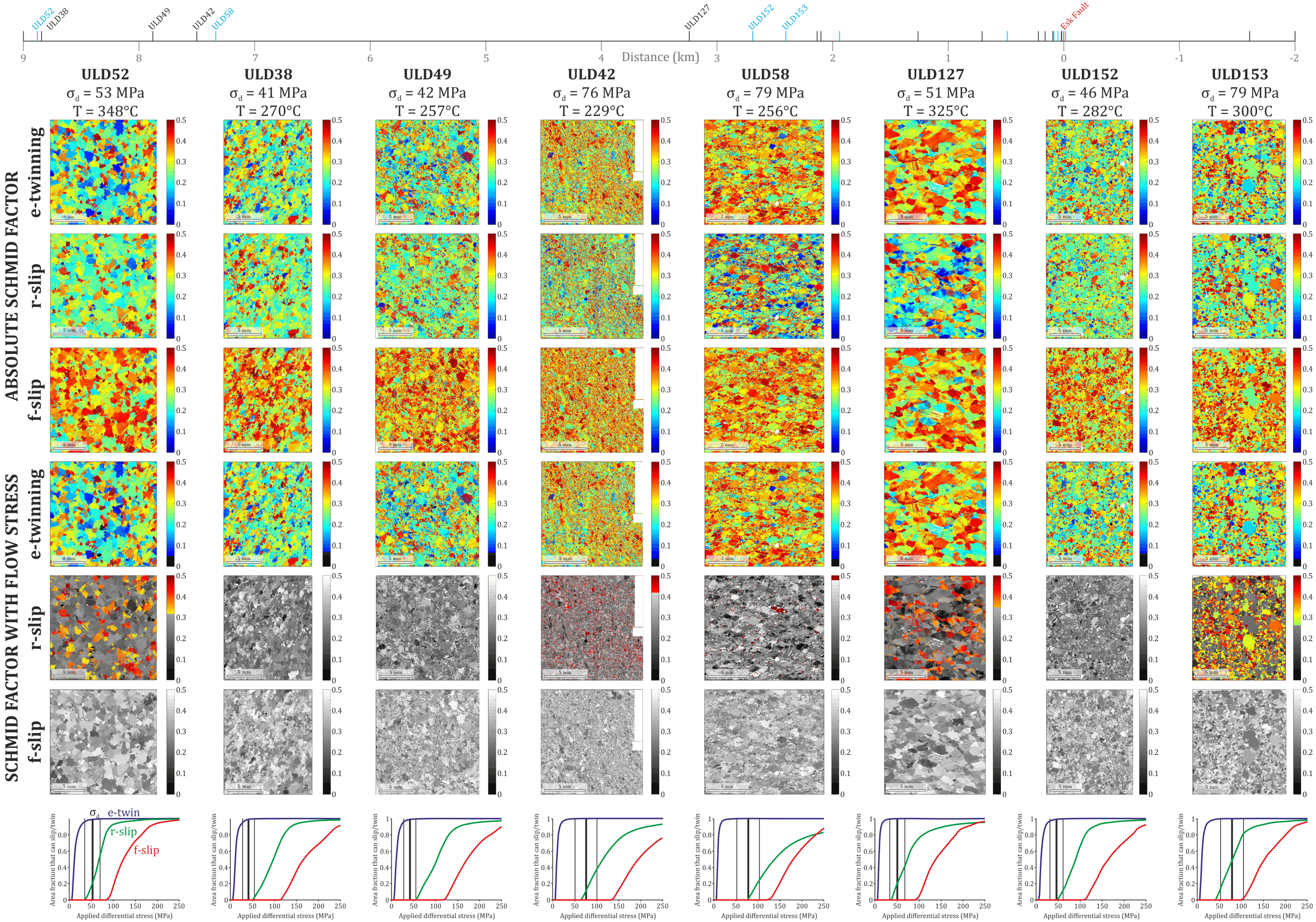
ULD52
ULD38
ULD49
ULD42
ULD58
ULD127
ULD152
ULD153
Esk Fault
9
8
7
6
5
4
Distance (km)
3
2
1
0
-1
-2
ULD52
σ_d = 53 MPa
T = 348°C
ULD38
σ_d = 41 MPa
T = 270°C
ULD49
σ_d = 42 MPa
T = 257°C
ULD42
σ_d = 76 MPa
T = 229°C
ULD58
σ_d = 79 MPa
T = 256°C
ULD127
σ_d = 51 MPa
T = 325°C
ULD152
σ_d = 46 MPa
T = 282°C
ULD153
σ_d = 79 MPa
T = 300°C
ABSOLUTE SCHMID FACTOR
SCHMID FACTOR WITH FLOW STRESS
e-twinning
r-slip
f-slip
5 mm
0
0.1
0.2
0.3
0.4
0.5
σ_d
e-twin
r-slip
f-slip
Area fraction that can slip/twin
Applied differential stress (MPa)
0
50
100
150
200
250
0.2
0.4
0.6
0.8
1

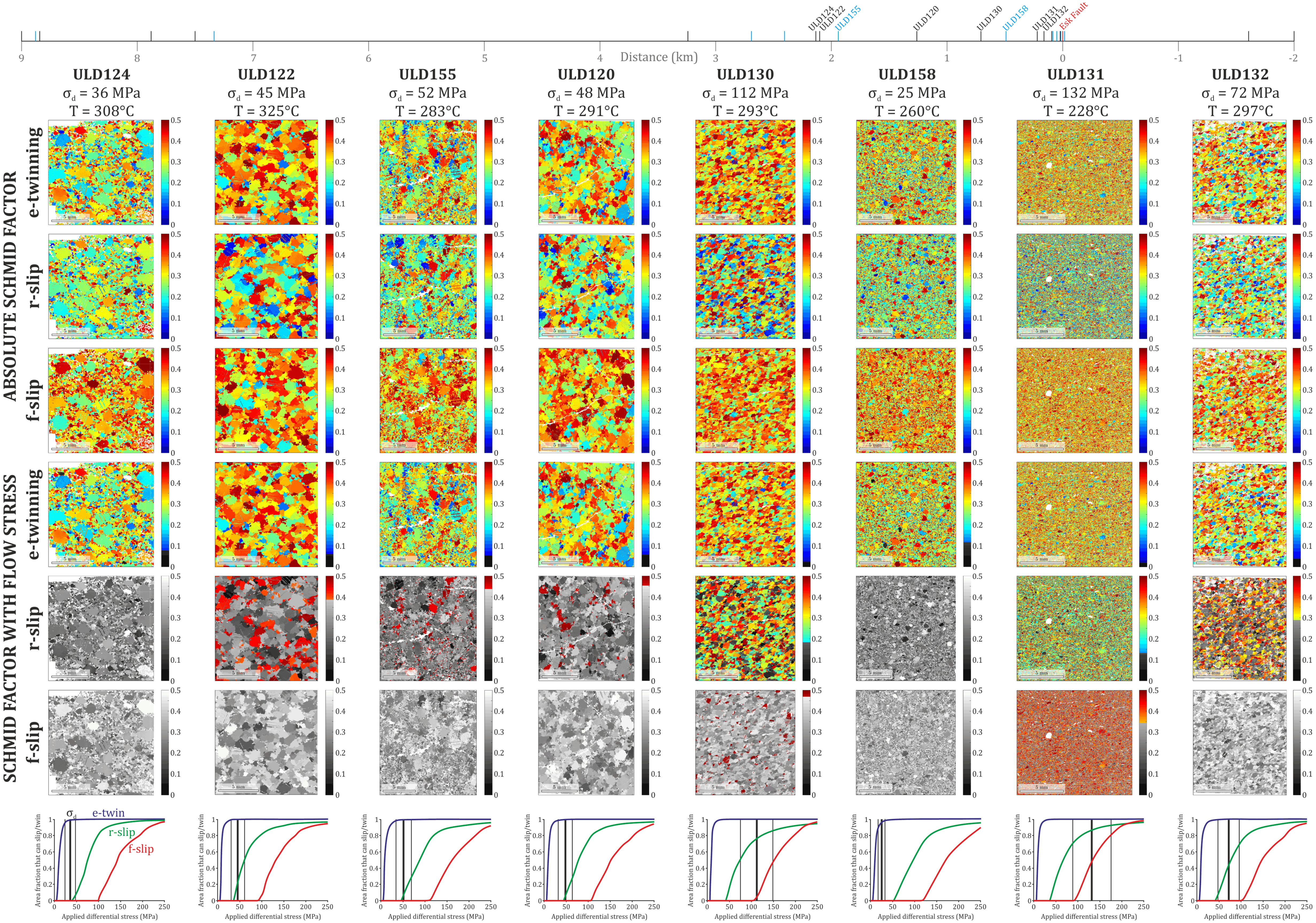
ULD124
ULD122
ULD155
ULD120
ULD130
ULD158
ULD131
ULD132
Esk Fault
9
8
7
6
5
4
Distance (km)
3
2
1
0
-1
-2
ULD124
σd = 36 MPa
T = 308°C
ULD122
σd = 45 MPa
T = 325°C
ULD155
σd = 52 MPa
T = 283°C
ULD120
σd = 48 MPa
T = 291°C
ULD130
σd = 112 MPa
T = 293°C
ULD158
σd = 25 MPa
T = 260°C
ULD131
σd = 132 MPa
T = 228°C
ULD132
σd = 72 MPa
T = 297°C
ABSOLUTE SCHMID FACTOR
SCHMID FACTOR WITH FLOW STRESS
e-twinning
r-slip
f-slip
e-twinning
r-slip
f-slip
0.5
0.4
0.3
0.2
0.1
0
5 mm
σd
e-twin
r-slip
f-slip
Area fraction that can slip/twin
Applied differential stress (MPa)
0
50
100
150
200
250
0.2
0.4
0.6
0.8
1

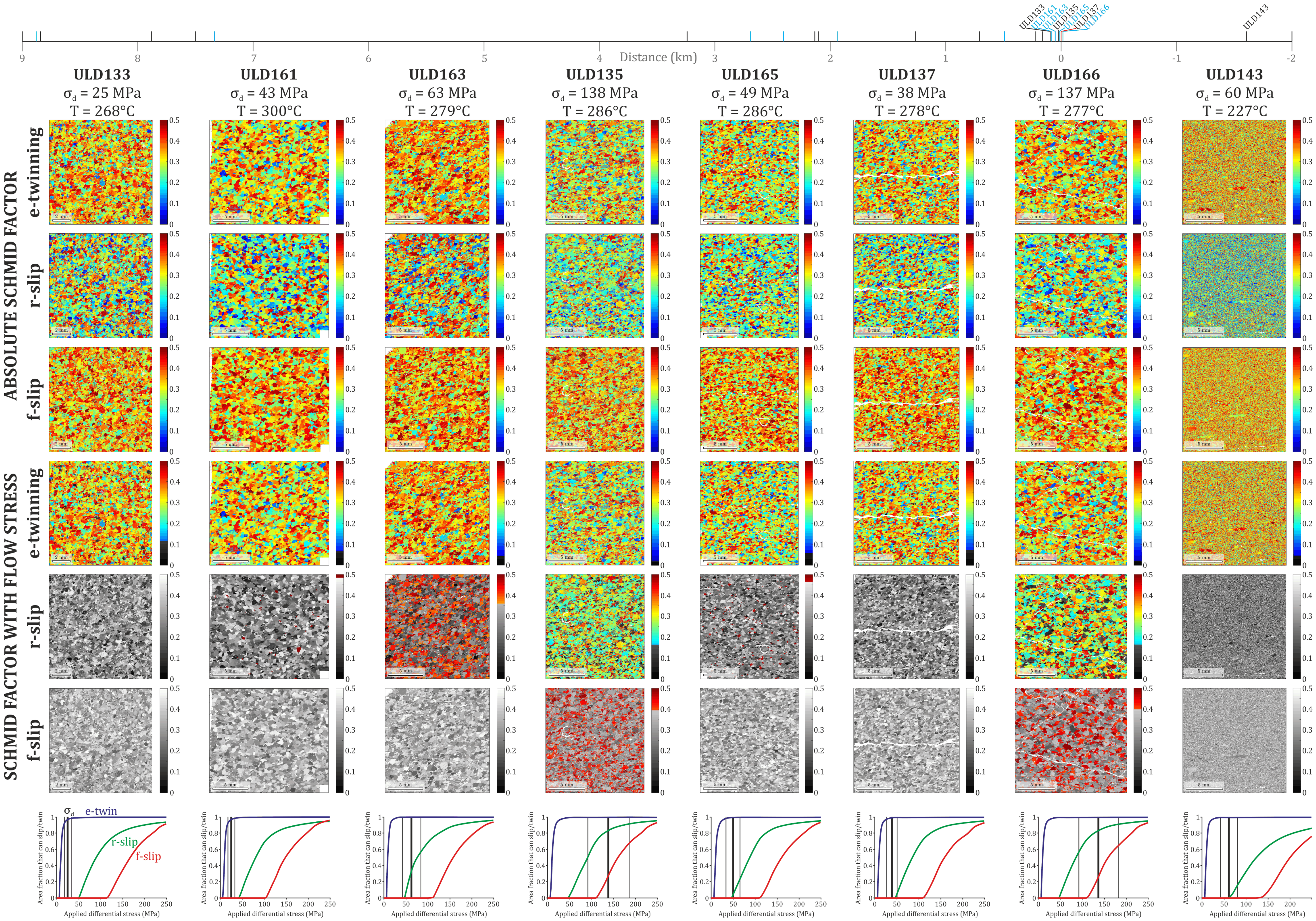
ULD133
ULD161
ULD163
ULD135
ULD165
ULD137
ULD166
ULD143
9
8
7
6
5
4
Distance (km)
3
2
1
0
-1
-2
ULD133
σ_d = 25 MPa
T = 268°C
ULD161
σ_d = 43 MPa
T = 300°C
ULD163
σ_d = 63 MPa
T = 279°C
ULD135
σ_d = 138 MPa
T = 286°C
ULD165
σ_d = 49 MPa
T = 286°C
ULD137
σ_d = 38 MPa
T = 278°C
ULD166
σ_d = 137 MPa
T = 277°C
ULD143
σ_d = 60 MPa
T = 227°C
ABSOLUTE SCHMID FACTOR
e-twinning
r-slip
f-slip
SCHMID FACTOR WITH FLOW STRESS
e-twinning
r-slip
f-slip
0.5
0.4
0.3
0.2
0.1
0
2 mm
5 mm
σ_d
e-twin
r-slip
f-slip
Area fraction that can slip/twin
Applied differential stress (MPa)
0
50
100
150
200
250

Figure 5.11a-c. Absolute Schmid factor and Schmid factor maps with specific flow stress for all calcite samples, distance relative to the Eskisehir Fault at 0km. Samples on transect 1 and 2 in black and blue respectively. a) The samples closest to the Bursa Fault and in the northern section of the massif. b) The samples in the southern section of the massif, closer to the Eskişehir Fault. c) The samples closest to the Eskişehir Fault and to the south, within the South Uludağ Granite.

When a flow stress is applied in the Matlab calculations (code written by David Wallis, Oxford University, 29/09/2016), so that only the grains where the applied stress exceeds the resolved stress on the specific slip or twin system will slip, the responses are completely different. The majority of samples show that e-twinning is active in the majority of grains and at the majority of Schmid factors (Figure 5.11). Samples ULD130, ULD135 and ULD166 also show r-slip is active at a range of Schmid factors (Figure 5.11). Samples such as ULD122 and ULD163 show r-slip activity only in some grains that have the highest Schmid factors (Figure 5.11). The majority of samples, however show no activity in the r-slip system. For f-slip, most samples do not show any activity. Only three samples do, ULD131, ULD135 and ULD166 but only grains with the highest Schmid factors are favourable for slip (Figure 5.11).

Three samples that have varying stress and temperature are shown in Figure 5.13. ULD143 has an average stress for the samples in the shear zone and a low temperature (60MPa, 227°C). At these conditions e-twinning is active. ULD153 also has an average stress but a higher temperature (79MPa, 300°C) and under these conditions both e-twinning and r-slip are active. ULD131 has a high stress and a low temperature (132MPa, 228°C) and all three twin and slip systems are active.

Schmid factor maps were calculated at 300°C (Figure 5.14) and 500°C (Figure 5.15) for the same three samples with their individual stress estimates (Chapter 3, Section 3.5.2). At 300°C low temperature f-slip is active, at 500°C high temperature f-slip is active. At 300°C all samples show some degree of activity in the e-twin and r-slip systems but only sample ULD131 shows activity in the f-slip system (Figure 5.14).

At 500°C there is activity in all of the samples for e-twinning, all three samples show activity for r-slip and only ULD131 shows activity for f-slip (Figure 5.15).

5.1.1. Fabric Strength

Three parameters (*I*, M and J) have been calculated for all samples of calcite and quartz and are both shown in Figure 5.16. The trends for the two minerals are discussed separately. Fabric strength is only applied to the c-axis as application to other directions is complicated by the multiplicity (i.e. 3 a-axes etc).

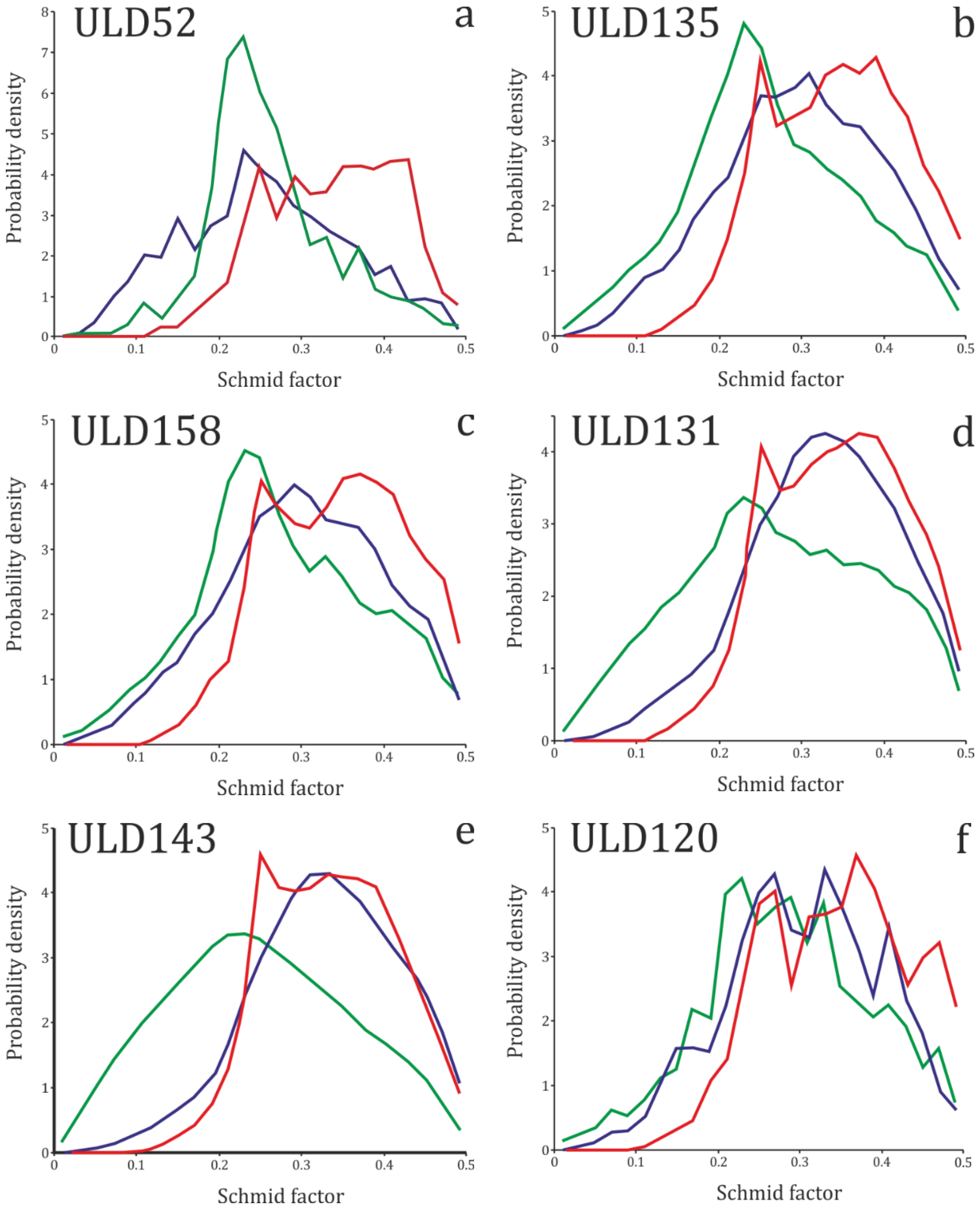

Figure 5.12. Probability density vs Schmid factor graphs for calcite samples in the Uludağ massif. For all graphs e-twinning is in blue, r-slip is in green and f-slip is in red. a) ULD52. b) ULD135. c) ULD158. d) ULD131. e) ULD143. f) ULD120.

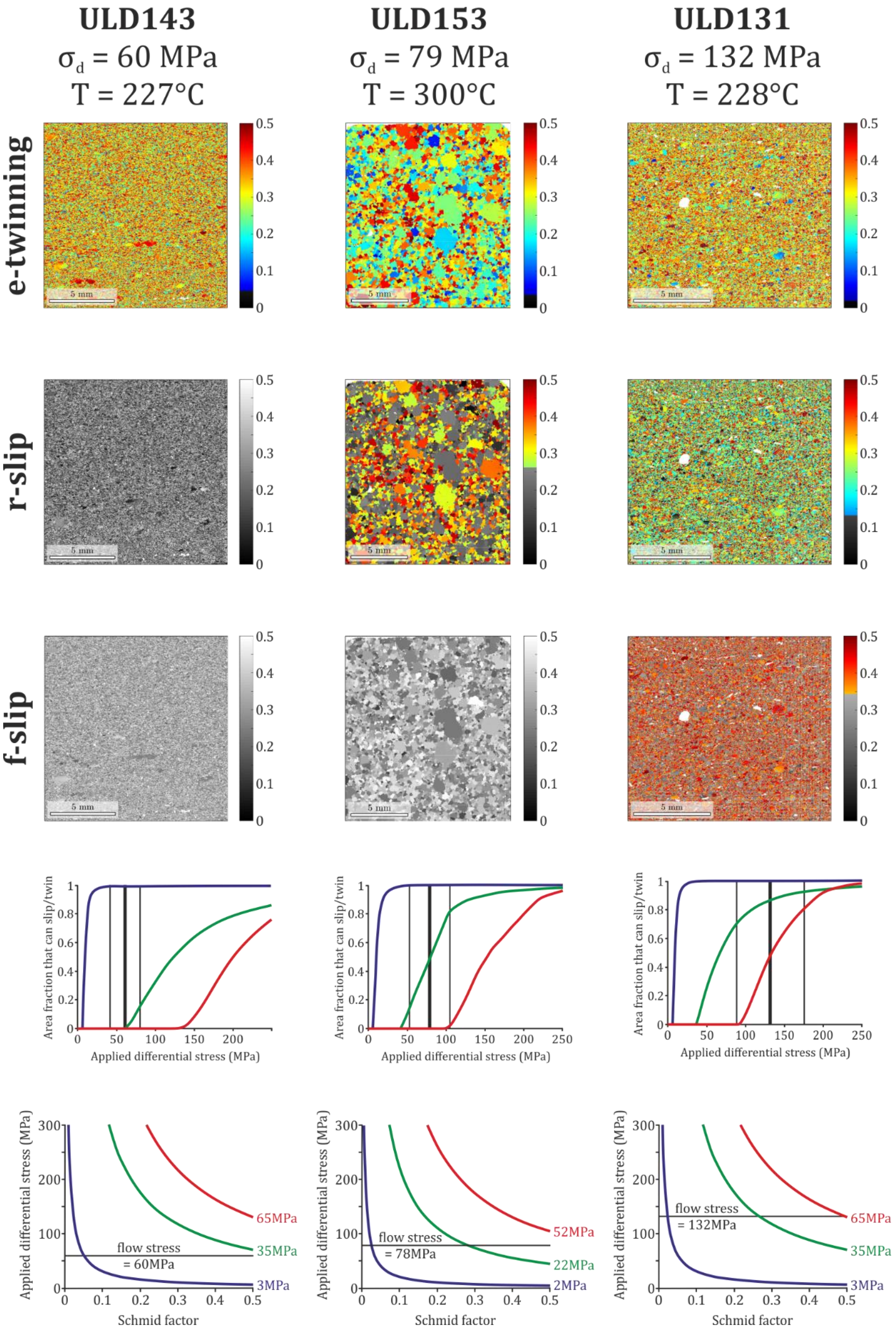

Figure 5.13. Schmid factor maps for selected samples. Maps for e-twinning, r- and f-slip are shown with an imposed flow stress for each sample. The graphs display the effect of stress on the activation of twin/slip systems.

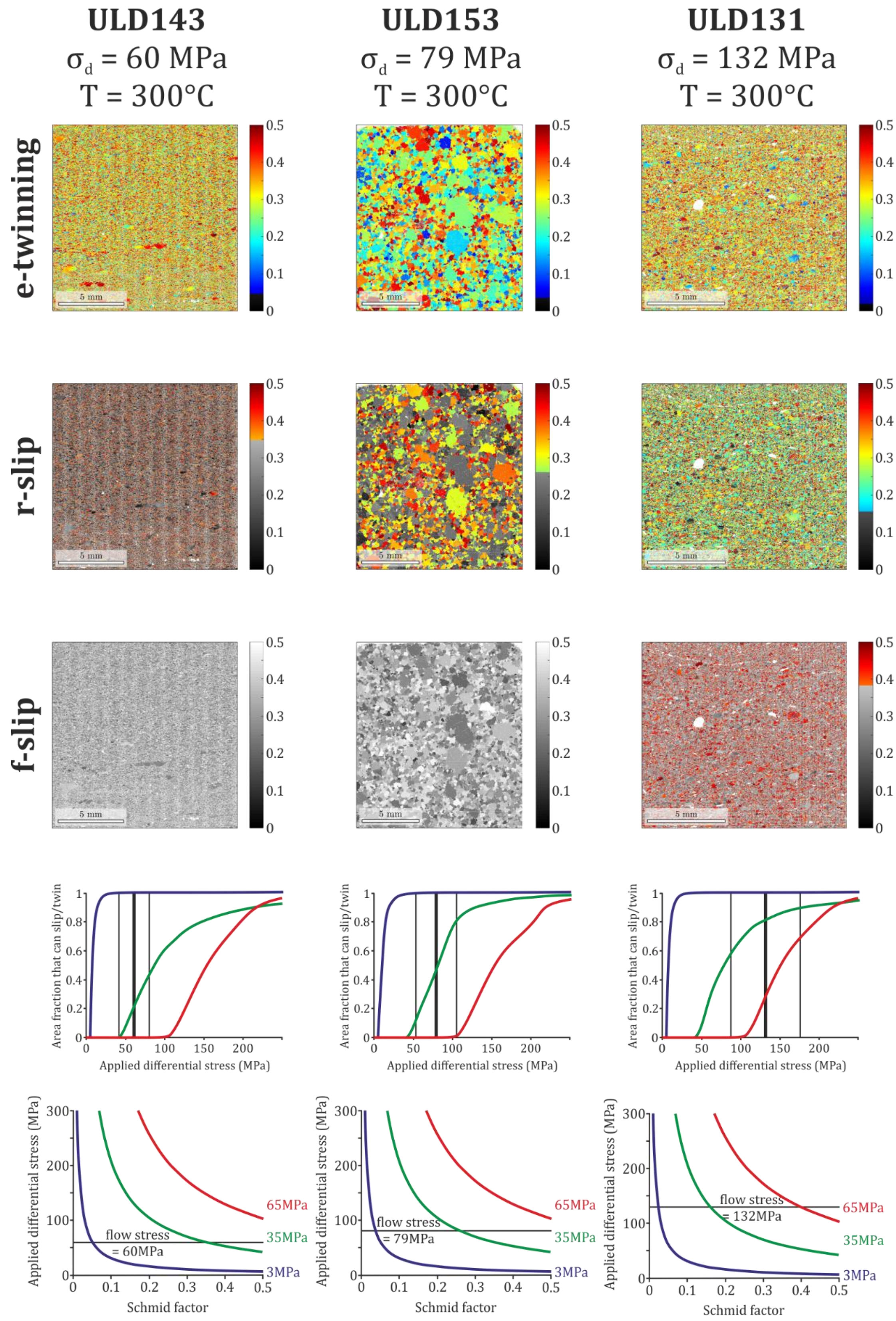

Figure 5.14. e-twin, r- and f-slip Schmid factor maps for the same three samples as in Figure 5.13 but at 300°C and the same individual stresses. Again, the graphs display the effect of stress on the activation of twin/slip systems.

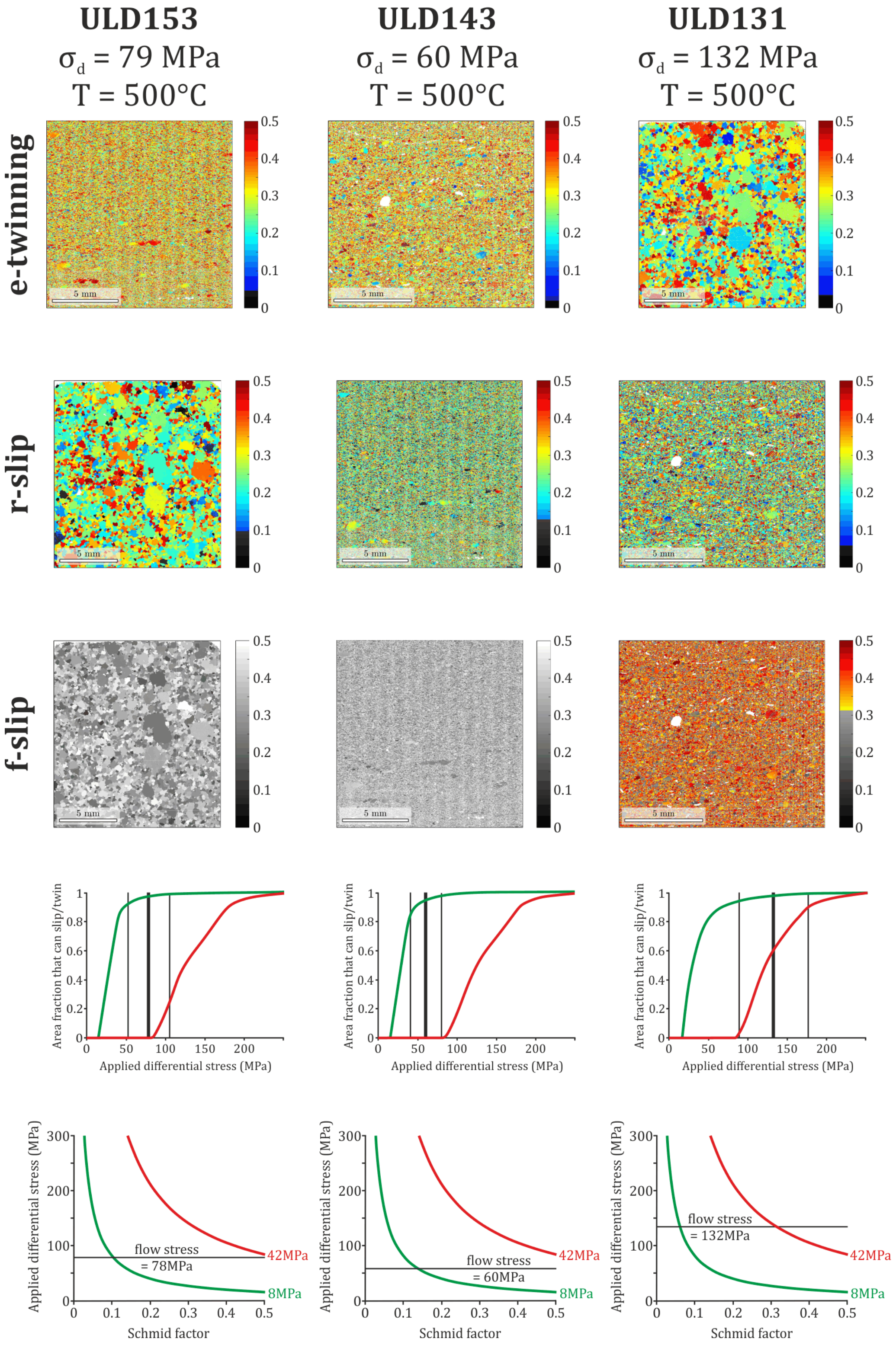

Figure 5.15. e-twin, r- and f-slip Schmid factor maps for the same three samples as in Figure 5.13 but at a higher temperature, 500°C and the same individual stresses. Again, the graphs display the effect of stress on the activation of twin/slip systems.

(a) Calcite

All three measures of CPO fabric intensity show similar patterns across the massif (Figure 5.16a). The overall trend starts quite high with the two samples in the south, within the South Uludağ Granite, reducing at the Eskişehir Fault. North of the Eskişehir Fault, in the Uludağ Massif, the trend shows the three fabric strength parameters decreasing, before increasing again at ~2km. The values at the Bursa Fault are relatively high compared to the rest of the samples.

On the Eskişehir Fault there is quite a wide range of values within the results for the J and M strength parameters; from ~1.5-2 and ~07-1 respectively. The intensity (*I*) parameter on the other hand does not vary as much, with values of approximately 0.6. Again, there is considerable variation in the north, towards the Bursa Fault.

(b) Quartz

All three parameters are plotted in Figure 5.16. They all show similar patterns across the Eskişehir Fault and Uludağ Massif. The general trend begins in the South Uludağ Granite with a mid-range value, and steadily increases towards the Eskişehir Fault with the sample at ~-0.65km. The values on, and close to, the Eskişehir Fault show considerable variation. In each of the three parameters the values on the fault range from the lowest (ULD164: *I*-0.07, J-1.29 and M-0.01) to the highest (ULD140: *I*-2.28, J-5.41 and M-0.3241) seen in the dataset. North of the fault the general trend rises steadily towards the Bursa Fault.

5.1.2. VPSC

The VPSC simulation was run for calcite only, with relative CRSS at 300°C, the lower temperature bound for the Uludağ Massif and shear zone (Chapter 4, Section 4.4.1) (Figure 5.4). Only calcite was used for this simulations as there is a lot of experimental data constraining the contribution of slip systems at different temperatures, based on their CRSS (Figure 5.4) (De Bresser and Spiers, 1997). The intensity, J-index and M-index values were calculated from the Euler angles at strain increments of 0.2 up to a total shear strain (γ) of 6, using Mtex-4.0.23 (Bachmann et al., 2010b). These values were used to create the calibration curves in Figure 5.17. From these the shear strain for each sample of calcite can be obtained using the individual *I*, J and M parameters from Section 4.3.4.

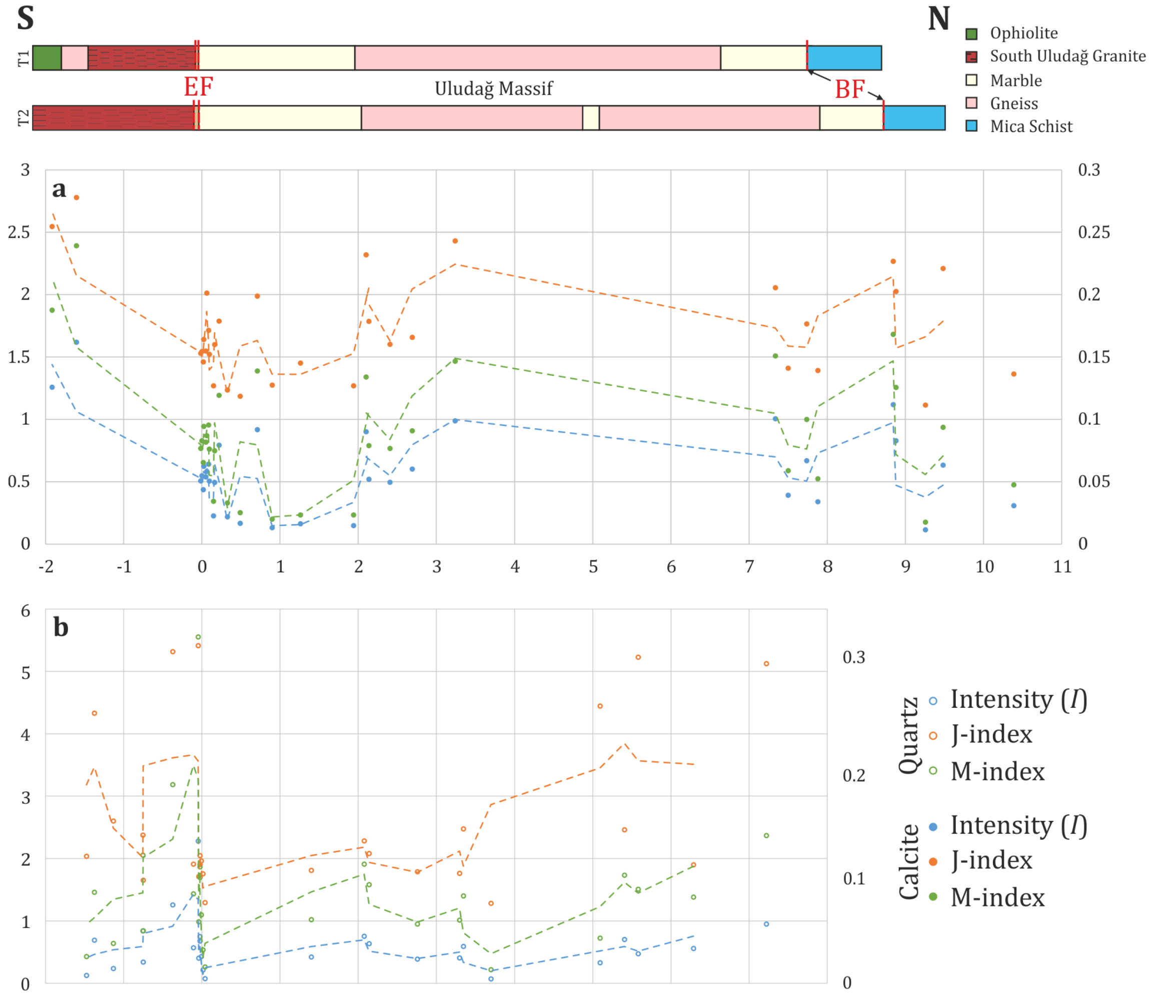

Figure 5.16. (a) All calcite c-axis CPO fabric strengths. (b) All quartz c-axis CPO fabric strengths (Lisle, 1985, Bunge, 1982, Skemer et al., 2005). Due to the small values of the M-index, they are plotted on a different vertical scale on the right hand side for each graph. Trend lines for all data sets are 2 period moving averages. On the lithology transect at the top EF is the Eskişehir Fault and BF is the Bursa Fault. Distance along the x-axis is in kilometres relative to the Eskişehir Fault which is at 0m.

The initial subsample was obtained from sample ULD16, which is north of the Bursa Fault, outside of the shear zone (Chapter 3, Figure 3.1). The choice of this sample is explained in the discussion, Section 5.4.4.

The values of shear strain from each sample are shown on Figure 5.18. An arbitrary value of γ = 0.2 was used to differentiate between deformed and undeformed (justification in Section 5.4.4). Using this value deformed and undeformed sections of the massif can be recognised. The Eskişehir Fault shows up as deformed along with strands within the South Uludağ Granite and the central massif. Close to the Bursa Fault there are also some sections that show up as deformed from the CPO fabric and VPSC analysis.

5.2. Discussion

What follows is a discussion of the results and evidence for active slip systems and temperature from CPO and Schmid Factor analysis and fabric strength, which is calibrated for shear strain via VPSC simulation.

5.2.1. Active slip systems and deformation temperature

The calcite CPO for marble samples are shown in Figure 5.9a-f. The majority of the samples show (c)-axis point maxima sub-parallel to the kinematic Z-axis, with some (eg. ULD133, ULD134, ULD135 and ULD137) showing girdle-like distributions (Figure 5.9e,f). The girdle fabrics become better developed within ~3km of the Eskişhir Fault, for example ULD157, ULD158, ULD132 and ULD160 (Figure 5.9c.d). Other samples (eg ULD120), show a dispersed and even toward random (c)-axis fabrics. The strongest (c)-axis fabrics are found to the south of the Eskişehir Fault.

From the pole figures it is evident that most of the samples have experienced a combination of all of the slip systems during deformation. In most of the samples the (c), {e}, {r} and {f} planes are aligned with the shear plane and the {a} poles to planes and <e>, <r> and <f> directions are all aligned with the direction of shear (i.e. have maxima sub-parallel to the transport (Z) direction) (Pieri et al., 2001b). This suggests all of the slip systems have been active at some point over the deformation history and have contributed to the final CPO. Twinning is the most prevalent, often showing strong point maxima on the {e}-axis CPO and well-developed girdle fabrics in the e-twinning direction (eg. ULD124 and ULD131). This is due to the low CRSS required from activation of e-twinning (Figure 5.4). Most samples also show a degree of slip on {r}- and {f}- planes as well (eg. ULD38, ULD58, ULD133-135, ULD137 and ULD143. These systems are indicated by point maxima sub parallel to Z in the {e}-, {r}- and {f}-axes CPO, and girdles sub-parallel to the XY foliation plane in the e-twinning and the two r- and f-slip directions (Figure 5.9a-f) (Pieri et al., 2001b).

In some samples (eg ULD134, ULD135, ULD165 and ULD143) the {a}-axes show a distributed girdle in the XY foliation plane with maxima in the X direction, indicating that some slip on the (c)<a> was active during deformation (Romeo et al., 2007). Sample ULD144, and ULD127 to a lesser extent, show a monoclinic CPO; the {r}-, {f}- and {a}-axes all show three distinct maxima distributed around the c-axis according to the trigonal symmetry of calcite. Again, the most suitable slip system in this case is (c)<a> which indicates temperatures of >500°C (Romeo et al., 2007).

From the microstructural evidence in Chapter 3, Section 3.4.1, it is clear that the majority of samples within, and outside of, the massif have some degree of twinning (giving temperatures of ~300°C).

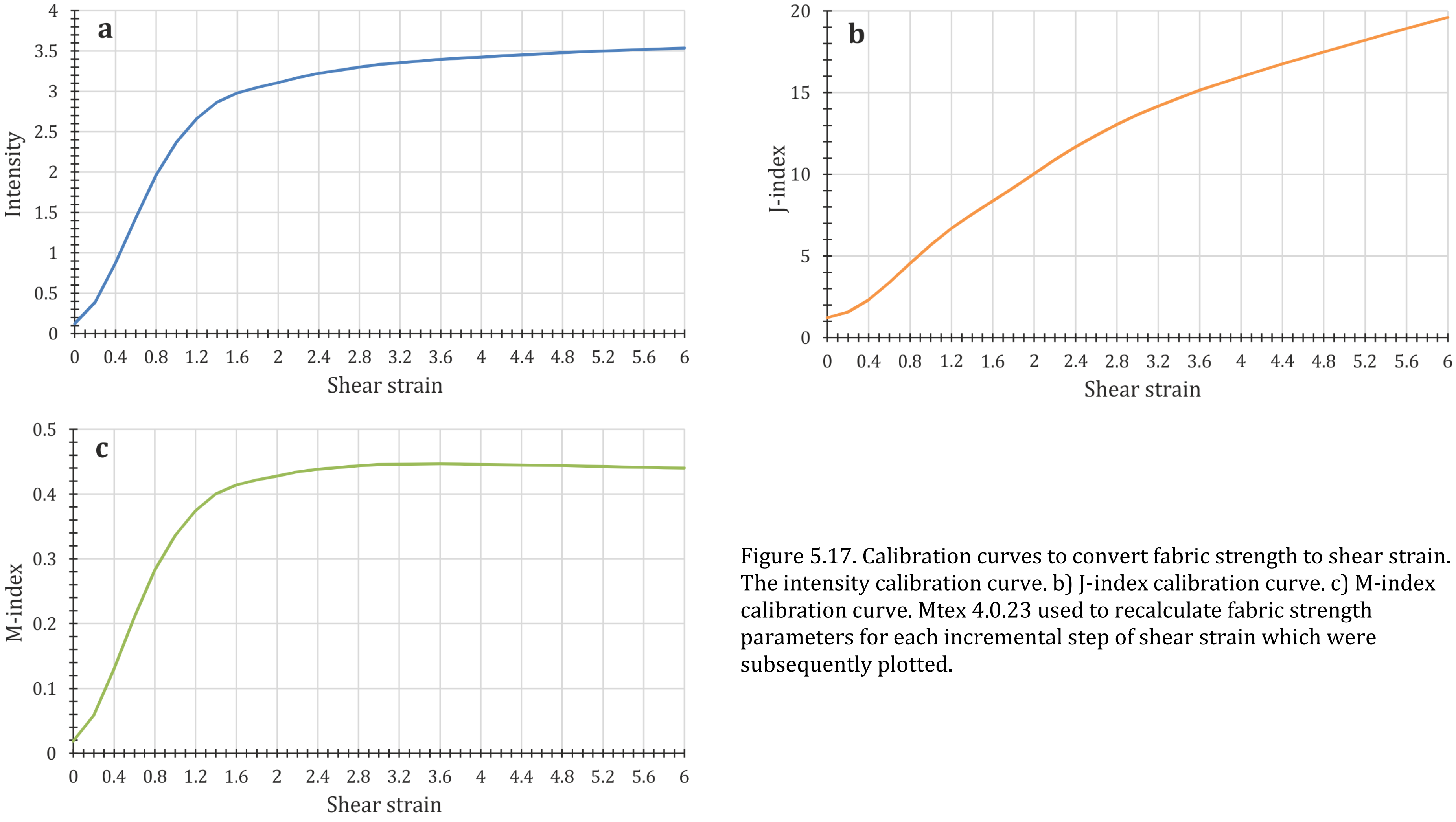

Figure 5.17. Calibration curves to convert fabric strength to shear strain. a) The intensity calibration curve. b) J-index calibration curve. c) M-index calibration curve. Mtex 4.0.23 used to recalculate fabric strength parameters for each incremental step of shear strain which were subsequently plotted.

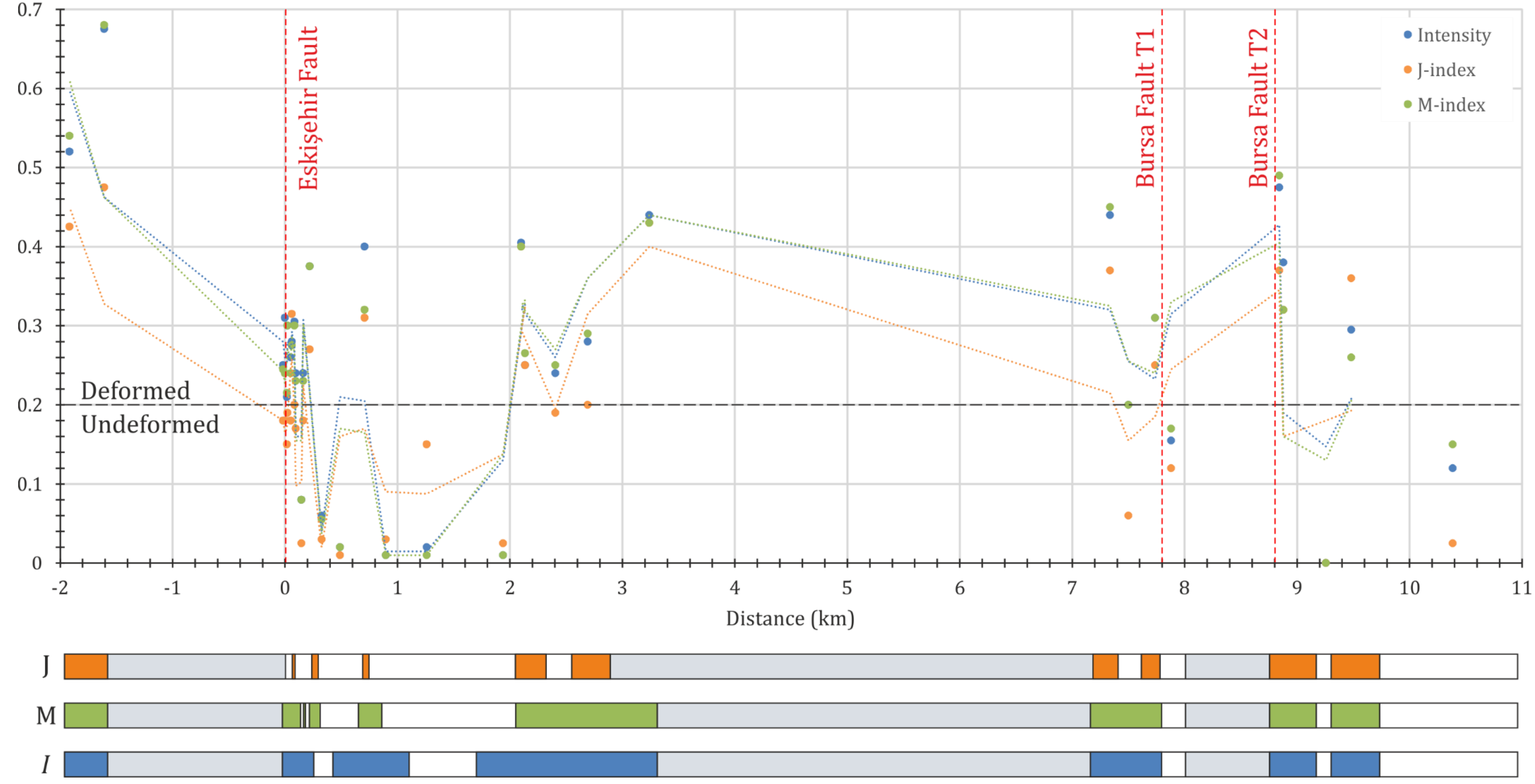

Figure 5.18. Shear strain across the Uludağ massif. Orange is J-index, green is M-index and blue is intensity. An arbitrary value of γ=0.2 differentiates between deformed and undeformed zones. On the bars, solid colours is deformed, no colour is undeformed and grey is no data.

So it can be assumed that if there is any asymmetry in the (c)-axis pole figures it is against the sense of shear. The Uludağ shear zone has undergone right lateral movement (Chapter 3, Section 3.4 and Chapter 4, Section 4.3.1), so the rotation of (c)-axes should be anticlockwise. Some samples (Figure 5.9a-f) show this anticlockwise rotation (eg ULD38, ULD39, ULD127 and ULD152). The thin sections for ULD127 and ULD134 show extensive twinning with little or no recrystallisation. Other samples (eg ULD144, ULD157 and to a lesser extent, ULD131 and ULD124) display (c)-axis maxima rotated with the sense of shear (i.e. clockwise). This is due to ULD144 and ULD157 being completely recrystallised to a very fine grain size and ULD131 and ULD124 are also recrystallised with some twinning in coarser grains (e.g. Figure 4.8f).

The Eskişehir Fault has been the focus of deformation so it is to be expected that the CPO would reflect the effects of this deformation, showing stronger, more well-developed fabrics closer to the fault. However this is not the case. From sample ULD130–137 (transect 1), the CPO starts off strong with a definite point maximum in the (c) and {e} CPO (eg ULD130 and ULD131). This strong fabric dissipates towards the Eskişehir Fault where a girdle fabric develops (eg ULD135 and ULD137). On transect 2, the samples closest to the Eskişehir Fault also show girdle fabrics (eg ULD159 and ULD160). This is a result of the complicated history of the Uludağ Massif. During ductile strike slip shear, a preferred orientation will have developed, which has been subsequently destroyed and overprinted as the massif was exhumed along the Eskişehir Fault (Figure 5.19). Therefore, in the middle of the massif, the strike slip CPO is preserved but on the fault this CPO has been destroyed and reorganised to reflect the effects of exhumation through the ductile portion of the crust, resulting in girdle fabrics and more dispersed CPO (Figure 5.19). The original ductile shear CPO could also have been further reorganised by brittle processes in the shallower crust, including brittle cataclasis. This is evident on the northern side of the Massif where there are some weaker, more disorganised fabrics (eg. ULD55 and ULD49), where cataclasis is evident from thin section (Figure 4.7).

Samples containing quartz in the field area comprise gneisses and granites. CPO for quartz (c)- and {a}-axes and {m}-, {r}- and {z}-poles to planes are shown in Figure 5.10a-d. Some of these samples display strong CPO (eg ULD43 and ULD60), which are found close to the Bursa Fault. Both of these samples have (c)-axes parallel to Y, 6 strong {a} and {m} maxima perpendicular (in the XZ plane) and 3 {r}- and {z}-axis maxima at ~50° to the (c)-axis CPO. This is a single crystal CPO (Figure 5.10a) and suggests that the CPO pole figures are derived from one crystal. The EBSD maps for these two samples are well-indexed and display a pegmatitic, graphic texture with intergrowth of quartz and K-feldspar single crystals. Such intergrowths of quartz and K-feldspar occur at the eutectic point of crystallising granitic melt (Philpotts and Ague, 2009). Both of these samples are likely to be related to undeformed intrusions. Sample ULD60 is found close to a granitic intrusion (Chapter 3, Figure 3.1) of late Oligocene age, after shear zone activity had ceased (Chapter 4, Section 4.4.2). Sample ULD43 is found within the gneiss closer to the edge of the massif (Chapter 3, Figure 3.1) but could be related to the large post-kinematic granitic intrusions found to the north west.

Most of the remaining samples show either (c)-axis girdles or maxima parallel to the Y direction, and some have a combination of both. The samples showing a cross-girdle structure (eg ULD46, ULD139 and ULD168) indicate that a combination of prism<a>, rhomb<a> and basal<a> slip were active at temperatures between 400-500°C (Schmid and Casey, 1986, Lloyd et al., 1992, Lloyd and Freeman, 1994). The samples show c-axis maxima parallel to Y (eg ULD150, ULD140 and ULD141) which indicate prism<a> slip and temperatures above 500°C. These temperatures are in agreement with the temperature ascertained from microstructure in Chapter 4, Section 4.5.1 and also with the temperature obtained by Okay et al. (2008).

The {r}- and {z}- CPO show either quite dispersed fabrics, or cross girdle like patterns (eg. ULD172, Figure 5.10d and ULD154, Figure 5.10b. The dispersed fabrics (eg ULD151 and ULD136) reflect the more dispersed (c)-axis CPO whilst the girdle-like fabrics (eg ULD123) reflect similar (c)-axis CPO patterns. Samples ULD61, ULD150 and ULD140 show three maxima in the r- and z-axis maxima that are distributed around the c-axis maxima (parallel to Y). These samples are where prism<a> slip is the dominant slip system contributing to the CPO to explain the well-organised fabric (Schmid and Casey, 1986, Lloyd and Freeman, 1994).

As well as the c-axis distributions revealing the temperature of deformation; the opening angles of c-axes cross girdles have also been shown to increase with increasing temperature (Law, 1990, Law, 2014, Kruhl, 1998). This is considered to be a result of the change in slip system dominance (basal <a> vs. prism <c>) (Kruhl, 1998, Law, 1990, Law, 2014). Thus, c-axis opening angles can be used as a thermometer, although the temperatures have an uncertainty of ±50°C (Kruhl, 1998, Law, 2014). All the samples used to compile this thermometer had independently obtained temperature estimates, allowing the opening angle thermometer to be calibrated (Kruhl, 1998, Law, 1990, Law, 2014, Faleiros et al., 2016). Unfortunately only few samples provide suitable opening angles for use with this thermometer. Two of the samples that are suitable, and show measurable asymmetric cross girdles give temperatures in concordance with those given by the texture and microstructure in Chapter 4, of ~500°C (Law, 2014).

5.2.2. Schmid Factor

The absolute and stress dependent Schmid factors for each calcite marble sample are shown in Figure 5.11a-c. There are some assumptions that have been made regarding the temperature estimates. It was concluded by Rutter (1995) that dynamically recrystallised grain size is independent of temperature so the estimates come from the grain size vs temperature relationship derived by Covey-Crump and Rutter (1989). This relationship is calibrated for grain growth during static recrystallisation. Some marble samples in the Uludağ shear zone do show evidence for dynamic recyrstallisation (Chapter 3, Figure 3.15f), such that grain size has been reduced during deformation. If it is assumed that once deformation stopped, temperatures were still elevated to allow grain growth via static annealing, the temperature estimates from the relationship derived by Covey-Crump and Rutter (1989) will give a lower temperature bound. The protolith grain size would have been larger before deformation, deformation reduces grain size via dynamic recrystallisation, then static annealing starts to increase grain size once deformation stops. Therefore the temperature estimates using this relationship will only give a lower temperature bound. The assumption that deformation had ceased whilst the massif was still at elevated temperature in the mid-lower crust is valid because there are no vertical ductile structures within the rocks. Even if deformation had not ceased, a lower bound can still be obtained via this method. Samples ULD153, ULD124 and ULD158 clearly show a bi-modal grain size distribution which could be due to static grain growth at the expense of other grains (Figure 5.11a, b).

Conventional Schmid factor analysis would suggest that the most favourable slip/twin system is revealed by the 'reddest' maps. Schmid factor analysis has also previously been applied in uniaxial extension (for example in Channel5 ©1998-2015 Oxford Instruments NanoAnalysi) so has been adapted to apply in simple shear situations (Wallis et al., *Unpublished Manuscript*). From the absolute Schmid factor maps (Figure 5.11a-c) it could be concluded that the most favourable slip system is f-slip along with e-twinning. However, this ignores the impact of CRSS (τ_c) and applied stress (σ_A). Slip or twin systems only become active if the CRSS on that system is exceeded by the product of the applied stress and schmid factor (Schmid, 1928, Schmid and Boas, 1950, De Bresser and Spiers, 1997). In calcite, CRSS is strongly temperature dependent; see Section 4.2.3 (De Bresser and Spiers, 1997). Absolute Schmid factors do not take the applied stress field into account and therefore cannot represent the geological situations.

When the differential stress is applied to each sample the results are very different. For most samples the differential stress is insufficient to activate f-slip, which appeared most favourable in the absolute Schmid factor maps. Most samples have sufficient applied differential stress to activate r-slip, in some only the grains with the highest schmid factors show any r-slip activity. All samples show e-twinning activity due to the low CRSS required to activate e-twinning at temperatures <500°C. This information is summarised in the summary diagram in Figure 5.20.

The effect of temperature and stress can be seen on Figure 5.13. Samples ULD143 and ULD153 have similar stresses (60MPa and 79MPa respectively) but whereas only e-twinning is active in ULD143, e-twinning and r-slip are active in ULD153 due to the higher temperature. Both ULD143 and ULD131 have similar temperatures (227°C and 228°C respectively) but in ULD131 all three slip/twin systems are active due to the higher applied stress (60MPa vs 132MPa) and the higher stress allows the slip systems (i.e. f-slip) with higher CRSS to become active. Similarly, higher temperature lowers the CRSS required for slip/twin systems to become active allowing these slip/twin systems to become active at lower applied differential stresses. For example ULD143 has a lower temperature than ULD153 (227°C and 300°C respectively) but similar stress but the higher temperature lowers the CRSS of r-slip allowing that system to become active in sample ULD153. The relationship between applied differential stress and the activity of the three slip/twin systems can be seen on the stress vs Schmid factor graphs for each sample (Figure 5.13). Again, the effect of temperature and stress is summarised on Figure 5.20.

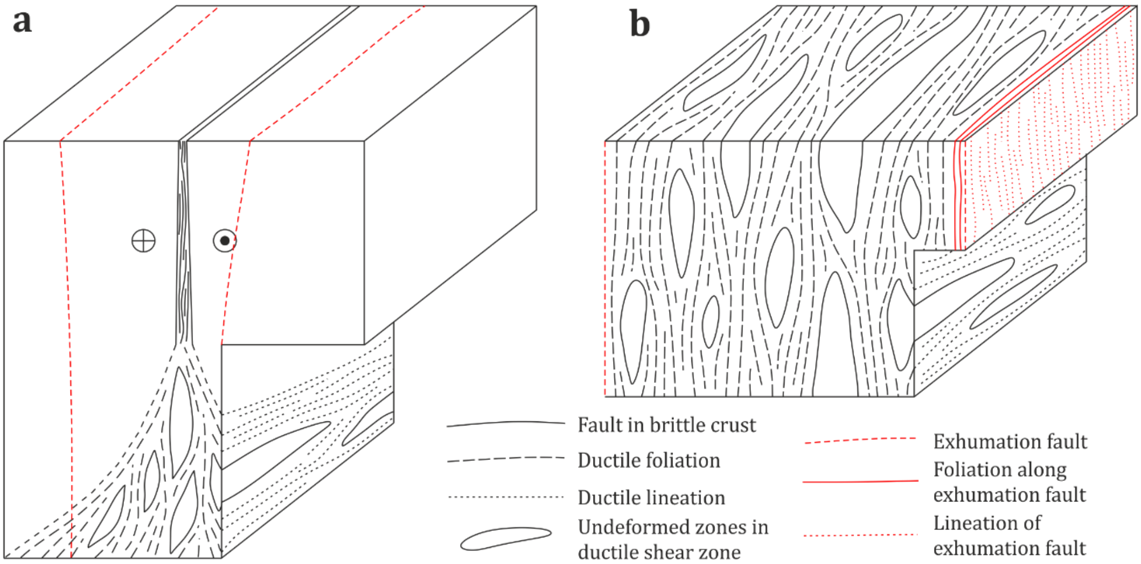

Figure 5.19. Fabric overprinting of a ductile shear zone during exhumation. a) An active ductile shear zone in the mid crust with zones of deformation separated with zones that are relatively undeformed. b) Exhumation of the mid-crustal ductile shear zone along the faults shown in a). Overprinting of the original sub-horizontal ductile lineation occurs along the faults involved in exhumation with a sub-vertical lineation.

The effect of stress on the activity of slip/twin systems is complicated when the temperature is increased to 500°C which is the upper bound temperature for the Uludağ Massif (Chapter 4, Section 4.4.1) (Figure 5.15). At this temperature e-twinning becomes unrecognisable and there are no data to support its presence and contribution to CPO at temperatures >500°C (Figure 5.4 and Figure 5.20) (De Bresser and Spiers, 1997). Due to the higher temperature, r-slip has become active in ULD143 where previously at 227°C it was inactive. At higher temperature De Bresser and Spiers (1997) found that a different, higher temperature f-slip system became dominant which requires a higher CRSS to become active (Figure 5.4). This explains why f-slip is not active in the other samples, as instead of the CRSS decreasing for f-slip with the increased temperature, it has actually increased because the slip system has changed to high temperature f-slip as at higher temperatures low-temperature f-slip is no longer possible even though it has a lower CRSS (Figure 5.4 and Figure 5.20) (De Bresser and Spiers, 1997).

Whilst CPO distributions can give an indication to which slip/twin systems were active, Schmid factor analysis provides a quantitative interpretation. From this analysis, it is evident that e-twinning is the dominant deformation mechanism active in these samples at lower deformation temperatures. Twinning does not accommodate much strain so r-slip also contributes in most samples, with low temperature f-slip only contributing in those samples with sufficient applied differential stress to activate it, which are the samples with the smallest grain size (Rutter, 1995).

There are limitations to this approach in that it assumes homogeneous stress as σ_A is an average of the stress, but in reality stress and strain vary between and within grains. It also assumes that the sample has reached a steady-state deformation, and does not recognise any deformation path if the final state is not steady state deformation. Finally, the Schmid factor only applies to the single crystal, not the polycrystal. This single crystal analysis must be adapted to the Taylor factor for the full polycrystal analysis and also to relate yield strength to texture or slip systems (Taylor, 1938). Schmid factor analysis can only be applied in cases where there is information on CRSS with temperature such as the case of calcite (Figure 5.4) (De Bresser and Spiers, 1997). There is no CRSS information for quartz therefore it is not used in this study.

5.2.3. Fabric Strength

The general trends in changing fabric strength of the calcite CPO were described in Section 4.3.4, and are shown on Figure 5.16. The CPO for the two samples in the South Uludağ Granite (ULD143 and ULD144) that show the highest fabric strengths in all three parameters are shown in Figure 5.9f. They both show very strong (c)-axis maxima. The values of the different fabric strength calculations on the Eskişehir Fault are not the highest, as might be expected from field observations (Chapter 3, Section 3.1). From field observations it was apparent that the Eskişehir Fault had accommodated significant strain, with the intense foliation in the phyllites. Also, the stress and strain-rate calculations (Chapter 4, Section 4.4.2) suggest that this fault had accommodated significant deformation. It could be assumed therefore that the samples on the fault should have the strongest and most well-developed fabrics. However, as has been described in Section 5.4.1, the exhumation on the Eskişehir Fault has destroyed the strike slip ductile shear fabric resulting in a weaker than expected CPO (Figure 5.19).

There are much higher values of fabric intensity elsewhere in the massif (eg at 0.707km, 2.101km and 3.24km from the Eskişehir Fault), although lower values appear again around the Bursa Fault (Figure 5.16). Another anomaly, south of the Bursa Fault, ULD38, records a high value for all three fabric strength parameters. This sample shows no sign of recrystallisation and is coarse grained in comparison to other samples. The CPO (Figure 5.16a) displays a strong (c)-axis maximum, but quite dispersed {a}-axis girdle. This suggests that localisation has occurred during ductile shear on different strands across the massif (Figure 5.19 and Figure 5.20). The higher values in the massif represent penetrative deformation at higher temperatures during shear. As the exhumation was localised on the Eskişehir and Bursa Faults the massif was preserved, and thereby preserving the higher CPO strengths. This can also be seen in the calcite pole figures in Figure 5.9a-f, with samples ULD130 – ULD137, moving southwards towards the fault. It starts off with a well-developed point maxima parallel to the x-direction (ULD130) which degrades into a more distributed girdle closer to the fault, ending with ULD137. This sequence shows that closer to the fault the original CPO is increasingly destroyed and overprinted (Figure 5.19).

For the quartz fabric strengths, ULD43, ULD60 and ULD61 have been removed from the transect as they exhibited single crystal CPO (Figure 5.10a). The highest value for quartz in all three parameters is located very close to the Eskişehir Fault, around 50m south (Figure 5.16). That particular sample, ULD140, seems to be an anomaly as the rest of the samples closer to the fault show quite a range of lower values. It is a deformed granite sample with a well-developed mylonitic fabric, which accounts for the CPO and high fabric strength. Similar to the calcite values, whilst there do appear to be peaks in increased fabric strength, the Eskişehir Fault does not show a strong peak. This can, again be explained by the exhumation, which was discussed in detail earlier. There are other fabric strength peaks within the massif, ~2km from the Eskişehir Fault, before reducing around 4km and then peaking again at 5.4km. These three peaks can be attributed to strain localisation when the shear zone was active in the mid-crust at different points in the Uludağ Massif, and appear to correlate well with similar peaks in the calcite values (Figure 5.16).

The J-index can be difficult to interpret as it is heavily biased by sample size; the fewer grains measured, the less reliable the estimate. Therefore in cases where there are clear anomalies compared to the other parameters, it is due to poor indexing during EBSD (ie not enough points on the map gave results) and consequently not enough grains are indexed to calculate a robust J-index. A way around this would be using one point per grain to create the ODF that is used when calculating the J-index. However, the analysis could be done using one point per grain which would make the J-index more robust. It has not been done in this study as the other strength parameters provide enough evidence for analysis.

5.2.4. Shear strain

The VPSC analysis to calibrate CPO fabric strength with shear strain used a protolith that was outside of the shear zone, north of the Bursa Fault, ULD16 (Chapter 3, Section 3.1). It is important that the sample used for the initial protolith 1) comes from the same sample suite and 2) is outside of the shear zone. Using a random protolith is unrealistic as it is unlikely that the initial protolith, prior to deformation, was completely random.

From the calibration (Figure 5.18) it is evident that some areas of the massif show more deformation (ie increased shear strain) than others. The arbitrary value of γ = 0.2 was used to differentiate between deformed and undeformed zones within the Uludağ Massif. This value is taken from the value used in previous studies (Wallis *Pers Comm*) which was based on microstructural evidence. Samples without deformation related microstructure all fell below γ = 0.2.

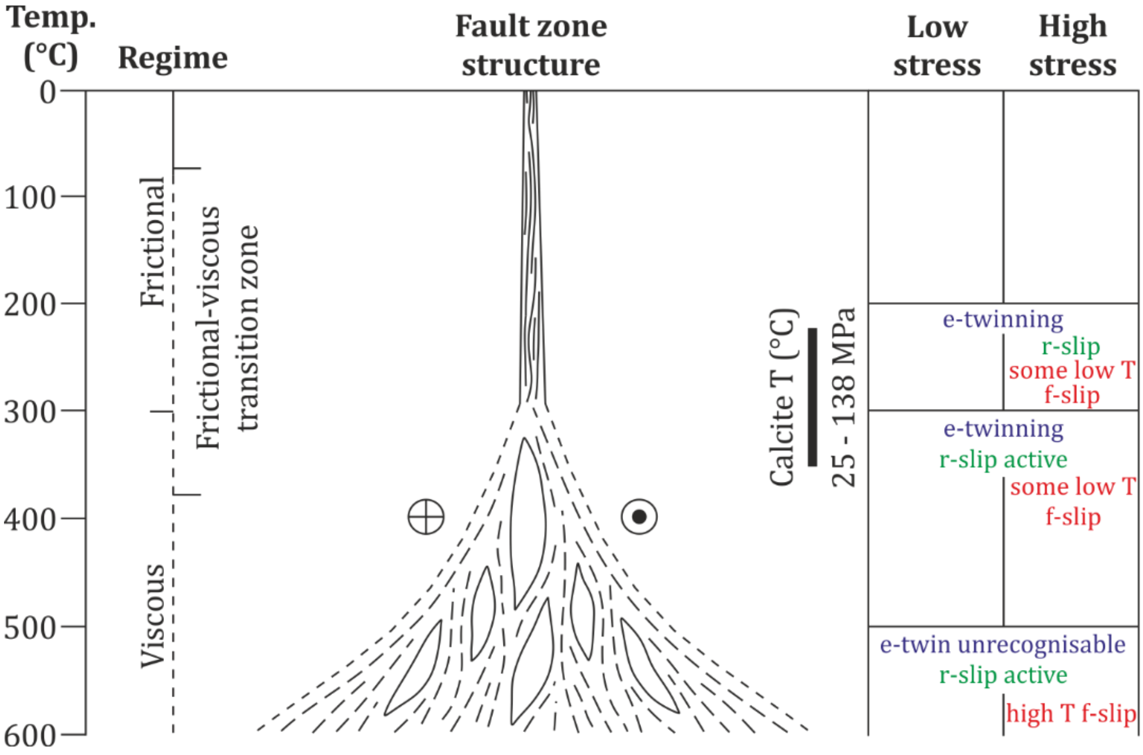

Figure 5.20. Fault zone structure, calcite temperature range from relationship in Covey-Crump and Rutter (1989), stress from flow law in Rutter (1995). Results from schmid factor analysis of active slip systems shown on right.

Due to calcite recording the similar microstructures (twinning) even at very low shear strains a unique value cannot be obtained in this study. Therefore the value from the previous study is taken to differentiate between relatively deformed part of the massif and relatively undeformed sections. The values obtained for shear strain are not really realistic for a shear zone of this size (~8km wide) that has accommodated ~100km of offset. However, the distribution of shear strain is still evident from the results, with sections that show more strain than others.

From this and from previous work in Chapter 3 on stress and strain-rate, a picture is building of deformation either being partitioned on a small scale into strands of higher stress and strain between zones of less deformation, or being diffuse over the larger scale (Figure 5.20). This will be considered further in Chapter 7.

6. CHAPTER SIX

Seismic modelling of the field area: Transferring results onto the North Anatolian Fault.

6.1. Introduction

The aim of this chapter is to present the crystal preferred orientation (CPO) derived seismic properties of the samples across the Uludağ Massif. In the ductile mid-crust CPO is believed to be the main contributor to the seismic properties of a rock, along with mineralogy and mineral proportions (Mainprice and Nicolas, 1989, Babuška and Cara, 1991, Lloyd et al., 2011a). The second part of this chapter will then use the seismic properties of the samples to model the seismic response of the Uludağ Massif and the ductile portion beneath the North Anatolian Fault (NAF). The modelling will use a wide angle, one-way wave equation approximation (Audet et al., 2007) which will produce synthetic seismograms of geologically informed crustal structures. These are then used to produce synthetic receiver functions to analyse the lithologies, structures and features that create certain seismic responses and compare these to the receiver functions across the NAF (Kahraman et al., 2015). This approach provides a method for detailed analysis of the effects of varying structure, anisotropy and lithology. It also uses seismic properties from in-situ rocks which is important when using specific examples of real seismic data to interpret the geology of the crust (Audet, 2015, Cossette et al., 2016).

6.2. Background methods and theory

Knowing the seismic properties of rocks is important when trying to interpret geology from the seismic response, particularly for mid-crustal structure where seismic resolution is often too poor to determine discrete structures. There are several factors that critically influence the seismic properties of rocks including mineralogy and lithology, layering (Valcke et al., 2006), grain shape, cracks and fractures (Kendall et al., 2007), and lastly crystallographic preferred orientation (CPO) (Mainprice and Nicolas, 1989, Babuška and Cara, 1991). CPO is particularly important as the seismic velocities of single crystals vary with symmetry and direction, and the alignment of crystal lattices can lead to significant increases in the seismic anisotropy of the bulk rock (Mainprice and Nicolas, 1989, Babuška and Cara, 1991). The CPO of rocks often defines a foliation which can affect the anisotropy, as waves travel at different speeds along the foliation as opposed to perpendicular to it.

6.2.1. Seismic properties

The CPO-derived seismic properties of particular interest here are the compressional (Vp) and the anisotropic shear waves (Vs_1 and Vs_2), along with shear wave splitting. The latter can be expressed as the difference in shear wave velocities ($dVs = Vs_1 - Vs_2$) or shear wave anisotropy ($AVs\% = 100(Vs_1 - Vs_2)/[(Vs_1 + Vs_2)0.5]$) (Mainprice and Silver, 1993).

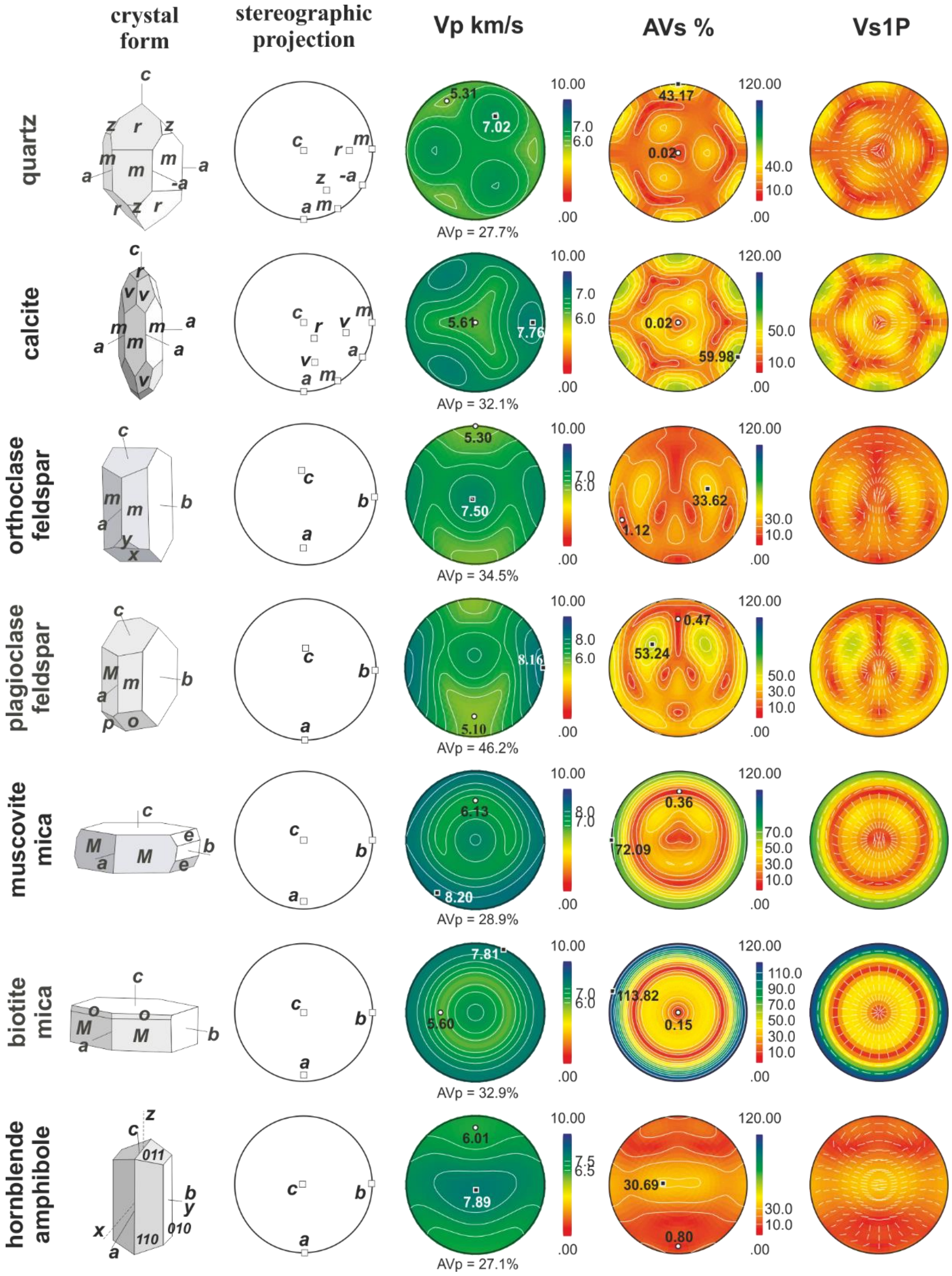

Figure 6.1. The seismic properties of common rock forming minerals. Vp - compressional wave velocities, AVs – percentage anisotropy, Vs_1P – polarisation direction of fastest shear wave, all contoured with the same interval for comparison. The crystallographic axes for each crystal are shown stereographically in the second column. Figure taken from (Lloyd et al., 2011a). White and black dots are minimum and maximum values respectively.

Most rock forming minerals exhibit some degree of anisotropy in the single crystal form (Figure 6.1) (Barruol and Mainprice, 1993, Ji et al., 2002). However minerals such as quartz and feldspar often display diluting characteristics due to their symmetry; any misorientation between grains can interfere destructively, hence CPO is important (Lloyd et al., 2009). In the mid-crust mica has a big influence on the seismic properties due to its very large anisotropy (Figure 6.1) (Kern and Wenk, 1990, Lloyd et al., 2009), and in the lower crust amphibole contributes significantly also (Rudnick and Fountain, 1995, Tatham et al., 2008). Therefore understanding the lithology through exhumed mid to lower-crustal rocks and determining mineral proportions can help understand seismic responses, especially anisotropy.

The methodology for determining the CPO-controlled seismic properties of a sample starts with acquiring the CPO via EBSD (described in Chapter 4, Section 4.1). Conventionally, CPO are represented in the kinematic reference frame (XYZ) but seismic surveys require the geographic (NSEW) reference frame. The CPO are therefore rotated from the former into the latter through a series of rotations about axes defined by dip and azimuth and amount of rotation in Mtex. The rotated CPO data is next combined with the single crystal elastic stiffness properties, defined through the elastic tensor (C_{ijkl}) and mineral density (ρ), according to the modal proportions (F) of each mineral phase in the bulk rock composition to create an elastic tensor for the whole sample (Mainprice, 1990, Mainprice and Humbert, 1994, Lloyd and Kendall, 2005). The modal proportions or volume fraction are calculated automatically from the indexed proportions of minerals when processing EBSD data in Matlab toolbox, Mtex (Mainprice et al., 2011).

The elastic stiffness tensors for the constituent minerals of the gneisses, granites, marbles and phyllonites of the Uludağ Massif have been collated and are shown in Appendix 6.A. The tensor takes the form of a 4th rank tensor and relates stress to strain:

$$\sigma_{ij} = C_{ijkl}\,\varepsilon_{kl}$$

$$\begin{bmatrix}\sigma_1\\\sigma_2\\\sigma_3\\\sigma_4\\\sigma_5\\\sigma_6\end{bmatrix} = \begin{bmatrix}C_{11} & C_{12} & C_{13} & C_{14} & C_{15} & C_{16}\\ C_{21} & C_{22} & C_{23} & C_{24} & C_{25} & C_{26}\\ C_{31} & C_{32} & C_{33} & C_{34} & C_{35} & C_{36}\\ C_{41} & C_{42} & C_{43} & C_{44} & C_{45} & C_{46}\\ C_{51} & C_{52} & C_{53} & C_{54} & C_{55} & C_{56}\\ C_{61} & C_{62} & C_{63} & C_{64} & C_{65} & C_{66}\end{bmatrix} \begin{bmatrix}\varepsilon_1\\\varepsilon_2\\\varepsilon_3\\\varepsilon_4\\\varepsilon_5\\\varepsilon_6\end{bmatrix}$$

where σ_{ij} is the stress tensor, C_{ijkl} is the elastic stiffness tensor and ε_{kl} is the strain tensor. The number of elastic constants needed to describe the elastic response of a crystal depends on the crystal symmetry; cubic minerals require 3 (C_{11}, C_{12} and C_{44}); hexagonal, 5; trigonal and tetragonal, 6-7; orthorhombic, 9 and monoclinic, 13 (see table - Babuška and Cara (1991)).

Due to assumptions made with stress and strain (e.g. stress or strain is constant everywhere; at every position it is set to equal the macroscopic stress of the sample to allow calculation) there are three different averaging methods that can be applied when calculating the elastic moduli of a crystal aggregate (Voigt, 1928, Reuss, 1929, Hill, 1952). The constant strain (Voigt) average provides the upper bound (Voigt, 1928), and the constant stress (Reuss) average providing the lower bound of the elastic modulus (Reuss, 1929), whilst Hill (1952) later proposed the mean of the two averages which is often taken as the best estimate of the elastic parameters and will be used in this study (Bunge et al., 2000, Lloyd et al., 2011b). All above calculations and figures of the seismic properties for the samples are created using Mtex-4.0.23 (Mainprice et al., 2011).

6.2.2. FaultLab

The FaultLab project at Leeds combines seismology, geology and geodesy to try to understand the deep structure of the North Anatolian Fault, how it is moving and deforming and how this affects the earthquake cycle. To do this an array of temporary broadband seismic stations, the Dense Array for North Anatolia (DANA) network, was installed over the North Anatolian Fault close to the 1999 Izmit rupture (Chapter 1, Figure 1.3). From the information gathered by the array, a receiver function (RF) study of the structure of the crust beneath the two branches of the NAF was carried out (Kahraman et al., 2015).

This chapter aims to bridge the gap between geophysical models and geological content. This will be done using the exhumed ductile shear zone of the Uludağ Massif as an analogue for the mid-crust beneath the NAF. The seismic properties of the samples collected from the Uludağ Massif will be used to populate seismic models in order to forward model the seismic signals from different lithologies and different structures (ie. Foliation orientation). The background to the modelling approach will be discussed in the next section, Section 6.2.3. These seismic responses can then be converted into receiver functions, the aim being to compare these synthetic receiver functions to the real receiver functions from the study on the NAF (Kahraman et al., 2015).

The results, in the form of profiles in the area of the DANA array are shown in (Figure 6.2) (profile locations shown on Figure 1.3). The RF study found that in the area of the DANA array (Chapter 1, Figure 1.3) there is a thin, low velocity, top layer of ~1.5km (Vs = 1.8-2.3km/s, Vp/Vs = 1.72-1.96) on top of a 'typical' mid crust that extends to the Moho in some areas (Vs = 3.5-3.7km/s and Vp/Vs = 1.72-1.81) (Kahraman et al., 2015). Other areas have a 10-13km wide higher velocity zone (Vs = 3.9-4.2km/s and Vp/Vs = 1.67-1.74) close to the Moho which is at 33-39km deep across the region and the upper mantle has Vs = 4.4-4.5km/s and Vp/Vs = 1.70-1.75 (Kahraman et al., 2015) (Figure 6.3).

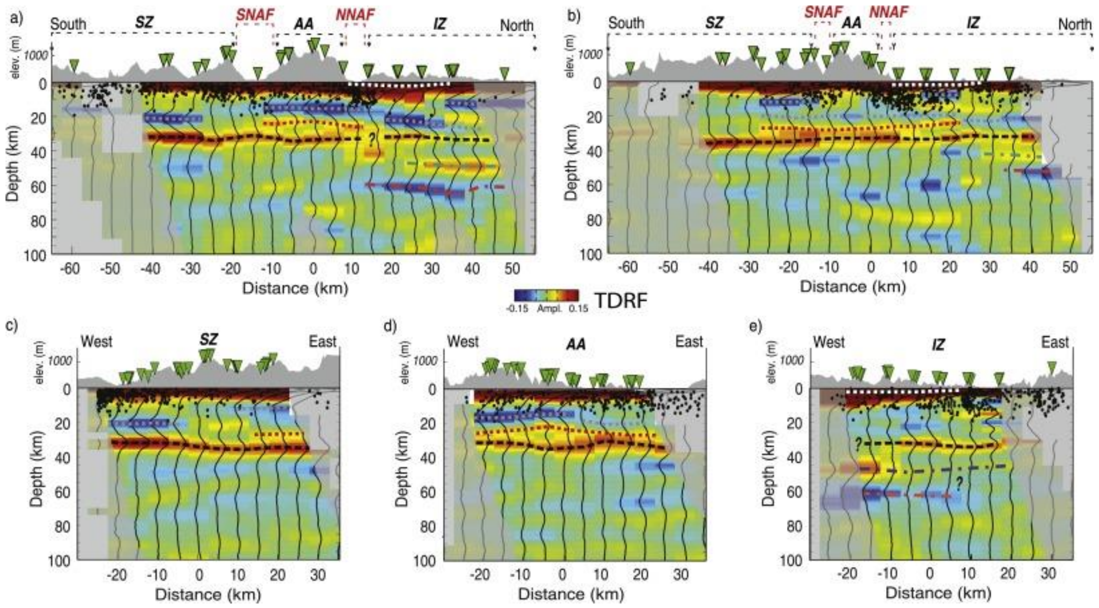

Figure 6.2. Receiver function plots (1.2Hz) in the vicinity of the DANA array. Green triangles represent seismic stations, black dots are seismicity, black line is the Moho, red dotted line – positive P-S conversion, dotted line – near surface P-S conversion, blue dash-dot line – upper mantle positive amplitudes, grey dotted line – crustal amplitudes, orange dotted line – upper mantle amplitudes, SNAF and NNAF are the southern and northern branches of the North Anatolian Fault respectively – locations on Figure 1.3 (Kahraman et al., 2015).

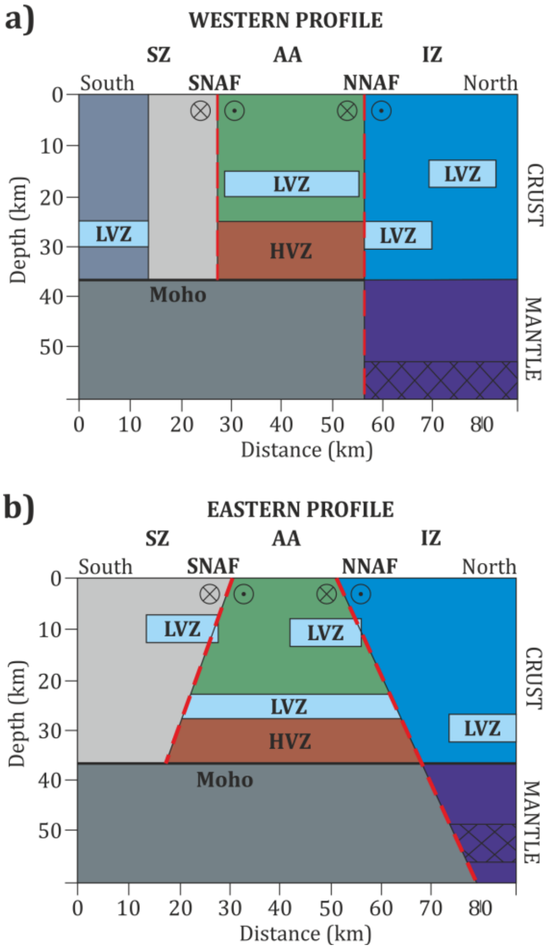

Figure 6.3. Schematic cross sections from Kahraman et al. (2015) of the north Anatolian Fault in the area of the DANA array (Chapter 1, Figure 1.3). a) The western profile and b) the eastern profile (line of cross section on Figure 1.3). SNAF – southern North Anatolian Fault, NNAF – northern North Anatolian Fault, SZ – Sakarya Zone (light and dark grey), AA – Armutlu-Almacik (green), IZ – Istanbul-Zonguldak Zone (blue), LVZ – low velocity zone (light blue), HVZ – high velocity zone (brown). Above the Moho the three sections, separated by faults show different characteristics (explained in text). Beneath the Moho, the mantle south of the NNAF is featureless (grey) and to the north of the NNAF the upper mantle (purple) lies beneath a weak moho and displays some sort of structure (hatched) (Kahraman et al., 2015).

The receiver functions were calculated using events with back azimuths shown in Figure 6.4. Most of the events are between back azimuths of 000° and ~120°. This will define the back azimuths used to create the synthetic receiver function stacks in Section 6.4 and Section 6.5, so as to be comparable to the RF study on the NAF (Kahraman et al., 2015).

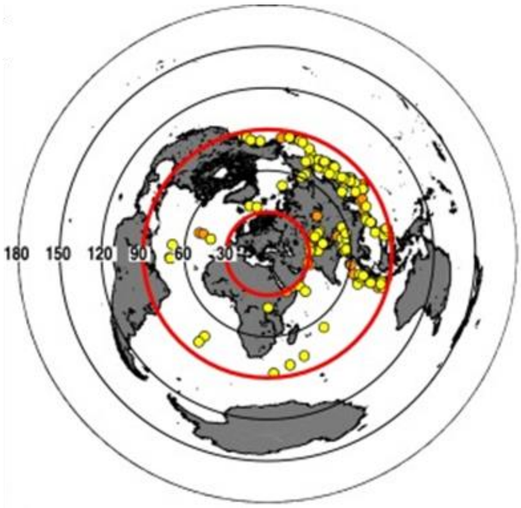

Figure 6.4. Event distribution for receiver functions analysis by Kahraman et al. (2015). Locations of earthquakes $m_b > 5.5$ that occurred during the deployment of the DANA array (yellow) and since 2009 (orange) for the permanent stations (station locations Chapter 1, Figure 1.3) that were used for receiver function calculation in the NAF study (Kahraman et al., 2015).

6.2.3. Seismic modelling

The seismic properties calculated from CPO data can be used to populate CPO-derived seismic models to investigate the effect of rock type and deformation on the seismic response. To do this a teleseismic waveform modelling approach is taken that uses the one-way wave equation (Audet et al., 2007). Audet et al. (2007) use the wide-angle, one-way wave equation to investigate variations in teleseismic 3D waveforms due to 2D elastic heterogeneity and anisotropy (representing crustal structure). Using the one-way wave equation is computationally more efficient than fully 3D techniques through finite difference models (Virieux (1986) and Levander (1988)). Currently, however, backward propagation (reflection/transmission) is not taken into account (Thomson, 1999). Thomson (2005) suggested the one-way operators could be extended to include these effects (and reflect results from full wave form modelling) but it would be computationally laborious and without practical advantage. Conversely ray tracing methods are computationally efficient but do not provide enough information on important wave effects such as diffractions, multiples and reflections and only provide local solutions that do not give appropriate approximations of the 2D structure (Thomson, 2005). The approach taken in Audet et al. (2007) is based on the solution of the one-way wave equation, identifying a preferred direction of propagation and splits the wavefield into constituents travelling in opposite directions (Thomson, 1999). In teleseismic studies, this approach is valid due to the wave fronts propagating at near-vertical incidence and advantages include only modelling the effects of forward wave propagation along with computational efficiency (Audet et al., 2007).

The three component seismic traces produced using this approach can be converted into receiver functions, which allow direct comparison to receiver functions of recorded seismic data (eg Kahraman et al. (2015)). This work flow has been implemented in only a few studies to date, including Audet (2015) and Cossette et al. (2016). In the example from the San Andreas Fault near Parkfield, California, Audet (2015) examines the seismic structure and anisotropy of the crust using teleseimic receiver functions and then uses synthetically produced receiver functions to investigate the results. End member models, the first with horizontally layered anisotropy in the upper and middle crust and the second with a vertical low-velocity fault zone running through the entire crust, were produced to ascertain the best fit to the recorded data (Audet, 2015).

Cossette et al. (2016) study the structure and crustal anisotropy of the crust in the Cyclades, Greece through receiver functions. These data were then compared to modelled synthetic receiver functions constrained through in-situ rock properties (measured via EBSD) and indicated a shallow upper crust characterised by metapelite (~5% anisotropy) underlain by a 20km thick anisotropic layer of blueschists and eclogite (Cossette et al., 2016).

Both of these studies demonstrate the possibilities and also importance of using modelled data in conjunction with real seismic and receiver function data when interpreting crustal structure. The second example from Cossette et al. (2016) builds on the approach from Audet (2015) by using real rock seismic properties obtained through EBSD, which is the approach followed in this study for the Uludağ Massif and North Anatolian Fault. However this seismic study is preceded by a detailed understanding of the particular ductile shear zone that is being modelled, a complete sample suite across the exhumed shear zone and application to an active fault.

6.2.4. Receiver functions

Receiver functions are computed from three component seismograms and show the relative response of the Earth's structure near the receiver. A teleseismic P-wave generates P to S conversions at boundaries within the lithosphere beneath a seismometer. For near vertical incidence angles the P to Sv conversions are recorded on the radial component. Using the P-wavelet recorded on the vertical as an approximation for the source time function and deconvolution from the radial allows the response of the structure beneath the station from the P-S conversions to be estimated (Figure 6.5) (Ammon, 1991).

Seismic anisotropy in receiver functions is characterised by the appearance of seismic energy on the transverse receiver function components and systematic change of Ps converted waveforms on receiver functions with varying back azimuth (Nagaya et al., 2008). Also anisotropy, like that defined by a foliation, displays a distinctive 180° back azimuthal periodicity in Ps conversion amplitudes (Frederiksen and Bostock, 2000).

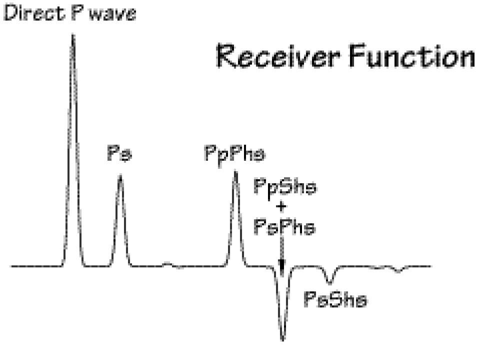

Figure 6.5. Receiver function waveform, upper case latters denote upgoing travel paths, lower case latters denote downgoing travel paths and h indicates reflection for the interface (Ammon, 1991).

6.3. Seismic properties

This section presents the seismic properties of the rocks across the Uludağ Shear Zone, dealing with the massif, the Eskişehir Fault, Bursa Fault and Granitic intrusions separately. Not all the samples across the massif have been used to calculate seismic properties, only those considered representative, the locations of which are indicated on the schematic transect shown on Figure 6.12. The samples were chosen based on lithology and proximity to the Eskişehir and Bursa faults to represent all the lithologies and structures. The samples used are discussed from north to south, starting with samples near the Bursa Fault, the Uludağ Massif, the Eskişehir Fault and the South Uludağ Granite. For each sample, the pole figures of each mineral within the particular sample are set to the same scale for comparison of their relative CPO strengths and fabrics. All seismic properties of all the samples are displayed using the same colour scales to allow comparison of lithological controls on the seismic properties of the region.

6.3.1. Bursa Fault

The two samples closest to the Bursa Fault (ULD49 and ULD52) are both marble, comprising calcite and very minor amounts of quartz (<1%) (Figure 6.12). They are both within 100m of the Bursa Fault (Figure 3.1). ULD 49 has a diffuse and weak fabric (Figure 6.6), but there is still a definite foliation defined by the c-axes distribution can be recognised. This foliation is reflected in the fast Vp and Vs1 orientations. This diffuse fabric has an effect on the Vs2 orientation and therefore on the AVs, where the foliation is not apparent. ULD 52 is closest to the Bursa Fault and has more well-developed and stronger CPO than ULD49, a foliation is also represented in the fast Vp, Vs1 and high AVs orientations.

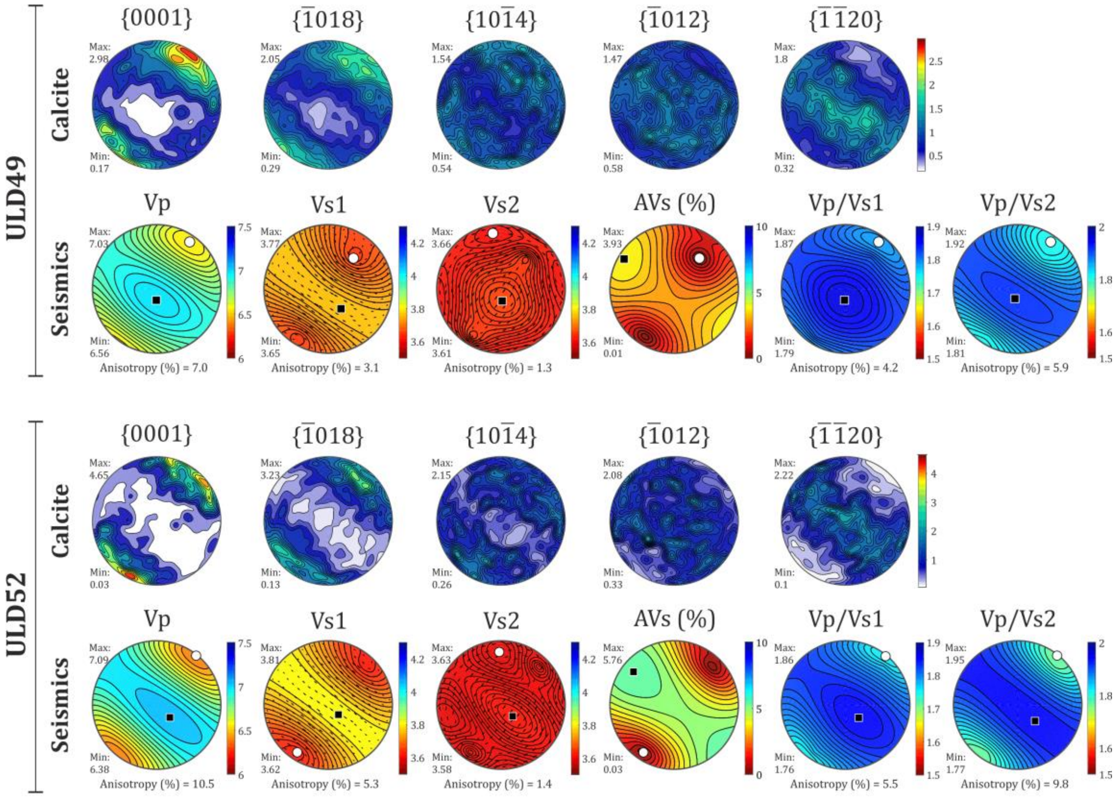

Figure 6.6. Samples found north of the Bursa Fault, locations indicated on (Figure 6.12). The individual seismic properties are set to the same scale to enable comparison. Max and min on seismic property plots indicated by black square and white circle respectively. Vp – compressional p-wave velocity, Vs1, Vs2 – shear wave velocities with polarisation directions, AVs(%) – percentage shear wave anisotropy.

6.3.2. Uludağ Massif

This part of the shear zone includes gneiss, marble and amphibolite in the central part of the massif between the Eskişehir Fault to the south and the Bursa Fault to the north (Figure 3.1). It was noted in Chapter 3, Section 3.5 and Chapter 4, Section 4.4 that deformation is not solely localised on the Eskişehir Fault; there was often a peak of higher stresses and strain-rates in the centre of the massif. To reflect this variation, seismic properties are calculated from samples in the centre of the massif, as well as the less deformed samples either side.

ULD47 and ULD46 (Figure 6.7) are located at 3.69km and 5.40km relative to the Eskişehir Fault, respectively. ULD47 contains quartz (60%), plagioclase (30%), biotite (5%), muscovite (5%) and chlorite (<1%). The low chlorite content explains the almost single crystal distribution and the strong maxima. Quartz, plagioclase, biotite and muscovite are relatively weak and show no strong fabric. This is reflected in the seismic velocities, with diffuse Vp, Vs1 and AVs patterns. As chlorite contributes <1% to the whole rock seismics, any foliation that may be defined by the single crystal CPO is not represented.

ULD46 is made up of quartz (40%), plagioclase (25%), K-feldspar (20%) and biotite (15%). Out of all the constituent minerals biotite, has the strongest CPO, and defines a foliation trending ~110°. Plagioclase and K-feldspar have relatively weak CPO. Quartz has quite a strong c-axis texture and CPO. The Vp, Vs1 and Vs2 reflect the foliation defined by the biotite, which is also reflected in the texture shown in the AVs. The maximum AVs is parallel to the b-axes of the biotite (Figure 6.1). The quartz contributes destructively to this pattern, which can be recognised in the lower anisotropy N-S, perpendicular to the foliation.

ULD123, ULD153 and ULD125 are found within 2-2.6km north of the Eskişehir Fault (Figure 6.12) and are displayed on Figure 6.8. ULD123 is at 2.07km and contains quartz (30%), plagioclase (40%), K-feldspar (15%), biotite (10%) and muscovite (5%). The quartz c-axes define a relatively strong maxima, and also foliation trending ~110° (parallel to the Eskişehir Fault). The plagioclase fabric is quite diffuse whereas K-feldspar is a little more developed into distinct maxima. The biotite and muscovite CPOs are relatively weak compared to the quartz and K-feldspar as the micas are much less abundant. However the mica does define a weak foliation trending ~115°. This weak mica-defined foliation is only slightly evident in the Vp and Vs1 plots, with fast velocities creating a faint foliation parallel girdle. The quartz c-axes maxima and N-S girdle weakens the foliation parallel seismic properties, causing the pattern of Vs2. AVs, being a combination of Vs1 and Vs2 forms maxima parallel to the b-axes (010) of biotite and muscovite. There is no foliation effect present in the AVs plot due to the quartz again diluting the effect of the micas.

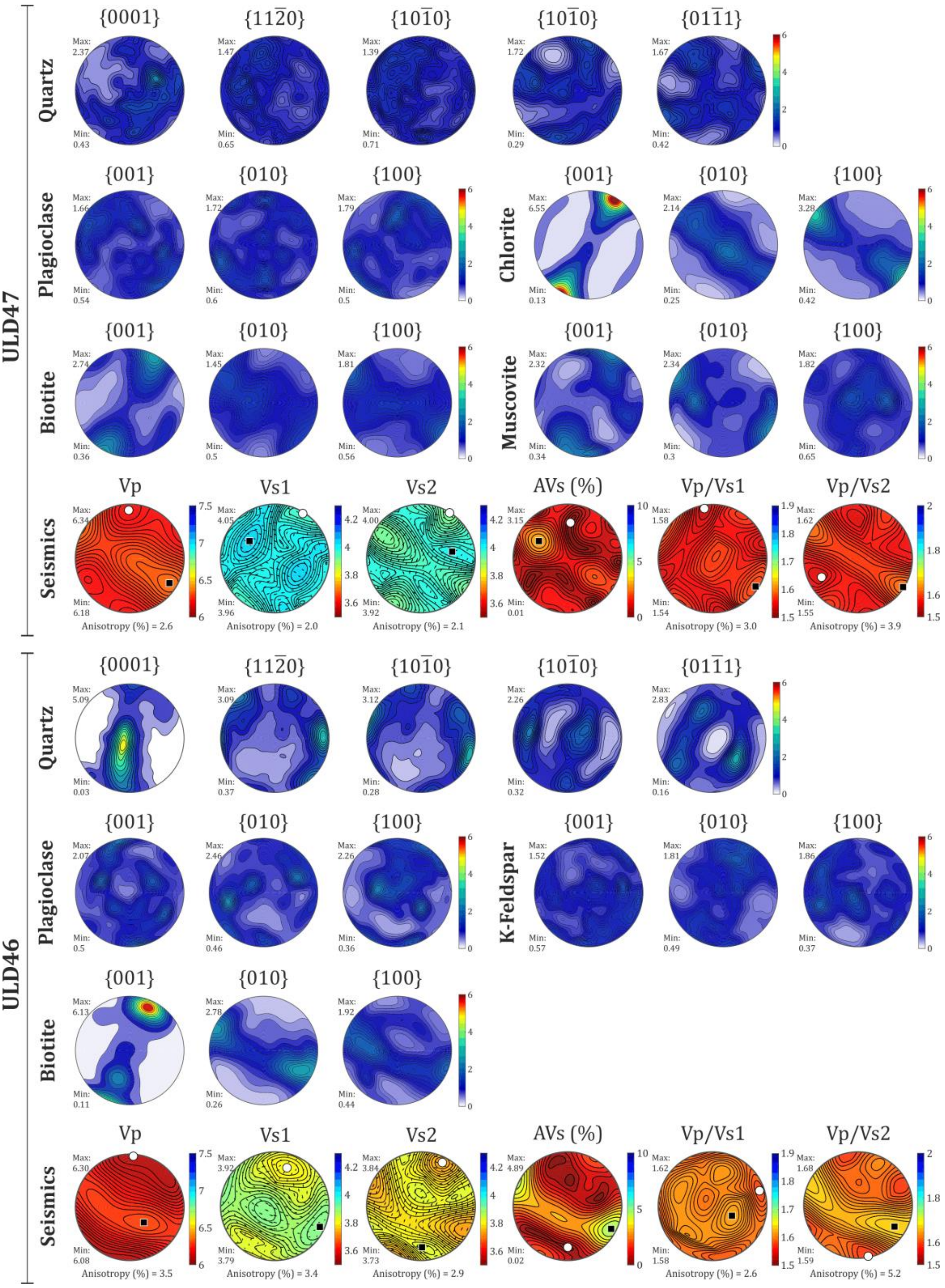

Figure 6.7. Samples found close to the Bursa Fault on the northern side of the massif, locations indicated on cross section (Figure 6.12). All minerals in each sample are set to the same scale and also all seismics, regardless of lithology, are also scaled the same for comparison. Max and min on seismic property plots indicated by black square and white circle respectively. Vp – compressional p-wave velocity, Vs1, Vs2 – shear-wave velocities with polarisation directions, AVs(%) – percentage shear wave anisotropy.

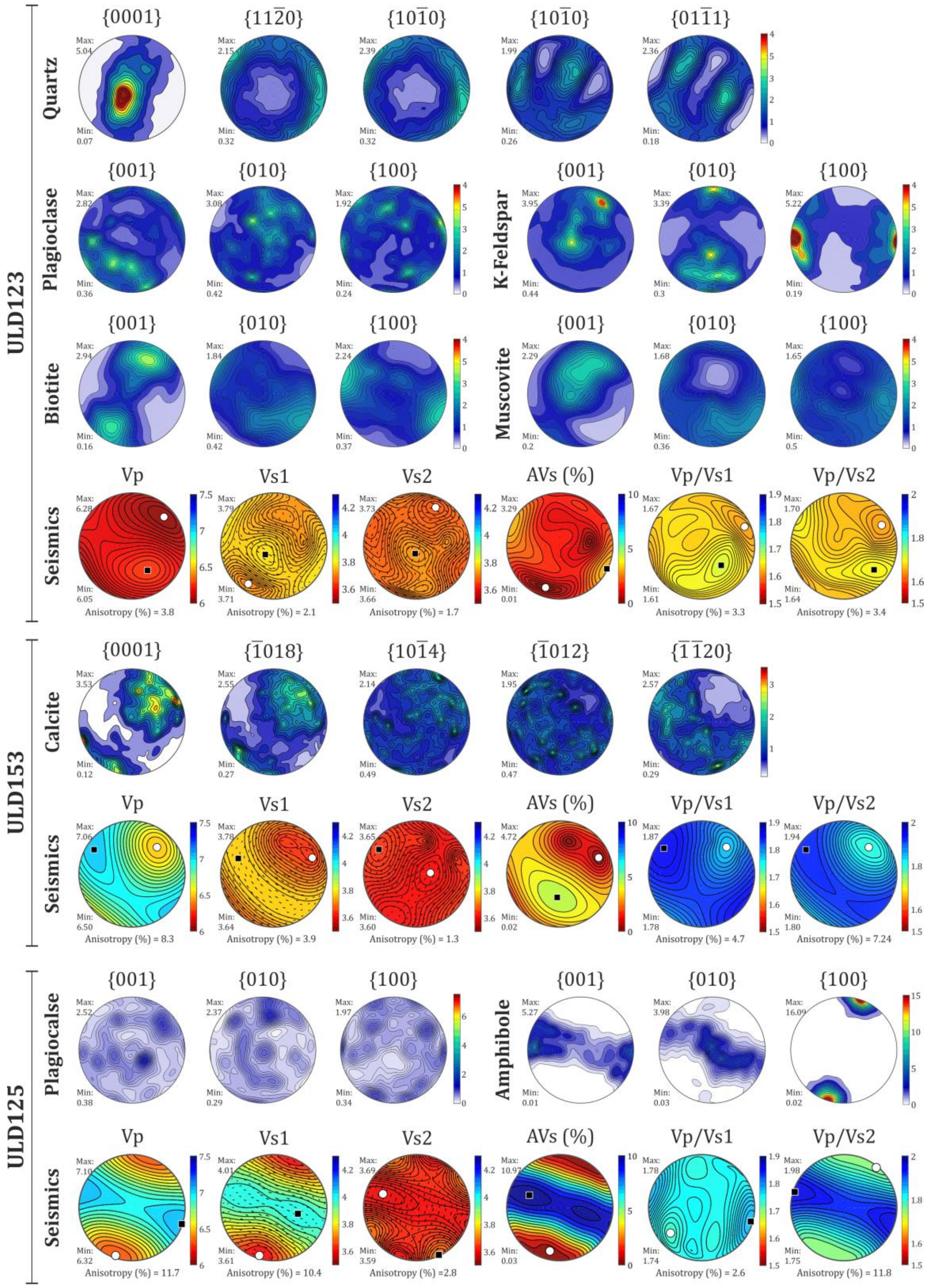

Figure 6.8. Samples found between 2 – 2.6km north of the Eskişehir Fault, locations indicated on cross section (Figure 6.12). All minerals in each sample are set to the same scale and also all seismics, regardless of lithology, are also scaled the same for comparison. Max and min on seismic property plots indicated by black square and white circle respectively. Vp – compressional p-wave velocity, Vs1, Vs2 – shear wave velocities with polarisation directions, AVs(%) – percentage shear wave anisotropy.

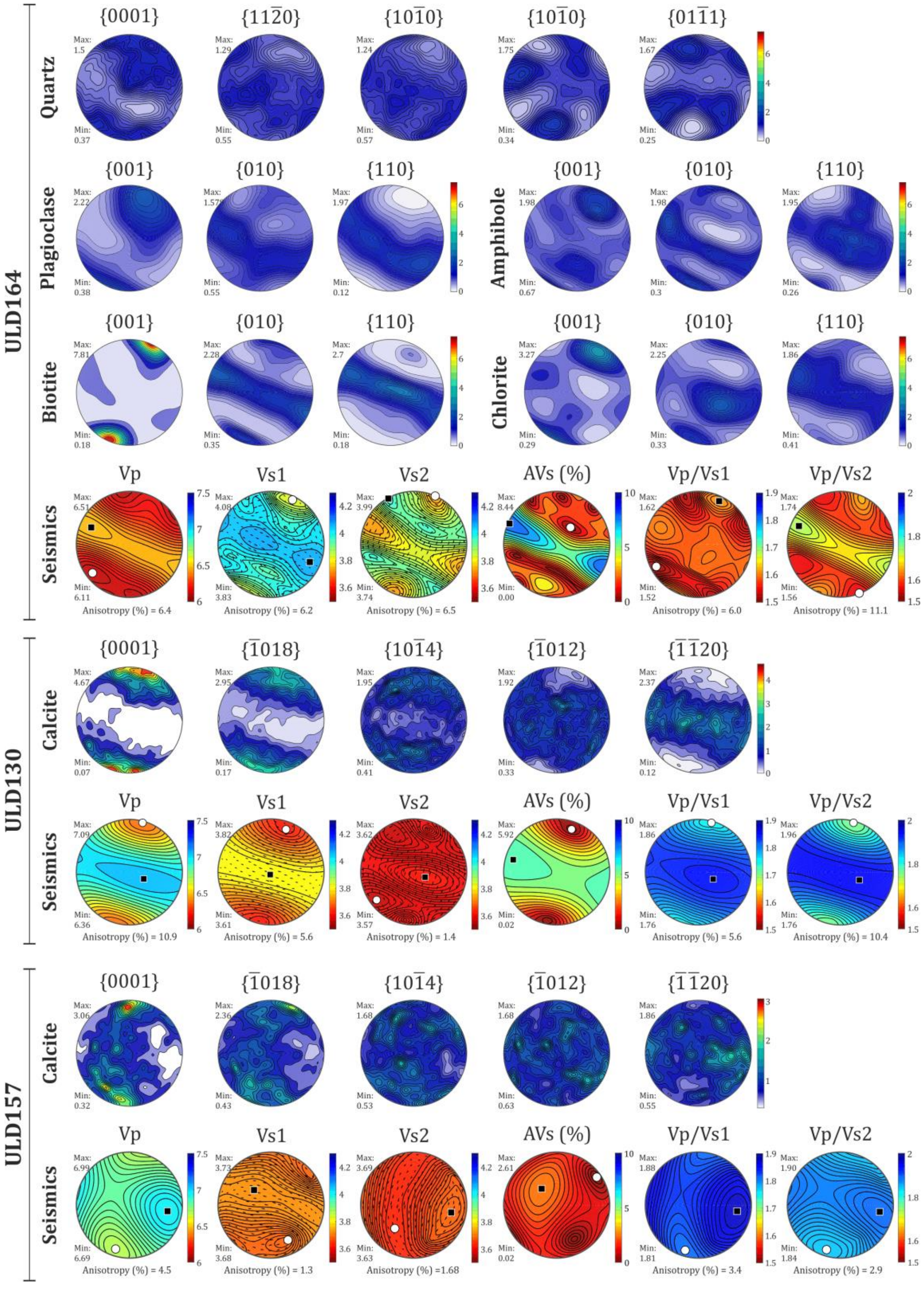

Figure 6.9. Samples found within 1km north of the Eskişehir Fault, locations indicated on schematic cross section on left hand side. All minerals in each sample are set to the same scale and also all seismics, regardless of lithology, are also scaled the same for comparison. Max and min on seismic property plots indicated by black square and white circle respectively. Vp – compressional p-wave velocity, Vs1, Vs2 – shear wave velocities with polarisation directions, AVs(%) – percentage shear wave anisotropy.

ULD153 is a marble, located 2.40km from the Eskişehir Fault. Again, the calcite c-axes define the foliation for the sample and fast Vp direction, Vs1 and high AVs are parallel to this. Vs2 is discordant to the foliation and follows the faint girdle joining the slightly diffuse maxima in the calcite c-axes. ULD125 is an amphibolite containing amphibole (66%) and plagioclase (33%) and is located at 2.61km north of the fault. In this sample it is very clear that amphibole is the controlling mineral on the seismic properties, with the plagioclase CPO being weak and hence contributing destructively to the overall seismic properties. Fast directions for Vp, Vs1 and maximum AVs% are all parallel to the foliation defined by amphibole. The anisotropy in this sample is the highest of all the samples analysed.

Samples ULD164, ULD130 and ULD157 are all within 1km north of the Eskişehir (Figure 6.9). ULD164 is located at 0.04km north of the Fault, and records a similar flow stress to the sample (ULD139) on the fault (Chapter 4, Figure 4.11). It contains quartz (45%), plagioclase (25%), biotite (18%), chlorite (7%) and amphibole (5%). The CPO for the biotite is the strongest of all the minerals, defining a strong lineation and foliation in the sample and quartz is relatively diffuse. The seismic properties display a foliation parallel to that defined by the biotite. The amphibole, chlorite and plagioclase all seem to add to the foliation parallel fast Vp, Vs1, slow Vs2 and high AVs, whereas the quartz contributes destructively due to its weak CPO.

ULD130 is another marble sample located at 0.70km (Figure 6.9). It is comprised of calcite and displays a relatively strong CPO, which is reflected in the seismic anisotropy. Again, a fast Vp and Vs1 lie parallel to foliation, as does the maximum anisotropy. ULD157 is another marble sample located at 0.89km north of the Eskişehir Fault (Figure 6.12) and comprises predominantly calcite with minor dolomite and quartz. The calcite c-axis CPO in this sample has two distinct point maxima (N-S) which are joined by a diffuse girdle. This girdle is clearly reflected in the seismics, creating a slow N-S girdle in Vp and Vs_2 properties. The Vs1 fast direction is parallel to the foliation defined by the calcite c-axis maxima but the misorientation with Vs_2 likely gives the non-foliation parallel anisotropy pattern.

6.3.3. Eskişehir Fault

This section of the Uludağ Massif represents the boundary of the South Uludağ Granite and the marble that is part of the rest of the exhumed massif. It is made up of alternating bands of intensely foliated marble and phyllosilicate rich rock (Figure 3.3). Two samples have been chosen from the fault zone, representing the two lithologies, one marble (ULD166) and one phyllosilicate (ULD139). ULD166 is made up entirely of calcite, and the CPO and seismic velocities reflect the alignment of the c-axes of the crystals (Figure 6.10).

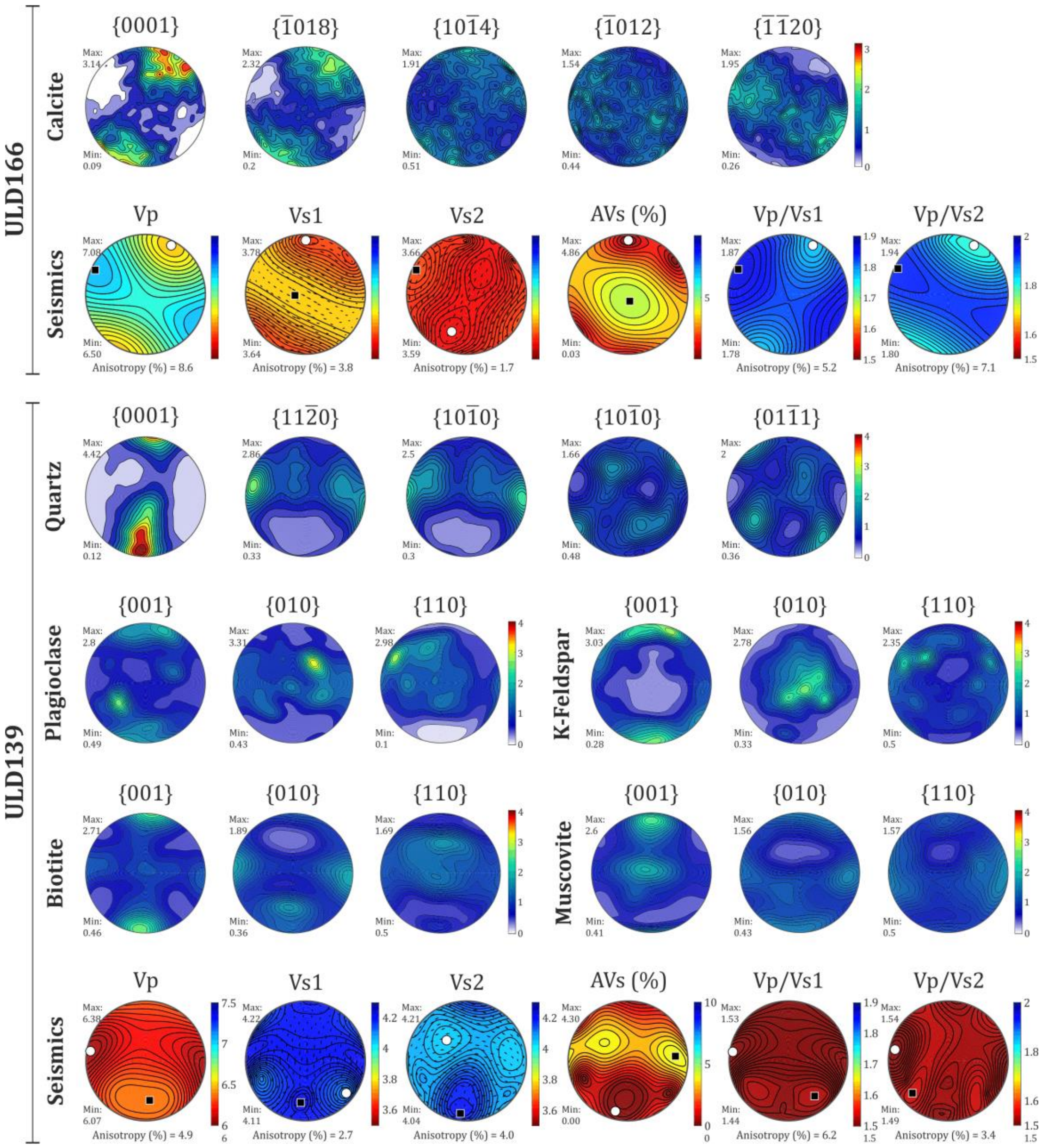

Figure 6.10. Samples found on the Eskişehir Fault, locations indicated on schematic cross section on left hand side. All minerals in each sample are set to the same scale and also all seismics, regardless of lithology, are also scaled the same for comparison. Max and min on seismic property plots indicated by black square and white circle respectively. Vp – compressional p-wave velocity, Vs1, Vs2 – shear wave velocities with polarisation directions, AVs(%) – percentage shear wave anisotropy.

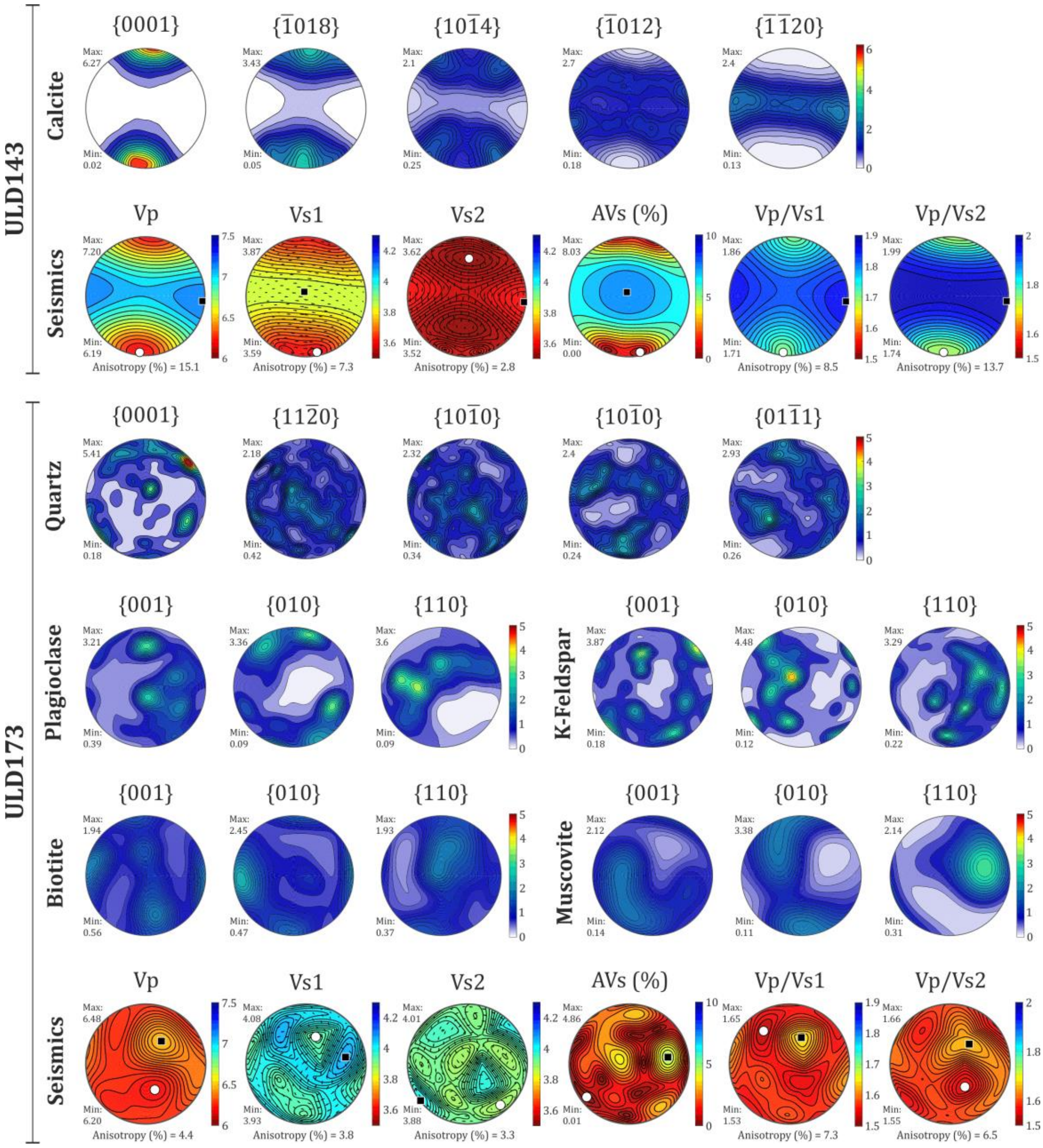

Figure 6.11. Samples found south of the Eskişehir Fault, locations indicated on schematic cross section on left hand side. All minerals in each sample are set to the same scale and also all seismics, regardless of lithology, are also scaled the same for comparison. Max and min on seismic property plots indicated by black square and white circle respectively. Vp – compressional p-wave velocity, Vs1, Vs2 – shear wave velocities with polarisation directions, AVs(%) – percentage shear wave anisotropy.

Once again, the maximum anisotropy in sample ULD166 runs parallel to the foliation in the fault zone, clearly recognised in the CPO.

ULD139 is made up of quartz (60%), plagioclase (15%), K-feldspar (12%), biotite (8%) and muscovite (5%). These minerals combine to produce a maximum 4.3% AVs anisotropy, and high anisotropy running parallel to the fabric, and foliation in the fault zone. The feldspar, especially plagioclase appear to destructively interfere with the strong foliation defined by the quartz, which seems to contribute mostly to the seismic properties. The mica, biotite and to a lesser extent, muscovite, contribute to the orientation of maximum Vp and AVs (%) shown in the seismics.

6.3.4. South of Eskişehir Fault

The South Uludağ Granite lies to the south of the Eskişehir Fault. It is deformed parallel to the fault, and displays varying intensities of mylonitic fabric. Within the granite, small outcrops of marble can be found, which are often highly deformed and display a well-developed CPO. Two samples from this section are displayed in Figure 6.11. ULD143 is furthest from the Eskişehir Fault at 1.6 km south. It displays a strong CPO, with a developed c-axis point maxima. As the sample is almost purely calcite, with only a little quartz (<1%), the seismic properties are controlled by the alignment of calcite crystals. This is seen clearly with the maximum percentage anisotropy (AVs) running parallel to the foliation within the massif, at approximately 100° in this sample. The strong alignment and monomineralic nature of this sample is reflected in the high maximum anisotropy of 8.03%.

ULD173 is a granite sample found slightly closer to the fault at 1.47km south. The sample contains; quartz (40%), plagioclase (40%), K-feldspar (8%), muscovite (7%) and biotite (5%). The quartz and feldspar, being the most abundant, seem to have the biggest influence on the seismic properties, the micas display quite weak fabrics. The seismic velocities do not show anisotropy relating to the general fabric of the shear zone; there are several maxima on the AVs(%) plot, possibly relating to the distributions of maxima in the quartz and feldspar CPOs. Overall there appears to be no discernible fabric in the seismic Vp or anisotropy plots.

6.4. Seismic modelling – Uludağ Massif

This section will present the results from seismic forward modelling of the Uludağ Massif using cross sections based on observations and maps presented in Chapter 3. The samples presented in the previous section will be used to populate 2.5D seismic models based on these cross sections, allowing receiver functions to be calculated from the seismogram traces.

6.4.1. Geological cross sections

Field observations have been made in this study and the cross section in Figure 6.12 is a compilation of these field observations. The cross section runs parallel to the two sample transects, and is shown in the map in Figure 6.12. A larger version of the map is shown in Chapter 3, Figure 3.1. Briefly, the massif comprising of gneiss and marble is bound by two faults, the Eskişehir to the south and the Bursa Fault to the north. To the south of the massif there is the deformed granite, the South Uludağ Granite. The massif and the granite are what makes up the exhumed ductile shear zone.

Due to modelling constraints, that will be discussed later, the 2.5D model had to be significantly simplified in order to assess the seismic response from each part of the massif. The ductile shear zone starts with the South Uludağ Granite in the south and ends at the Bursa Fault in the north. One, representative, sample was taken from each lithological unit: the South Uludağ Granite (ULD173), marble on the northern side of the Eskişehir Fault (ULD130), gneiss (ULD46) and marble on the southern side of the Bursa Fault (ULD49) (Figure 6.12, locations Chapter 3, Figure 3.1). This approach means that the properties of each unit are based on one sample, and any heterogeneity within the unit will not be expressed. This is not necessarily a problem however as these heterogeneities are likely not of sufficiently large scales to influence the seismic response. Samples from the localised Eskişehir Fault are not included because, again, they represent a section that is too small (~20-30m) and could not be picked up in a real seismic study.

The seismic properties of all the mentioned samples are shown in Figure 6.6-Figure 6.11. The seismic properties (defined as the elastic tensor) for each sample were input into the fault zone in the model cross section shown in Figure 6.13. Within this model regions 1, 2 and 4 are isotropic crust (ρ = 2700kg m^{-3}, Vp = 6400m s^{-1}, Vs = 3657 m s^{-1}), the fault zone (region 3) is populated with the properties of the previously mentioned samples, and layer 5 is the isotropic mantle (ρ = 3340kg m^{-3}, Vp = 8100m s^{-1}, Vs = 4500m s^{-1}). The properties for the wall rock surrounding the fault zone and the mantle were chosen based on average properties from the study on the NAF (Kahraman et al., 2015).

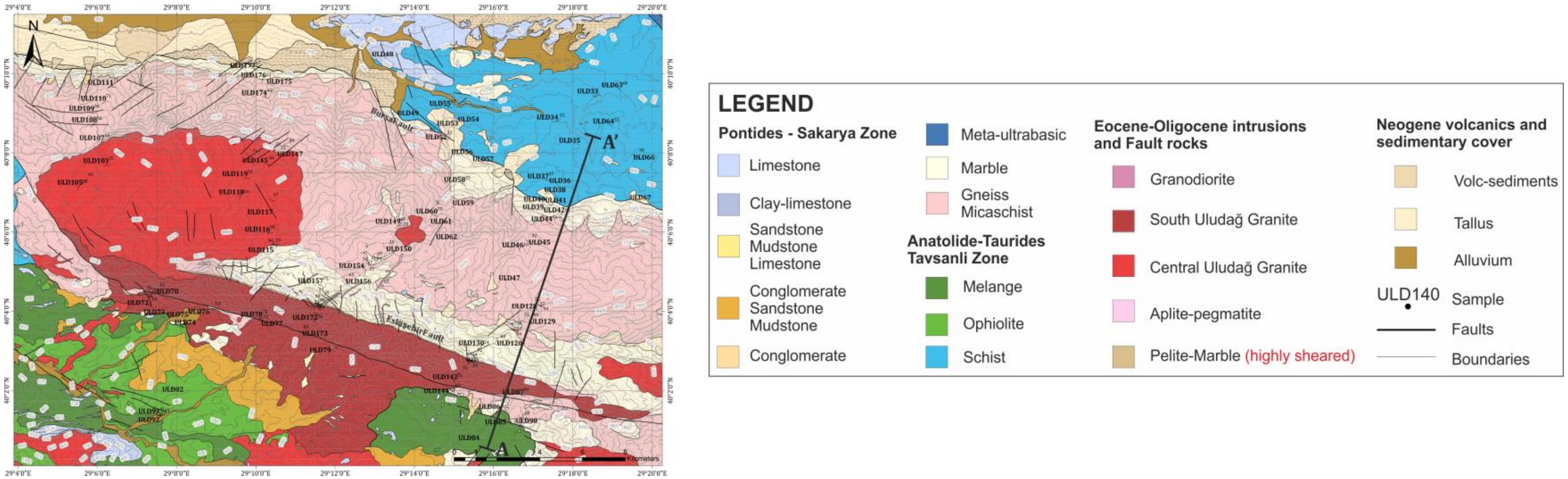
N
29°4'0"E
29°6'0"E
29°8'0"E
29°10'0"E
29°12'0"E
29°14'0"E
29°16'0"E
29°18'0"E
29°20'0"E
Bursa Fault
Eskişehir Fault
A
A'
Kilometers
LEGEND
Pontides - Sakarya Zone
Limestone
Clay-limestone
Sandstone Mudstone Limestone
Conglomerate Sandstone Mudstone
Conglomerate
Meta-ultrabasic
Marble
Gneiss Micaschist
Anatolide-Taurides Tavsanli Zone
Melange
Ophiolite
Schist
Eocene-Oligocene intrusions and Fault rocks
Granodiorite
South Uludağ Granite
Central Uludağ Granite
Aplite-pegmatite
Pelite-Marble (highly sheared)
Neogene volcanics and sedimentary cover
Volc-sediments
Tallus
Alluvium
ULD140 Sample
Faults
Boundaries

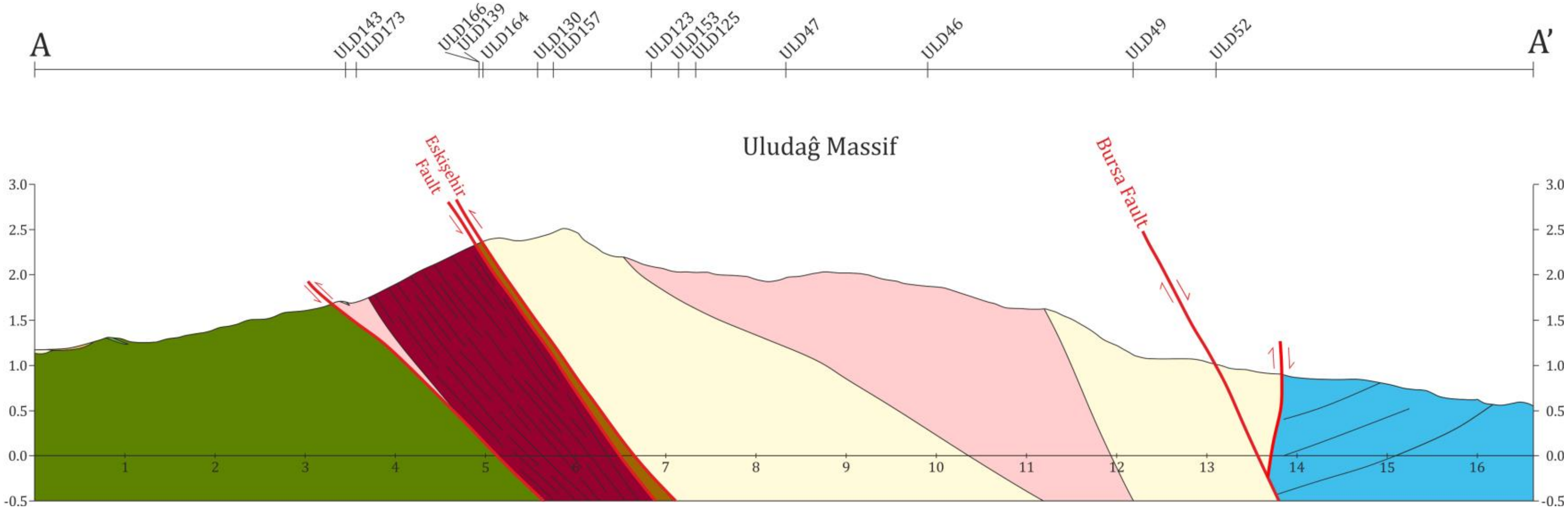
A
A'
ULD143
ULD173
ULD166
ULD139
ULD164
ULD130
ULD157
ULD123
ULD153
ULD125
ULD47
ULD46
ULD49
ULD52
Uludaĝ Massif
Eskişehir Fault
Bursa Fault
3.0
2.5
2.0
1.5
1.0
0.5
0.0
-0.5
1
2
3
4
5
6
7
8
9
10
11
12
13
14
15
16

Figure 6.12. Cross section across the Uludağ Massif. A – A' shown on map. Sample numbers relate to the samples used in the models of the Uludağ Massif and those relating to the NAF (Section 6.4). The inset map is that shown in Figure 3.1 (Akbaş et al.).

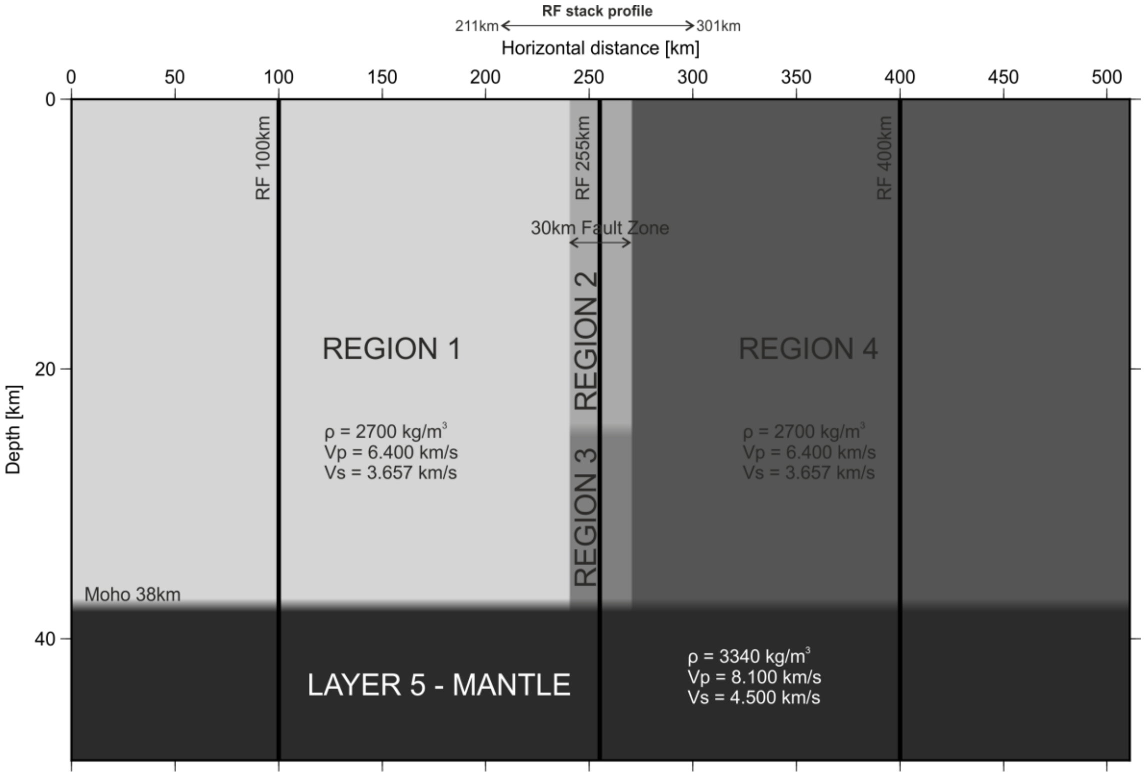

Figure 6.13. Model cross section. Regions 1, 2 and 4 are average isotropic crust. Region 3 is the fault zone populated with seismic properties of individual samples. Layer 5 is the mantle, with the Moho at 38km. Properties of wall rock and mantle are indicated in the figure, for discussion see Section 6.4.1. Vertical lines indicate RFs taken for azimuthal plots. Model parameters are displayed in Table 6-1 and explained in Section 6.5.2.

6.4.2. Model setup

The elastic tensor of the four samples (ULD173, ULD130, ULD46 and ULD49) were used to individually populate region 3 of the 2.5D model shown in Figure 6.13. To pick up any azimuthal variation and to avoid bias in the receiver functions, 18 events were run at 020° intervals starting with event 1 at an azimuth of 000° (Figure 6.14). The parameters for the numerical setup are shown in Table 6-1. From the dominant wavelength (λ) of 10.0km in the input parameters (Table 6-1) and the maximum velocity of 6.4km s^{-1} for the crust (V_{max}) the maximum frequency (F_{max}) is 0.64Hz using Equation 6.1

$$F_{max} = V_{max}/\lambda \qquad (6.1)$$

There should be at least 4 grid points per wavelength at the shortest wavelength from the equation:

$$dx = \frac{Vs_{min}}{(dx\ x\ F_{max})} \qquad (6.2)$$

Where n is the number of grid points (ie. 4) and Vs_{min} is the minimum S-wave velocity (3.675km s^{-1} – Section 6.4.1). Equation 6.2 gives dx = 1.44km meaning a grid spacing of 1km is appropriate. The time spacing (dt) should be short enough so that the wave travels less than 50% of the grid spacing in one time step. Using the equation:

$$dt = \frac{dx}{(2 \, x \, V_{max})} \qquad (6.3)$$

Where dx is 1 (grid spacing) and V_{max} is 6.4km s^{-1} and 3.675km s^{-1} for Vp and Vs respectively (Section 6.4.1). This gives 0.078s for Vp and 0.13s for Vs. The time increment (dt - Table 6-1) is 0.0625s which is appropriate for both the P-wave and the S-wave. As the receiver functions are Ps converted at the Moho this is still suitable as this study is primarily concerned with the S-wave velocity in the crust. The slowness of 0.04 s/km describes an incidence angle of 18.9° with the Moho and 8.4° with the surface in the wall rock.

nx	dx (km)	nz	dz (km)	nt	dt (s)	nb_tp	λ (km)	Slowness (s/km)
512	1	50	1	512	0.0625	20	10.0	0.04

Table 6-1. Model parameters. nx – number of horizontal grid points, dx – distance between horizontal grid points, nz – number of vertical grid points, dz – distance between vertical grid points, nt – time increments, dt – time sampling (s), nb_tp – number of points tapered at each side, λ – dominant wavelength.

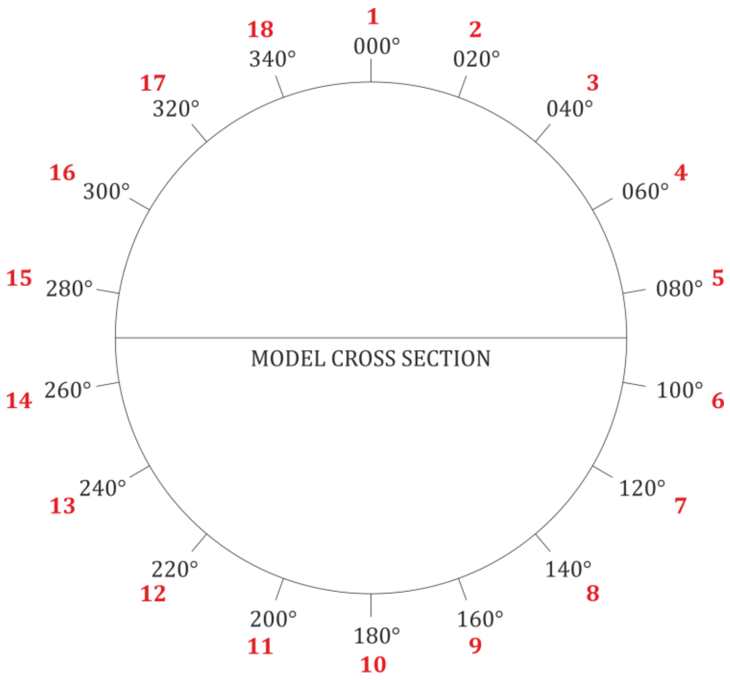

Figure 6.14. Event distribution around the model cross section. Back azimuth in degrees, corresponding event number is shown in red.

6.4.3. Testing model setup

In order to test the model setup a number of test models were run. The first with a simple 2-layer model of isotropic crust above isotropic mantle, the Moho at 38km (Figure 6.15). The second is a 3 layer model with an isotropic upper crust, and isotropic lower crust and an isotropic upper mantle (Figure 6.16). The third has three regions, representing a vertical structure, that all have the same isotropic properties above the mantle with a Moho at 38km to ensure the boundaries of the model do not influence the seismic response (Figure 6.17).

In the azimuthal plot for the first 2 layer model (Figure 6.18), the first P-wave arrival is visible at ~0.5s and the Ps Moho is clearly distinguishable at ~4.5s. In the 3 layer model (Figure 6.19) again the first P-wave arrival can be seen at 0.5s, the top on the mid-crust (layer 2) at ~1.5s and the Ps conversion from the Moho at ~4s. The Moho arrival is slightly quicker in the three layer model due to the faster P- and S-wave properties of the mid to lower crust (layer 2). The third model with a vertical structure has a similar response to the 2 layer model (Figure 6.20). This is due to all three regions of the crust having the same properties. All three test models show what would be expected given the input parameters and the third model clearly shows that a laterally varying model does not influence the output providing the parameters remain the same. This means any variation in the response for region 2 in subsequent models is a factor of the properties populating that region.

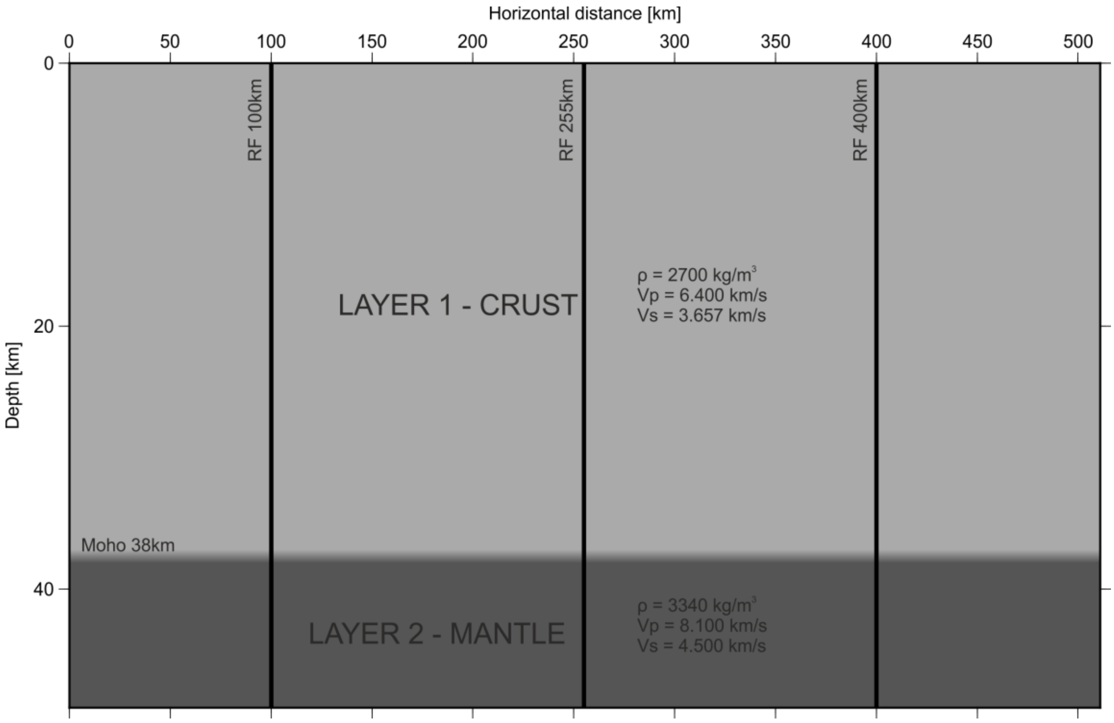

Figure 6.15. Model cross section for test 1 – the 2 layer isotropic crust (layer 1) and isotropic mantle model (layer 2).

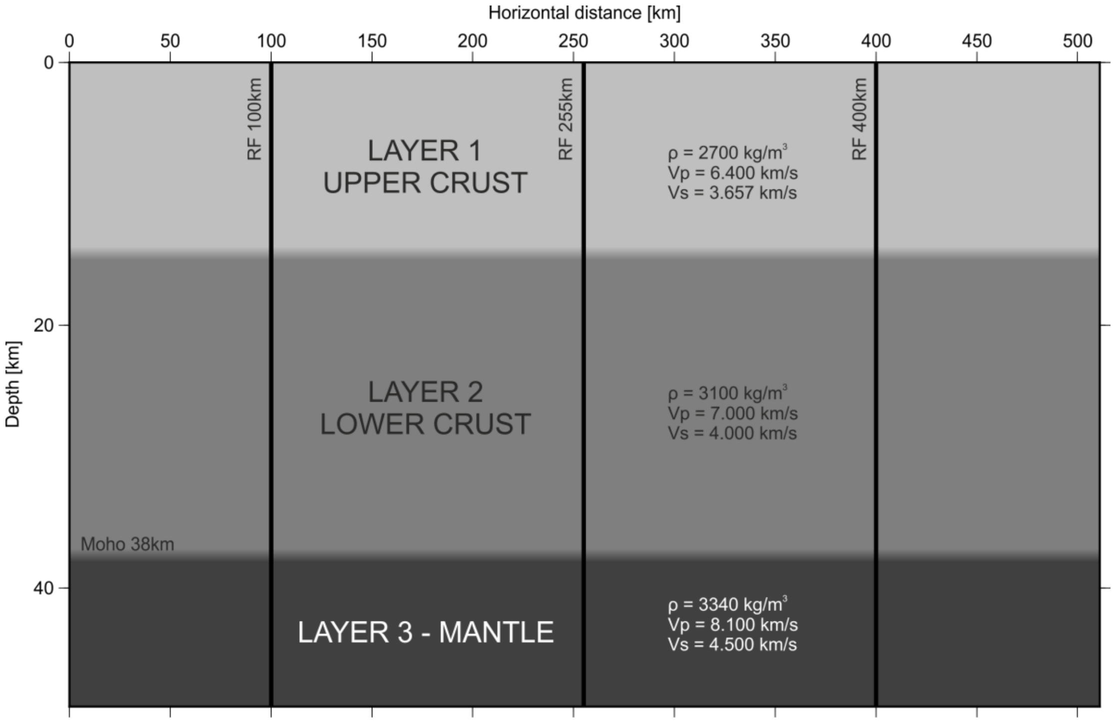

Figure 6.16. Model cross section for test 2 – 3 layer isotropic upper crust (layer 1), lower crust (layer 2) and isotropic mantle (layer 3).

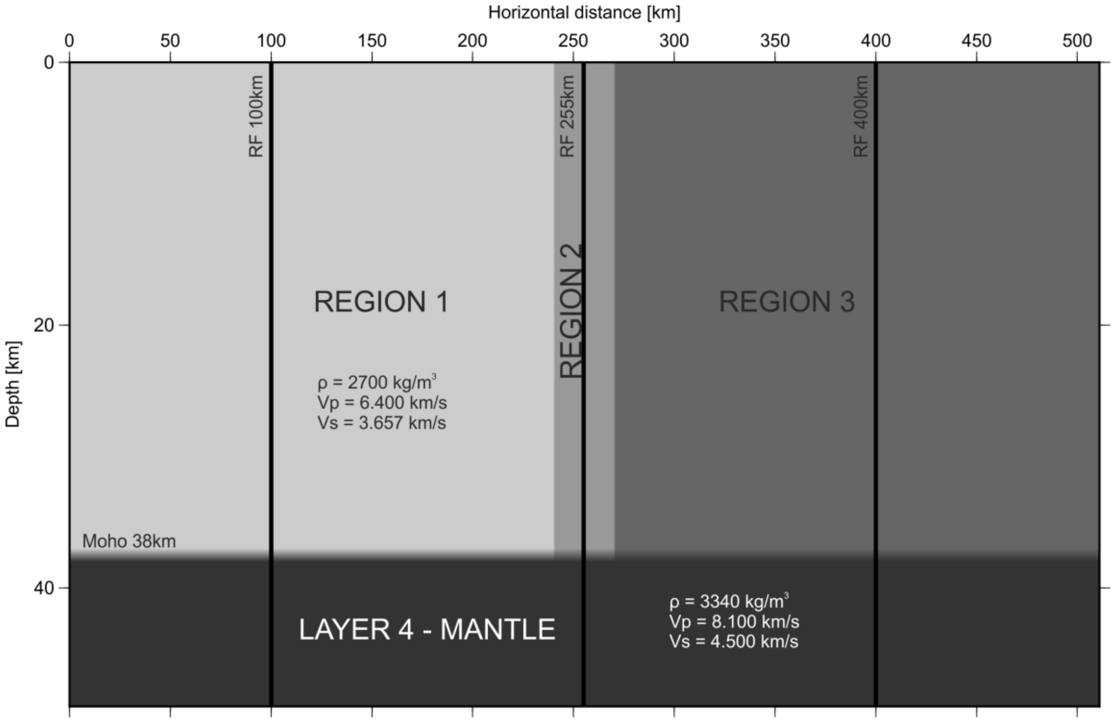

Figure 6.17. Model cross section for test 3 – crust split by a vertical feature, region 1, 2 and 3 all have the isotropic properties (indicated in region 1), above an isotropic mantle (layer 4).

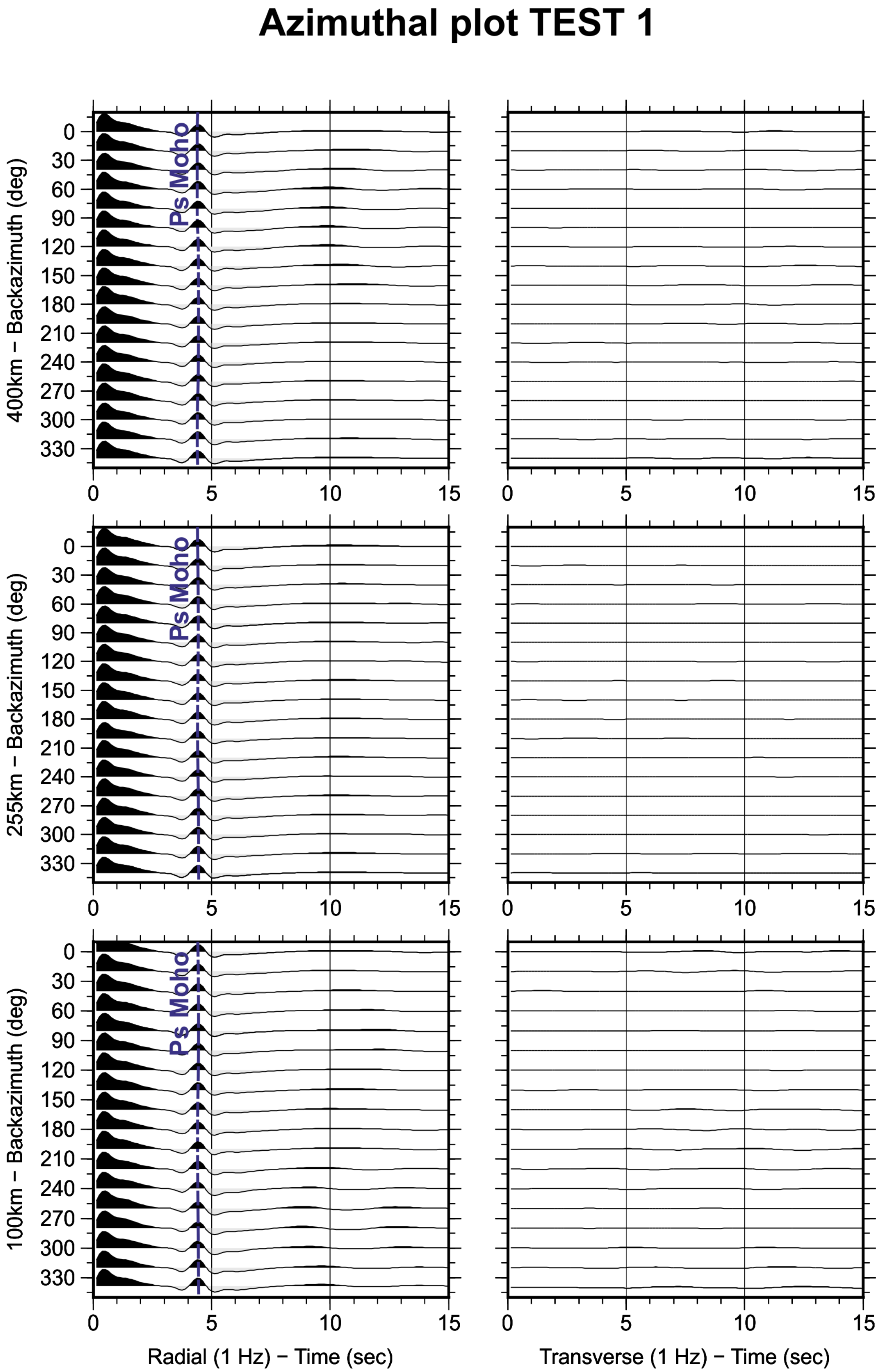

Figure 6.18. Azimuthal plot for test 1, the two layer model, RFs taken laterally at 100km, 255km and 400km (Figure 6.15). Blue dashed line indicates the Moho.

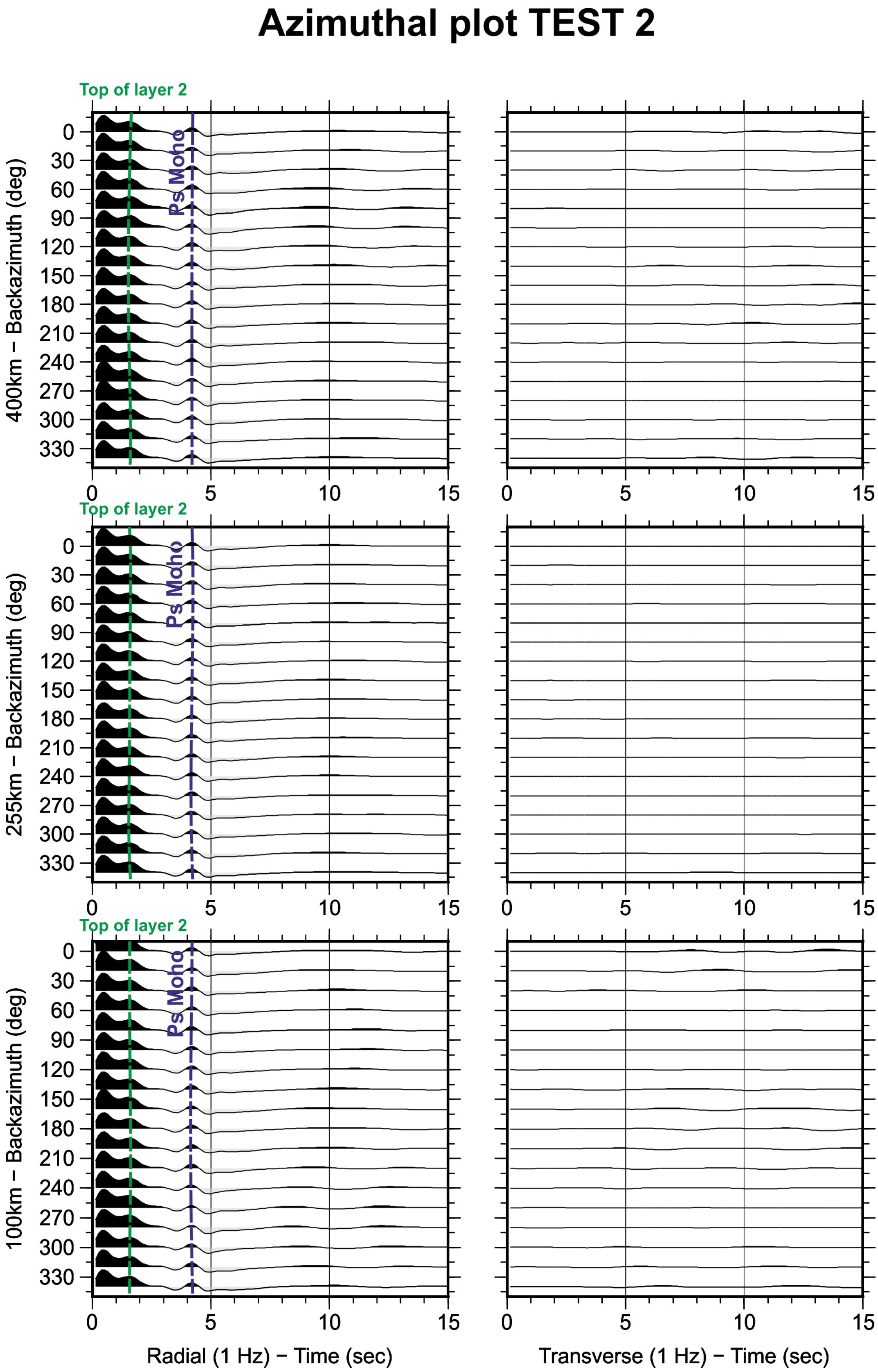

Figure 6.19. Azimuthal plot for test 2, the three layer model, RFs taken laterally at 100km, 255km and 400km (Figure 6.16). Blue dashed line indicates the Moho and the green line is the response from the top of layer 2.

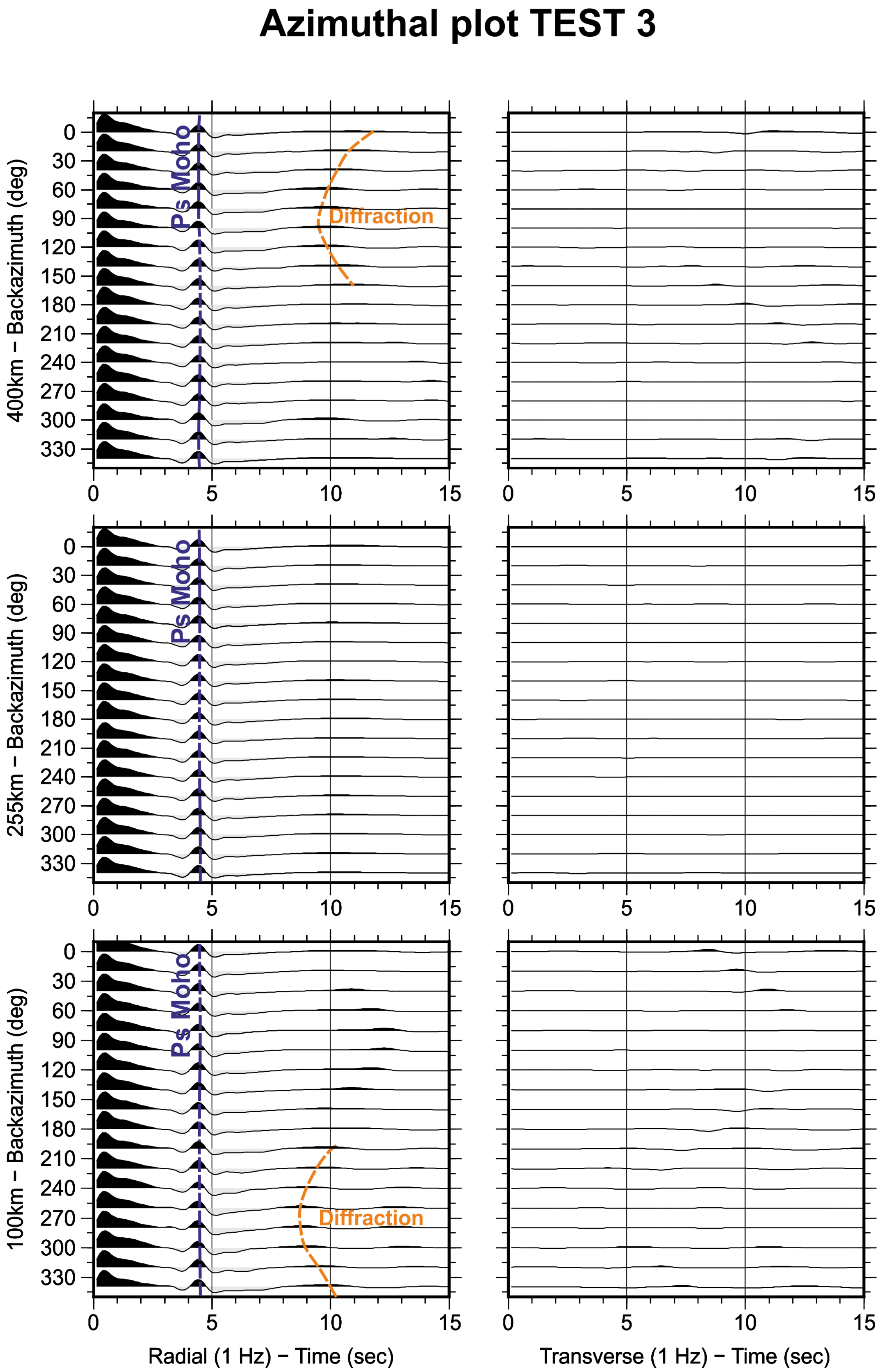

Figure 6.20. Azimuthal plot for test 3, the two layer model, RFs taken at 100km, 255km and 400km (Figure 6.17). Blue dashed line indicates the Moho and orange indicates diffractions from the sides of the fault zone.

6.4.4. Receiver functions

This section presents receiver function (RF) back azimuthal plots for the 2.5D model (Figure 6.13) populated by the elastic tensors of each of the four samples, outlined in Section 6.5.1, in turn (seismic properties of each sample shown in Figure 6.21 -Figure 6.24). RFs were sampled at locations of 100km, 255km and 400km along the profile for each model, sample points indicated by the lines on Figure 6.13. The receiver function at location 255km is always within the fault zone. For the plotting, the amplitudes at 100km and 400km are multiplied by 10 in order to see the arrivals and at 255km the amplitudes are multiplied by 2 for clarity (x10 produces messy plots as the amplitudes are too big to discern features).

At 100km and 400km all four models display similar radial component azimuthal plots for the receiver function showing the Ps from the Moho at ~4.5s and some diffraction between 10-15s. The variation between the models is evident in the RF taken at 255km, within the fault. In the 255km RFs the Ps Moho can still be seen in all 4 models at ~4s, as well as the signal from the top of region 3 at ~2.5s (Figure 6.21 -Figure 6.24). The Moho can be seen to be split into two signals at 255km from each of the four models, signifying the presence of a fast and slow shear wave and indicating the presence of anisotropy. In the transverse component each sample displays strong polarity reversal in the azimuthal plots indicative of anisotropy. All four models also contain positive signals at ~ 7.5 and ~12.5 seconds.

6.4.5. Receiver function stacks

RF stacks for each model were calculated at 1km spacing starting at 211km, across the fault zone to 301km (Figure 6.25 and Figure 6.26). The stacks consist of stacked trace back azimuths between 000° and 120° based on earthquake locations used in the RF study on the NAF, which are predominantly in the NE quadrant, as these synthetic receiver functions will be compared to this study (Kahraman et al., 2015) (Figure 6.4).

In all four models the wall rock to the fault zone show similar amplitude arrivals at similar times, eg the Moho at ~4.5s and the signal from the top of region 3 at ~2.5s (Figure 6.25 - Figure 6.28). Also present in each model is the low frequency, long period waves towards the edges of the fault zone, between 240km-245km and 265km-270km. For all four samples the Ps Moho is visible throughout some, if not all of the fault zone, but with small time variations. Again, in all four, there are other positive arrivals at ~6s and ~12s which are multiples from the top of region 3 and the Moho. The signal from the Moho is again split into two, the fast and slow shear waves, indicating anisotropy.

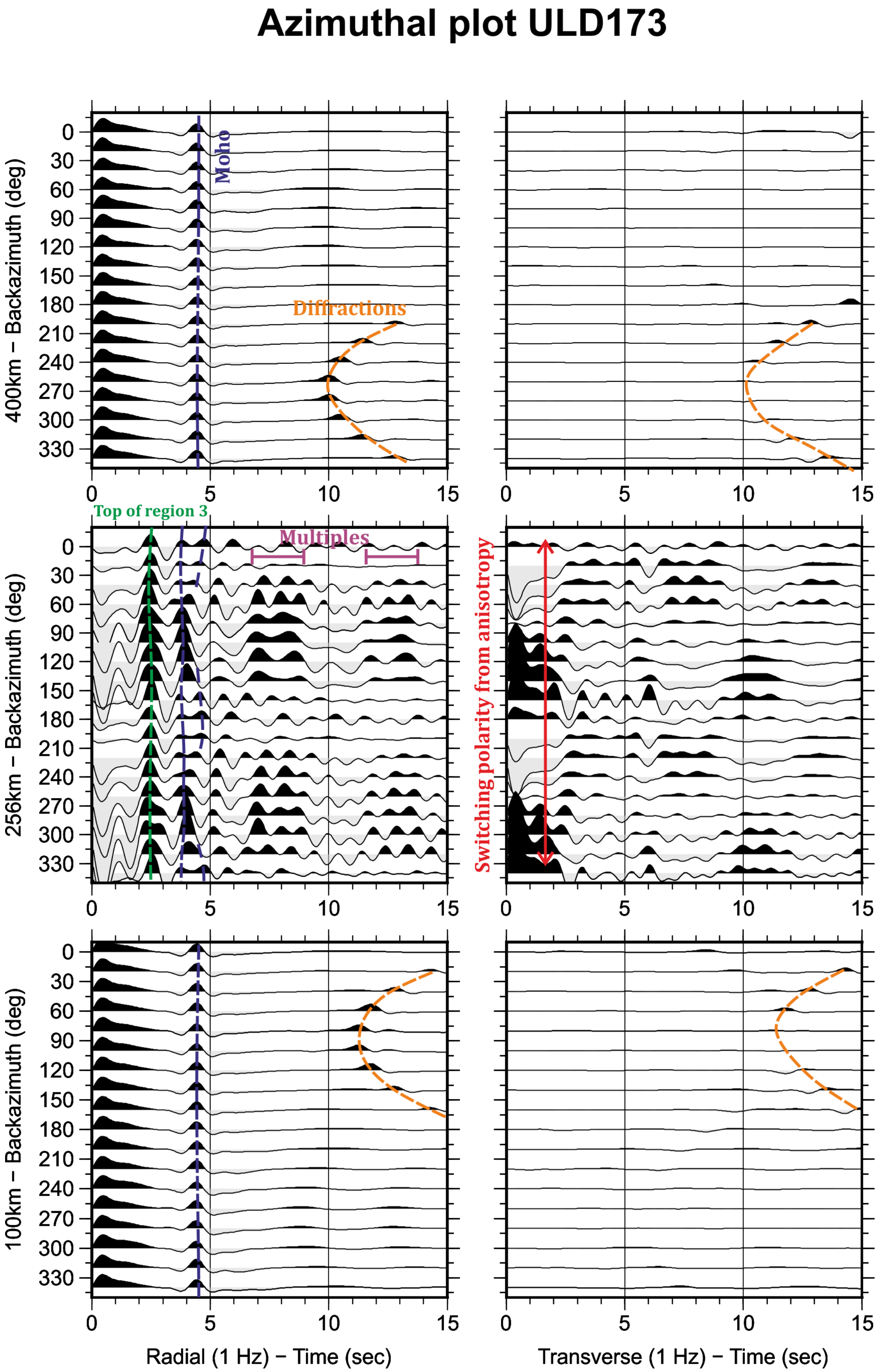

Figure 6.21. Transverse and radial azimuthal plot of 2.5D model with locations (100km, 255km and 400km) indicated by vertical lines on Figure 6.13. The elastic tensor of sample ULD173 granite populating the fault zone in region 3 (Figure 6.13). The Moho is indicated by the blue line and the orange highlights diffractions from the fault edges.

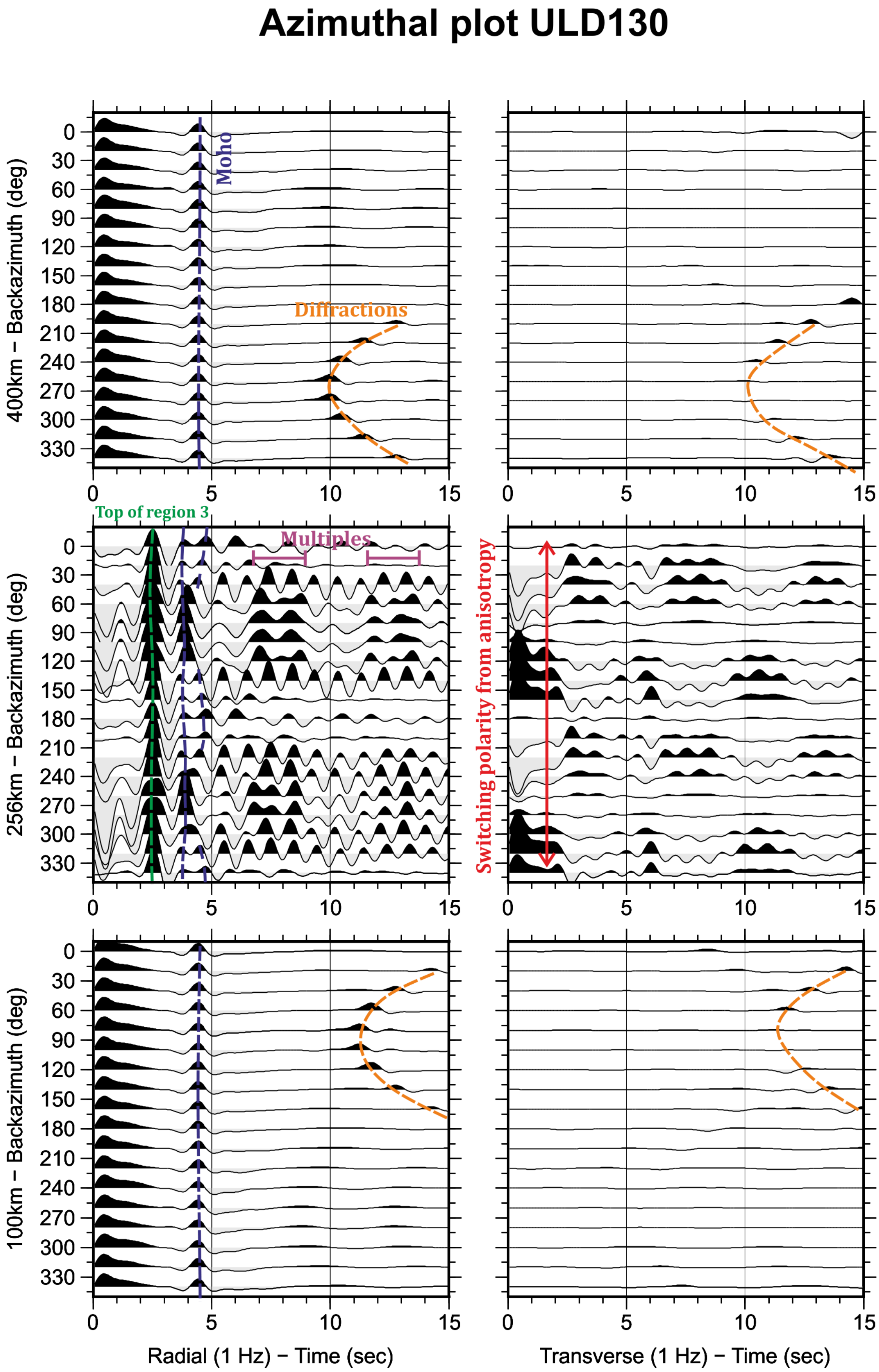

Figure 6.22. Transverse and radial azimuthal plot of 2.5D model with locations (100km, 255km and 400km) indicated by vertical lines on Figure 6.13. The elastic tensor of sample ULD130 marble populating the fault zone in region 3 (Figure 6.13). The Moho is indicated by the blue line and the orange highlights diffractions from the fault edges.

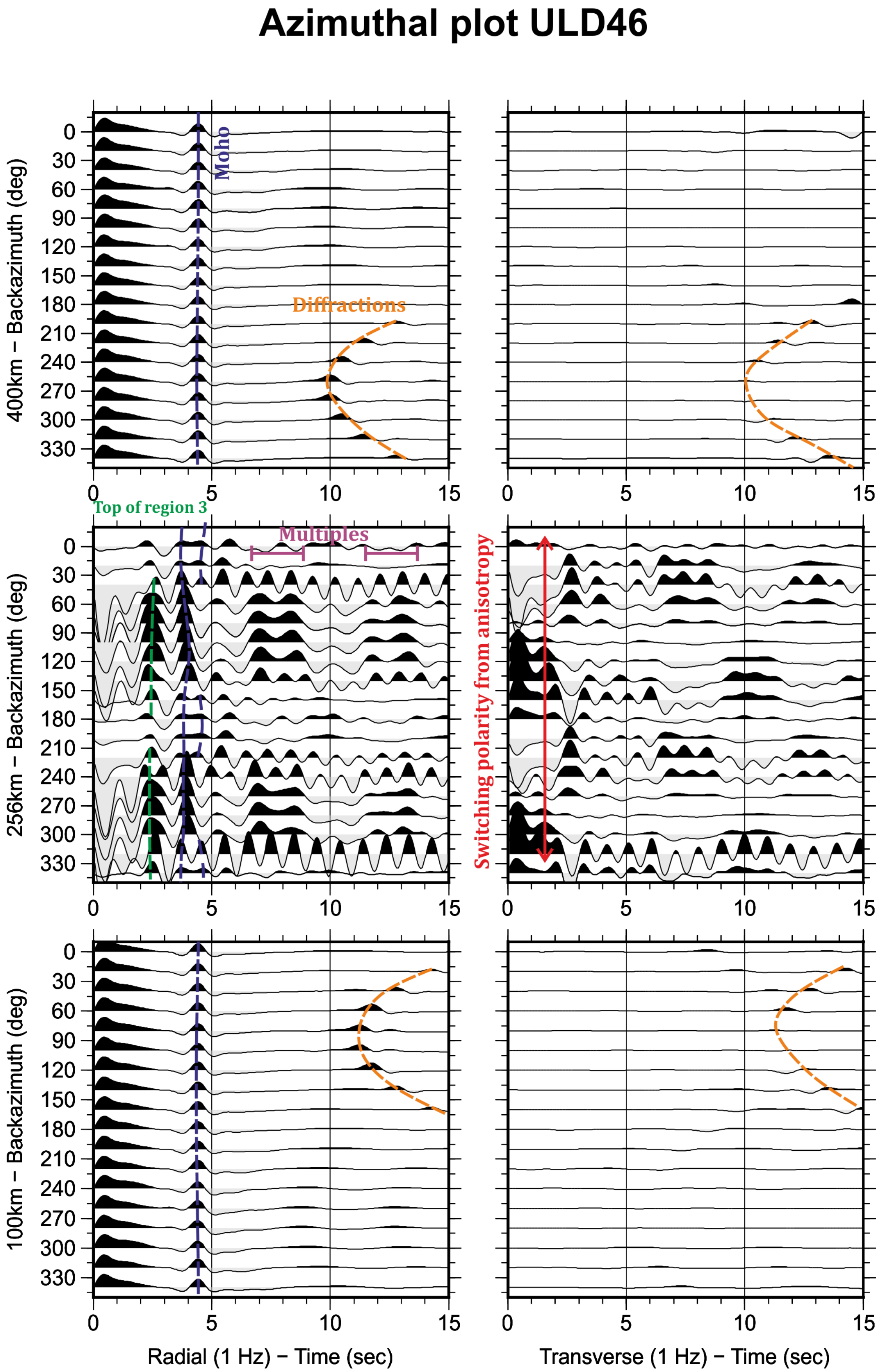

Figure 6.23. Transverse and radial azimuthal plot of 2.5D model with locations (100km, 255km and 400km) indicated by vertical lines on Figure 6.13. The elastic tensor of sample ULD46 gneiss populating the fault zone in region 3 (Figure 6.13). The Moho is indicated by the blue line and the orange highlights diffractions from the fault edges.

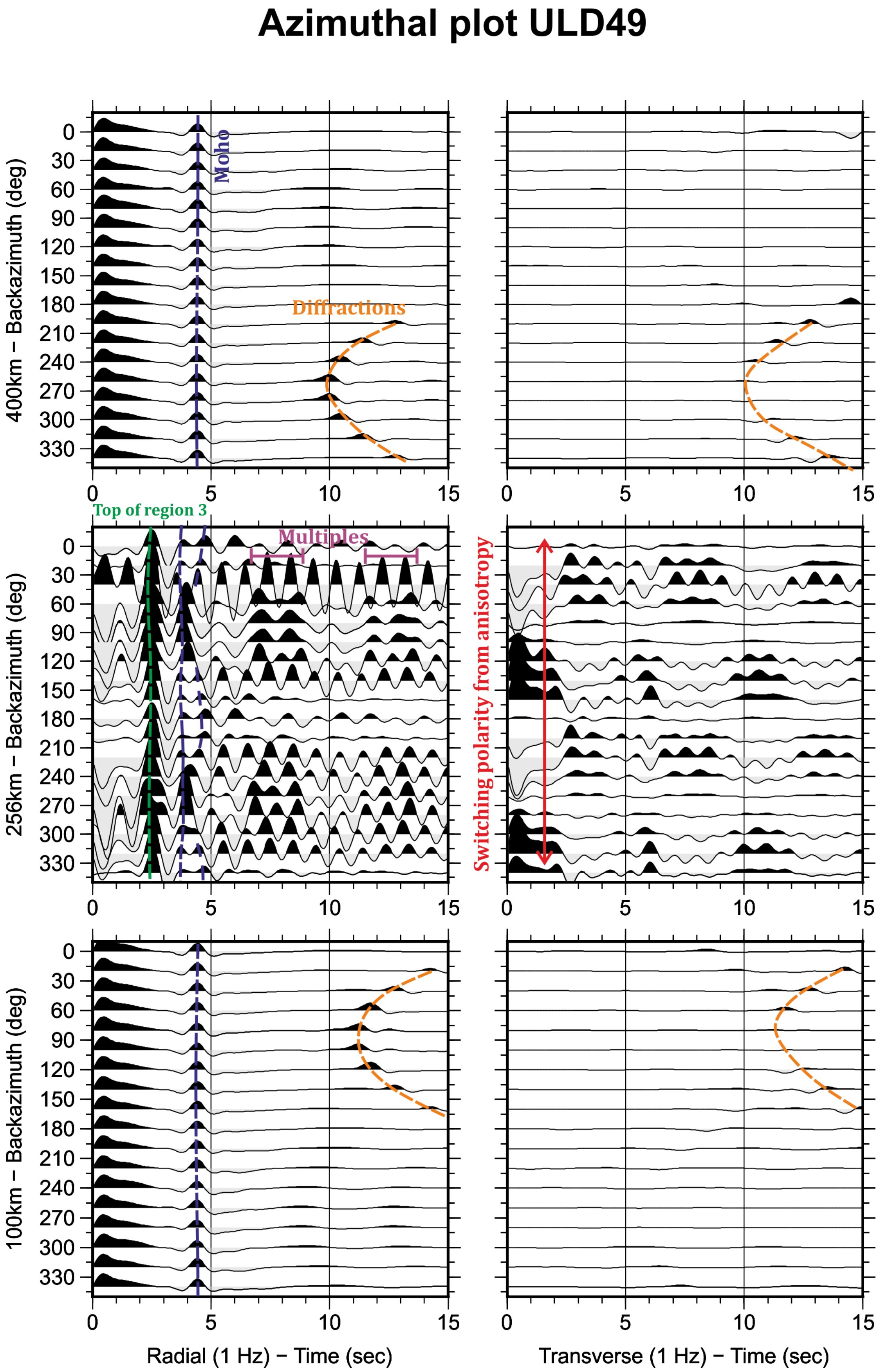

Figure 6.24. Transverse and radial azimuthal plot of 2.5D model with locations (100km, 255km and 400km) indicated by vertical lines on Figure 6.13. The elastic tensor of sample ULD49 marble populating the fault zone in region 3 (Figure 6.13). The Moho is indicated by the blue line and the orange highlights diffractions from the fault edges.

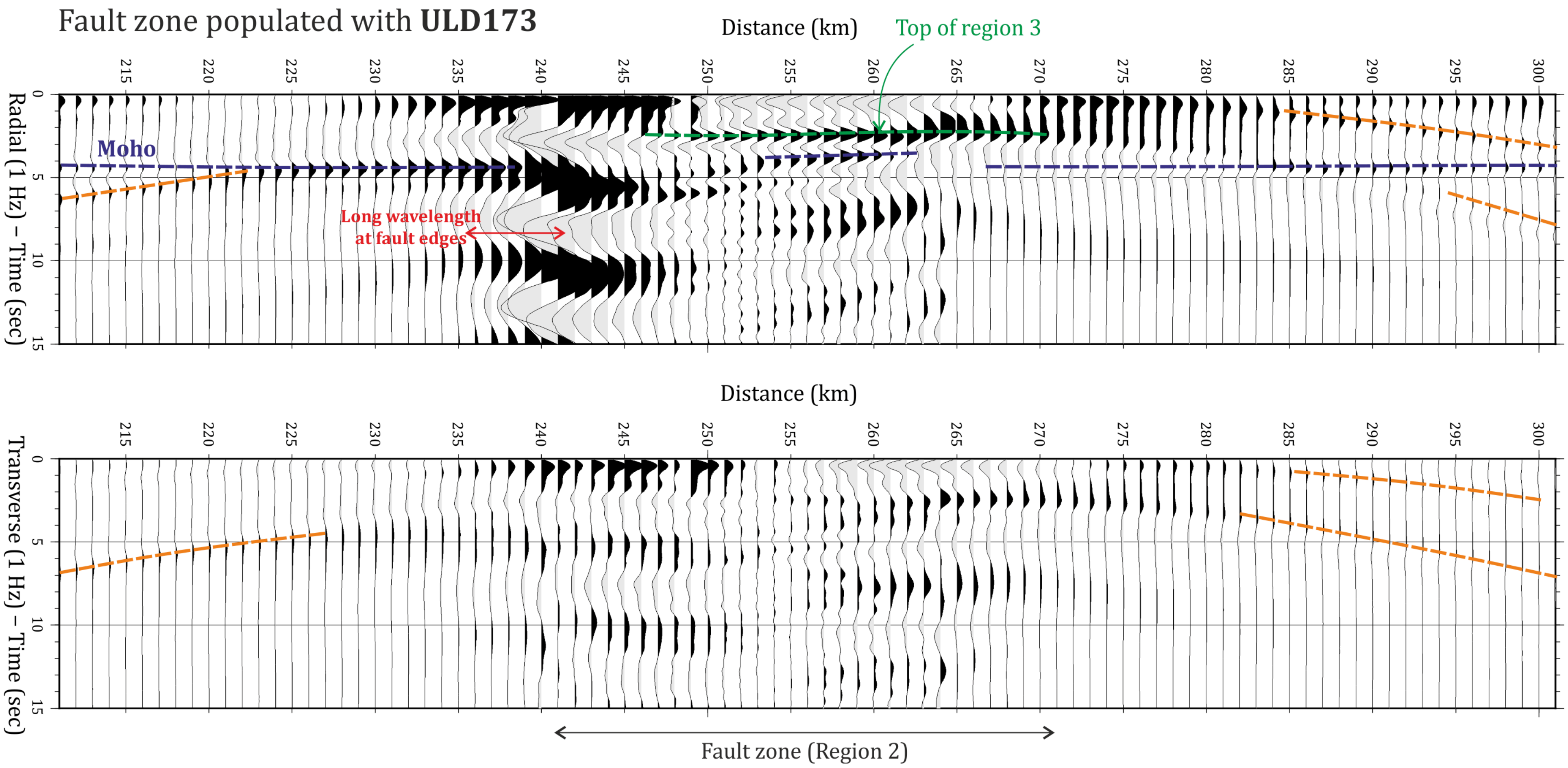

Figure 6.25. RF Stacks of the model in Figure 6.13 populated with sample ULD173 (granite) in region 2, the fault zone. RFs sampled at 1km intervals over the fault zone and orientated W-E, from 211km – 301km. Azimuths between 0°-120° stacked to represent azimuths used in NAF RF study (Kahraman et al., 2015) (Figure 6.4). Blue line indicates the Moho and orange are diffractions off the edges of the fault.

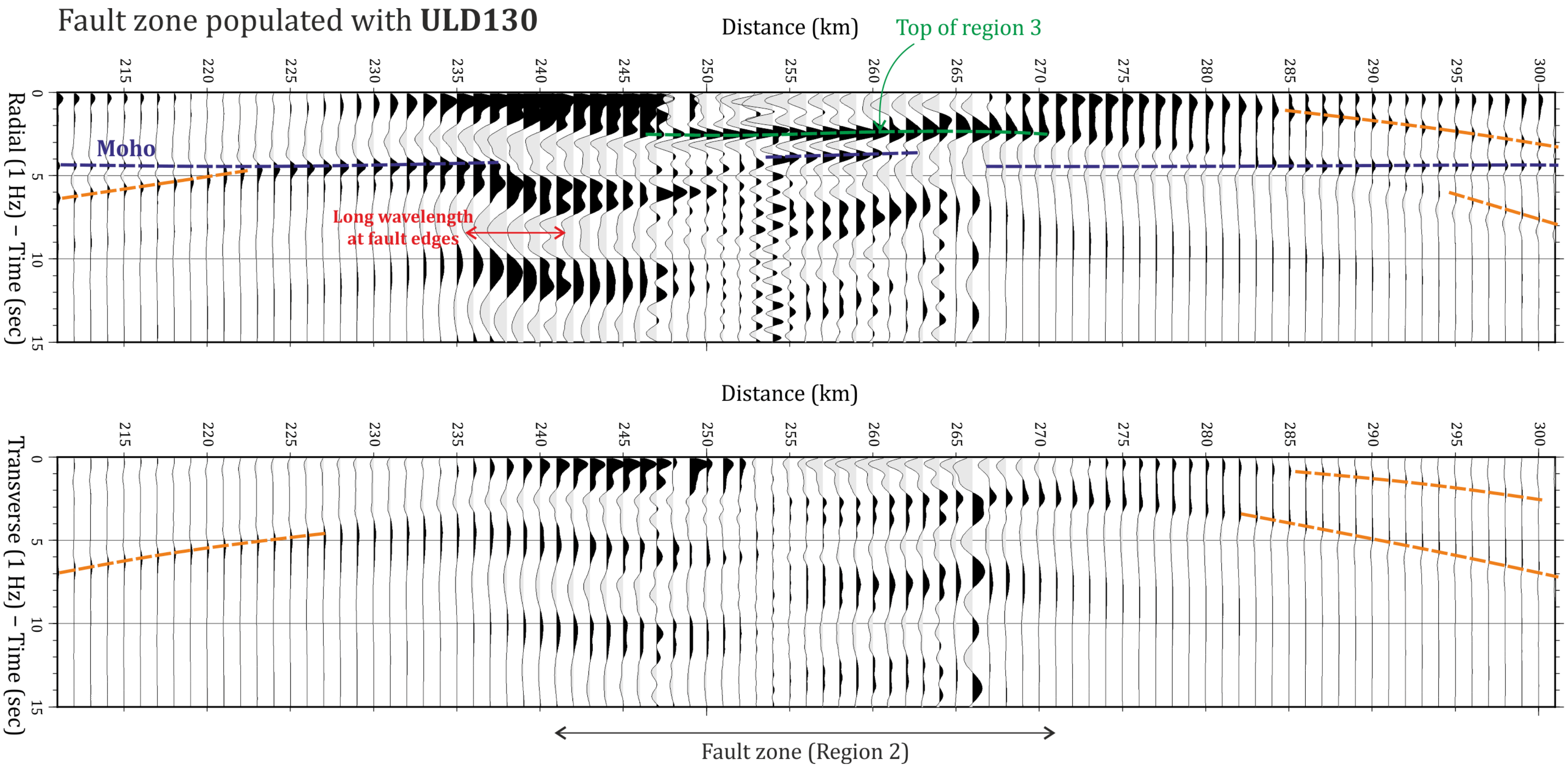

Figure 6.26. RF Stacks of the model in Figure 6.13 populated with sample ULD130 (marble near Eskişehir Fault) in region 2, the fault zone. RFs sampled at 1km intervals over the fault zone and orientated W-E, from 211km – 301km. Azimuths between 0°-120° stacked to represent azimuths used in NAF RF study (Kahraman et al., 2015) (Figure 6.4). Blue line indicates the Moho and orange are diffractions off the edges of the fault.

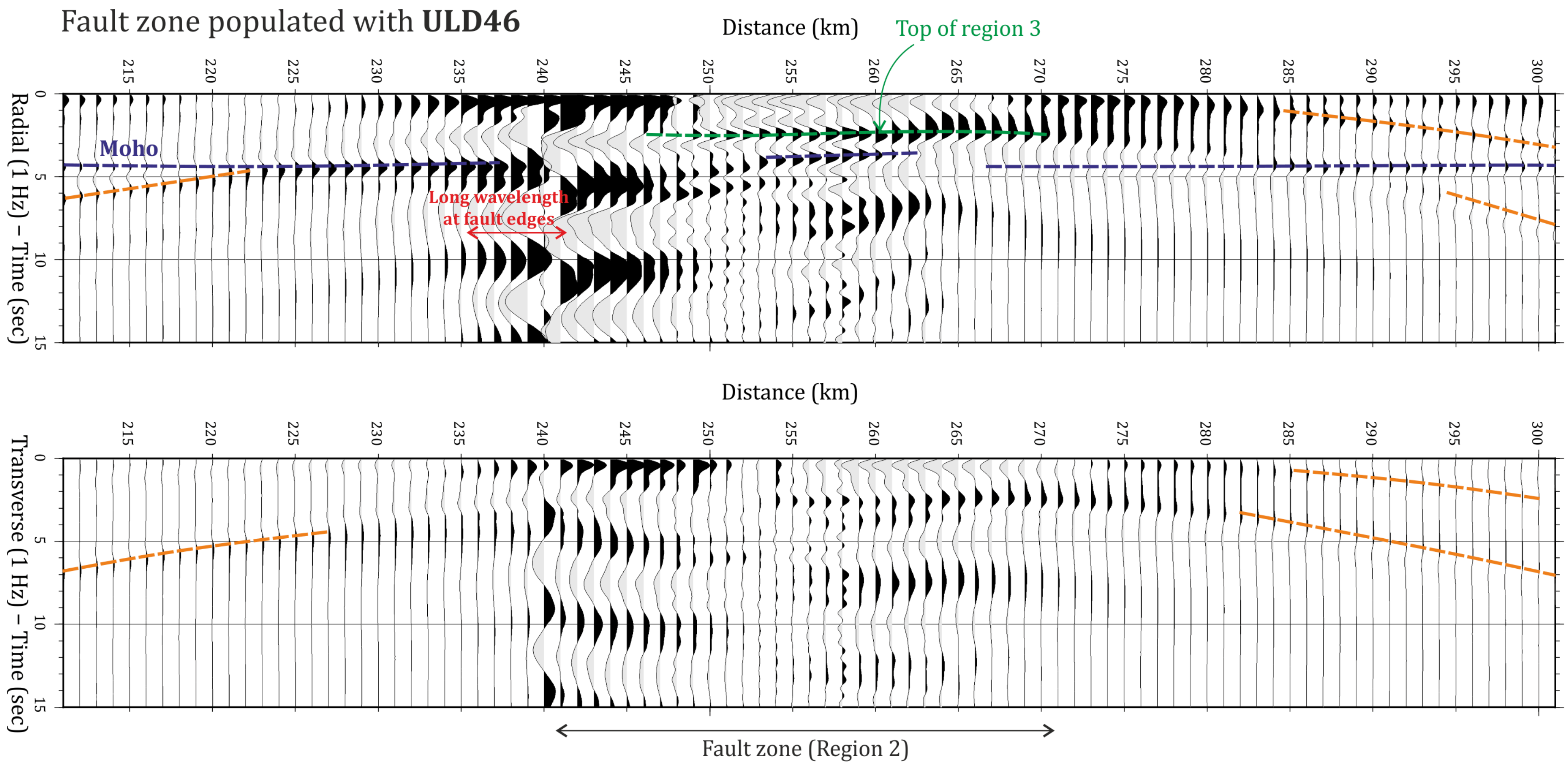

Figure 6.27. RF Stacks of the model in Figure 6.13 populated with sample ULD46 (gneiss within the massif) in region 2, the fault zone. RFs sampled at 1km intervals over the fault zone and orientated W-E, from 211km – 301km. Azimuths between 0°-120° stacked to represent azimuths used in NAF RF study (Kahraman et al., 2015) (Figure 6.4). Blue line indicates the Moho and orange are diffractions off the edges of the fault.

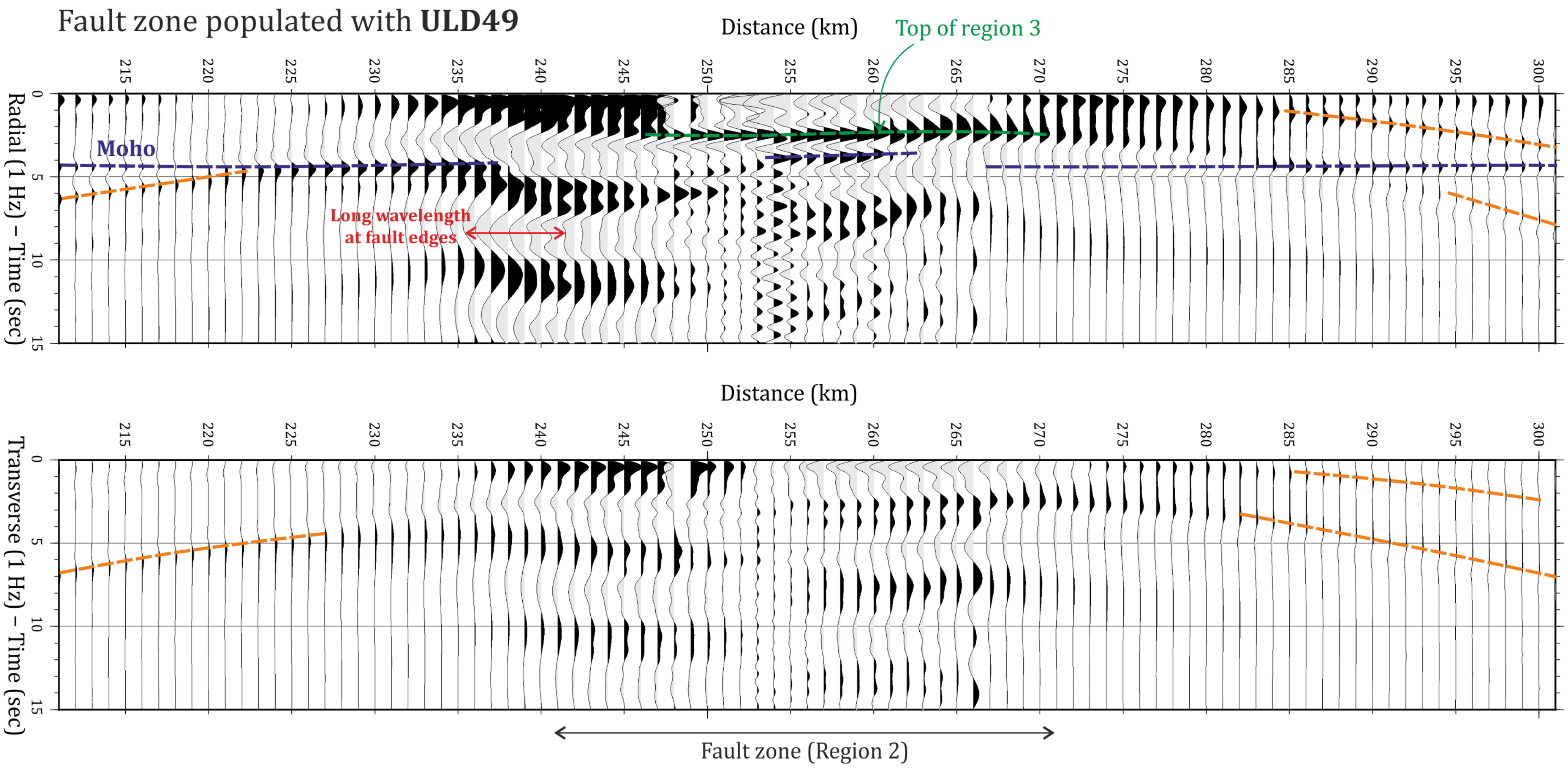

Figure 6.28. RF Stacks of the model in Figure 6.13 populated with sample ULD49 (marble near Bursa Fault) in region 2, the fault zone. RFs sampled at 1km intervals over the fault zone and orientated W-E, from 211km – 301km. Azimuths between 0°-120° stacked to represent azimuths used in NAF RF study (Kahraman et al., 2015) (Figure 6.4). Blue line indicates the Moho and orange are diffractions off the edges of the fault.

All models show a polarity switch from one side of the fault zone to the other in the transverse component, indicating the presence of anisotropy in the fault zone.

6.5. Seismic modelling – North Anatolian Fault

This section will use the results from Kahraman et al. (2015), namely the proposed schematic cross sections (Figure 6.3) as a basis for the model cross sections, specifically, the high velocity and low velocity zones identified from the RFs (Figure 6.2).

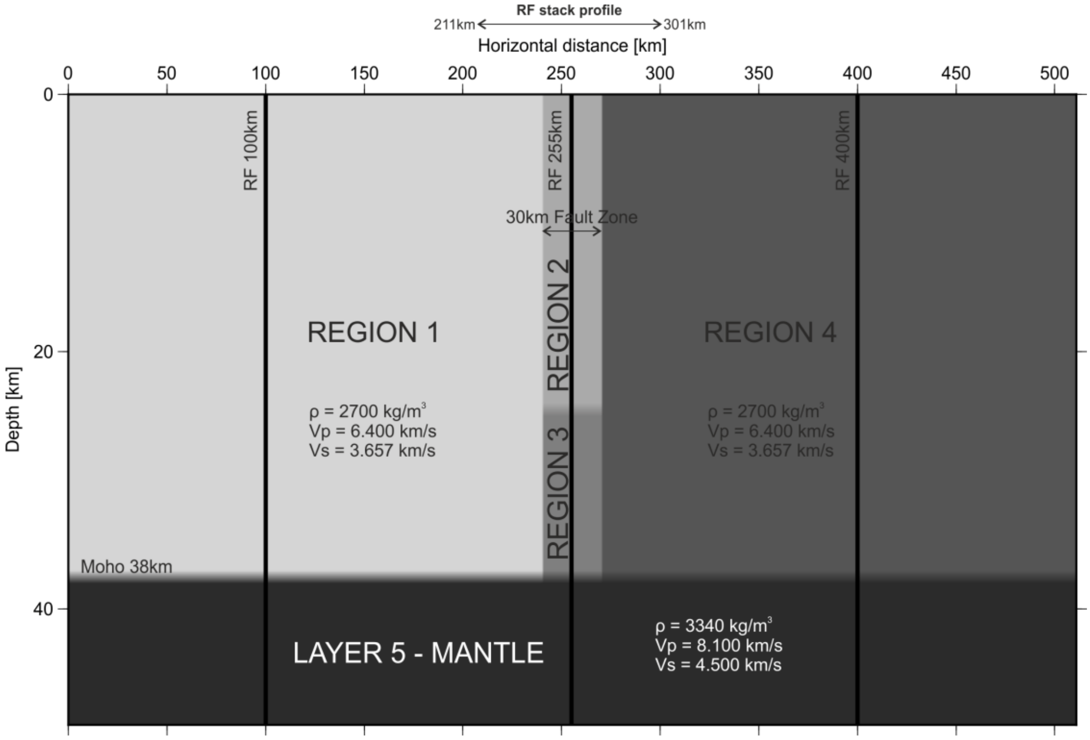

Figure 6.29. Model cross section to represent the high and low velocity zones in the NAF receiver function data (Figure 6.3). Regions 1, 2 and 4 are isotropic crust (all have the same properties), region 3 is populated with the seismic properties of ULD125 with a vertical fabric then subsequently ULD125 with a horizontal fabric. Layer 5 is the mantle. All properties discussed in text. Vertical lines represent the receiver function sample points for the azimuthal plots. Model parameters are displayed in Table 6-1 and explained in Section 6.5.2.

6.5.1. Cross sections

As stated above the models that will be used follow Kahraman et al. (2015) (Figure 6.3). Both cross sections show two faults, the southern North Anatolian Fault (SNAF) and the northern North Anatolian Fault (NNAF) that separate the three distinct blocks, the Istanbul Zone (IZ) to the south, the Armutlu-Almacik (AA) block in the centre and the Istanbul-Zonguldak (IZ) block to the north (Kahraman et al., 2015). The low velocity and high velocity zones identified by Kahraman et al. (2015) could indicate decoupling within the crust.

These schematic cross sections will be used as a basis to investigate the high and low velocity zone and whether or not they could be a function of fabric orientation. The model cross section that will be used is shown in Figure 6.29. This is a simplified representation of the Kahraman et al. (2015) models to look specifically at whether fabric orientation can cause the high and low velocity zones. Region 3 in the model will be populated with the seismic properties of ULD125, which is a strongly anisotropic amphibolite, chosen because it would give noticeable results (Figure 6.8). Firstly with a vertical fabric (ULD125 - VF) and secondly with a horizontal fabric (ULD125 – HF). The vertical fabric pertains to the high velocity zone in the teleseismic receiver function (Figure 6.3) and the horizontal fabric pertains to the low velocity zone. Sample ULD125 has the strongest fault parallel foliation which defines the highest fault parallel anisotropy. It was chosen as it will maximise effect to give the most dramatically different results for the different fabric orientations. Within this model regions 1, 2 and 4 are isotropic crust (ρ = 2700kg m^{-3}, Vp = 6400m s^{-1}, Vs = 3657 m s^{-1}), region 3 is populated with the properties of ULD125 with a vertical fabric and ULD125 with a horizontal fabric, and layer 4 is the mantle (ρ = 3340kg m^{-3}, Vp = 8100m s^{-1}, Vs = 4500m s^{-1}). The properties for the wall rock surrounding the fault zone and the mantle were chosen based on average properties from the study on the NAF (Kahraman et al., 2015).

6.5.2. Receiver functions

The azimuthal plots for the model in Figure 6.29 populated with ULD125 with a vertical fabric, and ULD125 with a horizontal fabric are shown in Figure 6.30 and Figure 6.31 respectively. Again the crust surrounding the region populated with the tensors (ULD125 – VF and ULD125 – HF) has average, isotropic crustal properties described in Section 6.5.1 meaning the receiver functions at 100km and 400km are similar to those described for the Uludağ Massif models. There is a distinct positive Moho conversion (Ps) at ~4.5s and diffraction features from the edges of the top of region 3, between 10-15s. The receiver function at 255km shows some variation for the 2 models, ULD125 – VF (Figure 6.30) and ULD125 – HF (Figure 6.31). The model containing ULD125 – VF has a distinct positive arrival at ~2.5s, from the top of region 3, and another positive arrival at ~4s is the Moho beneath the fault zone. The model containing ULD125 – HF again, has a positive arrival at ~2.5s which is from the top of region 3 and another arrival at 4-4.5s which is the Moho within the fault zone. Again anisotropy can be seen in both models from the energy on the transverse component at 255km and also the switching polarity with backazimuth.

6.5.3. Receiver functions stacks

The RF stacks for both models were again taken at 1km intervals, with the back azimuthal range the same as previous models (000°-120°).

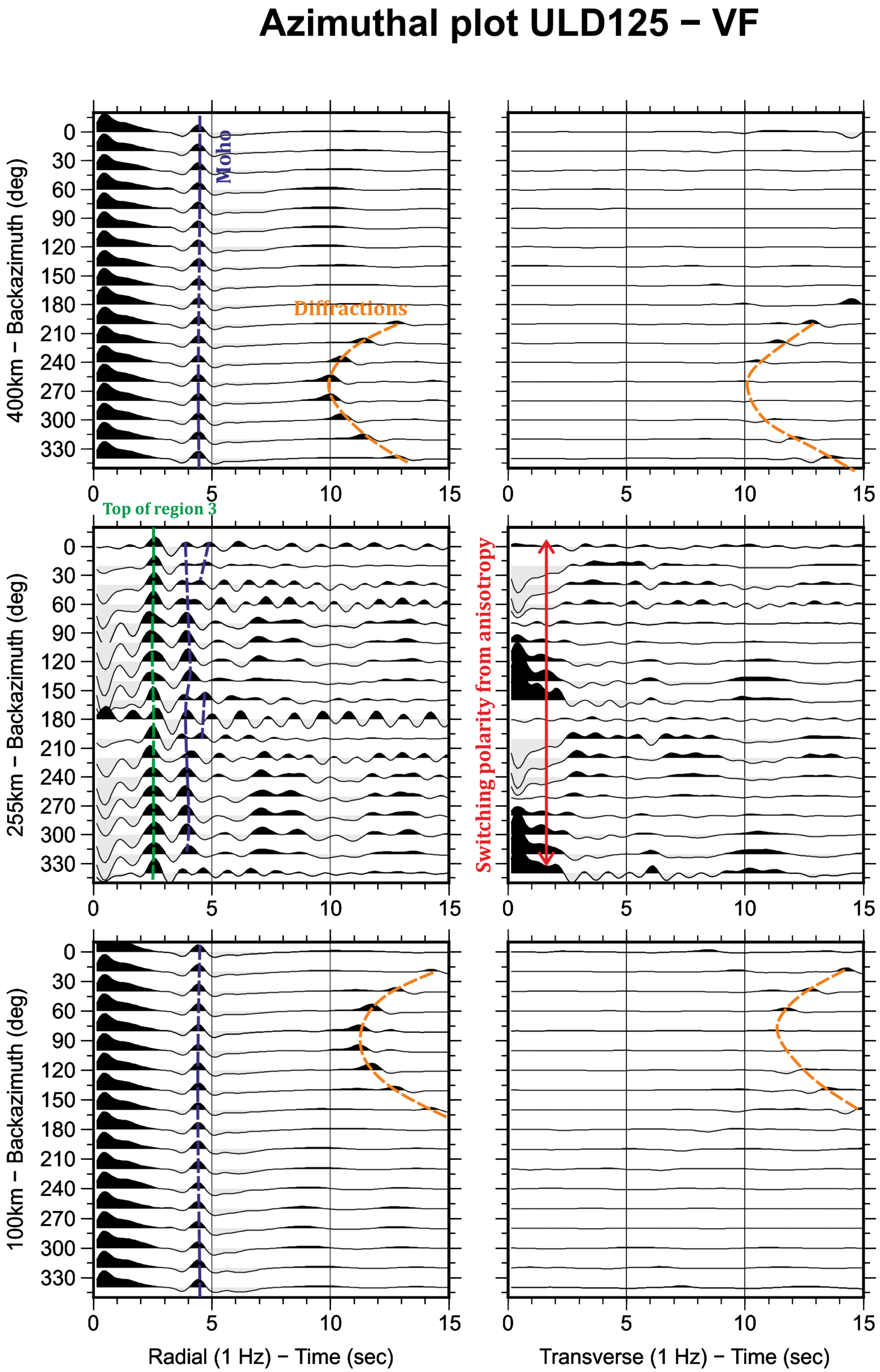

Figure 6.30. Receiver function azimuthal plot with the elastic tensor of ULD125 with a vertical fabric striking perpendicular to the model cross section populating layer 3 and sampled at 100km, 255km and 400km (Figure 6.29). The Moho is indicated by the blue line and the orange highlights diffractions from the fault edges.

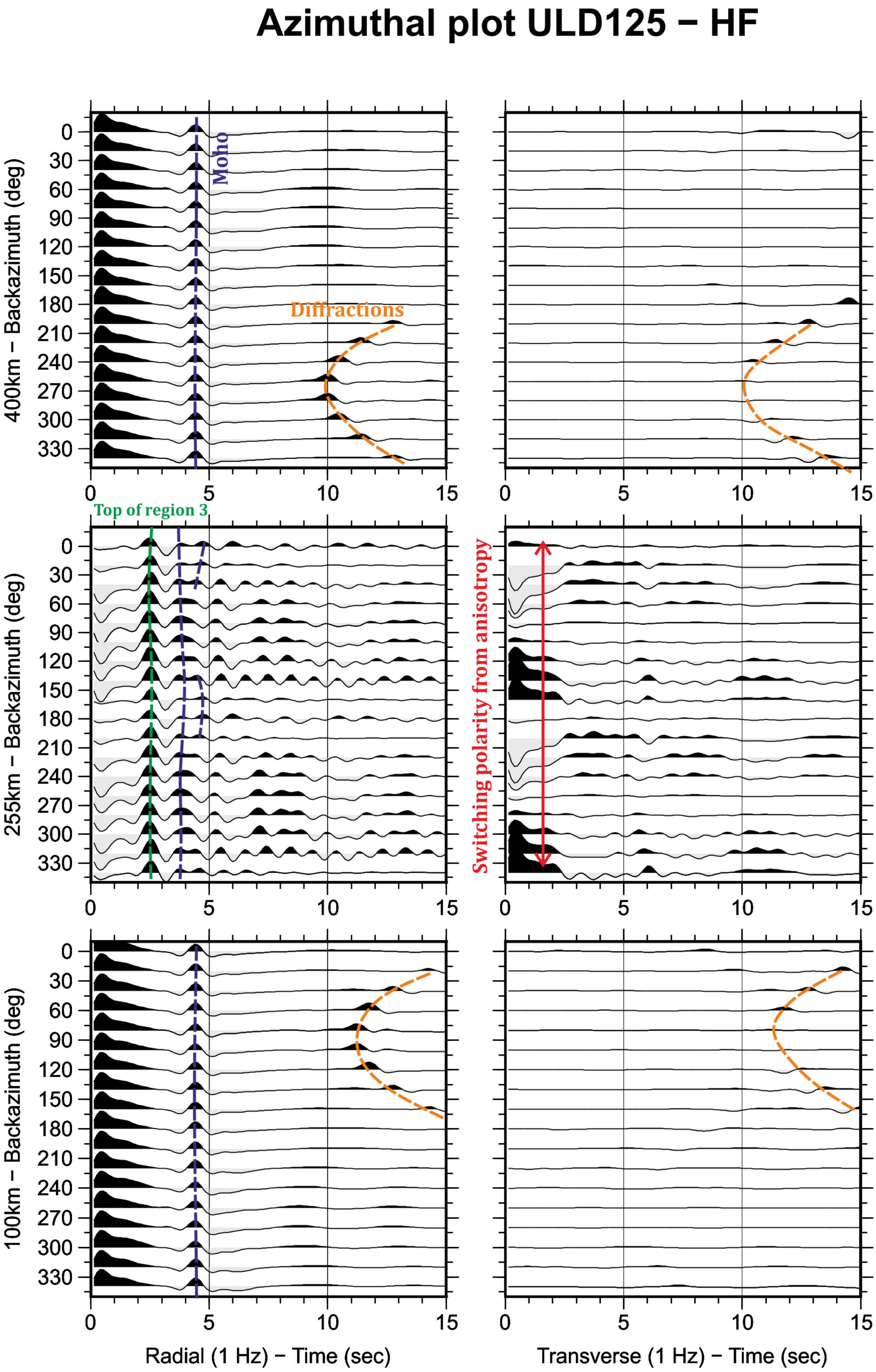

Figure 6.31. Receiver function azimuthal plot with the elastic tensor of ULD125 with a horizontal fabric populating layer 3 and sampled at 100km, 255km and 400km (Figure 6.29). The Moho is indicated by the blue line and the orange highlights diffractions from the fault edges.

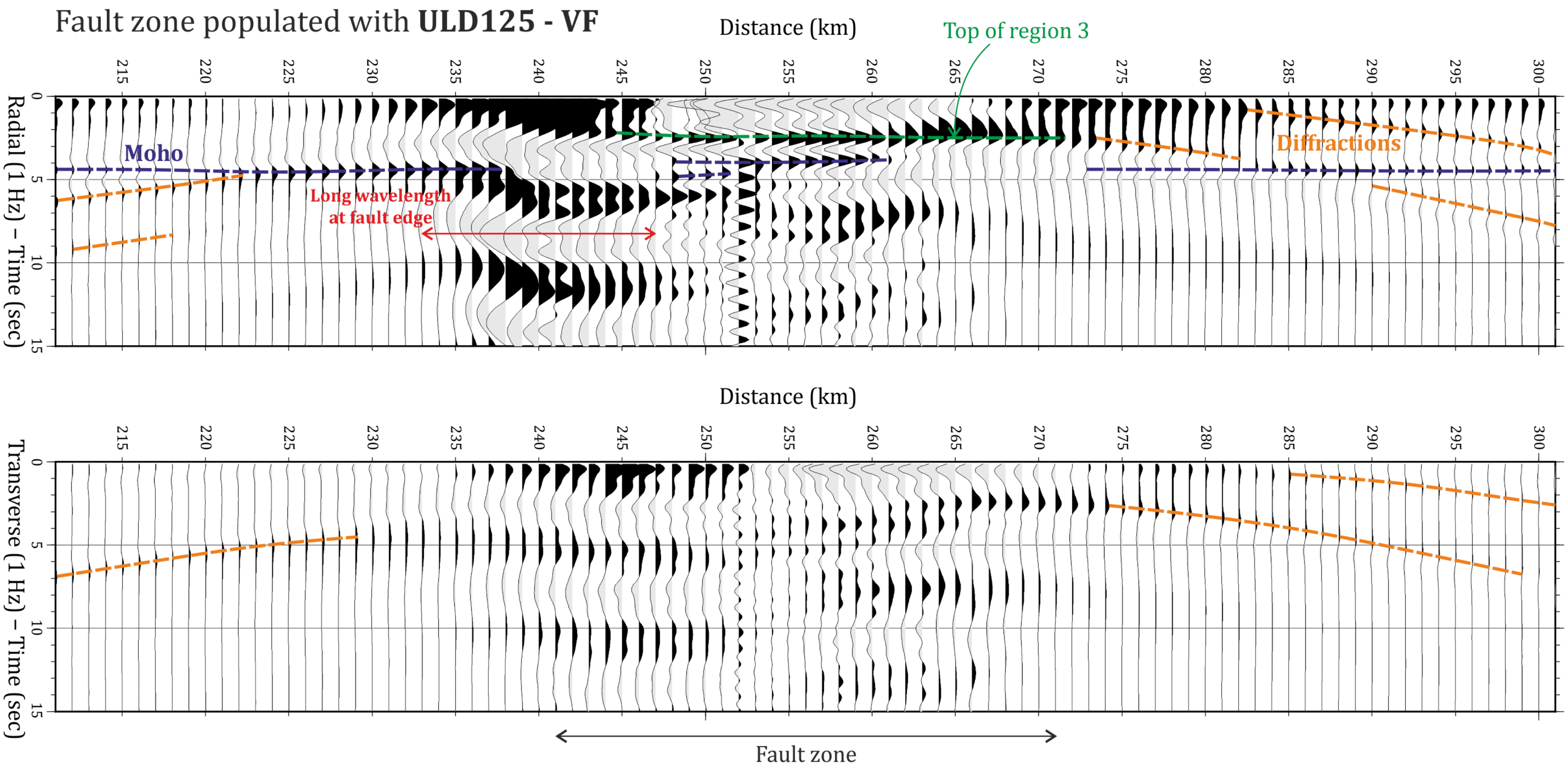

Figure 6.32. Receiver function stacks for of model Figure 6.29 populated with elastic tensor of ULD125 with a vertical fabric striking perpendicular to the model cross section (ULD125 – VF). RFs sampled at 1km intervals over the fault zone and orientated W-E. Azimuths between 0°-120° stacked to represent azimuths used in NAF RF study (Kahraman et al., 2015) (Figure 6.4). Blue indicates the Moho, orange is diffractions from the edges of the faults and green is the response from the top of region 3.

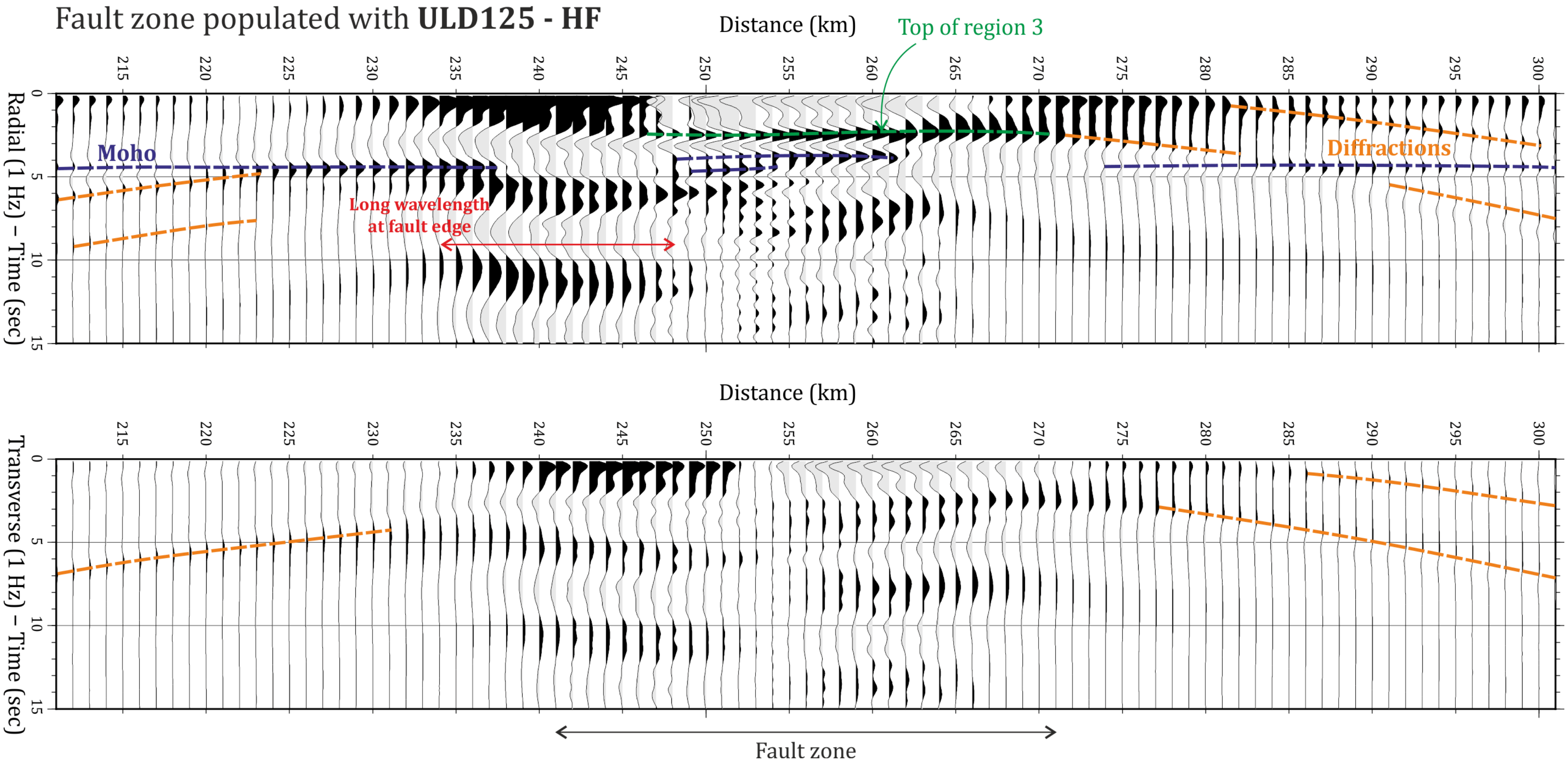

Figure 6.33. Receiver function stacks for model of Figure 6.29 populated with elastic tensor of ULD125 with a horizontal fabric (ULD125 – HF). RFs sampled at 1km intervals over the fault zone and orientated W-E. Azimuths between 0°-120° stacked to represent azimuths used in NAF RF study (Kahraman et al., 2015) (Figure 6.4). Blue indicates the Moho, orange is diffractions from the edges of the faults and green is the response from the top of region 3.

The RF stack profiles start at 211km and finish across the fault at 301km (Figure 6.32 and Figure 6.33). As could be predicted from the similarity of the azimuthal plots, these stacks also look very similar. For both models, the western side of the fault between 235km and 245km looks visually different from the eastern side (between 250km and 262km). Also diffractions can be seen in the wall rock surrounding the fault zone from the top and bottom of region 3 (Figure 6.32 and Figure 6.33). The transverse component for both show a switch in polarity from one side of the fault to the other, indicating anisotropy within the fault zone.

For the model populated with ULD125 with a vertical fabric (Figure 6.32), the radial component shows the Moho conversion (Ps) at ~4s between 254km and 261km and another positive arrival above at ~2.5s which is the top of region 3. Between 248km and 253km the Moho is split into two arrivals signifying the fast and slow shear waves (Vs_1 and Vs_2). The Moho can also be seen between 253km and 265km on the transverse component which is again split into the two shear wave arrivals. Both components show the low frequency signal on the western side of the fault zone which can also be seen, to a lesser extent, on the right at ~265km. In the wall rock on both sides of the fault zone, diffractions from the top and bottom of region 3 are visible (Figure 6.32).

For the model populated with ULD125 with a horizontal fabric (Figure 6.33), again, the radial component shows the Moho ~4s which splits into the fast and slow shear waves between 248km and 254km. There is another positive arrival at 2.5s which is from the top of region 3. The difference between the fast and slow shear wave arrivals is greater in time than on the model with the vertical fabric. The transverse component shows the Moho at ~4s which is again split. Both the transverse and radial components show the low frequency signal in the western side of the fault zone, between 238km and ~247km and the wall rocks show diffractions from the top and bottom of region

6.6. Discussion

What follows is a discussion of firstly the seismic properties of the samples within the Uludağ Massif, the influences of certain minerals within the individual samples and the overall influence lithology may have on the seismic properties of the massif. Secondly, the results from the seismic modelling of the Uludağ Massif, relating lithology to seismic response and the influence of fabric following the models of Kahraman et al. (2015). Lastly, a comparison of these results to the receiver function study on the NAF (Kahraman et al., 2015).

6.6.1. Seismic properties

The previous section presents the results of the computation of seismic properties from the CPO of samples across the Uludağ Massif. The majority of samples across the massif show a foliation represented in the seismic properties, through fast Vp and Vs1 velocities parallel to the foliation or high anisotropy parallel to the foliation. Out of the two samples south of the Eskişehir Fault, ULD143 and ULD173 (Figure 6.11), only the marble sample (ULD143) shows a distinct response to the foliation present in the sample. The sample is monomineralic with a well-defined and strong CPO, meaning there are no other minerals that destructively interfere with the seismic properties. This sample shows a much stronger anisotropy than the granite sample. Whilst the granite contains biotite and muscovite, highly anisotropic minerals (especially biotite) due to their monoclinic crystallography, it also contains a much larger proportion of quartz and feldspar that does not have a well-developed CPO fabric and dilutes the signal from the micas, resulting in a more 'random' response in the seismic properties.

There are two samples within the Eskişehir Fault zone, a marble (ULD166) and a phyllite (ULD139) shown in Figure 6.10. The marble again shows a bigger response to the foliation defined by the calcite as there are no dilutants, it is almost monomineralic. The phyllitic sample has higher shear wave velocities but due to the smaller difference between Vs1 and Vs2, a lower AVs than the marble sample. It also gives a lower Vp. This, again, highlights the fact that even though calcite is not considered highly anisotropic, unlike the biotite and muscovite in the phyllite, the monomineralic nature means there are no dilutants that destructively interfere with the CPO and foliation defined by the calcite. Both of these samples record lower anisotropy values than the marble to the south, within the granite, suggesting a less well-developed foliation/mineral alignment. This is clearly seen in the calcite pole figures, sample ULD166 which is on the fault, shows a more distributed CPO than the sample within the granite (ULD143). This is possibly because of the complex history of the fault zone and provides more evidence to support the theory that this portion of the massif has been re-worked during uplift, overprinting the previous strike-slip CPO.

Samples within the massif are displayed over three figures, Figure 6.9 shows samples located within 1km of the Eskişehir Fault. This area is predominantly marble with some smaller sections of gneiss that are on the scale of 10s of metres thick. The sample closest to the fault, ULD164, shows a much stronger seismic response than the phyllite on the fault, and it is polymineralic, hinting further at the possibility that the fault itself has been re-worked. In this sample it is very clear that biotite is the biggest contributor to the seismic response; fastest Vp, Vs1, slowest Vs2 and highest anisotropy (8.44%) are all parallel to the foliation defined by the biotite. The feldspar seems to constructively contribute to the seismics defined by the biotite, whereas the quartz is very diffuse and will only interfere with the signal from the other minerals. The other two samples are calcite marbles and again are both monomineralic. ULD130, which is the closest marble sample to the fault has a well-developed CPO and strong seismic signal parallel to the foliation and a maximum anisotropy of 5.92%. Whereas ULD157 has a more distributed CPO which is reflected in the seismics, with the lower anisotropy of 2.61%. Within 1km north of the fault, the polymineralic gneiss in this area will have the biggest effect on the seismic response.

Between 2-2.6km, gneiss and marble alternate on the scale of ~200-300 metres, and three samples from this area are shown in Figure 6.8. ULD123 is a gneiss and shows well-developed CPO in quartz and K-feldspar. Again it seems that the highly anisotropic micas that define the foliation are what control the seismic properties with the quartz and feldspar diluting these effects. The marble sample, ULD153, is again monomineralic and shows higher anisotropy and p-wave velocities than the polymineralic gneiss (ULD123) due to the lack of dilutants such as quartz in the sample. Sample ULD125 is an amphibolite and shows the highest anisotropy and p-wave velocities of the whole massif. The majority of the sample is amphibole which is very anisotropic and clearly controls the seismic properties in this sample. Any ductile shear zone with a significant amount of amphibolite will be very anisotropic and will result in a strong seismic response.

Two more gneiss samples further north, in roughly the centre of the massif are shown in Figure 6.7. The lithology between 3-6km within the massif is predominantly gneiss with only small pockets/bands of marble. In both samples, the mica is again the control on the seismic properties, the Vp and AVs in both samples reflecting the foliation that is defined by the alignment of biotite, muscovite and chlorite in ULD47 and biotite in ULD46.

Further north, towards the Bursa Fault there are only small amounts of gneiss; the area surrounding the fault is mainly marble. Figure 6.6 shows the two samples closest to the Bursa Fault, ULD49 is on the fault and ULD52 is to the north. Both samples are 100% calcite so the seismic properties represent the foliation defined by the alignment of calcite crystals. ULD49 has a slightly less well developed CPO than ULD52, again pointing towards the possibility of a re-working during exhumation. ULD52 has a higher anisotropy of 5.76% compared to 3.93% in ULD49, and also a faster P-wave velocity.

Overall it can be noted that all marble samples give strong anisotropy due to their monomineralic composition and generally well-developed CPOs. Both faults have samples with lower anisotropies than the surrounding samples, suggesting re-working during uplift. Biotite and amphibole are highly anisotropic minerals and where present contribute significantly to the seismic properties. If there is a significant proportion of amphibolite in a shear zone the seismic response from this will be very strong due to the simple mineralogy and high anisotropy of amphibole.

6.6.2. Seismic signal of the Uludağ Massif

As mentioned previously RF azimuthal plots of all 4 models for the Uludağ Massif are similar at the 100 and 400km profile locations. This is due to each model having the same isotropic crust with the same properties either side of the fault zone. The Ps Moho arrives at 4.5s which is consistent for the Vp and Vs velocities in the model (Section 6.5.1). The RF sampling within the fault zone is the one that shows the most complexity for all models.

All models show switching polarity with changing back azimuth in the transverse component, which is evidence of anisotropy. The seismic properties of the four samples that populate the models are shown in Figure 6.6 - Figure 6.11. All samples have some degree of anisotropy. In ULD130, ULD46 and ULD49 the highest anisotropy is parallel to the foliation and trace of the Eskişehir Fault (~110°), which is therefore perpendicular to the model cross sections. These three samples are found within the massif, between the Eskişehir and Bursa Faults. The perpendicular anisotropy is the cause of the reversing polarity with azimuth. Sample ULD173 which is the granite sample found to the south of the Eskişehir Fault has less fault parallel anisotropy and foliation which is evident from the seismic properties in Figure 6.11, but still shows anisotropy in the model (Figure 6.21).

The RF stacks shown in Section 6.4.4 were sampled at 1km intervals across the fault zone, from 211km – 301km. For all four models the RF stacks look visually similar. The Ps Moho, at ~4.5s, can be traced through the part of the fault zone in the all four models, which is also split into two signals for the fast and slow shear waves. This split in the Moho signal indicates anisotropy. In the RF stacks for all four models the sides of the fault (241km - 271km) show lower frequency waves. This longer wavelength may be an artefact of the waves reflecting within the 30km wide fault zone, from edge to edge. In all four RF stacks there is also a positive amplitude at ~10s which could refer to the 'depressed Moho' seen in the real RF data which is discussed in Section 6.6.3, which is likely multiples from the top of region 3 and the Moho. In the transverse components of all models the polarity switches from one side of the fault to the other (Figure 6.26 - Figure 6.28). The diffractions that can be seen in all of the models originate from the sides of the shear zone.

From these results it is clear that any sample with some degree of anisotropy will have an effect on the seismic response of a mid-crustal shear zone. In particular all four samples used, which are representative of a mid-crustal shear zone, have an effect on the Moho and how it appears in the RF stacks; present in the centre and less so towards the edge of the fault zone. Though this could be because it is being masked by the long wavelength signals or it is a result of azimuthal bias.

A complete 2.5D model representing the whole cross section shown in Figure 6.12 could not be achieved due to modelling constraints. It was too complicated to have more than one tensor populating the model. This does however allow the seismic responses to be looked at individually which is important because, from the results, it is evident that anisotropy and therefore foliation orientation is the main control on the seismic response, regardless of lithology.

A different approach to including an elastic tensor in the models is to approximate the Vp, Vs and the percentage s- and p-wave anisotropy from the seismic properties in Figure 6.6 - Figure 6.11. The properties for the four samples (ULD173, ULD120, ULD49 and ULD46) are shown in Table 6-2. These were used for the shear zone in models shown in Appendix 6B. For all four models the anisotropy is orientated perpendicular to the model cross section and dips at 80°.

Sample	Vp (m/s)	Vs (m/s)	% P anisotropy	% S anisotropy
ULD173	6480	4080	4.4	4.86
ULD130	7090	3820	10.9	5.92
ULD46	6300	3920	3.5	4.89
ULD49	7030	3770	7	3.93

Table 6-2. Seismic properties of the four samples used for the shear zone in the models in Appendix 6B.

The results are quite different from the results from the models populated with elastic tensors. This is due to the values being approximated from the seismic properties of the sample, an elastic tensor will produce an inherently more complicated result. In all four models the receiver functions in the wall rocks, at 100km and 400km, produce similar results with the Moho at ~4.5s. Within the shear zone the approximated values for ULD130 and ULD46 are similar, the Moho is at ~4.5s and the top of region 3 can be seen at ~2-2.5s. Both of these also show switching polarity in the transverse component indicating anisotropy. The models with approximated values for ULD173 and ULD46 are different however. The Moho in the ULD173 model is at ~4s due to the faster s-wave velocity (Table 6-2) and they both do not display anisotropy in the transverse component. In the ULD173 model this is due to the lack of foliation defining a fault parallel anisotropy (Figure 6.11).

Both of these approaches are valid, but the differences between the elastic tensor populated and approximated value populated models for the same sample raises questions. The models populated with elastic tensor are inherently more complicated as the tensor represents a real rock sample. The approximation comes when this small rock sample is used to represent the entire crust. The other method, uses a representative sample as an estimate for the model. So either method requires approximation at some stage, however using a real rock sample in a model to generate a seismic response is a new way to investigate the effect of a shear zone on seismic signals.

6.6.3. Comparison to NAF data

Section 6.5 looks at possible causes for the high and low velocity zones identified in the NAF RF data (Figure 6.3). It is already evident from the previous results on the Uludağ Massif that foliation is the main control on anisotropy and seismic response, irrespective of lithology, so foliation could be the reason for the high and low velocity zones around the NAF.

The first model, shown in Figure 6.30 and Figure 6.32, is populated with ULD125 that has a vertical fabric in layer 3 (Figure 6.29). The second, shown in Figure 6.31 and Figure 6.33, is populated with the same sample but with a horizontal fabric in layer 3 (Figure 6.29). Both of the RF azimuthal plots look very similar at all three locations. At 100km and 400km the Moho can be seen clearly and is a similar signal to the Uludağ Massif models as these two RFs are outside of the fault zone, within an isotropic crust with typical crustal velocities (Figure 6.30 and Figure 6.31). Within the fault zone, the azimuthal RF plot at 255km are similar for both models, with the Moho at ~4.5s and another positive feature above at 2.5s.

Both models also show similar signals in the 1km spaced RF stacks in Figure 6.32. The positive feature that can be seen in the azimuthal plots and in the RF stacks between 245km and 265km at ~2.5s is the signal from the top of the high/low velocity zones in the models. The Moho can be seen at ~4.5s in both models, but is represented much better on the right hand side of the fault, than on the left. This is due to azimuthal bias; only stacking traces with back azimuths between 000° and 120°. For comparison, both stacks have been overlain in Figure 6.34. They are quite similar, but one region of interest has been highlighted. The model populated with a horizontal fabric (red overlay) has two peaks in the arrival from the Moho whereas the model with a vertical fabric (black/grey trace) only has one. This could represent a bigger difference in the fast and slow shear waves arriving from the Moho through the horizontal fabric.

The RF data from the NAF shows a gap in the Moho underneath the northern strand of the NAF on the western S-N profile Figure 6.2a (Kahraman et al., 2015). Also present is a positive amplitude feature ~10km below (Kahraman et al., 2015). The positive amplitude feature in the RF stacks of the models of samples ULD173, ULD130, ULD46 and ULD49 at 10s could reflect this positive amplitude feature below the Moho in the NAF data.

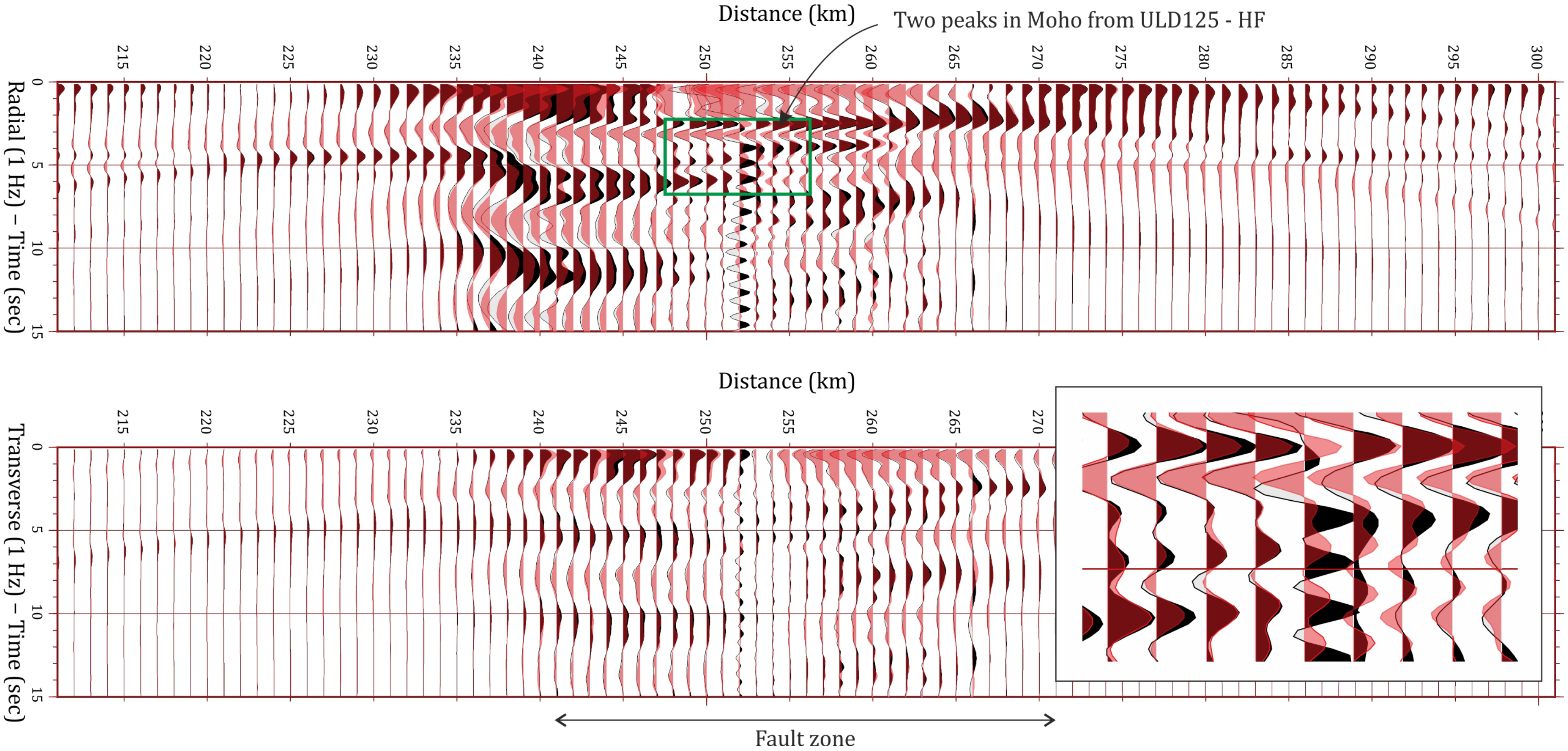

Figure 6.34. Overlay of the RF stack from the model with a horizontal fabric in region 3 (Figure 6.29) in red, on top of the RF stack from the model with a vertical fabric in black. In this figure, all 18 back azimuths have been stacked. The responses are very similar, however one region of interest has been highlighted and enlarged in the inset on the right.

The spacing of receiver functions is important when trying to resolve certain features. The spacing for the RF stacks of Kahraman et al. (2015) was 5km. The width of the northern and southern NAF is 10km or less in the N-S profiles (Figure 6.2) (Kahraman et al., 2015). This doesn't give very dense sampling through the fault and may result in certain features being missed. This may be the reason for the gap in the Moho underneath the northern NAF on the profile where the fault is likely to run through (Figure 6.2a). What is also apparent from the modelling is the effect azimuthal bias has on the stacked RFs. This is most evident in the results using sample ULD125 in Figure 6.32. The difference between the left and right hand sides of the fault zones highlights the problems with only stacking data from azimuths between 0°-120°. If the whole azimuthal range was stacked then the results would be symmetrical and some of the effects along the edges of the fault, the low frequency waves, would be removed.

From these results is can clearly be seen that a shear zone will have an effect on the seismic response, and it is certainly detectable. However, whilst differences in the seismic properties are apparent between lithology and varying structure (Figure 6.6 - Figure 6.11), these differences are not enough to cause a detectable difference in the seismic response that can be attributed to a particular lithology or fabric orientation. With the first models where the fault zone was populated with four different samples in turn, it was apparent that lithology did not have a big influence on the seismic response. The only big difference between the four models was the one that was populated with the elastic tensor for granite (ULD173 - Figure 6.21 and Figure 6.25). On the RF stack for this sample there was no switch in polarity from one side of the fault to the other, whereas on the other three there was a polarity switch. This feature could possibly be used to identify fault material. Looking at the seismic properties it was clear this sample had less of a fabric than the others which explained this difference.

The models that were populated with a sample that had a vertical fabric and then the same sample with a horizontal fabric showed a remarkably similar RF stack (Figure 6.32 and Figure 6.33). The only notable difference seen when they were overlain (Figure 6.34) was in the response from the Moho. In the model with a horizontal fabric there are two peaks due to shear wave splitting in the arrival, representing the difference in arrival time of the fast and slow shear waves travelling through the 'low velocity' or horizontal fabric region.

It is apparent that a shear zone will produce a strong and detectable signal in a seismic response. However trying to discern lithology or fabric orientation is impossible and the differences between the responses are too small.

Appendix 6A

The elastic matrices for the constituent minerals of the gneisses, granites, marbles and phyllonites of the Uludağ Massif. Units are Mb (megabar).

Mineral: Calcite **Density:** 2.71 g cm^{-3} (Dandekar, 1968)

Lattice Vectors			**Vector Angles**		
4.99	4.99	17.064	90	90	120
Elastic Matrix					
1.4627	0.5971	0.5076	-0.2076	0.0	0.0
0.5971	1.4627	0.5076	0.2076	0.0	0.0
0.5076	0.5076	0.8531	0.0	0.0	0.0
-0.2076	0.2076	0.0	0.3405	0.0	0.0
0.0	0.0	0.0	0.0	0.3405	-0.2076
0.0	0.0	0.0	0.0	-0.2076	0.4328

Mineral: Quartz **Density:** 2.65 g cm^{-3} (McSkimin et al., 1965)

Lattice Vectors			**Vector Angles**		
4.913	4.913	5.504	90	90	120
Elastic Matrix					
0.8680	0.0706	0.1191	-0.1804	0.0	0.0
0.0706	0.8680	0.1191	0.1804	0.0	0.0
0.1191	0.1191	1.0575	0.0	0.0	0.0
-0.1804	0.1804	0.0	0.5820	0.0	0.0
0.0	0.0	0.0	0.0	0.5820	-0.1804
0.0	0.0	0.0	0.0	-0.1804	0.3988

Mineral: Plagioclase **Density:** 2.68 g cm^{-3} (Aleksandrov et al., 1974)

Lattice Vectors			**Vector Angles**		
8.1553	12.8206	7.1397	93.95	116.47	89.62
Elastic Matrix					
0.82	0.398	0.41	0.0	-0.084	0.0
0.398	1.45	0.337	0.0	-0.063	0.0
0.41	0.337	1.328	0.0	-0.187	0.0
0.0	0.0	0.0	0.181	0.0	-0.01
-0.084	-0.063	-0.187	0.0	0.31	0.0
0.0	0.0	0.0	-0.01	0.0	0.335

Mineral: Orthoclase **Density:** 2.56 g cm^{-3} (Aleksandrov et al., 1974)

Lattice Vectors			**Vector Angles**		
8.56	13.0	7.17	90	116	90
Elastic Matrix					
0.67	0.453	0.265	0.0005	-0.0024	-0.0018
0.453	1.693	0.204	0.0015	-0.123	-0.0015
0.2650	0.204	1.182	-0.0017	-0.15	0.0004
0.0005	0.0015	-0.0017	0.1430	0.0003	-0.019
-0.0024	-0.123	-0.15	0.0003	0.2380	0.0007
-0.0018	-0.0015	0.0004	-0.0190	0.0007	0.3640

Mineral: Biotite **Density:** 3.09 g cm^{-3} (Aleksandrov and Ryzhova, 1961)

Lattice Vectors			**Vector Angles**		
5.357	9.245	20.234	90	94.98	90
Elastic Matrix					
1.86	0.3240	0.1160	0.0	0.0	0.0
0.3240	1.86	0.1160	0.0	0.0	0.0
0.1160	0.1160	0.54	0.0	0.0	0.0
0.0	0.0	0.0	0.058	0.0	0.0
0.0	0.0	0.0	0.0	0.058	0.0
0.0	0.0	0.0	0.0	0.0	0.7680

Mineral: Muscovite **Density:** 2.82 g cm^{-3} (Vaughan and Guggenheim, 1986)

Lattice Vectors			**Vector Angles**		
5.189	8.995	20.0970	90	95.18	90
Elastic Matrix					
1.81	0.488	0.256	0.0	-0.142	0.0
0.488	1.784	0.212	0.0	0.011	0.0
0.256	0.212	0.586	0.0	0.01	0.0
0.0	0.0	0.0	0.165	0.0	-0.052
-0.142	0.011	0.01	0.0	0.195	0.0
0.0	0.0	0.0	-0.052	0.0	0.72

Mineral: Chlorite **Density:** 3.2 g cm^{-3} (Katahara, 1996)

Lattice Vectors			Vector Angles		
5.3	9.2	14.3	90	97	90
Elastic Matrix					
1.8176	0.5676	0.2034	0.0	0.0	0.0
0.5676	1.8176	0.2034	0.0	0.0	0.0
0.2034	0.2034	1.0677	0.0	0.0	0.0
0.0	0.0	0.0	0.1141	0.0	0.0
0.0	0.0	0.0	0.0	0.1141	0.0
0.0	0.0	0.0	0.0	0.0	0.625

Mineral: Amphibole **Density:** 3.0 g cm^{-3} (Ahrens, 1995)

Lattice Vectors			Vector Angles		
9.87	18.058	5.307	90	105.2	90
Elastic Matrix					
1.3	0.614	0.592	0.0	0.0950	0.0
0.614	1.877	0.614	0.0	-0.069	0.0
0.592	0.614	1.984	0.0	-0.406	0.0
0.0	0.0	0.0	0.611	0.0	-0.009
0.0950	-0.069	-0.406	0.0	0.387	0.0
0.0	0.0	0.0	-0.0090	0.0	0.45

Appendix 6B

Model with approximated Vp, Vs and percentage p- and s-wave anisotropy for ULD173.

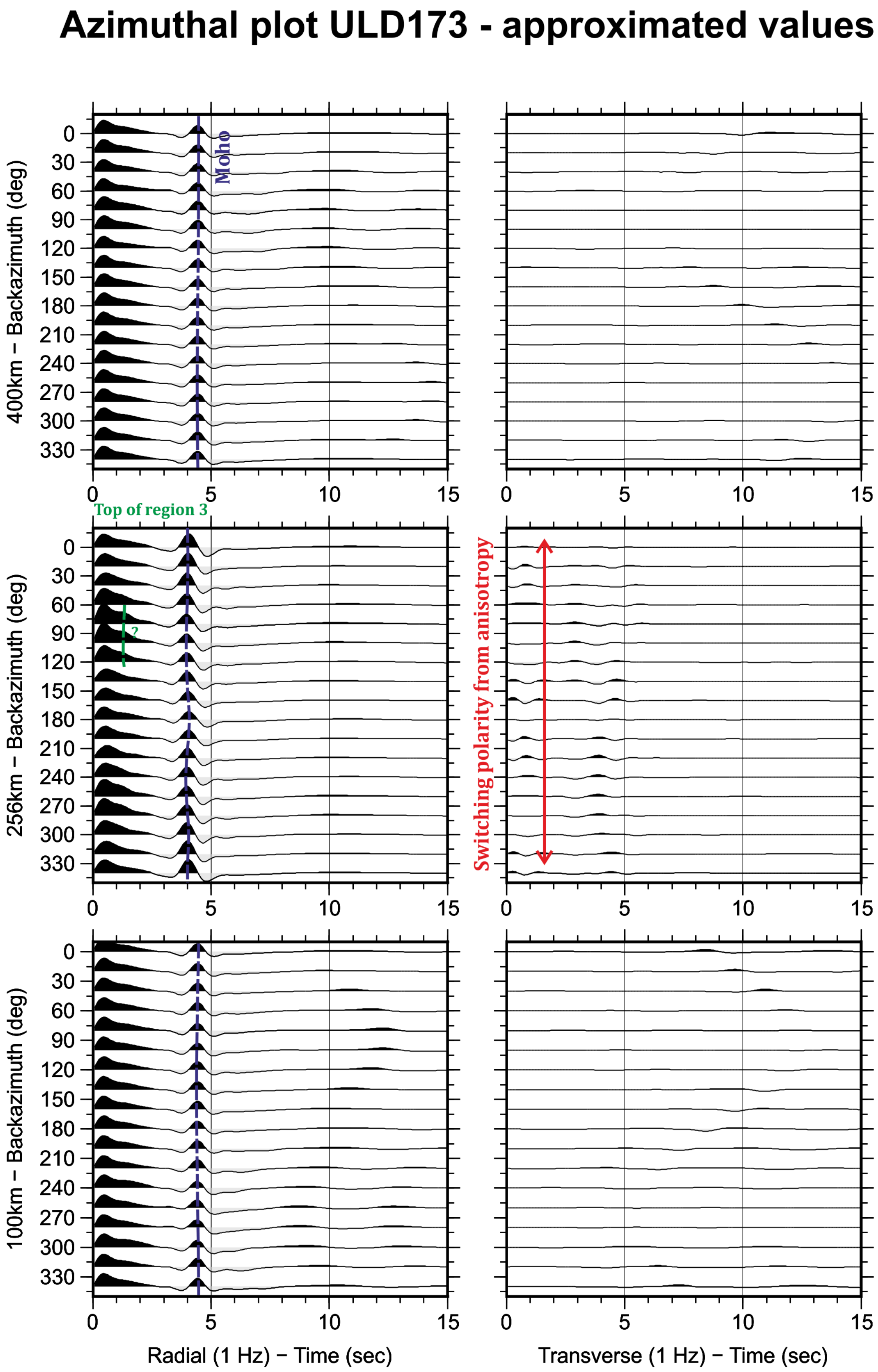

Model with approximated Vp, Vs and percentage p- and s-wave anisotropy for ULD130.

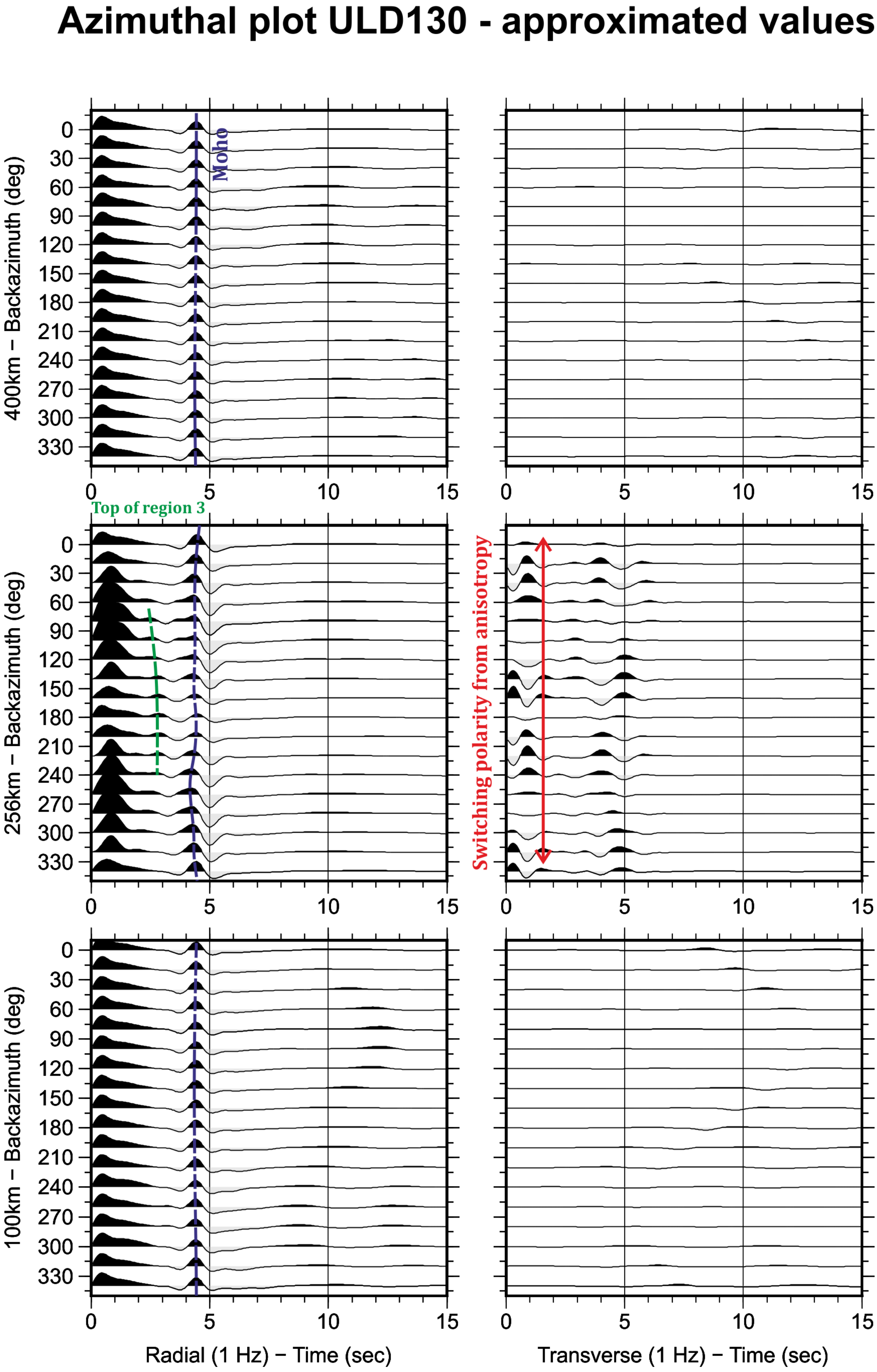

Model with approximated Vp, Vs and percentage p- and s-wave anisotropy for ULD46.

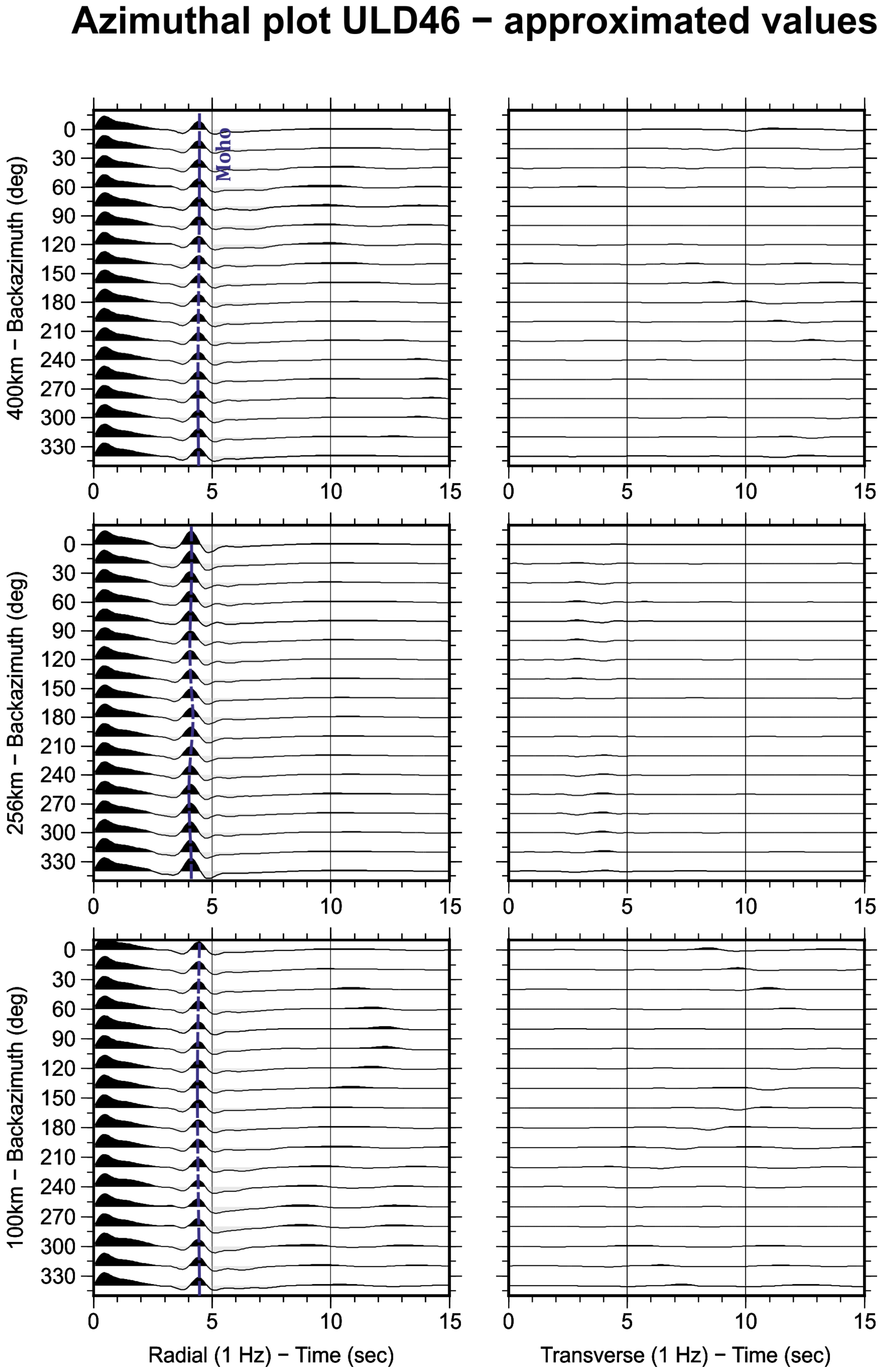

Model with approximated Vp, Vs and percentage p- and s-wave anisotropy for ULD49.

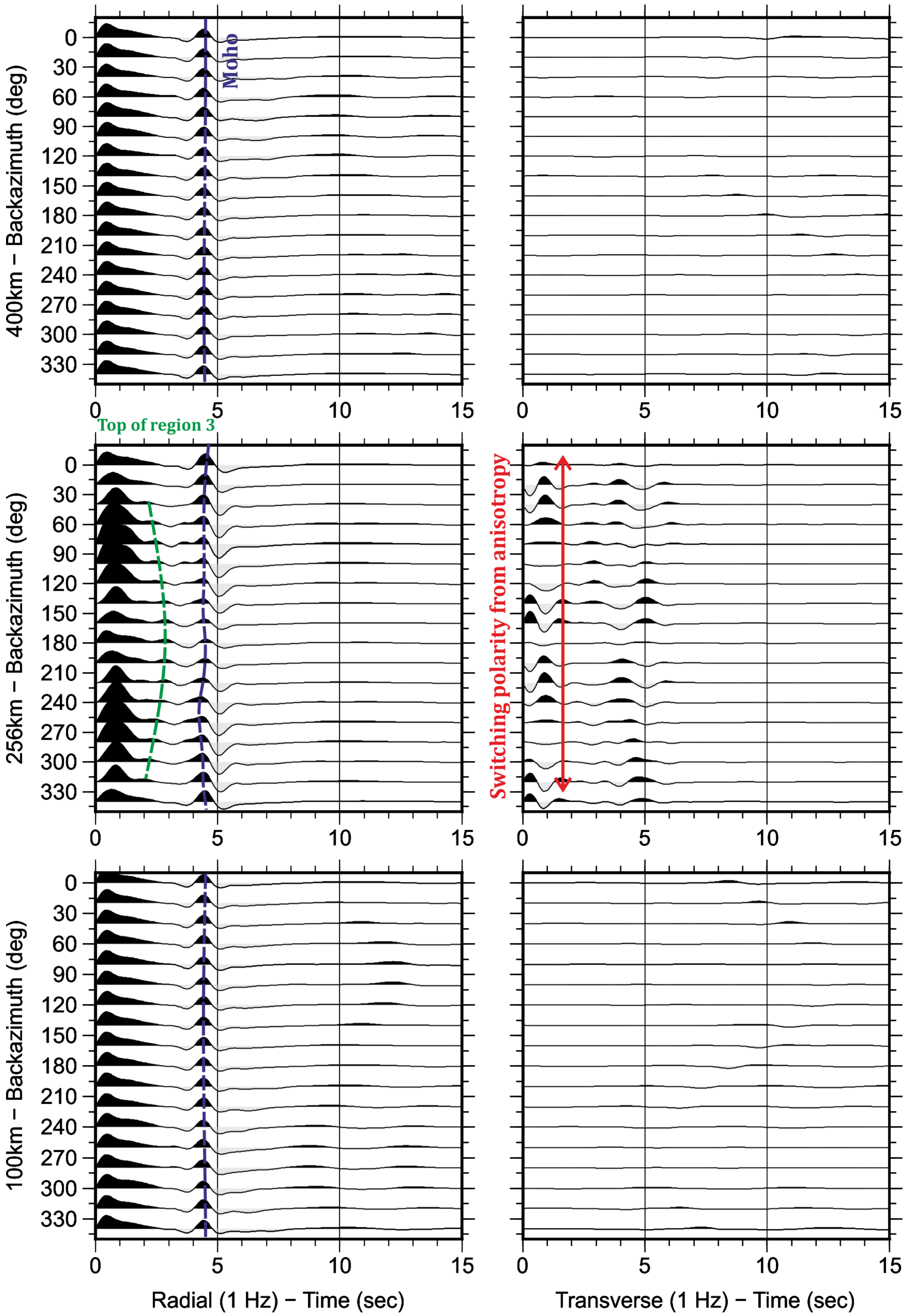

Azimuthal plot ULD49 - approximated values

7. CHAPTER SEVEN

Characterising the deep structure and seismic signature of an exhumed ductile shear zone.

7.1. Introduction

This chapter aims to bring together the information from the previous chapters to address the larger questions surrounding the project that were outlined in Chapter 1. Firstly to characterise the deep structure of a continental scale fault zone based on observations of the Uludağ Massif. Secondly to relate this to the North Anatolian Fault and the processes that affect specific aspects such as the seismic cycle of these large scale fault zones. Lastly to investigate the seismic signature of a ductile shear zone based on real rock data and field observations from the Uludağ Massif.

7.2. Large scale structure of the Uludağ Massif

From field observations, the Uludağ Massif comprises of exhumed mid crustal rocks; marble and gneiss along with granitic intrusions. The massif is bound to the south by the Eskişehir Fault and to the north by the Bursa Fault. The Eskişehir Fault in the south is identified by a well-foliated zone of ~20-30m containing phyllites and marbles (Figure 3.3). There is a dominant foliation within these units that strikes approximately ~110°, parallel to the Eskişehir Fault (Figure 3.1). Within the South Uludağ Granite and the Eskişehir Fault this foliation is mylonitic. Along with the foliation, the sub-parallel shear sense indicators described in the field (Figure 3.5) and in thin section (Figure 4.10) and the deformation microstructures such as calcite twinning and quartz recrystallisation (Figure 4.8, Figure 4.9) all suggest that the Uludağ Massif represents a right lateral ductile shear zone.

7.2.1. South Uludağ Granite and timing of the shear zone

The South Uludağ Granite (SUG) is deformed, evident from its pervasive fault parallel foliation (~110°), mylonitic fabric and elongated axis which is parallel to the Eskişehir fault. Other deformed granite intrusions exist for example in Donegal, NW Ireland (Hutton, 1982) and Red River, SW China (Anczkiewicz et al., 2007) shear zone. These examples both show similarities in the geometry and relationship with the shear zone, indicating that this example of a deformed granite in the Uludağ shear zone formed by a similar process. Okay et al. (2008) presented this granitic intrusion as synkinematic based on the lack of contact metamorphism, its pervasive foliation parallel to the strike of the Eskişehir

Fault, elongated shape, solid-state and crystal-plastic strain microstructure and prolonged crystallisation age of 30 to 39 Ma.

This study also found no evidence for contact metamorphism between the SUG and the marble bounding its northern edge suggesting that the surroundings were still at high ambient temperatures when the granite was emplaced. Samples taken from SUG in this study contain no evidence of magmatic microstructure consistent with rotation of crystals in a melt phase at a stage when the magma is sufficiently viscous to preserve the alignment, such as 1) sub parallel alignment of euhedral crystals of feldspar/hornblende with no internal deformation, 2) imbrication of elongate euhedral crystals with no internal deformation, 3) insufficient solid-state strain to allow phenocryst rotation, 4) magmatic flow foliation deflecting around xenoliths or 5) schleiren layering formed from crystal sorting due to convective or magmatic flow or shearing of xenoliths (Vernon, 2000).

Instead evidence of solid-state flow, in a shear zone was found within thin sections taken from the SUG. For example; 1) internal crystal deformation and recrystallisation (e.g. Figure 4.9c), 2) elongation of recrystallised quartz and mica aggregates (Figure 4.10d), 3) grain size reduction (e.g. Figure 4.9), 4) foliation anastomosing around 'stronger' minerals (e.g. Figure 4.9e), 5) microcline twinning in feldspar, 6) myrmekite and flame perthite (e.g. Figure 4.9d, e). These solid-state microstructures, the lack of any evidence in the microstructure of magmatic flow, along with the sharp boundary between the SUG and the marble do suggest that the granite was emplaced before shear zone activity. Outstanding issues to this include the lack of any contact metamorphism and the higher temperatures recorded by the quartz and feldspar microstructure (Section 4.4.1). However, the presence of the highly foliated zone adjacent to the SUG could mask any contact metamorphism (Figure 3.3). The presence of this localised zone of shear suggests that the granite posed a rheological weakness, in the form of a boundary, where strain could localise so had cooled significantly before shear zone activity commenced. However, the higher temperature microstructure does mean that the granite was still at elevated temperatures compared to its surrounding during deformation, meaning the shear zone was active before the granite had completely cooled to ambient temperatures.

Proposing that the SUG is not a syn-kinematic intrusion has significant implications for the timing of the Eskişehir Fault and Uludağ Shear Zone. Okay et al. (2008) attributed the wide range in crystallisation ages (30-39Ma) to prolonged crystallisation within an active shear zone and therefore suggesting that the shear zone was active from 38Ma to 27Ma (when the undeformed Central Uludağ Granite (CUG) was intruded). This present study suggests the SUG is pre-kinematic so the shear zone was active over a shorter and later period at~30-31Ma to 27Ma.

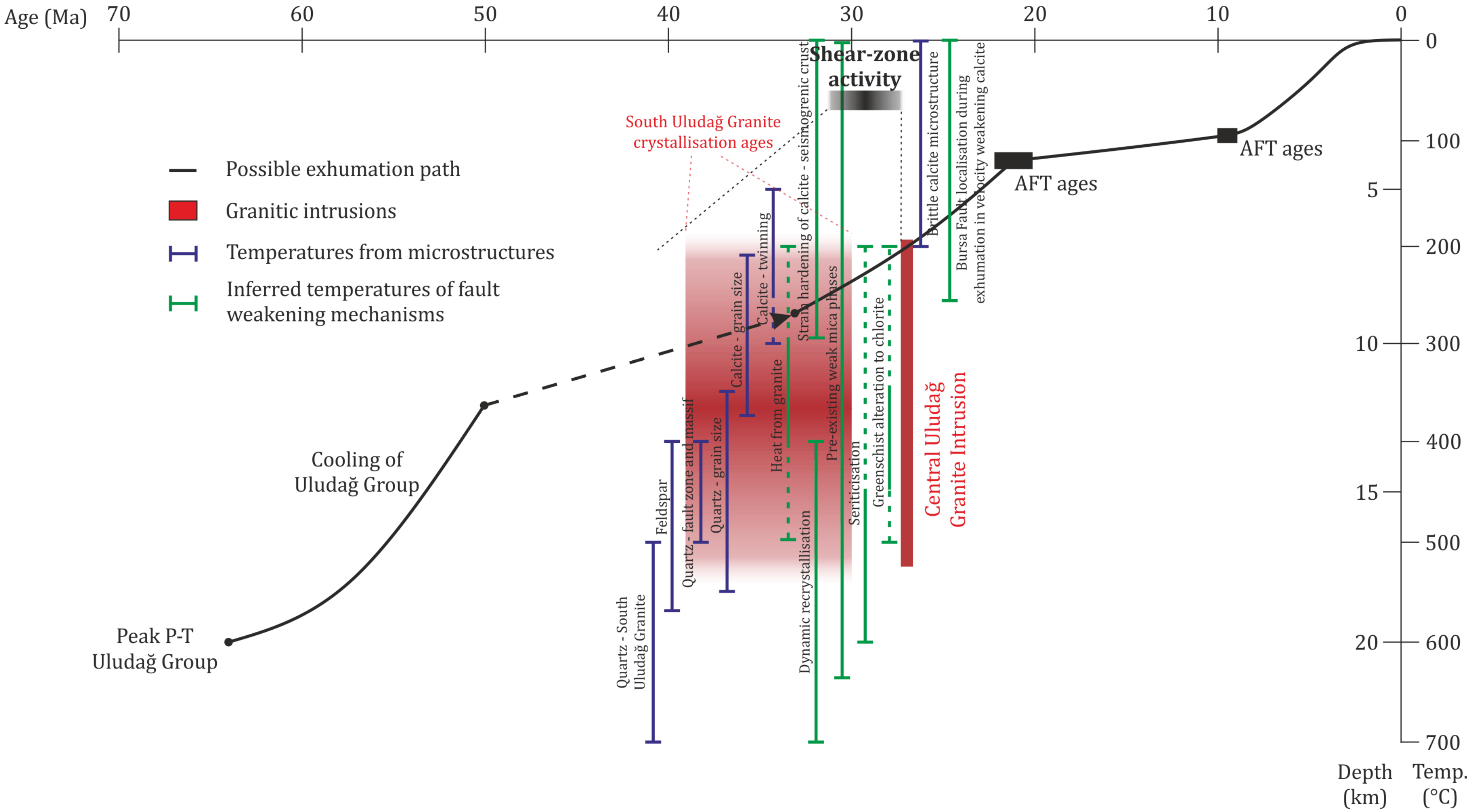

Figure 7.1. Exhumation path of the Uludağ Massif and shear zone. Temperature estimates from all microstructural evidence and grain size and later stage brittle structures. Fault weakening and strengthening mechanisms shown with approximate temperatures of activity.

7.3. Deformation conditions

Exhumed ductile shear zones provide opportunities to study processes active in the mid-crust. These include, temperature and stress variations, shear strain and strain rates.

Numerous studies have been performed on exhumed ductile shear zones to investigate their structure and the processes active during deformation. These studies include the Outer Hebrides Shear Zone (Coward, 1976, Sibson, 1977, Imber et al., 1997), the Karakoram Fault Zone (Phillips and Searle, 2007, Wallis et al., 2013), mid-crustal channel flow in the Annapurna-Dhaulagiri Himalaya (Godin et al., 2006, Parsons et al., 2016), the South Cyclades Shear Zone (Baldwin and Lister, 1998), the Norumbega Fault Zone (West and Hubbard, 1997).

The methods to ascertain the conditions of deformation on exhumed ductile shear zones used in this study include; microstructural analysis to ascertain temperature of deformation through calcite twinning (Burkhard, 1993) and recrystallisation in quartz (Stipp et al., 2002) and crystallographic preferred orientation (CPO) distributions (Baëta and Ashbee, 1969, Schmid and Casey, 1986, Law et al., 1990), grain size palaeopiezometry to obtain stress estimates (Stipp and Tullis, 2003, Rutter, 1995), strain-rate estimates using temperatures obtained from microstructure and stress estimates from palaeopiezometry (Rutter, 1995, Stipp et al., 2002) and shear strain from visco plastic self-consistency (VPSC) calibration (Morales et al., 2014).

7.3.1. Temperature

Within the microstructural analysis calcite, quartz and feldspar were the main focus. For calcite, most samples showed type I and type II twinning (Figure 4.8a), with some showing type III twinning (Figure 4.8b, e) and a large proportion of samples displaying some or pervasive type IV twinning, plus twin boundary migration (Figure 4.8d) (Burkhard, 1993). These twin microstructures yeild temperature estimates of 200°C to >250°C (Figure 7.1) (Burkhard, 1993). Close to the Bursa Fault, to the north of the Uludağ Massif the calcite marble samples show brittle microstructure such as fracture and veining which is associated with the later stage uplift of the massif (Figure 7.1). In some samples (eg ULD134, ULD135 and ULD144) (c)<a> slip is evident in pole figures (Figure 5.9a-f) giving temperature estimates of >500°C (Figure 7.1) (Romeo et al., 2007).

In calcite, temperature can also be obtained from grain size, however there are some assumptions with this approach. The relationship used is calibrated for grain growth during recrystallisation so an estimate using this method will give a lower temperature bound (Covey-Crump and Rutter, 1989). The assumption is that the marble recrystallised during deformation (Figure 4.8f) and once deformation ceased grain growth took over which is the reason this method provides a lower bound temperature estimate for this samples (Figure 7.2).

For quartz and feldspar, all samples showed subgrain rotation (SGR) recrystallisation (Figure 4.9b) giving temperatures of 400-500°C (Lloyd and Freeman, 1994, Stipp et al., 2002) (Figure 7.1). Microstructure in samples within the SUG show higher temperature deformation structures such as grain boundary migration (GBM) recrystallisation (500-700°C) (Figure 4.9c) and myrmekite (600°C) and flame perthite (400-500°C) in feldspar (Figure 4.9d, e) (Figure 7.1) (Stipp et al., 2002, Simpson and Wintsch, 1989). From c-axis CPO distributions and c-axis opening angles the temperature is between 400-500°C (Schmid and Casey, 1986, Lloyd et al., 1992, Lloyd and Freeman, 1994).

Within the sample suite the quartzo-feldspathic lithologies are recording the higher temperature deformation of the massif, and the calcite is recording the lower temperature deformation (Figure 7.1 and Figure 7.2). During exhumation the temperature obviously decreases which is recorded in brittle deformation evident in the calcite marble samples and the large scale structure of the Bursa Fault (Figure 3.4). The P-T-t path of the Uludağ Massif (Figure 7.1), including estimates from mineralogy will be discussed further in Section 7.4.

7.3.2. Stress and strain

Stress estimates have been obtained from recrystallised grain size using established palaeopiezometers for calcite (Rutter, 1995) and quartz (Stipp and Tullis, 2003). The estimates gave ranges of ~50-300MPa for calcite and ~15-60MPa for quartz. This difference in stress with calcite recording higher stresses could be a factor of calcite deforming ductiley to lower temperatures than quartz, therefore recording more deformation as grain size reduction. In both the calcite and quartz the highest stresses are found on the Eskişehir Fault (Figure 4.11). On the hundred metre scale, close to the fault the stress estimates show quite a wide range indicating the distribution of stress on smaller strands at this small scale. This stress distribution is evident on a much larger scale, across the massif, with higher stresses indicating localisation of strain during deformation (Figure 7.2). Brodie and Rutter (2000) compared flow data from calcite marble and quartzites at natural strain rates (3×10^{-14} s^{-1}) and found that due to grain size sensitive flow being dominant in calcite at the deformation temperatures found in this study (300-500°C), it is rheologically weaker than quartz where GSS flow occurs only in samples deformed at >700°C with unnaturally small grain sizes. Also whilst quartz is deforming via brittle processes at temperatures below 300°C, calcite is still behaving 'ductiley' allowing dynamic recrystallisation to continue even at low temperatures and therefore recording higher stresses (De Bresser et al., 2002, Bestmann and Prior, 2003).

Estimating stress from grain size has similar errors and limitations that are associated with estimating temperature from grain size (discussed in Section 4.4.1). These errors originate from the grain estimation in Channel5. For both calcite and quartz the grain sizes have quite a large range (17-1412μm and 13-954μm respectively) meaning the standard deviation is often equal to or larger than the mean resulting in a coefficient of variance of 1 or above. This is largely due to the points within the EBSD map not being indexed, therefore creating artificial grain boundaries between indexed and non-indexed points. Also an added problem with the calcite grain size is Channel5 not ignoring twinning, even though it is set to ignore rotations of a certain amount around a certain axis it still picks up some twins, which are often small, leading to a large amount of small grain sizes that are not representative of the sample.

Errors also arise when extrapolating relationships between grain size and stress derived experimentally to natural examples, especially due to differences in experimental conditions such as strain-rate and temperature that cannot be reproduced in laboratory experiments {Rutter, 1995 #151}{Stipp, 2003 #471}. Some samples close to the Bursa Fault have evidence in thin section for brittle processes such as cataclasis which have reduced the grain size further after ductile shear zone processes (Appendix 7A). These samples show higher stresses because of this further re-working through the brittle-ductile transition zone during exhumation, so are not representative of shear zone activity. The small grain size and intense reworking through cataclasis, however, suggests extreme localisation during exhumation on the Bursa Fault.

Estimates of shear strain for calcite have been acquired from first quantifying c-axis fabric strength and then calibrating this with shear strain via VPSC modelling (method explained in Section 5.2.5). From the results, based on fabric strength, samples from the Eskişehir Fault zone show a wide variety in shear strain with high and low values. There are sections of high values within the massif as well, indicating other localised zones of deformation. These results (Figure 7.2) are similar to those found for the Karakoram Fault Zone by Wallis et al. (*Pers Comm*). Previously, studies that have attempted to quantify strain across shear zones have relied on strain markers such as the change in shape of clusters of minerals or pebbles (Coward, 1976, Flinn, 1956), boudinaged layers (Ramsay, 1980) and more recently from the change in geometry of deformed quartz blebs in samples used to investigate CPO development with increasing strain (Menegon et al., 2008). Using VPSC strain calibration provides a method of quantifying strain more continuously across exhumed ductile shear zones as it does not rely on finding strain markers such as those outlined above. VPSC has been implemented in studies on quartz to investigate how CPO fabrics develop with increments of deformation up to a known strain (e.g. Morales et al. (2014)). VPSC can also be used to calibrate fabric strength, measured using the intensity parameter, J-index or M-index (Section 5.2.4), with shear strain to obtain finite shear strain across a shear zone.

The values that can be seen in Figure 5.18 are quite small and not really realistic for a shear zone of this width (~8km) with an offset of ~100km. A study on the Pinet Massif in southern France found shear strains up to $\gamma = 10$ {Dutruge, 1997 #653}. Therefore these values cannot be used as absolute values of shear strain for this shear strain but the pattern of distribution can still be identified.

7.3.3. Strain-rate

Strain rates observed on the surface of the Earth from geodesy can be translated in seismic hazard forecasts. A review paper by Elliott et al. (2016) presented data showing that areas of high strain rate correlate with the highest occurrences of, and strongest, earthquakes based on data from the global strain rate model (Kreemer et al., 2014). Typical 'geological' strain rates for ductile shear zones are in the order of $x10^{-8}$ to $x10^{-13}$. Average strain rates for the Uludağ Massif are 10^{-13} s^{-1} for quartz at 500°C and calcite at 300°C. The reason for the different temperatures for quartz and calcite is because the quartz has recorded higher temperature in the microstructure than calcite (Section 4.4.1). These strain rates fit with other studies of geodetic strain rate for the North Anatolian Fault in the order of 10^{-15} – 10^{-14} s^{-1} (Jiménez-Munt and Sabadini, 2002) and an upper bound of 10^{-8} – 10^{-7} s^{-1} from average interseismic crustal deformation rates (Wright et al., 2001). If the strain rates calculated for different depths of the crust (300°C = 10km, 500°C = ~16km based on an average geothermal gradient of 30°C/km) do not correlate with what is observed at the surface then this has important implications for the feedback loop between the brittle and ductile crust. If a higher strain rate is seen from surface observations then this potentially means the ductile shear zone is more diffuse.

7.1. Evolution of the Uludağ Massif

Figure 7.1 shows a summary of the P-T-t information for the Uludağ Massif, also summarised below. The peak metamorphic age of the gneisses and marble of the Uludağ Group was ~64 Ma, with P-T conditions of 670 ± 40°C and 7.0 ± 1.0 kbar (Okay et al., 2008).

Muscovite and biotite ages show that the gneisses cooled from 350 to 250°C (the closure temperatures of the minerals), between ~50 to 33 Ma (Okay et al., 2008). If a geothermal gradient of ~30°C/km is assumed a constant exhumation rate can be deduced from these data (Figure 7.1). Okay et al. (2008) proposed the range in crystallisation ages of the South Uludağ Granite (30-39Ma) was due to prolonged crystallisation in an active shear zone.

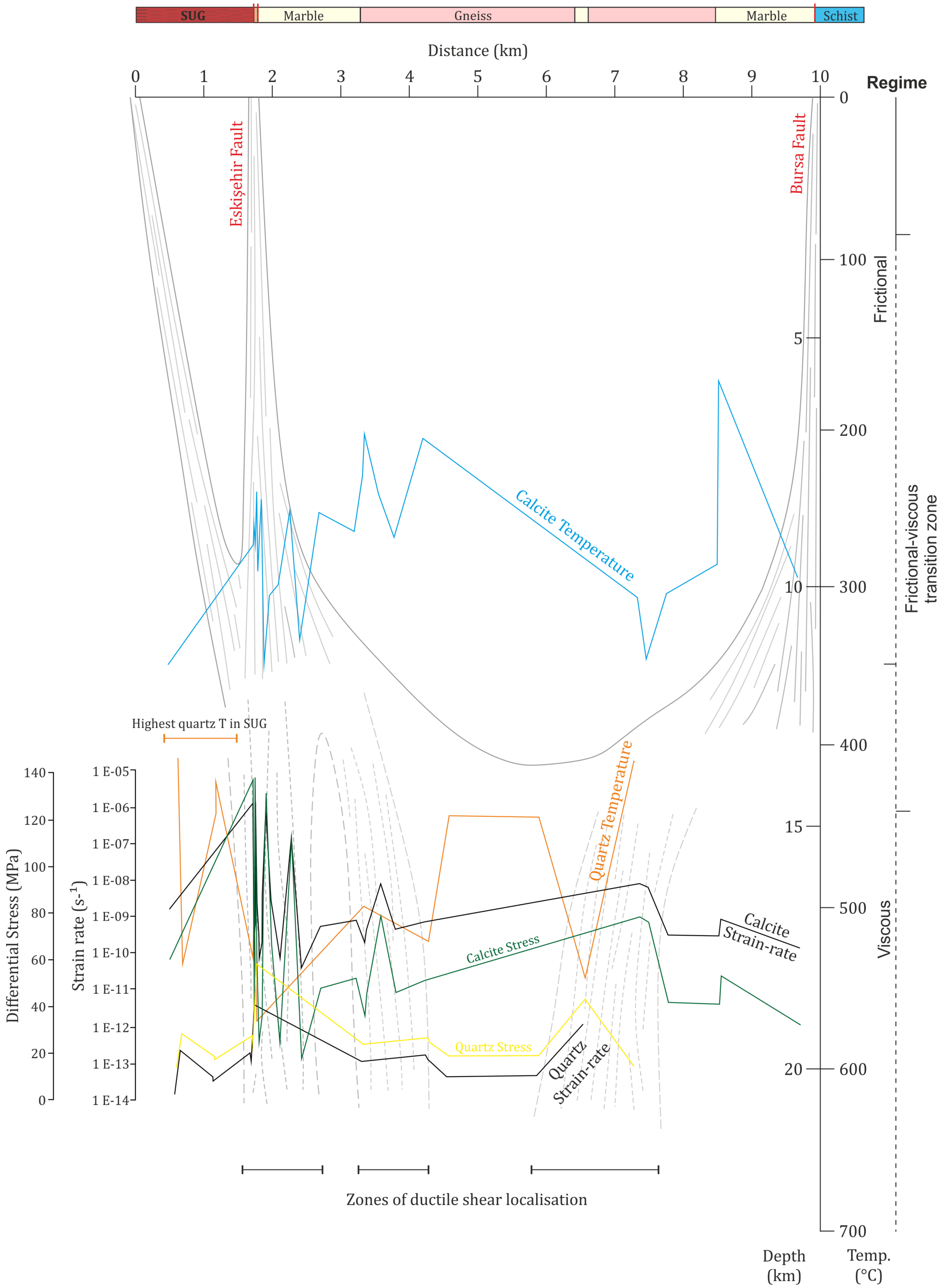

Figure 7.2. All temperature from grain size, stress and strain rate information for the Uludağ Massif. The locations of the faults on the surface are indicated by solid lines through the brittle part of the crust and zones of ductile shear localisation indicated by dashed lines.

For the reasons outlined in Section 7.2.1 it is proposed that the granite was intruded before shear activity but had not completely cooled to ambient temperature before shear initiated, therefore the shear zone must have initiated towards the end of these crystallisation ages (~30Ma). Further development and localisation of the Eskişehir Fault occurred during exhumation, when the rheological difference between the granite and the massif would have been large. This has important implications for the timing of the Uludağ shear zone. The undeformed Central Uludağ Granite gives an intrusion age of 27Ma (Okay et al., 2008), which defines an absolute age to the end of deformation in a strike slip shear zone. Therefore it is proposed by this present study that the age for shear activity was between ~30Ma to 27Ma, putting it in the early Oligocene.

The kinematics of the shear zone were right lateral strike slip shear evidenced from the pervasive fault parallel foliation containing right lateral shear indicators (Section 3.4.1). The conditions of this deformation were ductile with temperatures between 300-500°C, obtained from calcite and quartz-feldspath microstructures. Calcite provides a lower bound as it is more sensitive to deformation at lower temperatures, when quartz is deforming by brittle processes.

Differential stress values for both the calcite and quartz palaeopiezometers vary considerably. The highest stress was found on the Eskişehir Fault, where there has been considerable localisation. The higher stresses in the middle of the massif reflect the localisation of strain in different strands over time as well as the clear strain localisation that is seen in the phyllites and marbles on the Eskişehir Fault.

Apatite fission track ages from Okay et al. (2008) show the end of exhumation with age clusters at 20-22Ma, and at 10-9Ma indicating two periods of accelerated uplift. Exhumation resulted in the overprinting of previously ductile fabrics with more brittle structures, which can be seen mainly in the north of the Uludağ Massif, close to the Bursa Fault. These include fault breccia at a macro-scale, and veins, cataclasite and brittle fracturing of grains within marble at a micro-scale (Figure 4.7).

7.2. Fault structure – relating to the North Anatolian Fault

Numerous continental scale strike slip fault zones including the Alpine, San Andreas, North Anatolian, Dead Sea Transform and Altyn Tagh faults, have been studied to establish the mid to deep-crustal structure. The deep structure of the Alpine Fault, New Zealand, is thought to extend as a narrow zone of localised shear through most of the lower crust with a flatter, ductile detachment near the base of the crust (Norris and Cooper, 2003, Toy et al., 2013, Norris et al., 1990). Seismic data on the San Andreas Fault shows a steeply dipping narrow (few kilometres) zone extending to the base of the crust, and probably offsetting the Moho in northern California (Fuis and Clowes, 1993, Fuis et al., 2001, Fuis et al., 2007, Henstock et al., 1997). The North Anatolian Fault is a major continental scale structure displaying a highly localised zone of deformation accommodating most of the displacement in the westward translation of the Anatolian plate (McCluskey et al., 2000, Jiménez-Munt and Sabadini, 2002, Hubert-Ferrari, 2002). Deformation was found to be consistent with a narrow fault zone through the crust with the possibility of some widening downwards (Wright et al., 2001). In contrast to this, the Dead Sea Transform has been modelled to be a highly localised 20-40km wide zone through the lower crust and upper mantle which becomes more diffuse downwards (Sobolev et al., 2005, Weber et al., 2009). Similarly the Altyn Tagh fault has a wider zone of more distributed deformation including the development of crustal detachments (Devès et al., 2011, Li et al., 2011).

From the temperature, stress, shear strain and strain-rate results of this study it is evident that on this scale (8-10km) deformation is localised into bands separated by areas of weaker deformation (Figure 7.2). However, the Uludağ Massif is only ~10km wide which is realistically a narrow zone of deformation in itself. So strain localisation is dependent on the absolute scale; on the scale of kilometres within the Uludağ Massif, strain clearly localises in bands, but taken as a whole the massif represents diffuse deformation.

7.3. Fault weakening and strengthening

The rheology of the lithosphere and localisation of strain in ductile shear zones is controlled by weakening processes (Regenauer-Lieb et al., 2008). Conversely fault strengthening processes can influence the seismogenic portion of the crust. These weakening and strengthening processes inferred from the exhumed ductile shear zone of the Uludağ Massif may be analogous to processes happening at depth beneath and within the seismogenic zone along the North Anatolian Fault. There are several key weakening mechanisms active in fault zones; low friction phyllosilicate-rich fault gouge (Boulton et al., 2012, Scholz, 1988), elevated pore pressure (Smith et al., 2008), frictional-viscous flow within phyllonitic rocks (Bos and Spiers, 2001, Niemeijer and Spiers, 2005), grain size reduction (De Bresser et al., 2001), reaction softening (Wintsch et al., 1995), thermal perturbations, addition of melt (Leloup et al., 1999).

Fault strengthening and healing are processes active in the seismogenic portion of the crust during an interseismic period (Muhuri et al., 2003). Strengthening processes active in fault zones often include growth and wear of asperities, grain crushing, grain rotation, cementation, recrystallisation, grain bonding, pressure solution and crack sealing (Byerlee et al., 1978, Dieterich and Kilgore, 1994, Mair and Marone, 1999, Marone and Scholz, 1989, Olsen et al., 1998, Power et al., 1988, Sleep and Blanpied, 1992). More recently the activity of slip systems within calcite has been linked to strengthening behaviour which has implications on the depth of seismogenic zones within the crust (Wallis et al., *In Revision* 2017).

7.3.1. Fault weakening processes

It is clear from field observations and stress and strain estimates that the Eskişehir Fault is a localised zone of deformation between 20-30m wide. Within this zone there are numerous fault weakening mechanisms affecting the strength of the rocks and allowing this deformation to localise. It was previously thought that a major contributor to rheological weakening within fault zones was dynamic recrystallisation, however recent evidence from De Bresser et al. (2001) suggest it may be less than previously thought. Samples where dynamic recrystallisation is effective in reducing grain size are at the boundary between grain growth and grain size insensitive (GSI) dislocation creep and grain size reduction and grain size sensitive diffusion creep (De Bresser et al., 2001). At this boundary, and if both GSI and GSS contribute equally then only minor rheological weakening occurs (<25%) (De Bresser et al., 2001). All samples across the massif including within the Eskişehir Fault zone containing quartz, and some marble samples are either completely or partially recrystallised, and even if the above is correct this still represents a minor fault weakening mechanism.

Within the Eskişehir Fault potentially the biggest contributor to fault weakening and therefore velocity strengthening behaviour during deformation is the abundance of phyllosilicates. The samples within the fault contain ~30-50% biotite, muscovite and chlorite (Figure 7.9a), both biotite and muscovite are frictionally weak minerals with low coefficients of friction (μ) (biotite $\mu = 0.25\text{-}0.40$, muscovite $\mu = 0.35\text{-}0.43$ chlorite $\mu = 0.42$) and their high abundance leads to a low bulk rock frictional strength (Ikari et al., 2011, Barth et al., 2013, Boulton et al., 2012, Scruggs and Tullis, 1998, Shimamoto and Logan, 1981). This fault weakening, velocity strengthening behaviour of weak phyllosilicates is active over the whole ductile brittle crust (Wallis et al., 2013).

When dealing with thermal perturbations and temperature increases in shear zones the emphasis is with the process of shear heating. However, in this case the higher temperatures recorded in the microstructure of the SUG indicate a heat source unrelated to deformation. In natural examples, shear heating causes strain localisation in the deeper parts of shear zones (Leloup et al., 1999). The heat from the SUG could act similarly and help localise shear along its boundaries within the Eskişehir Fault.

The South Uludağ Granite also contains biotite, muscovite and chlorite but these minerals are significantly less abundant that in the Eskişehir Fault (Figure 4.10e). However the sericitisation of feldspar is a reaction softening process which forms interconnected layers of weak minerals with μ ~0.4 therefore adding to a low frictional strength of the bulk rock

(Handy, 1990, Tullis and Yund, 1991). This again, contributes to the velocity strengthening behaviour of the rock and promotes aseismic creep (i.e. measurable movement of the fault on the surface that is not associated with earthquakes).

7.3.2. Strain hardening and implications on seismogenic crust

The depth of crust that is seismogenic corresponds to the depth at which frictional failure stress is not exceeded due to aseismic creep processes (Scholz, 1988). Calcite displays velocity weakening behaviour which increases the likelihood of earthquake nucleation along faults within calcite rich lithologies (Han et al., 2010). From Schmid factor analysis some of the marble samples within the Uludağ Massif displayed activity on both {r}- and {f}-slip systems (eg. ULD131 Figure 5.13). De Bresser and Spiers (1997) suggested that strain hardening on the first slip systems to activate, {r}-slip, leads to the transition to a different dominant slip system, {f-}-slip. ULD131 represents a sample that was subject to high stress and localisation of shear at depths relating to 227°C (~7.5km) and ULD135 (Figure 5.11c) at 300°C (~10km) where, if the observations of De Bresser and Spiers (1997) are correct, strain hardening effects that caused the transition from {r}- to {f}-slip could have implications on the depth extent of the seismogenic crust (Wallis et al., *In Revision* 2017).

As mentioned in the previous section the presence of phyllosilicates are fault weakening and velocity strengthening over the ductile and brittle portions of the crust. This may suggest that the Eskişehir Fault have been velocity strengthening throughout its history due to the high proportion of phyllosilicate within the fault zone. However, marble is also present within this fault zone and calcite displays such strong velocity weakening behaviour, therefore any fault containing marble in the frictional crust is a significant seismic hazard (Han et al., 2010). If the Uludağ Massif is an analogue for the North Anatolian Fault, which is suggested in this study, the presence of marble within the seismogenic crust provides earthquake nucleation potential.

7.3.3. Comparison of the Eskişehir and Bursa Faults

The two faults within the Uludağ Massif display very different behaviours. The Eskişehir Fault, as explained above, contains a large proportion of phyllosilicates which promote creep-like behaviour and recorded a more ductile deformation, below the frictional-viscous transition zone in the crust. The Bursa Fault (Figure 3.4) and the samples around it show more brittle architecture and microstructure (Figure 4.7), with cataclasis, brecciated zones, fractures and veining. This fault has recorded brittle behaviour during exhumation in the portion of the crust that responds to deformation through frictional failure (Figure 7.1). The location of the Bursa Fault within marble presents a seismic hazard as outline previously. This seismic hazard is also evident from the earthquake locations in Figure 3.6.

7.4. Seismic response of ductile shear zones

From this study it is apparent that whilst there is variations in the strength of deformation over scales of 100m – 1km, on the scale of 10km strain can be treated as homogeneous. The NAF is thought to have formed at the boundary between two terranes, exploiting a weakness in the crust (i.e. the accretionary complex from the convergence of the two terranes, Section 2.3.1) (Şengör et al., 2005). Studies on the NAF has so far concluded that the fault carries on as a narrow zone of localised deformation at depth (McCluskey et al., 2000, Jiménez-Munt and Sabadini, 2002, Hubert-Ferrari, 2002). From GPS studies the most of the strain is seen in the western portion of the NAF where it transitions into the Aegean (Figure 2.1), partly caused by the transition to extensional tectonics in the southern Aegean (Kahle et al., 1998, McCluskey et al., 2000, Jiménez-Munt and Sabadini, 2002, Reilinger et al., 2006). Further modelling of this GPS field required a strong lithosphere in which the NAF was a major localised zone of lithospheric weakness accommodating all the strain seen in the GPS regional studies (Jiménez-Munt and Sabadini, 2002).

At the eastern end of the North Anatolian Fault, Wright et al. (2001) distinguished a 70km wide region of deformation, which is consistent with the observation of the NAF widening eastwards (Section 2.3.1). Whether this deformation at the surface continued at depth in smaller localised zones of deformation or as a similar distributed zone of shear is unclear, but it is possible that it does widen downwards towards the upper mantle (Wright et al., 2001, Norris and Toy, 2014). Continental plate boundaries are often associated with broad distributions of shear with rotations of crustal rocks about the vertical axis (Platzman et al., 1994). For example, along the San Andreas Fault these rotations affect a zone ~150km adjacent to the fault indicating quite a broad zone of deformation (Luyendyk et al., 1980). Palaeomagnetic data was collected from Eocene and Miocene volcanic rocks associated with the NAF that showed no clockwise crustal rotations leading Platzman et al. (1994) to conclude the zone of deformation is quite narrow, or that possibly the rotations have been masked by elongate fault blocks subparallel to the NAF. Shear wave splitting analysis could reveal information about the distribution of deformation at depth. Within a fault zone it is expected that anisotropy develops parallel to the transport direction, so in a strike slip shear zone, anisotropy would be orientation sub-vertical and parallel to the trace of the fault. However, in the area of the DANA array (Figure 1.3) there are numerous fault splays and segments and also the inherited structure from the NAF exploiting a pre-determined lithospheric weakness means it would not be so simple.

7.4.1. Inferences on structure from this study

From the above it is likely that in the area of the DANA array (Figure 1.3) the NAF continues as a narrow zone of deformation throughout the crust to the mantle this is confirmed by the results from the receiver function study (Kahraman et al., 2015). The results from this study are outlined in Section 6.2.2 and Figure 6.2. In the two north-south profiles, the northern strand of the NAF is seen to disrupt features in a narrow ~10km wide zone, from its ~5km wide surface expression whilst the southern strand of the NAF has a much wider surface expression, ~10km on the western north-south profile (Figure 6.2a), and can be traced down to the Moho as a wider zone reflecting the surface expression.

This study aimed to 'bridge the gap' between geological studies of ductile shear zones and seismological ones by providing models constrained by rock data to investigate any difference in seismic response resulting from differences in lithology or fabric orientation. The Uludağ Massif provides an analogue of the mid-crustal shear zone beneath the NAF. It was chosen as it is within the same terrane as the NAF, the Sakarya terrane and has comparable strike slip kinematics and offset (Section 2.4).

Firstly 4 petrophysical models, each with a shear zone populated with a different sample from the Uludağ Massif, were presented in Section 6.4. All four of these samples had some degree of fault parallel foliation, especially within the gneiss and marble samples. The fault parallel foliation herefore defined a fault parallel anisotropy. This anisotropy was reflected in the transverse components of the gneiss and marble samples (Figure 6.26 – Figure 6.28). The granite sample however, did not promote a big anisotropic response in the transverse component (Figure 6.25) because it did not have a clearly defined foliation (Figure 6.11).

From these models it is apparent that any lithology, with a fault parallel foliation, will produce a similar seismic response. The differences between the seismic properties of different lithologies inferred to be present in the mid-crust beneath the NAF is not large enough to expect a detectable difference in the seismic response.

Secondly, the influence of fabric orientation was investigated using a highly anisotropic amphibolite sample, ULD125 (Figure 6.8). It was thought that a difference between a vertical fabric and horizontal fabric would produce a marked difference in the seismic response. However, again this was not the case, other than a small difference in the Moho arrival within the fault zone (Figure 6.34), which is too small to really be detected, the responses were quite similar.

It is clear however that a shear zone produces a detectable result in the seismic response. A shear zone generally produces a fault parallel foliation and an anisotropy which then produces a significant seismic response. It may not be possible to determine lithology or fabric orientation but the presence of a fault is obvious.

One thing of note is the width of the fault zone in the models influences the wavelength at the sides of the fault, which disrupt the arrivals from the Moho. This isn’t anything new, but could be a possible explanation for the observed ‘gap’ in the Moho beneath the northern strand of the NAF in the receiver function study (Figure 6.2a). In that study, RFs were calculated at 5km spacings, and if two are taken at the sides of the fault to infer the structure in between then this would result in the observed Moho ‘gap’ (Kahraman et al., 2015). This could be further evidence for a narrow shear zone extending toward the Moho, and potentially cutting it.

Appendix 7A

Table containing all information for samples used in this study, blue indicates marble samples.

SAMPLE	Lithology	Mineralogy	Rock Type	LAT	LONG	Foliation (RHR)	Lineation	Distance	Grain Size (µm)	Stress (MPa)	Temp (°C)	Strain rate (T = 300°C)	Strain rate (T = 500°C)	Intensity	J-index	M-index
ULD144	Marble	Cct	Breccia	40.0316	29.2465			-1.916						1.2593	2.5472	0.1876
ULD143	Marble	Cct		40.033296	29.24914	053/60	02/055	-1.607	94.16	60.46	270	2.0737E-15	1.62073E-09	1.6189	2.7799	0.2393
ULD173	Granite	Qtz, Ksp, Plag, Bio, Chl, Musc	Mylonite	40.057611	29.18622	117/70		-1.477	127.40	14.28	558	1.84068E-17	2.80385E-14	0.1256	2.036	0.0251
ULD78	Granite	Qtz, Plag, Ksp, Chl, Bio	Protomylonite	40.063965	29.16861	107/70		-1.376	53.56	28.40	427	2.88135E-16	4.38905E-13	0.6916	4.3326	0.0852
ULD142	Granite	Qtz, Plag, Ksp, Bio, Musc, Chl	Protomylonite	40.0375	29.2502	323/71		-1.134						0.2367	2.6038	0.0373
ULD141	Granite	Qtz, Play, Ksp, Bio, Apt	Protomylonite	40.040554	29.25219	320/75		-0.755	90.82	18.68	523	5.38913E-17	8.20907E-14	0.8393	2.3757	0.12
ULD172	Granite	Qtz, Plag, Ksp, Bio, Musc, Chl	Mylonite	40.062537	29.19114	129/50	43/243	-0.752	97.56	17.65	543	4.29469E-17	6.54196E-14	0.3424	1.6526	0.0492
ULD171	Granite	Qtz, Plag, Ksp, Bio, Musc, Chl	Protomylonite	40.0659	29.1924			-0.374						1.2562	5.3169	0.1859
ULD170	Granite	Qtz, Plag, Ksp, Bio, Musc, Chl	Mylonite	40.0682	29.1930	114/84	08/112	-0.109						0.5718	1.9122	0.0837
ULD140	Granite	Qtz, Plag, Ksp, Bio, Musc, Chl	Mylonite	40.0457	29.2570	292/51	12/303	-0.049						2.2827	5.4125	0.3241
ULD168	Pelite	Qtz, Plag, Hbl, Epd	Ultramylonite	40.068927	29.19271	288/78	08/285	-0.041	55.28	27.69	431	2.60594E-16	3.96953E-13	0.4035	1.7141	0.0577
ULD139	Granite	Qtz, Ksp, Plag, Bio, Musc	Ultramylonite	40.045909	29.25717	288/57	36/324	-0.025	65.69	24.15	464	1.50702E-16	2.29559E-13	0.7535	2.0496	0.109
ULD166	Marble	Cct	Protomylonite	40.069108	29.19279	109/74	11/284	-0.016	26.72	137.13	228	1.69917E-12	1.32802E-06	0.5081	1.5303	0.0768
ULD138	Pelite	Qtz, Plag, Ksp, Bio, Musc, Chl, Epd	Ultramylonite	40.0460	29.2573	278/63	56/331	-0.008						0.4309	1.9641	0.0642
ULD137	Marble	Cct	Mylonite	40.046137	29.25743	285/64		0.000	158.67	38.15	297	2.9449E-16	2.30164E-10	0.5488	1.5458	0.083
ULD136	Pelite	Qtz, Plag, Ksp, Bio, Musc, Chl	Ultramylonite	40.0462	29.2575	290/30	04/292	0.013						0.2145	1.7578	0.0313
ULD165	Marble	Cct		40.06938	29.19298	104/64	08/279	0.017	120.33	49.13	282	7.69532E-16	6.01442E-10	0.4366	1.4623	0.0655
ULD135	Marble	Cct	Protomylonite	40.046243	29.25752	288/75	08/105	0.022	26.37	138.03	227	1.83798E-12	1.43651E-06	0.6249	1.6426	0.0945

ULD164	Pelite	Qtz, Plag, Bio, Hbl, Chl	Mylonite	40.069538	29.19301	275/64	16/284	0.040	21.60	58.39	390	5.14844E-15	7.84243E-12	0.0741	1.2945	0.0153
ULD163	Marble	Cct	Protomylonite	40.069674	29.19308	109/85	80/178	0.051	88.89	63.34	268	2.6674E-15	2.08475E-09	0.5392	1.5489	0.0819
ULD134	Marble	Cct	Protomylonite	40.0465	29.2579	272/52	58/359	0.062						0.5842	2.0144	0.0871
ULD161	Marble	Cct		40.070064	29.193	286/67	21/040	0.085	139.63	42.99	290	4.49657E-16	3.51438E-10	0.6416	1.7139	0.0957
ULD133	Marble	Cct	Protomylonite	40.046917	29.25776	286/60	53/342	0.095	241.30	25.04	325	9.34633E-17	7.30479E-11	0.506	1.5235	0.0763
ULD160	Marble	Cct	Protomylonite	40.070582	29.19326	291/72	12/291	0.146	167.23	36.28	300	2.50012E-16	1.95401E-10	0.227	1.2694	0.0344
ULD132	Marble	Cct		40.04735	29.25832	290/45	02/106	0.162	75.10	72.21	260	5.79673E-15	4.53054E-09	0.4943	1.6006	0.075
ULD131	Marble	Cct	Ultramylonite	40.047824	29.25869	302/72	12/120	0.220	29.07	131.51	230	1.03882E-12	8.11911E-07	0.7943	1.7881	0.1194
ULD159	Marble	Cct	Protomylonite	40.071977	29.1944	102/37	38/204	0.326	82.97	66.89	265	3.63897E-15	2.8441E-09	0.2199	1.2367	0.0331
ULD158	Marble	Cct	Mylonite	40.073617	29.19452	359/07	05/097	0.490	243.34	24.81	325	9.16616E-17	7.16398E-11	0.1672	1.1857	0.0253
ULD130	Marble	Cct		40.051726	29.26103	206/14	06/026	0.707	39.20	111.67	238	1.83046E-13	1.43063E-07	0.9183	1.9901	0.1389
ULD157	Marble	Cct	Protomylonite	40.077895	29.19399	300/75		0.897	325.52	18.02	348	5.05832E-17	3.95342E-11	0.1333	1.2751	0.0202
ULD120	Marble	Cct	Protomylonite	40.054306	29.26798	121/60		1.261	123.28	48.09	283	7.02709E-16	5.49215E-10	0.1634	1.4529	0.0234
ULD156	Gneiss	Qtz, Plag, Bio, Musc, Chl, Epd, Hbl	Mylonite	40.0798	29.2045	120/24	01/299	1.400						0.4213	1.811	0.0596
ULD155	Marble	Cct	Ultramylonite	40.082702	29.21273	020/21		1.940	111.89	52.33	278	1.01844E-15	7.95982E-10	0.1487	1.2696	0.0234
ULD123	Gneiss	Qtz, Plag, Ksp, Bio, Musc	Protomylonite	40.059076	29.2757	287/57		2.076	65.69	24.15	464	1.50702E-16	2.29559E-13	0.7539	2.2839	0.1115
ULD124	Marble	Cct	Protomylonite	40.059098	29.27567	278/50		2.101	167.53	36.22	301	2.48646E-16	1.94334E-10	0.9013	2.3197	0.1341
ULD122	Marble	Cct		40.058952	29.27557	288/67	70/353	2.134	130.68	45.66	286	5.67768E-16	4.4375E-10	0.522	1.7875	0.079
ULD154	Gneiss	Qtz, Plag, Ksp, Bio, Chl, Hbl	Mylonite	40.0848	29.2124	280/22	08/318	2.139						0.6385	2.0822	0.0924
ULD153	Marble	Cct		40.086372	29.21443	311/56		2.405	66.83	78.72	256	1.02458E-14	8.00779E-09	0.4963	1.6034	0.0769
ULD152	Marble	Cct	Ultramylonite	40.088562	29.21658	307/49		2.691	129.09	46.16	286	5.93404E-16	4.63786E-10	0.6031	1.6592	0.091
ULD151	Gneiss	Qtz, Plag, Ksp, Bio, Musc, Chl	Mylonite	40.0894	29.2167	282/40	23/311	2.756						0.3886	1.7903	0.0555
ULD127	Marble	Cct		40.069133	29.2867	294/44	01/294	3.240	114.07	51.47	279	9.44522E-16	7.38208E-10	0.99	2.4316	0.1468
ULD128	Gneiss	Qtz, Plag, Bio, Musc, Chl	Mylonite	40.067519	29.28498	303/32	02/311	3.296	57.92	26.69	441	2.24761E-16	3.4237E-13	0.4089	1.764	0.0591

ULD150	Gneiss	Qtz, Plag, Ksp, Bio, Hbl	Protomylonite	40.093446	29.22142	312/20	318/14	3.344	63.37	24.85	455	1.68978E-16	2.57398E-13	0.5929	2.4767	0.0818
ULD47	Gneiss	Qtz, Plag, Bio, Musc, Chl	Mylonite	40.079116	29.26876	335/32	26/043	3.697	89.20	18.94	521	5.70689E-17	8.6931E-14	0.072	1.2823	0.0129
ULD61	Granite	Qtz, Plag, Ksp, Bio, Musc, Chl, Epd		40.103	29.2400			5.093						0.331	4.4445	0.0424
ULD46	Gneiss	Qtz, Plag, Ksp, Bio	Mylonite	40.092953	29.27757	345/82	84/043	5.406	87.40	19.25	520	6.08712E-17	9.2723E-14	0.7053	2.4639	0.1011
ULD60	Gneiss	Qtz, Plag, Ksp, Bio, Musc, Chl		40.107	29.2420	297/75		5.581						0.4742	5.2308	0.0881
ULD59	Gneiss	Qtz, Plag, Ksp, Musc, Bio, Chl	Mylonite	40.110669	29.2493	331/65		6.288	31.55	43.23	418	1.54688E-15	2.35631E-12	0.5593	1.9	0.0806
ULD43	Granite	Qtz, Plag, Ksp, Musc, Gnt, Apt		40.106135	29.29008			7.220	122.41	14.74	556	2.08966E-17	3.18311E-14	0.953	5.1257	0.1383
ULD58	Marble	Cct	Cataclasite	40.120456	29.25358	310/58NE	22/336	7.336	66.90	78.66	256	1.01963E-14	7.9691E-09	1.0061	2.0564	0.151
ULD42	Marble	Cct	Cataclasite	40.107714	29.29502			7.500	70.00	76.09	258	8.14397E-15	6.36507E-09	0.3935	1.411	0.0589
ULD39	Marble	Cct		40.112	29.2872	345/82	84/043	7.736						0.6704	1.7662	0.1
ULD49	Marble	Cct	Cataclasite	40.148385	29.22612			7.880	143.39	41.95	291	4.10622E-16	3.20929E-10	0.3412	1.3921	0.0524
ULD38	Marble	Cct		40.11618	29.28792			8.843	146.25	41.19	293	3.84129E-16	3.00223E-10	1.1193	2.2682	0.1682
ULD52	Marble	Cct		40.138356	29.24558			8.879	109.86	53.16	277	1.09523E-15	8.55996E-10	0.8289	2.0261	0.1257
ULD16	Marble	Cct	Breccia	40.129	29.2897			9.256						0.1167	1.1153	0.0178
ULD53	Marble	Cct	Fracture	40.144	29.2457			9.481						0.6343	2.2103	0.0937
ULD55	Marble	Cct	Mylonite	40.152425	29.24773	170/06	02/313	10.385	187.76	32.39	308	1.77903E-16	1.39043E-10	0.3096	1.365	0.0476

8. CHAPTER EIGHT

Conclusions and further work

8.1. Conclusions

The Uludağ Massif represents an exhumed mid-crustal shear zone that is analogous to the mid-crust beneath the North Anatolian Fault (NAF). Within this study, the shear zone has been investigated with respect to microstructural evidence for temperature, deformation kinematics, and differential stress and strain-rate estimates to provide a tectonic and thermal evolution for the Uludağ Massif. The fault-weakening and strengthening processes active within shear zones have also been investigated to ascertain the influence of these processes on the seismogenic response of shear zones. CPO derived seismic models have been used to demonstrate the responses of certain lithologies and fabric orientations on the seismic response and lastly, all of the above have been put into wider context relating to the NAF. A summary of the main findings of this study are given below.

8.1.1. Kinematics and deformation conditions

The Uludağ Massif is an exhumed ductile shear zone showing right lateral deformation kinematics evidenced from macro-structural observations in the field and micro-structural evidence from thin sections (Section 3.3.3 and Section 4.3.1 respectively).

From microstructural and electron back scattered diffraction (EBSD) derived crystallographic preferred orientations (CPO) the temperature of deformation is bracketed between ~500°C from quartz-bearing lithologies and ~200-300°C from calcite marbles (Stipp et al., 2002, Burkhard, 1993). The difference in temperature pertaining to the rheological differences between the two minerals, calcite records deformation to lower temperatures than quartz before it behaves in a brittle manner (Kennedy and Logan, 1998, Stipp et al., 2002).

Differential stress estimates, obtained from grain size analysis, gives stresses in the range of 50-300 MPa for calcite and 15-60 MPa for quartz (Rutter, 1995, Stipp and Tullis, 2003). Again, this difference between the two minerals is due to calcite recording ductile deformation through grain size reductions to lower temperatures than quartz.

An average strain rate for the massif, calculated using microstructural temperatures and stress estimates from grain size, are 10^{-13} s^{-1}

Shear strain, calibrated using fabric intensity and VPSC analysis, gives finite shear strains (γ) between 0-0.7.

When plotted against distance, all of the above parameters indentify zones of localised deformation within the shear zone. However this is only evident on the 100m – 1km scale, whereas if viewed on a larger scale (i.e. ~10km) strain appears distributed and homogeneous. Therefore scaling this study on the distribution of strain within larger fault and shear zones must be done with care.

8.1.2. Fault weakening and strengthening mechanisms

The processes that are active during deformation influence the response of a fault seismogenically. In this study several fault weakening mechanisms have been inferred to have been active during deformation on the Eskişehir Fault. These include: high mica content lowering the bulk rock coefficient of friction, grain size reduction in calcite and quartz, sericitisation of feldspar and heating due to the South Uludağ Granite intrusion. All of these factors not only help to localise strain but are also velocity strengthening, allowing a fault to creep.

Marbles have been shown to display strong velocity weakening behaviour which increases the likelihood of earthquake nucleation along faults containing calcite rich lithologies (Han et al., 2010). This is important as if the rocks exposed in the Uludağ Massif are also along the NAF within the seismogenic zone it could have implications on the seismic response and earthquake cycle. Also, Schmid factor analysis identifies the occurrence of f-slip at ~300°C (~10km depth) which could have implications for the depth extent of the seismogenic zone in the crust. For example, De Bresser and Spiers (1997) have proposed that strain hardening on an initial slip system (e.g. r-slip) leads to a change in dominant slip system (e.g. to f-slip).

8.1.3. Seismic signature of the Uludağ Massif – relating to the NAF

It was originally thought that lithology and fabric orientation would have a measurable influence on the seismic response. It was found within this study however, that this is not the case. All samples with a definite foliation-parallel anisotropy evident from their seismic properties gave a similar seismic response. The only sample that differed was the granite as this sample does not show any anisotropy parallel to the foliation (and therefore fault). Varying the fabric response also did not produce a detectable difference in the seismic response. One thing of note is that the width of the fault zone in the models influences the wavelength at the sides of the fault, which disrupt the arrivals from the Moho. This is not a new observation, but could be a possible explanation for the observed ‘gap’ in the Moho beneath the northern strand of the NAF in the receiver function study (Figure 6.2a). In the study, RFs were calculated at 5km spacings, and if two are taken at the sides of the fault to infer the structure in between then this would result in the observed

Moho ‘gap’ (Kahraman et al., 2015). This could be further evidence for a narrow shear zone extending toward the Moho, and potentially cutting it.

8.2. Future Work

The main area of future work lies with the seismic properties and seismic modelling. It would be interesting to look in detail at what influences the response and what can change it. This study found that as long as there is a fabric present, lithology has little influence on the seismic response. What needs to be investigated next is whether samples with the same lithology but varying degrees of fabric strength have any affect.

There were also some problems with the parameters used for the modelling, mainly in that the time spacing (dt) is too long for the input P-wave velocity. The effect on the response if this time spacing parameter is altered should be investigated thoroughly. At the time it was not perceived to be a problem as the receiver functions were sampling s-wave conversions.

To make the results more comparable to the RF study on the NAF (Kahraman et al., 2015) it would be useful to use a similar back azimuthal range for the seismograms, which can then be used to compute RFs and subsequent RF stacks that will contain comparable information. Also trying to populate more complicated models with more than one sample-derived elastic tensor. For example having two fault zones, separated by the high velocity or low velocity zone in the crust. Rather than fabric orientation the high and low velocity zones could be related to lithology, with either granitic intrusions that have no fabric being the low velocity zones or amphibolites being the high velocity zones.

There are many factors that could influence the seismic response of the mid to lower-crust but the fact that lithology and/or fabric do not seem be one of them is surprising and needs to be looked into in more detail.

On the topic of elastic tensors and modelling, one line of investigation could be to populate fault initiation and growth models with elastic tensors from the rock data in this study. For example, an exhumation model using samples relating to the different lithological units of the Uludağ Massif and exploring what kind of deformation field (kinematics) would result in exhumation, or where faults that aid in exhumation will naturally localise. It is thought that the NAF initiated along a pre-defined weakness due to the suture zone between two continents (Şengör et al., 2005) which means the original fabric before strike slip initiated would be quite different to what it is now. There were a number of ophiolitic lithologies in the field area that were sampled, it could be interesting to populate models with these and a fabric orientated to replicate continental collision to see where faults would localise and how they would grow.

A section of this thesis that was not really explored in a lot of detail was the Schmid factor analysis. It would be useful to look at the microstructure of individual calcite samples and really constrain temperatures so that a detailed exhumation, or temperature variation path could be constructed. Identifying samples with a bi-modal grain size where the original size of weakly recrystallised grains can be established would give an upper bound on temperatures using the grain growth relationship of Covey-Crump and Rutter (1989). This would allow further analysis of the impact of temperature and/or stress on the activity of slip systems and the seismogenic potential relating to stratigraphic height in the crust.

One major problem is scaling up the observations in the Uludağ Massif to a large scale shear zone. As has been stated previously stress, strain, temperature and strain-rate all vary across the massif, highlighting zones of more intense deformation. However this is apparent only on the scale of 100m – 1km. It is often said that the small scale is indicative of the larger scale but up-scaling must be done with care. Other studies such as on the Karakoram Fault Zone (Wallis, 2014) and the Annapurna Massif (Parsons, 2015) had the advantage of exposure on a much larger scale and into undeformed regions at the same structural level. This study does not have this same advantage, either side of the massif is undeformed, but at different (higher) structural levels than the ductile shear zone. It would advantageous to investigate this further and ascertain if any scalable relationship does exist with what is seen in the Uludağ Massif and what is beneath other shear zones and the NAF especially.

AHRENS, T. J. 1995. Mineral Physics and Crystallography: A Handbook of Physical Constants. *American Geophysical Union, United States of America*.

AKBAŞ, B., AKDENIZ, N., AKSAY, A., ALTUN, İ., BALCı, V., BILGINER, E., BILGIÇ, T., DURU, M., ERCAN, T., GEDIK, İ., GÜNAY, Y., GÜVEN, İ. H., HAKYEMEZ, H. Y., KONAK, N., PAPAK, İ., PEHLIVAN, Ş., SEVIN, M., ŞENEL, M., TARHAN, N., TURHAN, N., TÜRKECAN, A., ULU, Ü., UĞUZ, M. F. & YURTSEVER, A. Turkey Geology Map, General Directorate of Mineral Research and Exploration Publications. *Ankara, Turkey*.

ALEKSANDROV, K., ALCHIKOV, U., BELIKOV, B., ZASLAVSKII, B. & KRUPNYI, A. 1974. Velocities of elastic waves in minerals at atmospheric pressure and increasing precision of elastic constants by means of EVM. *Izv. Acad. Sci. USSR, Geol. Ser,* 10**,** 15-24.

ALEKSANDROV, K. & RYZHOVA, T. 1961. Elastic properties of rock-forming minerals II: Layered silicates. *Izv. Acad. Sci. USSR, Geophys. Ser,* 12**,** 186-189.

ALPTEKIN, Ö. 1973. *Focal mechanisms of earthquakes in western Turkey and their tectonic implications.* PhD Thesis, New Mexico Institute of Mining and Technology.

AMBRASEYS, N. & JACKSON, J. 2000. Seismicity of the Sea of Marmara (Turkey) since 1500. *Geophysical Journal International,* 141**,** F1-F6.

AMMON, C. J. 1991. The isolation of receiver effects from teleseismic P waveforms. *Bulletin of the seismological Society of America,* 81**,** 2504-2510.

ANCZKIEWICZ, R., VIOLA, G., MÜNTENER, O., THIRLWALL, M., VILLA, I. M. & QUONG, N. Q. 2007. Structure and shearing conditions in the Day Nui Con Voi massif: Implications for the evolution of the Red River shear zone in northern Vietnam. *Tectonics,* 26.

ANDERSON, E. M. 1951. *The Dynamics of Faulting, Etc.(Revised.)*, Edinburgh, London.

AUDET, P. 2015. Layered crustal anisotropy around the San Andreas Fault near Parkfield, California. *Journal of Geophysical Research: Solid Earth,* 120**,** 3527-3543.

AUDET, P., BOSTOCK, M. G. & MERCIER, J.-P. 2007. Teleseismic waveform modelling with a one-way wave equation. *Geophysical Journal International,* 171**,** 1212-1225.

BABUŠKA, V. & CARA, M. 1991. *Seismic anisotropy in the Earth*, Springer.

BACHMANN, F., HIELSCHER, R. & SCHAEBEN, H. 2010. Texture analysis with MTEX–free and open source software toolbox. *Solid State Phenomena, Trans Tech Publ,* 160**,** 63-68.

BAËTA, R. & ASHBEE, K. 1969. Slip systems in quartz. 1. Experiments. *American Mineralogist,* 54**,** 1551-1573.

BALDWIN, S. L. & LISTER, G. S. 1998. Thermochronology of the South Cyclades Shear Zone, Ios, Greece: Effects of ductile shear in the argon partial retention zone. *Journal of Geophysical Research: Solid Earth,* 103**,** 7315-7336.

BARBER, D., HEARD, H. & WENK, H. 1981. Experimental deformation of dolomite crystals from 20–800 C. *Phys Chem Minerals,* 7**,** 271-286.

BARBER, D. J. & WENK, H.-R. 2001. Slip and dislocation behaviour in dolomite. *European Journal of Mineralogy,* 13**,** 221-243.

BARKA, A. & KADINSKY-CADE, K. 1988. Strike-slip fault geometry in Turkey and its influence on earthquake activity. *Tectonics,* 7**,** 663-684.

BARNHOORN, A., BYSTRICKY, M., BURLINI, L. & KUNZE, K. 2004. The role of recrystallisation on the deformation behaviour of calcite rocks: large strain torsion experiments on Carrara marble. *Journal of Structural Geology,* 26**,** 885-903.

BARRUOL, G. & MAINPRICE, D. 1993. 3D seismic velocities calculated from LPOs and reflectivity of a lower crustal section—example of the Val Sesia (Ivrea Zone, Northern Italy). *Geophys. J. Int,* 115, 1169-1188.

BARTH, N., BOULTON, C., CARPENTER, B., BATT, G. & TOY, V. 2013. Slip localization on the southern Alpine fault, New Zealand. *Tectonics,* 32, 620-640.

BEHRMANN, J. & PLATT, J. 1982. Sense of nappe emplacement from quartz c-axis fabrics; an example from the Betic Cordilleras (Spain). *Earth and Planetary Science Letters,* 59, 208-215.

BEHRMANN, J. H. 1983. Microstructure and fabric transitions in calcite tectonites from the Sierra Alhamilla (Spain). *Geologische Rundschau,* 72, 605-618.

BERBERIAN, F. & BERBERIAN, M. 1981. Tectono-plutonic episodes in Iran. *In: Zagros, Hindu Kush, Himalaya Geodynamic Evolution. American Geophysical Union, Washington, DC*, 5-32.

BESTMANN, M. & PRIOR, D. J. 2003. Intragranular dynamic recrystallization in naturally deformed calcite marble: diffusion accommodated grain boundary sliding as a result of subgrain rotation recrystallization. *Journal of Structural Geology,* 25, 1597-1613.

BINGÖL, E. 1976. Evolution geotectonique de l'Anatolie de l'Ouest. *Bull. Soc. géol. France,* 18, 431-450.

BONS, P. D. & DEN BROK, B. 2000. Crystallographic preferred orientation development by dissolution–precipitation creep. *Journal of Structural Geology,* 22, 1713-1722.

BORG, I. & HEARD, H. 1969. Mechanical twinning and slip in experimentally deformed plagioclases. *Contributions to Mineralogy and Petrology,* 23, 128-135.

BORGES, F. S. & WHITE, S. 1980. Microstructural and chemical studies of sheared anorthosites, Roneval, South Harris. *Journal of Structural Geology,* 2, 273-280.

BOS, B. & SPIERS, C. 2001. Experimental investigation into the microstructural and mechanical evolution of phyllosilicate-bearing fault rock under conditions favouring pressure solution. *Journal of Structural Geology,* 23, 1187-1202.

BOUCHEZ, J.-L. 1977. Plastic deformation of quartzites at low temperature in an area of natural strain gradient. *Tectonophysics,* 39, 25-50.

BOULTON, C., CARPENTER, B., TOY, V. & MARONE, C. 2012. Physical properties of surface outcrop cataclastic fault rocks, Alpine Fault, New Zealand. *Geochemistry, Geophysics, Geosystems,* 13.

BOZKURT, E. 2001. Neotectonics of Turkey–a synthesis. *Geodinamica Acta,* 14, 3-30.

BRAILLON, P. & SERUGHETTI, J. 1976. Déformation plastique de monocristaux de calcite en compression suivant 〈001〉. *physica status solidi (a),* 36, 637-646.

BRINKMANN, R. 1976. *Geology of Turkey*, Enke Stuttgart.

BRODIE, K. & RUTTER, E. 2000. Deformation mechanisms and rheology: why marble is weaker than quartzite. *Journal of the Geological Society,* 157, 1093-1096.

BUNGE, H.-J. 1982. Texture analysis in materials science: mathematical methods. Butterworth's, London.

BUNGE, H., KIEWEL, R., REINERT, T. & FRITSCHE, L. 2000. Elastic properties of polycrystals—influence of texture and stereology. *Journal of the Mechanics and Physics of Solids,* 48, 29-66.

BURKHARD, M. 1993. Calcite twins, their geometry, appearance and significance as stress-strain markers and indicators of tectonic regime: a review. *Journal of Structural Geology,* 15, 351-368.

BYERLEE, J., MJACHKIN, V., SUMMERS, R. & VOEVODA, O. 1978. Structures developed in fault gouge during stable sliding and stick-slip. *Tectonophysics,* 44**,** 161-171.

CARTER, N. L. & RALEIGH, C. B. 1969. Principal stress directions from plastic flow in crystals. *Geological Society of America Bulletin,* 80**,** 1231-1264.

COSSETTE, É., AUDET, P., SCHNEIDER, D. & GRASEMANN, B. 2016. Structure and anisotropy of the crust in the Cyclades, Greece, using receiver functions constrained by in situ rock textural data. *Journal of Geophysical Research: Solid Earth,* 121**,** 2661-2678.

COVEY-CRUMP, S. & RUTTER, E. 1989. Thermally-induced grain growth of calcite marbles on Naxos Island, Greece. *Contributions to Mineralogy and Petrology,* 101**,** 69-86.

COWARD, M. 1976. Strain within ductile shear zones. *Tectonophysics,* 34**,** 181-197.

CZAPLIŃSKA, D., PIAZOLO, S. & ZIBRA, I. 2015. The influence of phase and grain size distribution on the dynamics of strain localization in polymineralic rocks. *Journal of Structural Geology,* 72**,** 15-32.

DANDEKAR, D. P. 1968. Variation in the elastic constants of calcite with temperature. *Journal of Applied Physics,* 39**,** 3694-3699.

DE BRESSER, J., EVANS, B. & RENNER, J. 2002. On estimating the strength of calcite rocks under natural conditions. *Geological Society, London, Special Publications,* 200**,** 309-329.

DE BRESSER, J., PEACH, C., REIJS, J. & SPIERS, C. 1998. On dynamic recrystallization during solid state flow: Effects of stress and temperature. *Geophysical Research Letters,* 25**,** 3457-3460.

DE BRESSER, J. & SPIERS, C. 1997. Strength characteristics of the r, f, and c slip systems in calcite. *Tectonophysics,* 272**,** 1-23.

DE BRESSER, J., TER HEEGE, J. & SPIERS, C. 2001. Grain size reduction by dynamic recrystallization: can it result in major rheological weakening? *International Journal of Earth Sciences,* 90**,** 28-45.

DEVÈS, M., KING, G. C., KLINGER, Y. & AGNON, A. 2011. Localised and distributed deformation in the lithosphere: Modelling the Dead Sea region in 3 dimensions. *Earth and Planetary Science Letters,* 308**,** 172-184.

DEWEY, J. & ŞENGÖR, A. C. 1979. Aegean and surrounding regions: complex multiplate and continuum tectonics in a convergent zone. *Geological Society of America Bulletin,* 90**,** 84-92.

DÍAZ AZPIROZ, M., LLOYD, G. & FERNÁNDEZ, C. 2007. Development of lattice preferred orientation in clinoamphiboles deformed under low-pressure metamorphic conditions. A SEM/EBSD study of metabasites from the Aracena metamorphic belt (SW Spain). *Journal of Structural Geology,* 29**,** 629-645.

DIETERICH, J. H. & KILGORE, B. D. 1994. Direct observation of frictional contacts: New insights for state-dependent properties. *Pure and Applied Geophysics,* 143**,** 283-302.

ELLIOTT, J., WALTERS, R. & WRIGHT, T. 2016. The role of space-based observation in understanding and responding to active tectonics and earthquakes. *Nature communications,* 7**,** 1-16.

ESHELBY, J. D. The determination of the elastic field of an ellipsoidal inclusion, and related problems. Proceedings of the Royal Society of London A: Mathematical, Physical and Engineering Sciences, 1957. The Royal Society, 376-396.

EVANS, M. A. & DUNNE, W. M. 1991. Strain factorization and partitioning in the North Mountain thrust sheet, central Appalachians, USA. *Journal of Structural Geology,* 13**,** 21-35.

FALEIROS, F., MORAES, R., PAVAN, M. & CAMPANHA, G. 2016. A new empirical calibration of the quartz c-axis fabric opening-angle deformation thermometer. *Tectonophysics,* 671**,** 173-182.

FARLA, R., GERALD, J. F., KOKKONEN, H., HALFPENNY, A., FAUL, U. H. & JACKSON, I. 2011. Slip-system and EBSD analysis on compressively deformed fine-grained polycrystalline olivine. *Geological Society, London, Special Publications,* 360**,** 225-235.

FERRILL, D. A. 1991. Calcite twin widths and intensities as metamorphic indicators in natural low-temperature deformation of limestone. *Journal of Structural Geology,* 13**,** 667-675.

FERRILL, D. A., MORRIS, A. P., EVANS, M. A., BURKHARD, M., GROSHONG, R. H. & ONASCH, C. M. 2004. Calcite twin morphology: a low-temperature deformation geothermometer. *Journal of Structural Geology,* 26**,** 1521-1529.

FLINN, D. 1956. On the Deformation of the Funzie Conglomerate, Fetlar, Shetland. *The Journal of Geology,* 64**,** 480-505.

FLINN, D. 1965. On the symmetry principle and the deformation ellipsoid. *Geological Magazine,* 102**,** 36-45.

FLOYD, P. A., GÖNCÜOĞLU, M. C., WINCHESTER, J. A. & YALINIZ, M. K. 2000. Geochemical character and tectonic environment of Neotethyan ophiolitic fragments and metabasites in the Central Anatolian Crystalline Complex, Turkey. *Geological Society, London, Special Publications,* 173**,** 183-202.

FRANCSIS, M. K. 2012. Piezometry and Strain Rate Estimates Along Mid-Crustal Shear Zones. *Masters Thesis, Blacksburg VA.*

FREDERIKSEN, A. & BOSTOCK, M. 2000. Modelling teleseismic waves in dipping anisotropic structures. *Geophysical Journal International,* 141**,** 401-412.

FRIEDMAN, M. & HEARD, H. 1974. Principal stress ratios in Cretaceous limestones from Texas Gulf Coast. *AAPG Bulletin,* 58**,** 71-78.

FUIS, G. & CLOWES, R. 1993. Comparison of deep structure along three transects of the western North American continental margin. *Tectonics,* 12**,** 1420-1435.

FUIS, G., RYBERG, T., GODFREY, N., OKAYA, D. & MURPHY, J. 2001. Crustal structure and tectonics from the Los Angeles basin to the Mojave Desert, southern California. *Geology,* 29**,** 15-18.

FUIS, G. S., KOHLER, M. D., SCHERWATH, M., BRINK, U. T., VAN AVENDONK, H. J. & MURPHY, J. M. 2007. A comparison between the transpressional plate boundaries of South Island, New Zealand, and southern California, USA: The Alpine and San Andreas fault systems. *A Continental Plate Boundary: Tectonics at South Island, New Zealand***,** 307-327.

GAUTIER, P., BRUN, J.-P., MORICEAU, R., SOKOUTIS, D., MARTINOD, J. & JOLIVET, L. 1999. Timing, kinematics and cause of Aegean extension: a scenario based on a comparison with simple analogue experiments. *Tectonophysics,* 315**,** 31-72.

GENC, S. 1987. Geology of the Region between Uludag and Iznik Lake. *IGCP, Project N,* 5**,** 19-25.

GODIN, L., GRUJIC, D., LAW, R. & SEARLE, M. 2006. Channel flow, ductile extrusion and exhumation in continental collision zones: an introduction. *Geological Society, London, Special Publications,* 268**,** 1-23.

GOK, E. & POLAT, O. 2011. An Assessment of the Seismicity of the Bursa Region from a Temporary Seismic Network. *Pure and Applied Geophysics,* 169**,** 659-675.

GÖRÜR, N., OKTAY, F., SEYMEN, I. & ŞENGÖR, A. 1984. Palaeotectonic evolution of the Tuzgölü basin complex, Central Turkey: sedimentary record of a Neo-Tethyan closure. *Geological Society, London, Special Publications,* 17**,** 467-482.

GRIGGS, D. T., TURNER, F. & HEARD, H. 1960. Deformation of Rocks at 500° to 800° C. *Geological Society of America Memoirs,* 79**,** 39-104.

GROSHONG, R. H., PFIFFNER, O. A. & PRINGLE, L. R. 1984. Strain partitioning in the Helvetic thrust belt of eastern Switzerland from the leading edge to the internal zone. *Journal of Structural Geology,* 6**,** 5-18.

HAN, R., HIROSE, T. & SHIMAMOTO, T. 2010. Strong velocity weakening and powder lubrication of simulated carbonate faults at seismic slip rates. *Journal of Geophysical Research: Solid Earth,* 115.

HANDY, M. R. 1990. The solid-state flow of polymineralic rocks. *Journal of Geophysical Research,* 95**,** 8647-8661.

HARRIS, N. B., KELLEY, S. & OKAY, A. I. 1994. Post-collision magmatism and tectonics in northwest Anatolia. *Contributions to Mineralogy and Petrology,* 117**,** 241-252.

HEARD, H. & RALEIGH, C. 1972. Steady-state flow in marble at 500 to 800 C. *Geological Society of America Bulletin,* 83**,** 935-956.

HEILBRONNER, R. & TULLIS, J. 2006. Evolution of c axis pole figures and grain size during dynamic recrystallization: Results from experimentally sheared quartzite. *Journal of Geophysical Research: Solid Earth,* 111. doi: 10.1029/2005JB004194.

HENSTOCK, T. J., LEVANDER, A. & HOLE, J. A. 1997. Deformation in the lower crust of the San Andreas fault system in northern California. *Science,* 278**,** 650-653.

HERWEGH, M., LINCKENS, J., EBERT, A., BERGER, A. & BRODHAG, S. 2011. The role of second phases for controlling microstructural evolution in polymineralic rocks: A review. *Journal of Structural Geology,* 33**,** 1728-1750.

HILL, R. 1952. The elastic behaviour of a crystalline aggregate. *Proceedings of the Physical Society. Section A,* 65**,** 349.

HIPPERTT, J. 1994. Microstructures and c-axis fabrics indicative of quartz dissolution in sheared quartzites and phyllonites. *Tectonophysics,* 229**,** 141-163.

HIRTH, G., TEYSSIER, C. & DUNLAP, J. W. 2001. An evaluation of quartzite flow laws based on comparisons between experimentally and naturally deformed rocks. *International Journal of Earth Sciences,* 90**,** 77-87.

HIRTH, G. & TULLIS, J. 1992. Dislocation creep regimes in quartz aggregates. *Journal of Structural Geology,* 14**,** 145-159.

HUBERT-FERRARI, A. 2002. Morphology, displacement, and slip rates along the North Anatolian Fault, Turkey. *Journal of Geophysical Research,* 107.

HUSSAIN, E., WRIGHT, T. J., WALTERS, R. J., BEKAERT, D., HOOPER, A. & HOUSEMAN, G. A. 2016. Geodetic observations of postseismic creep in the decade after the 1999 Izmit earthquake, Turkey: Implications for a shallow slip deficit. *Journal of Geophysical Research: Solid Earth,* 121**,** 2980-3001.

HUTTON, D. 1982. A tectonic model for the emplacement of the Main Donegal Granite, NW Ireland. *Journal of the Geological Society,* 139**,** 615-631.

IKARI, M. J., MARONE, C. & SAFFER, D. M. 2011. On the relation between fault strength and frictional stability. *Geology,* 39**,** 83-86.

IMBACH, T. 1992. *Thermalwässer von Bursa: geologische und hydrogeologische Untersuchungen am Berg Uludag (NW-Türkei).* PhD Thesis, ETH, Zurich.

IMBER, J., HOLDSWORTH, R., BUTLER, C. & LLOYD, G. 1997. Fault-zone weakening processes along the reactivated Outer Hebrides Fault Zone, Scotland. *Journal of the Geological Society,* 154**,** 105-109.

IMBER, J., HOLDSWORTH, R., SMITH, S., JEFFERIES, S. & COLLETTINI, C. 2008. Frictional-viscous flow, seismicity and the geology of weak faults: a review and future directions. *Geological Society, London, Special Publications,* 299**,** 151-173.

IŞIK, V. & TEKELI, O. 2001. Late orogenic crustal extension in the northern Menderes massif (western Turkey): evidence for metamorphic core complex formation. *International Journal of Earth Sciences,* 89**,** 757-765.

ISMAıL, W. B. & MAINPRICE, D. 1998. An olivine fabric database: an overview of upper mantle fabrics and seismic anisotropy. *Tectonophysics,* 296**,** 145-157.

JAMISON, W. R. & SPANG, J. H. 1976. Use of calcite twin lamellae to infer differential stress. *Geological Society of America Bulletin,* 87**,** 868-872.

JI, S. & MAINPRICE, D. 1990. Recrystallization and fabric development in plagioclase. *The Journal of Geology***,** 65-79.

JI, S., WANG, Q. & XIA, B. 2002. *Handbook of seismic properties of minerals, rocks and ores*, Polytechnic International Press, Canada.

JIMÉNEZ-MUNT, I. & SABADINI, R. 2002. The block-like behavior of Anatolia envisaged in the modeled and geodetic strain rates. *Geophysical research letters,* 29. doi: 10.1029/2002GL015995.

KAHLE, H.-G., STRAUB, C., REILINGER, R., MCCLUSKY, S., KING, R., HURST, K., VEIS, G., KASTENS, K. & CROSS, P. 1998. The strain rate field in the eastern Mediterranean region, estimated by repeated GPS measurements. *Tectonophysics,* 294**,** 237-252.

KAHRAMAN, M., CORNWELL, D. G., THOMPSON, D. A., ROST, S., HOUSEMAN, G. A., TÜRKELLI, N., TEOMAN, U., POYRAZ, S. A., UTKUCU, M. & GÜLEN, L. 2015. Crustal-scale shear zones and heterogeneous structure beneath the North Anatolian Fault Zone, Turkey, revealed by a high-density seismometer array. *Earth and Planetary Science Letters,* 430**,** 129-139.

KATAHARA, K. 1996. Clay mineral elastic properties. *Society of Exploration Geophysicists Technical Program,* Expanded Abstract**,** 1691-1694.

KENDALL, J. M., FISHER, Q. J., CRUMP, S. C., MADDOCK, J., CARTER, A., HALL, S. A., WOOKEY, J., VALCKE, S. L. A., CASEY, M., LLOYD, G. & ISMAIL, W. B. 2007. Seismic anisotropy as an indicator of reservoir quality in siliciclastic rocks. *Geological Society, London, Special Publications,* 292**,** 123-136.

KENNEDY, L. A. & LOGAN, J. M. 1998. Microstructures of cataclasites in a limestone-on-shale thrust fault: implications for low-temperature recrystallization of calcite. *Tectonophysics,* 295**,** 167-186.

KERN, H. & WENK, H. R. 1990. Fabric-related velocity anisotropy and shear wave splitting in rocks from the Santa Rosa mylonite zone, California. *Journal of Geophysical Research: Solid Earth,* 95**,** 11213-11223.

KETIN, İ. 1947. Über die Tektonik des Uludağ-massivs. *Türkiye Jeoloji Kurumu Bülteni,* 1**,** 75-88.

KNIPE, R. & LAW, R. 1987. The influence of crystallographic orientation and grain boundary migration on microstructural and textural evolution in an SC mylonite. *Tectonophysics,* 135**,** 155-169.

KOÇYIGIT, A. 1991. Neotectonic structures and related landforms expressing the contractional and extensional strains along the North Anatolian Fault at the northwestern margin of the Erzincan Basin, NE Turkey. *Bull. Tech. Univ. Istanbul,* 44**,** 455-473.

KOÇYIĞIT, A. 1988. Basic geological characteristics and total offset of the North Anatolian Fault Zone in Suşehri area, NE Turkey. *METU Pure and Applied Sciences,* 22**,** 43-68.

KOÇYIĞIT, A. 2005. The Denizli graben-horst system and the eastern limit of western Anatolian continental extension: basin fill, structure, deformational mode, throw amount and episodic evolutionary history, SW Turkey. *Geodinamica Acta,* 18**,** 167-208.

KOZUR, H. First evidence of Middle Permian ammonitico rosso and further new stratigraphie results in the Permian and Triassic of the Sosio Valley area, western Sicily. Proceedings First Croatian Geological Congress, 1995. 307-310.

KOZUR, H. W., AYDIN, M., DEMIR, O., YAKAR, H., GÖNCÜOGLU, M. & KURU, F. 2000. New stratigraphic and palaeogeographic results from the Palaeozoic and early Mesozoic of the Middle Pontides (northern Turkey) in the Azdavay, Devrekani, Küre and Inebolu areas: implications for the Carboniferous-Early Cretaceous geodynamic evolution and some related remarks to the Karakaya oceanic rift basin. *Geologia Croatica,* 53**,** 209-268.

KREEMER, C., BLEWITT, G. & KLEIN, E. C. 2014. A geodetic plate motion and global strain rate model. *Geochemistry, Geophysics, Geosystems,* 15**,** 3849-3889.

KRUHL, J. 1998. Reply: Prism-and basal-plane parallel subgrain boundaries in quartz: A microstructural geothermobarometer. *Journal of Metamorphic Petrology,* 16**,** 581-589.

LAFRANCE, B., JOHN, B. E. & SCOATES, J. S. 1996. Syn-emplacement recrystallization and deformation microstructures in the Poe Mountain anorthosite, Wyoming. *Contributions to Mineralogy and Petrology,* 122**,** 431-440.

LARSON, K., LAMMING, J. & FAISAL, S. 2014. Microscale strain partitioning? Differential quartz crystallographic fabric development in Phyllite, Hindu Kush, Northwestern Pakistan. *Solid Earth,* 5**,** 1319.

LAW, R. 1990. Crystallographic fabrics: a selective review of their applications to research in structural geology. *Geological Society, London, Special Publications,* 54**,** 335-352.

LAW, R., SCHMID, S. & WHEELER, J. 1990. Simple shear deformation and quartz crystallographic fabrics: a possible natural example from the Torridon area of NW Scotland. *Journal of Structural Geology,* 12**,** 29-45.

LAW, R. D. 2014. Deformation thermometry based on quartz c-axis fabrics and recrystallization microstructures: a review. *Journal of Structural Geology,* 66**,** 129-161.

LEBENSOHN, R. & TOMÉ, C. 1993. A self-consistent anisotropic approach for the simulation of plastic deformation and texture development of polycrystals: application to zirconium alloys. *Acta metallurgica et materialia,* 41**,** 2611-2624.

LEBENSOHN, R., WENK, H.-R. & TOMÉ, C. 1998. Modelling deformation and recrystallization textures in calcite. *Acta Materialia,* 46**,** 2683-2693.

LELOUP, P. H., RICARD, Y., BATTAGLIA, J. & LACASSIN, R. 1999. Shear heating in continental strike-slip shear zones: model and field examples. *Geophysical Journal International,* 136**,** 19-40.

LEVANDER, A. R. 1988. Fourth-order finite-difference P-SV seismograms. *Geophysics,* 53**,** 1425-1436.

LI, Y., WU, Q., ZHANG, F., FENG, Q. & ZHANG, R. 2011. Seismic anisotropy of the Northeastern Tibetan Plateau from shear wave splitting analysis. *Earth and Planetary Science Letters,* 304, 147-157.

LISLE, R. J. 1985. The use of the orientation tensor for the description and statistical testing of fabrics. *Journal of Structural Geology,* 7, 115-117.

LISTER, G. & DORNSIEPEN, U. 1982. Fabric transitions in the Saxony granulite terrain. *Journal of Structural Geology,* 4, 81-92.

LISTER, G. & HOBBS, B. 1980. The simulation of fabric development during plastic deformation and its application to quartzite: the influence of deformation history. *Journal of Structural Geology,* 2, 355-370.

LISTER, G. & WILLIAMS, P. 1979. Fabric development in shear zones: theoretical controls and observed phenomena. *Journal of Structural Geology,* 1, 283-297.

LISTER, G. & WILLIAMS, P. 1983. The partitioning of deformation in flowing rock masses. *Tectonophysics,* 92, 1-33.

LLOYD, G. 1987. Fabric analysis using SEM electron channeling. *Journey of Geological Society,* 144, 675-678.

LLOYD, G., LAW, R., MAINPRICE, D. & WHEELER, J. 1992. Microstructural and crystal fabric evolution during shear zone formation. *Journal of Structural Geology,* 14, 1079-1100.

LLOYD, G. E., BUTLER, R. W. H., CASEY, M. & MAINPRICE, D. 2009. Mica, deformation fabrics and the seismic properties of the continental crust. *Earth and Planetary Science Letters,* 288, 320-328.

LLOYD, G. E., BUTLER, R. W. H., CASEY, M., TATHAM, D. J. & MAINPRICE, D. 2011a. Constraints on the seismic properties of the middle and lower continental crust. *Geological Society, London, Special Publications,* 360, 7-32.

LLOYD, G. E. & FREEMAN, B. 1994. Dynamic recrystallization of quartz under greenschist conditions. *Journal of Structural Geology,* 16, 867-881.

LLOYD, G. E., HALLIDAY, J. M., BUTLER, R. W. H., CASEY, M., KENDALL, J. M., WOOKEY, J. & MAINPRICE, D. 2011b. From crystal to crustal: petrofabric-derived seismic modelling of regional tectonics. *Geological Society, London, Special Publications,* 360, 49-78.

LLOYD, G. E. & KENDALL, J.-M. 2005. Petrofabric-derived seismic properties of a mylonitic quartz simple shear zone: Implications for seismic reflection profiling. *Geological Society, London, Special Publications,* 240, 75-94.

LUYENDYK, B. P., KAMERLING, M. J. & TERRES, R. 1980. Geometric model for Neogene crustal rotations in southern California. *Geological Society of America Bulletin,* 91, 211-217.

MAINPRICE, D. 1990. A FORTRAN program to calculate seismic anisotropy from the lattice preferred orientation of minerals. *Computers & Geosciences,* 16, 385-393.

MAINPRICE, D., BOUCHEZ, J.-L., BLUMENFELD, P. & TUBIÀ, J. M. 1986. Dominant c slip in naturally deformed quartz: implications for dramatic plastic softening at high temperature. *Geology,* 14, 819-822.

MAINPRICE, D., HIELSCHER, R. & SCHAEBEN, H. 2011. Calculating anisotropic physical properties from texture data using the MTEX open-source package. *Geological Society, London, Special Publications,* 360, 175-192.

MAINPRICE, D. & HUMBERT, M. 1994. Methods of calculating petrophysical properties from lattice preferred orientation data. *Surveys in Geophysics,* 15, 575-592.

MAINPRICE, D., LLOYD, G. E. & CASEY, M. 1993. Individual orientation measurements in quartz polycrystals: advantages and limitations for texture and petrophysical property determinations. *Journal of Structural Geology,* 15**,** 1169-1187.

MAINPRICE, D. & NICOLAS, A. 1989. Development of shape and lattice preferred orientations: application to the seismic anisotropy of the lower crust. *Journal of Structural Geology,* 11**,** 175-189.

MAINPRICE, D. & SILVER, P. G. 1993. Interpretation of SKS-waves using samples from the subcontinental lithosphere. *Physics of the Earth and Planetary Interiors,* 78**,** 257-280.

MAIR, K. & MARONE, C. 1999. Friction of simulated fault gouge for a wide range of velocities and normal stresses. *Journal of Geophysical Research: Solid Earth,* 104**,** 28899-28914.

MALPAS, J., CALON, T. & SQUIRES, G. 1993. The development of a late Cretaceous microplate suture zone in SW Cyprus. *Geological Society, London, Special Publications,* 76**,** 177-195.

MARONE, C. & SCHOLZ, C. 1989. Particle-size distribution and microstructures within simulated fault gouge. *Journal of Structural Geology,* 11**,** 799-814.

MASLEN, E., STRELTSOV, V. & STRELTSOVA, N. 1993. X-ray study of the electron density in calcite, CaCO3. *Acta Crystallographica Section B: Structural Science,* 49**,** 636-641.

MATTHIES, S. & WAGNER, F. 1996. On a 1/n law in texture related single orientation analysis. *physica status solidi (b),* 196**,** K11-K15.

MCCLUSKEY, S., BALASSIAN, S., BARKA, A., DEMIR, C., ERGINTAV, S., GEORGIEV, I., GURKAN, O., HAMBURGER, M., HURST, K. & KAHLE, H. 2000. GPS constraints on plate motions and deformations in the eastern Mediterranean: implications for plate tectonics. *J. Geophys. Res,* 105**,** 5695-5719.

MCKENZIE, D. 1972. Active tectonics of the Mediterranean region. *Geophysical Journal of the Royal Astronomical Society,* 30**,** 109-185.

MCKENZIE, D. P. 1970. Plate tectonics of the Mediterranean region. *Nature,* 226**,** 239-243.

MCSKIMIN, H., ANDREATCH JR, P. & THURSTON, R. 1965. Elastic moduli of quartz versus hydrostatic pressure at 25 and− 195.8 C. *Journal of Applied Physics,* 36**,** 1624-1632.

MEADE, B. J., HAGER, B. H., MCCLUSKY, S. C., REILINGER, R. E., ERGINTAV, S., LENK, O., BARKA, A. & ÖZENER, H. 2002. Estimates of seismic potential in the Marmara Sea region from block models of secular deformation constrained by Global Positioning System measurements. *Bulletin of the Seismological Society of America,* 92**,** 208-215.

MENEGON, L., PENNACCHIONI, G., HEILBRONNER, R. & PITTARELLO, L. 2008. Evolution of quartz microstructure and c-axis crystallographic preferred orientation within ductilely deformed granitoids (Arolla unit, Western Alps). *Journal of Structural Geology,* 30**,** 1332-1347.

MICHIBAYASHI, K., MAINPRICE, D., FUJII, A., UEHARA, S., SHINKAI, Y., KONDO, Y., OHARA, Y., ISHII, T., FRYER, P. & BLOOMER, S. H. 2016. Natural olivine crystal-fabrics in the western Pacific convergence region: A new method to identify fabric type. *Earth and Planetary Science Letters,* 443**,** 70-80.

MINGARD, K., ROEBUCK, B., BENNETT, E., THOMAS, M., WYNNE, B. & PALMIERE, E. 2007. Grain size measurement by EBSD in complex hot deformed metal alloy microstructures. *Journal of microscopy,* 227**,** 298-308.

MOIX, P., BECCALETTO, L., KOZUR, H. W., HOCHARD, C., ROSSELET, F. & STAMPFLI, G. M. 2008. A new classification of the Turkish terranes and sutures and its implication for the paleotectonic history of the region. *Tectonophysics,* 451**,** 7-39.

MOLNAR, P. & TAPPONNIER, P. 1975. Cenozoic tectonics of Asia: Effects of a continental collision. *Science,* 189**,** 419-426.

MOLNAR, P. & TAPPONNIER, P. 1978. Active tectonics of Tibet. *Journal of Geophysical Research: Solid Earth,* 83**,** 5361-5375.

MORALES, L. F., LLOYD, G. E. & MAINPRICE, D. 2014. Fabric transitions in quartz via viscoplastic self-consistent modeling part I: Axial compression and simple shear under constant strain. *Tectonophysics,* 636**,** 52-69.

MORALES, L. F., MAINPRICE, D., LLOYD, G. E. & LAW, R. D. 2011. Crystal fabric development and slip systems in a quartz mylonite: an approach via transmission electron microscopy and viscoplastic self-consistent modelling. *Geological Society, London, Special Publications,* 360**,** 151-174.

MOTOHASHI, Y., BRAILLON, P. & SERUGHETTI, J. 1976. Elastic energy, stress field of dislocations, and dislocation parameters in calcite crystals. *physica status solidi (a),* 37**,** 263-270.

MUHURI, S. K., DEWERS, T. A., SCOTT, T. E. & RECHES, Z. E. 2003. Interseismic fault strengthening and earthquake-slip instability: Friction or cohesion? *Geology,* 31**,** 881-884.

NAGAYA, M., ODA, H., AKAZAWA, H. & ISHISE, M. 2008. Receiver functions of seismic waves in layered anisotropic media: Application to the estimate of seismic anisotropy. *Bulletin of the Seismological Society of America,* 98**,** 2990-3006.

NICOLAS, A. 1976. Flow in upper-mantle rocks: some geophysical and geodynamic consequences. *Tectonophysics,* 32**,** 93-106.

NICOLAS, A. & POIRIER, J. P. 1976. *Crystalline plasticity and solid state flow in metamorphic rocks*, John Wiley & Sons.

NIEMEIJER, A. & SPIERS, C. 2005. Influence of phyllosilicates on fault strength in the brittle-ductile transition: Insights from rock analogue experiments. *Geological Society, London, Special Publications,* 245**,** 303-327.

NIKO, S., PILLEVUIT, A. & NISHIDA, T. 1996. Early Late Permian (Wordian) non-ammonoid cephalopods from the Hamrat Duru Group, central Oman Mountains. *Transactions and proceedings of the Palaeontological Society of Japan. New series***,** 522-527.

NORRIS, R., KOONS, P. & COOPER, A. 1990. The obliquely-convergent plate boundary in the South Island of New Zealand: implications for ancient collision zones. *Journal of structural geology,* 12**,** 715-725.

NORRIS, R. J. & COOPER, A. F. 2003. Very high strains recorded in mylonites along the Alpine Fault, New Zealand: implications for the deep structure of plate boundary faults. *Journal of Structural Geology,* 25**,** 2141-2157.

NORRIS, R. J. & TOY, V. G. 2014. Continental transforms: A view from the Alpine Fault. *Journal of Structural Geology,* 64**,** 3-31.

NOWELL, M. M., WITT, R. A. & TRUE, B. 2005. EBSD sample preparation: Techniques, tips, and tricks. *Microscopy and Microanalysis,* 11**,** 504-505.

OCAKOĞLU, F. 2007. A re-evaluation of the Eskişehir Fault Zone as a recent extensional structure in NW Turkey. *Journal of Asian Earth Sciences,* 31**,** 91-103.

OCAKOĞLU, F. & AÇIKALIN, S. 2010. Field evidences of secondary surface ruptures occurred during the 20 February 1956 Eskişehir earthquake in the NW Anatolia. *Journal of earth system science,* 119**,** 841-851.

OKAY, A. & SATIR, M. 2006. Geochronology of Eocene plutonism and metamorphism in northwest. *Geodinamica Acta,* 19**,** 251-266.

OKAY, A., SIYAKO, M. & BURKAN, K. 1991. Geology and tectonic evolution of the Biga Peninsula, northwest Turkey. *Bulletin of the Technical University of Istanbul,* 44**,** 191-256.

OKAY, A. I. 2008. Geology of Turkey: a synopsis. *Anschnitt,* 21**,** 19-42.

OKAY, A. I. & GÖNCÜOĞLU, M. 2004. The Karakaya Complex: a review of data and concepts. *Turkish Journal of Earth Sciences,* 13**,** 77-95.

OKAY, A. I., MONOD, O. & MONIÉ, P. 2002. Triassic blueschists and eclogites from northwest Turkey: vestiges of the Paleo-Tethyan subduction. *Lithos,* 64**,** 155-178.

OKAY, A. I. & SATıR, M. 2000. Coeval plutonism and metamorphism in a latest Oligocene metamorphic core complex in northwest Turkey. *Geological Magazine,* 137**,** 495-516.

OKAY, A. I., SATIR, M., ZATTIN, M., CAVAZZA, W. & TOPUZ, G. 2008. An Oligocene ductile strike-slip shear zone: The Uludag Massif, northwest Turkey--Implications for the westward translation of Anatolia. *Geological Society of America Bulletin,* 120**,** 893-911.

OKAY, A. I., TANSEL, I. & TÜYSÜZ, O. 2001. Obduction, subduction and collision as reflected in the Upper Cretaceous–Lower Eocene sedimentary record of western Turkey. *Geological Magazine,* 138**,** 117-142.

OKAY, A. I. & TUYSUZ, O. 1999. Tethyan sutures of northern Turkey. *Geological Society, London, Special Publications,* 156**,** 475-515.

OKAY, A. I., TUYSUZ, O., SATIR, M., OZKAN-ALTINER, S., ALTINER, D., SHERLOCK, S. & EREN, R. H. 2006. Cretaceous and Triassic subduction-accretion, high-pressure-low-temperature metamorphism, and continental growth in the Central Pontides, Turkey. *Geological Society of America Bulletin,* 118**,** 1247-1269.

OLSEN, M. P., SCHOLZ, C. H. & LÉGER, A. 1998. Healing and sealing of a simulated fault gouge under hydrothermal conditions: Implications for fault healing. *Journal of Geophysical Research: Solid Earth,* 103**,** 7421-7430.

OLSEN, T. S. & KOHLSTEDT, D. L. 1985. Natural deformation and recrystallization of some intermediate plagioclase feldspars. *Tectonophysics,* 111**,** 107-131.

ÖZSAYıN, E. & DIRIK, K. 2007. Quaternary activity of the Cihanbeyli and Yeniceoba fault zones: İnönü-Eskişehir fault system, Central Anatolia. *Turkish Journal of Earth Sciences,* 16**,** 471-492.

PARSONS, A. 2015. Validating models of channel flow, ductile extrusion and exhumation - The Greater Himalayan Sequence, Annapurna Massif. *PhD Thesis*.

PARSONS, A., LAW, R., LLOYD, G., PHILLIPS, R. & SEARLE, M. 2016. Thermo-kinematic evolution of the Annapurna-Dhaulagiri Himalaya, central Nepal: The Composite Orogenic System. *Geochemistry, Geophysics, Geosystems,* 17**,** 1511-1539.

PASSCHIER, C. & TROUW, R. 2005. Microtectonics. 2nd. *Berlin, Springer–Verlag*.

PASSCHIER, C. W. 1991. Geometric constraints on the development of shear bands in rocks. *Geologie en Mijnbouw,* 70**,** 203-211.

PHILLIPS, R. J. & SEARLE, M. P. 2007. Macrostructural and microstructural architecture of the Karakoram Fault: Relationship between magmatism and strike-slip faulting. *Tectonics,* 26.

PHILPOTTS, A. & AGUE, J. 2009. *Principles of igneous and metamorphic petrology*, Cambridge University Press.

PIERI, M., BURLINI, L., KUNZE, K., STRETTON, I. & OLGAARD, D. L. 2001a. Rheological and microstructural evolution of Carrara marble with high shear strain: results from high temperature torsion experiments. *Journal of Structural Geology,* 23, 1393-1413.

PIERI, M., KUNZE, K., BURLINI, L., STRETTON, I., OLGAARD, D., BURG, J.-P. & WENK, H.-R. 2001b. Texture development of calcite by deformation and dynamic recrystallization at 1000K during torsion experiments of marble to large strains. *Tectonophysics,* 330, 119-140.

PLATT, J. 1984. Secondary cleavages in ductile shear zones. *Journal of Structural Geology,* 6, 439-442.

PLATZMAN, E., PLATT, J., TAPIRDAMAZ, G., SANVER, M. & RUNDLE, C. 1994. Why are there no clockwise rotations along the North Anatolian Fault Zone? *Journal of Geophysical Research,* 99, 5695-5719.

POKHAREL, R., LIND, J., KANJARLA, A. K., LEBENSOHN, R. A., LI, S. F., KENESEI, P., SUTER, R. M. & ROLLETT, A. D. 2014. Polycrystal plasticity: comparison between grain-scale observations of deformation and simulations. *Annu. Rev. Condens. Matter Phys.,* 5, 317-346.

POWER, W. L., TULLIS, T. E. & WEEKS, J. D. 1988. Roughness and wear during brittle faulting. *Journal of Geophysical Research: Solid Earth,* 93, 15268-15278.

PRYER, L. & ROBIN, P.-Y. 1995. Retrograde metamorphic reactions in deforming granites and the origin of flame perthite. *Journal of metamorphic Geology,* 13, 645-658.

PRYER, L. L. 1993. Microstructures in feldspars from a major crustal thrust zone: the Grenville Front, Ontario, Canada. *Journal of Structural Geology,* 15, 21-36.

RAMSAY, J. 1980. Shear zone geometry: a review. *Journal of structural geology,* 2, 83-99.

RANDLE, V. & RALPH, B. 1986. A practical approach to the determination of the crystallography of grain boundaries. *Journal of materials science,* 21, 3823-3828.

REGENAUER-LIEB, K., ROSENBAUM, G. & WEINBERG, R. F. 2008. Strain localisation and weakening of the lithosphere during extension. *Tectonophysics,* 458, 96-104.

REILINGER, R., MCCLUSKY, S., ORAL, M., KING, R., TOKSOZ, M., BARKA, A., KINIK, I., LENK, O. & SANLI, I. 1997. Global Positioning System measurements of present-day crustal movements in the Arabia-Africa-Eurasia plate collision zone. *Journal of Geophysical Research: Solid Earth (1978–2012),* 102, 9983-9999.

REILINGER, R., MCCLUSKY, S., VERNANT, P., LAWRENCE, S., ERGINTAV, S., CAKMAK, R., OZENER, H., KADIROV, F., GULIEV, I., STEPANYAN, R., NADARIYA, M., HAHUBIA, G., MAHMOUD, S., SAKR, K., ARRAJEHI, A., PARADISSIS, D., AL-AYDRUS, A., PRILEPIN, M., GUSEVA, T., EVREN, E., DMITROTSA, A., FILIKOV, S. V., GOMEZ, F., AL-GHAZZI, R. & KARAM, G. 2006. GPS constraints on continental deformation in the Africa-Arabia-Eurasia continental collision zone and implications for the dynamics of plate interactions. *Journal of Geophysical Research,* 111.

REMPE, M., MITCHELL, T., RENNER, J., NIPPRESS, S., BEN-ZION, Y. & ROCKWELL, T. 2013. Damage and seismic velocity structure of pulverized rocks near the San Andreas Fault. *Journal of Geophysical Research: Solid Earth,* 118, 2813-2831.

REUSS, A. 1929. Berechnung der fließgrenze von mischkristallen auf grund der plastizitätsbedingung für einkristalle. *ZAMM-Journal of Applied Mathematics and Mechanics/Zeitschrift für Angewandte Mathematik und Mechanik,* 9, 49-58.

ROMEO, I., CAPOTE, R. & LUNAR, R. 2007. Crystallographic preferred orientations and microstructure of a Variscan marble mylonite in the Ossa-Morena Zone (SW Iberia). *Journal of Structural Geology,* 29, 1353-1368.

ROSENBERG, C. L. & STÜNITZ, H. 2003. Deformation and recrystallization of plagioclase along a temperature gradient: an example from the Bergell tonalite. *Journal of Structural Geology,* 25, 389-408.

ROWE, K. & RUTTER, E. 1990. Palaeostress estimation using calcite twinning: experimental calibration and application to nature. *Journal of Structural Geology,* 12**,** 1-17.

RUDNICK, R. L. & FOUNTAIN, D. M. 1995. Nature and composition of the continental crust: a lower crustal perspective. *Reviews of geophysics,* 33**,** 267-309.

RUTTER, E. & BRODIE, K. 2004. Experimental intracrystalline plastic flow in hot-pressed synthetic quartzite prepared from Brazilian quartz crystals. *Journal of Structural Geology,* 26**,** 259-270.

RUTTER, E., CASEY, M. & BURLINI, L. 1994. Preferred crystallographic orientation development during the plastic and superplastic flow of calcite rocks. *Journal of Structural Geology,* 16**,** 1431-1446.

RUTTER, E. H. 1995. Experimental study of the influence of stress, temperature, and strain on the dynamic recrystallization of Carrara marble. *Journal of Geophysical Research: Solid Earth (1978–2012),* 100**,** 24651-24663.

SACHS, G. 1928. Plasticity problems in metals. *Transactions of the Faraday Society,* 24**,** 84-92.

SANDISON, D. 1855. Notice of the Earthquakes at Brussa. *Quarterly Journal of the Geological Society,* 11**,** 543-544.

SAROGLU, F. 1988. Age and offset of the North Anatolian Fault. *Middle East Tech. Univ. J. Pure Appl. Sci,* 31**,** 65-79.

SAROGLU, F., EMRE, O. & KUSCU, I. 1992. Active fault map of Turkey. *General Directorate of Mineral Research and Exploration, Ankara*.

SAYıT, K. & GÖNCÜOGLU, M. C. 2009. Geochemistry of mafic rocks of the Karakaya complex, Turkey: evidence for plume-involvement in the Palaeotethyan extensional regime during the Middle and Late Triassic. *International Journal of Earth Sciences,* 98**,** 367-385.

SAYıT, K. & GÖNCÜOGLU, M. C. 2013. Geodynamic evolution of the Karakaya Mélange Complex, Turkey: A review of geological and petrological constraints. *Journal of Geodynamics,* 65**,** 56-65.

SAYIT, K., TEKIN, U. K. & GÖNCÜOGLU, M. C. 2011. Early-middle Carnian radiolarian cherts within the Eymir Unit, Central Turkey: Constraints for the age of the Palaeotethyan Karakaya Complex. *Journal of Asian Earth Sciences,* 42**,** 398-407.

SCHMID, E. Zn-normal stress law. Proceedings of International Congress on Applied Mechanics, 1928.

SCHMID, E. & BOAS, W. 1950. Plasticity of crystals. *Chapman and Hall, London*.

SCHMID, S. 1994. Textures of geological materials: computer model predictions versus empirical interpretations based on rock deformation experiments and field studies. *Textures of Geological Materials. DGM Informationsgesellschaft Verlag, Oberursel***,** 279-301.

SCHMID, S. & CASEY, M. 1986. Complete fabric analysis of some commonly observed quartz c-axis patterns. *Mineral and Rock Deformation: Laboratory Studies,* Geophysical Monograph 36**,** 263-286.

SCHMID, S., CASEY, M. & STARKEY, J. 1981. The microfabric of calcite tectonites from the Helvetic nappes (Swiss Alps). *Geological Society, London, Special Publications,* 9**,** 151-158.

SCHMID, S., PANOZZO, R. & BAUER, S. 1987. Simple shear experiments on calcite rocks: rheology and microfabric. *Journal of Structural Geology,* 9**,** 747-778.

SCHMID, S., PATERSON, M. & BOLAND, J. 1980. High temperature flow and dynamic recrystallization in Carrara marble. *Tectonophysics,* 65, 245-280.

SCHOLZ, C. 1988. The brittle-plastic transition and the depth of seismic faulting. *Geologische Rundschau,* 77, 319-328.

SCRUGGS, V. & TULLIS, T. 1998. Correlation between velocity dependence of friction and strain localization in large displacement experiments on feldspar, muscovite and biotite gouge. *Tectonophysics,* 295, 15-40.

SELÇUK, A. S. & GÖKTAN, Y. E. 2012. Neotectonic Characteristics of the İnönü-Eskişehir Fault System in the Kaymaz (Eskişehir) Region: Influence on the Development of the Mahmudiye-Çifteler-Emirdağ Basin. *Turkish Journal of Earth Sciences,* 21, 521-545.

SELIM, H. H. & TÜYSÜZ, O. 2013. The Bursa–Gönen Depression, NW Turkey: a complex basin developed on the North Anatolian Fault. *Geological Magazine,* 150, 801-821.

SELLAMI, S., PAVONI, N., MAYER-ROSA, D., MUELLER, S., EYIDOGAN, H., AKTAR, M., GÜRBÜZ, C., BARIS, S., POLAT, O. & YALCIN, N. 1997. Seismicity and seismotectonics of the Bursa region. *The Marmara Poly-Project,* ETH, Zurich, 449-486.

SENGÖR, A. 1979. The North Anatolian transform fault: its age, offset and tectonic significance. *Journal of the Geological Society,* 136, 269-282.

ŞENGÖR, A. 1985. Strike-slip faulting and related basin formation in zones of tectonic escape: Turkey as a case study. *Journal of Society of Economic Paleontology and Mineralogists,* 37, 227-264.

ŞENGÖR, A. 1987. Tectonics of the Tethysides: Orogenic collage development in a collisional setting. *Annual Review of Earth and Planetary Sciences,* 15, 213.

SENGÖR, A. & YILMAZ, Y. 1981. Tethyan evolution of Turkey: a plate tectonic approach. *Tectonophysics,* 75, 181-241.

ŞENGÖR, A. M. C., TÜYSÜZ, O., İMREN, C., SAKıNÇ, M., EYIDOĞAN, H., GÖRÜR, N., LE PICHON, X. & RANGIN, C. 2005. The North Anatolian Fault: A New Look. *Annual Review of Earth and Planetary Sciences,* 33, 37-112.

SHIMAMOTO, T. & LOGAN, J. M. 1981. Effects of simulated clay gouges on the sliding behavior of Tennessee sandstone. *Tectonophysics,* 75, 243-255.

SIBSON, R. 1977. Fault rocks and fault mechanisms. *Journal of the Geological Society,* 133, 191-213.

SIBSON, R. H. 1983. Continental fault structure and the shallow earthquake source. *Journal of the Geological Society,* 140, 741-767.

SIMPSON, C. & WINTSCH, R. 1989. Evidence for deformation-induced K-feldspar replacement by myrmekite. *Journal of metamorphic Geology,* 7, 261-275.

SKEMER, P., KATAYAMA, I., JIANG, Z. & KARATO, S.-I. 2005. The misorientation index: Development of a new method for calculating the strength of lattice-preferred orientation. *Tectonophysics,* 411, 157-167.

SLEEP, N. H. & BLANPIED, M. L. 1992. Creep, compaction and the weak rheology of major faults. *Nature,* 359, 687-692.

SMITH, S., COLLETTINI, C. & HOLDSWORTH, R. 2008. Recognizing the seismic cycle along ancient faults: CO 2-induced fluidization of breccias in the footwall of a sealing low-angle normal fault. *Journal of Structural Geology,* 30, 1034-1046.

SOBOLEV, S., PETRUNIN, A., GARFUNKEL, Z., BABEYKO, A. Y. & GROUP, D. 2005. Thermo-mechanical model of the Dead Sea Transform. *Earth and Planetary Science Letters,* 238, 78-95.

SPANG, J. H. 1972. Numerical method for dynamic analysis of calcite twin lamellae. *Geological Society of America Bulletin,* 83**,** 467-472.

SPIERS, C. 1979. Fabric development in calcite polycrystals deformed at 400-degrees-c. *Bulletin de Minéralogie,* 102**,** 282-289.

SPIERS, C. & RUTTER, E. 1984. A calcite twinning palaeopiezometer. *Progress in Experimental Petrology.* N. E. R. C Publication Series, 241-245.

SPIERS, C. & WENK, H. R. Evidence for slip on r and f in the positive sense in deformed calcite single crystals. American Geophysical Union; 1980 fall meeting. Eos, Transactions 61 (46), 1128., 1980.

STALLARD, A. & SHELLEY, D. 1995. Quartz c-axes parallel to stretching directions in very low-grade metamorphic rocks. *Tectonophysics,* 249**,** 31-40.

STAMPFLI, G. M. 2000. Tethyan oceans. *Geological Society, London, Special Publications,* 173**,** 1-23.

STAMPFLI, G. M. & KOZUR, H. W. 2006. Europe from the Variscan to the Alpine cycles. *Geological Society, London, Memoirs,* 32**,** 57-82.

STAMPFLI, G. M., MOSAR, J., FAVRE, P., PILLEVUIT, A. & VANNAY, J.-C. 2001. Permo-Mesozoic evolution of the western Tethys realm: The Neo-Tethys east Mediterranean basin connection. *Mémoires du Muséum national d'histoire naturelle,* 186**,** 51-108.

STEIN, R. S., BARKA, A. A. & DIETERICH, J. H. 1997. Progressive failure on the North Anatolian fault since 1939 by earthquake stress triggering. *Geophysical Journal International,* 128**,** 594-604.

STESKY, R., BRACE, W., RILEY, D. & ROBIN, P.-Y. 1974. Friction in faulted rock at high temperature and pressure. *Tectonophysics,* 23**,** 177-203.

STIPP, M., STUÈNITZ, H., HEILBRONNER, R. & SCHMID, S. M. 2002. The eastern Tonale fault zone: a 'natural laboratory'for crystal plastic deformation of quartz over a temperature range from 250 to 700 C. *Journal of Structural Geology,* 24**,** 1861-1884.

STIPP, M. & TULLIS, J. 2003. The recrystallized grain size piezometer for quartz. *Geophysical Research Letters,* 30.

STORCHAK, D. A., DI GIACOMO, D., BONDÁR, I., ENGDAHL, E. R., HARRIS, J., LEE, W. H., VILLASEÑOR, A. & BORMANN, P. 2013. Public release of the ISC–GEM global instrumental earthquake catalogue (1900–2009). *Seismological Research Letters,* 84**,** 810-815.

SUN, L., THOMAS, M., WYNNE, B., PALMIERE, E., MINGARD, K. & ROEBUCK, B. 2010. Mapping microstructure inhomogeneity using electron backscatter diffraction in 316L stainless steel subjected to hot plane strain compression tests. *Materials Science and Technology,* 26**,** 1477-1486.

SYLVESTER, A. & CHRISTIE, J. 1968. The origin of crossed-girdle orientations of optic axes in deformed quartzites. *The Journal of Geology,* 76**,** 571-580.

TAPPONNIER, P., PELTZER, G., LE DAIN, A., ARMIJO, R. & COBBOLD, P. 1982. Propagating extrusion tectonics in Asia: New insights from simple experiments with plasticine. *Geology,* 10**,** 611-616.

TATHAM, D. J., LLOYD, G. E., BUTLER, R. W. H. & CASEY, M. 2008. Amphibole and lower crustal seismic properties. *Earth and Planetary Science Letters,* 267**,** 118-128.

TAYLOR, G. I. 1938. Analysis of plastic strain in a cubic crystal. *Journal of Institute of Metals,* 62**,** 307-325.

TEN GROTENHUIS, S. M., PASSCHIER, C. W. & BONS, P. D. 2002. The influence of strain localisation on the rotation behaviour of rigid objects in experimental shear zones. *Journal of Structural Geology,* 24, 485-499.

THOMSON, C. 1999. The 'gap'between seismic ray theory and 'full'wavefield extrapolation. *Geophysical Journal International,* 137, 364-380.

THOMSON, C. 2005. Accuracy and efficiency considerations for wide-angle wavefield extrapolators and scattering operators. *Geophysical Journal International,* 163, 308-323.

TÖDHEIDE, K. 1972. Water at high temperature and pressure. *In: Water: a comprehensive treatise, The Physics and Physical Chemistry of Water, Springer, New York*, 463-514.

TOMÉ, C., LEBENSOHN, R. & KOCKS, U. 1991. A model for texture development dominated by deformation twinning: application to zirconium alloys. *Acta Metallurgica et Materialia,* 39, 2667-2680.

TOY, V., NORRIS, R., PRIOR, D., WALROND, M. & COOPER, A. 2013. How do lineations reflect the strain history of transpressive shear zones? The example of the active Alpine Fault zone, New Zealand. *Journal of Structural Geology,* 50, 187-198.

TOY, V. G., PRIOR, D. J. & NORRIS, R. J. 2008. Quartz fabrics in the Alpine Fault mylonites: Influence of pre-existing preferred orientations on fabric development during progressive uplift. *Journal of Structural Geology,* 30, 602-621.

TRULLENQUE, G., KUNZE, K., HEILBRONNER, R., STÜNITZ, H. & SCHMID, S. M. 2006. Microfabrics of calcite ultramylonites as records of coaxial and non-coaxial deformation kinematics: Examples from the Rocher de l'Yret shear zone (Western Alps). *Tectonophysics,* 424, 69-97.

TULLIS, J. 1970. Quartz: preferred orientation in rocks produced by Dauphiné twinning. *Science,* 168, 1342-1344.

TULLIS, J. 1977. Preferred orientation of quartz produced by slip during plane strain. *Tectonophysics,* 39, 87-102.

TULLIS, J. & YUND, R. A. 1987. Transition from cataclastic flow to dislocation creep of feldspar: mechanisms and microstructures. *Geology,* 15, 606-609.

TULLIS, J. & YUND, R. A. 1991. Diffusion creep in feldspar aggregates: experimental evidence. *Journal of Structural Geology,* 13, 987-1000.

TURNER, F. J. 1953. Nature and dynamic interpretation of deformation lamellae in calcite of three marbles. *American Journal of Science,* 251, 276-298.

TURNER, F. J. 1954. Deformation twinning on and in experimentally deformed calcite. *Mineralogy and Petrology,* 4, 28-33.

TURNER, F. J., T GRIGGS, D. & HEARD, H. 1954. Experimental deformation of calcite crystals. *Geological Society of America Bulletin,* 65, 883-934.

TWISS, R. J. 1977. Theory and applicability of a recrystallized grain size paleopiezometer. *Stress in the Earth.* Springer.

VALCKE, S., CASEY, M., LLOYD, G., KENDALL, J.-M. & FISHER, Q. 2006. Lattice preferred orientation and seismic anisotropy in sedimentary rocks. *Geophysical Journal International,* 166, 652-666.

VAUGHAN, M. T. & GUGGENHEIM, S. 1986. Elasticity of muscovite and its relationship to crystal structure. *Journal of Geophysical Research: Solid Earth,* 91, 4657-4664.

VERATI, C. & JOURDAN, F. 2014. Modelling effect of sericitization of plagioclase on the 40K/40Ar and 40Ar/39Ar chronometers: implication for dating basaltic rocks and mineral deposits. *Geological Society, London, Special Publications,* 378, 155-174.

VERNON, R. 2000. Review of microstructural evidence of magmatic and solid-state flow. *Visual Geosciences,* 5, 1-23.

VIRIEUX, J. 1986. P-SV wave propagation in heterogeneous media: Velocity-stress finite-difference method. *Geophysics,* 51, 889-901.

VOEGELÉ, V., CORDIER, P., SAUTTER, V., SHARP, T., LARDEAUX, J. & MARQUES, F. 1998. Plastic deformation of silicate garnets: II. Deformation microstructures in natural samples. *Physics of the Earth and Planetary Interiors,* 108, 319-338.

VOIGHT, W. 1928. Lehrbuch der kristallphysik (mit ausschluss der kristalloptik). *Leipzig–Berlin: BG Teubner*.

VOLLMER, F. W. 1990. An application of eigenvalue methods to structural domain analysis. *Geological Society of America Bulletin,* 102, 786-791.

WALKER, A., RUTTER, E. & BRODIE, K. 1990. Experimental study of grain-size sensitive flow of synthetic, hot-pressed calcite rocks. *Geological Society, London, Special Publications,* 54, 259-284.

WALLIS, D. 2014. Micro-geodynamics of the Karakoram Fault Zone, Ladakh, NW Himalaya. *PhD Thesis*.

WALLIS, D., LLOYD, G., PHILLIPS, R. J., PARSONS, A. & WALSHAW, R. D. *Pers Comm*. Quantifying strain distribution in crustal shear zones.

WALLIS, D., LLOYD, G. E. & HANSEN, L. N. *Unpublished Manuscript*. The transition from dislocation creep to frictional failure in carbonate faults: Schmid factor analysis of marbles within the Karakoram Fault, NW India.

WALLIS, D., LLOYD, G. E., PHILLIPS, R. J., PARSONS, A. J. & WALSHAW, R. D. 2015. Low effective fault strength due to frictional-viscous flow in phyllonites, Karakoram Fault Zone, NW India. *Journal of Structural Geology,* 77, 45-61.

WALLIS, D., PHILLIPS, R. J. & LLOYD, G. E. 2013. Fault weakening across the frictional-viscous transition zone, Karakoram Fault Zone, NW Himalaya. *Tectonics,* 32, 1227-1246.

WALLIS, S., KOBAYASHI, H., NISHII, A., MIZUKAMI, T. & SETO, Y. 2011. Obliteration of olivine crystallographic preferred orientation patterns in subduction-related antigorite-bearing mantle peridotite: an example from the Higashi–Akaishi body, SW Japan. *Geological Society, London, Special Publications,* 360, 113-127.

WEBER, J. C., FERRILL, D. A. & RODEN-TICE, M. K. 2001. Calcite and quartz microstructural geothermometry of low-grade metasedimentary rocks, Northern Range, Trinidad. *Journal of Structural Geology,* 23, 93-112.

WEBER, M., ABU-AYYASH, K., ABUELADAS, A., AGNON, A., ALASONATI-TAŠÁROVÁ, Z., AL-ZUBI, H., BABEYKO, A., BARTOV, Y., BAUER, K. & BECKEN, M. 2009. Anatomy of the Dead Sea Transform from lithospheric to microscopic scale. *Reviews of Geophysics,* 47, doi: 10.1029/2008RG000264.

WEISS, L. & TURNER, F. 1972. Some observations on translation gliding and kinking in experimentally deformed calcite and dolomite. *Flow and Fracture of Rocks,* 16, 95-107.

WEISS, L. E. 1954. *A Study of Tectonic Style. Structural Investigation of a Marble-quartzite Complex in Southern California.,* University of California, Publications of the Geological Society.

WENK, H.-R. 2002. Texture and anisotropy. *Reviews in mineralogy and geochemistry,* 51, 291-329.

WENK, H.-R., CANOVA, G., BRECHET, Y. & FLANDIN, L. 1997. A deformation-based model for recrystallization of anisotropic materials. *Acta Materialia,* 45, 3283-3296.

WENK, H.-R. & CHRISTIE, J. 1991. Comments on the interpretation of deformation textures in rocks. *Journal of Structural Geology,* 13**,** 1091-1110.

WENK, H.-R., TAKESHITA, T., BECHLER, E., ERSKINE, B. & MATTHIES, S. 1987. Pure shear and simple shear calcite textures. Comparison of experimental, theoretical and natural data. *Journal of Structural Geology,* 9**,** 731-745.

WEST, D. P. & HUBBARD, M. S. 1997. Progressive localization of deformation during exhumation of a major strike-slip shear zone: Norumbega fault zone, south-central Maine, USA. *Tectonophysics,* 273**,** 185-201.

WHEELER, J., PRIOR, D., JIANG, Z., SPIESS, R. & TRIMBY, P. 2001. The petrological significance of misorientations between grains. *Contributions to Mineralogy and Petrology,* 141**,** 109-124.

WILSON, C. 1975. Preferred orientation in quartz ribbon mylonites. *Geological Society of America Bulletin,* 86**,** 968-974.

WILSON, C. 1984. Shear bands, crenulations and differentiated layering in ice-mica models. *Journal of structural geology,* 6**,** 303-319.

WINTSCH, R., CHRISTOFFERSEN, R. & KRONENBERG, A. 1995. Fluid-rock reaction weakening of fault zones. *Journal of Geophysical Research: Solid Earth,* 100**,** 13021-13032.

WONG, H., LÜDMANN, T., ULUG, A. & GÖRÜR, N. 1995. The Sea of Marmara: a plate boundary sea in an escape tectonic regime. *Tectonophysics,* 244**,** 231-250.

WOODCOCK, N. 1977. Specification of fabric shapes using an eigenvalue method. *Geological Society of America Bulletin,* 88**,** 1231-1236.

WOODCOCK, N. & NAYLOR, M. A. 1983. Randomness testing in three-dimensional orientation data. *Journal of Structural Geology,* 5**,** 539-548.

WRIGHT, T., PARSONS, B. & FIELDING, E. 2001. Measurement of interseismic strain accumulation across the North Anatolian Fault by satellite radar interferometry. *Geophys. Res. Lett,* 28**,** 2117-2120.

YAMASAKI, T., WRIGHT, T. J. & HOUSEMAN, G. A. 2014. Weak ductile shear zone beneath a major strike-slip fault: Inferences from earthquake cycle model constrained by geodetic observations of the western North Anatolian Fault Zone. *Journal of Geophysical Research: Solid Earth,* 119**,** 3678-3699.

YıLDıRıM, C., EMRE, Ö. & DOĞAN, A. 2005. The uplift of the Uludağ Massif and the Bursa and Uludağ faults. *Abstracts: Eskişehir, Eskişehir Osmangazi University***,** 8.

YOUNG, J., PRESGRAVE, B., AICHELE, H., WIENS, D. & FLINN, E. 1996. The Flinn-Engdahl regionalisation scheme: the 1995 revision. *Physics of the Earth and Planetary Interiors,* 96**,** 223-297.